/N-02

/63 /

p 214

Compressible Flows With Periodic Vortical Disturbances Around Lifting Airfoils

James R. Scott
Lewis Research Center
Cleveland, Ohio

January 1991

NASA

COMPRESSIBLE FLOWS WITH PERIODIC VORTICAL DISTURBANCES AROUND LIFTING AIRFOILS

James R. Scott
National Aeronautics and Space Administration
Lewis Research Center
Cleveland, Ohio 44135

Abstract

A numerical method is developed for solving periodic, three-dimensional, vortical flows around lifting airfoils in subsonic flow. The first-order method that is presented fully accounts for the distortion effects of the nonuniform mean flow on the convected upstream vortical disturbances. The unsteady velocity is split into a vortical component which is a known function of the upstream flow conditions and the Lagrangian coordinates of the mean flow, and an irrotational field whose potential satisfies a nonconstant-coefficient, inhomogeneous, convective wave equation. Using an elliptic coordinate transformation, the unsteady boundary value problem is solved in the frequency domain on grids which are determined as a function of the Mach number and reduced frequency.

The numerical scheme is validated through extensive comparisons with known solutions to unsteady vortical flow problems. In general, it is seen that the agreement between the numerical and analytical results is very good for reduced frequencies ranging from 0 to 4, and for Mach numbers ranging from .1 to .8.

Numerical results are also presented for a wide variety of flow configurations for the purpose of determining the effects of airfoil thickness, angle of attack, camber, and Mach number on the unsteady lift and moment of airfoils subjected to periodic

vortical gusts. It is seen that each of these parameters can have a significant effect on the unsteady airfoil response to the incident disturbances, and that the effect depends strongly upon the reduced frequency and the dimensionality of the gust. For a one-dimensional (transverse) or two-dimensional (transverse and longitudinal) gust, the results indicate that airfoil thickness increases the unsteady lift and moment at the low reduced frequencies but decreases it at the high reduced frequencies. It is seen that mean airfoil loading leads to a significant reduction in the unsteady lift for the low reduced frequencies for both the 2-D and 3-D gust cases, but has little effect for the 1-D case. Finally, the results show that an increase in airfoil Mach number leads to a significant increase in the unsteady lift and moment for the low reduced frequencies, but a significant decrease for the high reduced frequencies.

ACKNOWLEDGEMENTS

There are many people to whom I feel indebted for their help and encouragement as I worked on my dissertation during the last few years. While I cannot mention them all by name, there are some I would like to specifically acknowledge.

First, I would like to acknowledge my advisor, Professor Hafiz Atassi, for his help and guidance during my dissertation research. Working with him has been a rich and rewarding experience which I will long remember.

I would also like to acknowledge Professor Sal Anastasio of the State University of New York at New Paltz. His excellent advice back in the days when I was preparing for a technical career led me to pursue a strong background in applied mathematics and computer science which well prepared me to do theoretical and numerical work in unsteady aerodynamics.

I would like to thank my committee members, Professor Stuart McComas, Professor Victor Nee, and Professor Mihir Sen, for the time they spent reading my dissertation and for their valuable comments.

I would also like to thank Dr. John F. Groeneweg at the NASA Lewis Research Center for his constant support. In addition, I would like to acknowledge numerous other people at NASA Lewis who have helped me in one way or another. Among those I would like to specifically acknowledge are Dr. Charles Feiler, Dr. Ed Rice, Dr. Marvin Goldstein, Dr. Pete Sockol, Dr. John Adamczyk, Dr. Aaron Snyder, Dr. Sin-Chung Chang, Dr. John Lavery, Dr. John Goodrich, Dr. David Jacqmin, Dr. Meng-Sing Liou, and Dr. S. I. Hariharan of ICOMP.

TABLE OF CONTENTS

CHAPTER I

INTRODUCTION

Most flows encountered in aerodynamics are high speed flows where the Reynolds number is large and the effects of viscosity are confined to small regions such as boundary layers and wakes. Because major portions of these flow fields are essentially inviscid and irrotational, potential flow theory has been used extensively by aerodynamicists in the analysis of flows about streamlined bodies. Today steady potential flow solvers are widely used in the design of aircraft wings, turbomachinery blades, and helicopter rotors.

In many real flow applications, however, the flow is not steady but unsteady. Frequently the unsteadiness in the flow is due to the occurrence of upstream vortical disturbances that are convected downstream and induce an unsteady flow field as they interact with the body. For an aircraft wing, such upstream flow distortion can be caused by atmospheric turbulence. For propeller and turbomachinery blades, the vortical disturbances may be caused by the viscous wakes of an upstream rotor or stator, installation effects, or upstream turbulence.

When viewed from the blade frame of reference, the upstream vortical disturbances will appear as propagating vorticity waves that are called gusts. There are a number of undesirable effects that can be associated with such vortical gusts. They will, for example, induce unsteady forces on the airfoil surface which can cause forced vibrations and radiate noise into the far field. In some instances, the impinging gusts may cause flow separation and loss of aerodynamic performance. For rotating blades, the fundamental frequency of the upstream disturbances will equal the blade passing frequency. If the frequency of the aerodynamic excitation equals a natural frequency of the rotating blades and the amplitude is sufficient, then catastrophic structural failure may result.

Another possible source of unsteadiness in the flow is the unsteady motion of

1

the airfoils or blades themselves. Such unsteady structural motion can be caused by structure-borne vibrations as well as the flow-induced oscillations described above. There can also be unsteady interactions between the airfoil motion and the incident disturbances which can dampen or increase the magnitude of the airfoil unsteady motion.

Because of the undesirable effects associated with these unsteady flows, there is considerable interest in controlling and understanding the aerodynamic excitations which can cause such unsteady blade motion.

The earliest attempts to analyze these kinds of unsteady flow fields goes back to the 1920's and 30's when aeronautical engineers sought to deal with vibration problems that arose due to higher flight speeds. The early work dealt with flat plate airfoils at zero mean incidence in incompressible flow. By considering small disturbances to a uniform mean flow, it was possible to linearize about the mean flow state and uncouple the unsteady part of the flow from the underlying steady flow. The basic mathematical tools used by researchers at that time were primarily conformal mapping techniques and the simple concepts of circulation theory. Theodorsen[1] was the first to present a complete analysis for the problem of a flat plate airfoil undergoing sinusoidal, oscillatory motion in an incompressible flow.

The analysis of vortical flows about thin airfoils in incompressible flow was pursued along similar lines. The standard mathematical treatment consisted of decomposing the unsteady velocity into solenoidal and irrotational components. By splitting the unsteady velocity in this way, the mathematical formulation of the gust response problem becomes similar to that of the oscillating airfoil problem. The solenoidal part of the unsteady velocity represents a purely convected vorticity wave whose mathematical expression is a known function of the upstream vortical disturbances. There is no pressure associated with the vortical velocity. The irrotational component of the unsteady velocity is expressed as the gradient of a scalar potential, and is coupled to the vortical component only through the airfoil bound-

2

ary condition. The pressure is determined entirely from the unsteady potential, which for incompressible flows is governed by Laplace's equation. Sears[2] derived an analytical solution for the unsteady lift on a rigid flat plate airfoil moving through a sinusoidal vortical gust pattern in an incompressible flow.

When the mean flow is compressible, the unsteady potential satisfies a homogeneous, constant coefficient, convective wave equation. In this case the mathematical problem can be formulated in terms of an integral equation known as Possio's equation.[3] Numerical results are usually obtained using collocation techniques. Solutions of periodic vortical flows around flat plate airfoils in compressible flow can be found in the recent review paper of Atassi.[4]

For flows around real airfoils with thickness, camber, or angle of attack, the mean flow is no longer uniform. Later work in the analysis of unsteady, vortical flows about airfoils dealt with the problem of mean flow nonuniformities and its effect on the airfoil unsteady response. Horlock[5] used a heuristic approach to partially account for the effects of airfoil incidence on the unsteady lift of airfoils in incompressible flow. Naumann and Yeh[6] used a similar approach to account for the effects of airfoil camber. However, both of these treatments neglected the coupling between the unsteady velocity and the mean potential flow about the airfoil, and only took into account the modified boundary condition at the airfoil surface.

Goldstein and Atassi[7] were the first to present a systematic theory that fully accounts for the effects of the nonuniform mean flow on the airfoil unsteady response. Their analysis of two-dimensional, periodic vortical flows around thin airfoils with small camber and angle of attack showed that the vortical waves are nonlinearly distorted as they are convected by the mean potential flow about the airfoil. Their results showed that the mean flow distortion has a strong effect on the airfoil unsteady response, and that the wave number in the normal direction has a significant effect on the unsteady lift for these kinds of distorted flows.

In a subsequent paper[8], Atassi showed that for thin airfoils in an incompress-

ible flow, it is possible to obtain the airfoil unsteady lift due to two-dimensional, periodic vortical gusts by linear superposition to the Sears lift of three independent components accounting separately for the effects of airfoil thickness, camber, and angle of attack. Explicit analytical formulas are presented in References 7 and 8 for the unsteady lift due to two-dimensional, sinusoidal, vortical gusts about thin airfoils with small mean loading.

By fully accounting for the effects of the nonuniform mean flow, Goldstein and Atassi[7] have introduced the concept of the "rapid distortion theory" of turbulence in unsteady aerodynamics. The rapid distortion approximation was first used by Prandtl[9], Taylor[10], Ribner and Tucker[11], and Batchelor and Proudman[12] to study the change in turbulent structure in a contracting stream. It is based on the approximation that in high speed nonuniform flows, the distortion of large eddies is mainly caused by mean flow variation. This leads to neglecting inter-eddy interaction and subsequently to the linearization of the unsteady governing equations about the nonuniform mean flow.

While the theoretical treatments described above have afforded significant insight in unsteady aerodynamics, they are limited to incompressible flows about airfoils with small mean loading and thickness, or to compressible flows around unloaded, flat plate airfoils with zero thickness. In addition, the vortical disturbances are in general limited to the two-dimensional case, so that spanwise variation of the unsteady flow is not included, except for flat plate results such as are found in Atassi[4] and in Graham.[13]

For most flows encountered in applications, however, one deals with heavily loaded airfoils at high Mach number and with three-dimensional upstream gusts. This is particularly true for turbomachinery and propeller blades, where recent technological trends have led to the development of highly swept, heavily loaded blades that operate in the transonic flow regime. Because of the high sweep, three-dimensional effects are important. In addition, compressibility effects are significant

4

due to the high relative Mach numbers of the rotating blades. Due to the complications of compressibility, heavy loading, and three-dimensional effects, the analysis of these kinds of unsteady flows is clearly beyond the realm of analytical mathematical treatments. The study of such complex flow fields requires the development of computational schemes which can obtain approximate numerical solutions to the unsteady equations governing the flow.

Up until recently, most numerical efforts to solve these kinds of unsteady flows concentrated on potential methods. The early work dealt with solving the unsteady small disturbance potential equation as a way of obtaining the unsteady flow around oscillating airfoils or cascades. Later work was directed toward solving the linearized unsteady potential equation and the unsteady full potential equation. References 14 through 18 represent some of the numerical work that has been done using an unsteady potential formulation.

Potential methods have proven to work well for oscillating airfoil problems, but unfortunately they cannot adequately account for the vortical part of the flow. Previous potential formulations which have included the effects of the upstream vorticity have invoked the linear thin airfoil approximation and assumed that the imposed vortical gust is convected without distortion by the nonuniform mean flow. This was the approach used by McCroskey and Goorjian[19] and McCroskey[20]. However, as shown by Goldstein and Atassi[7] and Atassi[8], the assumption that the gust is convected without distortion is not justified and is a poor approximation for flows with a spatially varying mean flow. This is especially true for turbomachinery and propeller flow fields where the blades are heavily loaded and there are strong mean flow gradients.

In the past few years, computational efforts in unsteady aerodynamics have concentrated on the so-called primitive variable methods, wherein a system of nonlinear equations such as the unsteady Euler or Navier-Stokes equations are solved in time along with certain specified boundary conditions. References 21 through

25 represent some of the recent work in this area. Unlike the potential methods, the primitive variable methods are equally well-suited to both oscillating airfoil problems and flows with convected upstream vorticity.

The major disadvantage of the primitive variable approach is that it requires solving a system of unsteady, nonlinear, partial differential equations. While much progress has been made in this area, there are still a number of difficulties associated with this approach. Among the difficulties are the need for large computer memory and lengthy solution times. Sophisticated algorithms are required to solve the equations, and special grid generation capabilities may also be needed. In addition, uncertainties about far field boundary conditions for time dependent calculations governed by nonlinear equations leaves some question about the accuracy of the solutions. More progress is needed in the development of efficient, accurate algorithms and accurate far field boundary conditions for unsteady, nonlinear problems to make the primitive variable approach more generally useful.

In many unsteady flows, and in particular many turbomachinery flows, the upstream disturbances are small compared to the mean flow, and it is possible to use the linearized approach of the rapid distortion theory to study these "weakly rotational" flows.[4] Goldstein[26] recently proposed a general theory for this approach which leads to a formulation which is valid for compressible, three-dimensional vortical flows around arbitrary bodies. Considering the problem of periodic vortical and entropic disturbances imposed upstream on a mean potential flow field, he showed that the unsteady velocity due to the imposed upstream disturbances can be decomposed into the sum of a known vortical component, a known entropic component, and an unknown irrotational (potential) component. The expressions of the vortical and entropic components are known functions of the upstream unsteady disturbances and the mean flow Lagrangian coordinates. The unsteady potential satisfies a nonconstant-coefficient, inhomogeneous, convective wave equation.

Goldstein's decomposition of the unsteady velocity greatly simplifies the math-

6

ematical treatments of potential mean flows with imposed upstream vortical and entropic disturbances. Whereas a previous formulation by Hunt[27] led to a system of three Poisson equations for the vortical velocity and a Laplace equation for the potential part of the unsteady velocity, Goldstein's formulation leads to a single convective wave equation for the potential part of the unsteady velocity, and the vortical part is obtained from its known functional expression of the upstream disturbances and mean flow quantities.

For most aerodynamic flows of practical interest, there will be a stagnation point near the airfoil leading edge, and at this point the mean flow Lagrangian coordinates will become singular and will remain so along the airfoil surface and its wake. Since Goldstein's vortical velocity is proportional to the gradients of the Lagrangian coordinates, it will also be singular along these surfaces. In order to ensure that the normal velocity vanishes at the airfoil surface, it will then be necessary for the potential part of the unsteady velocity to cancel the singular behavior of the vortical velocity, and therefore the potential must satisfy a singular airfoil boundary condition. Because of these features, it is not possible to use Goldstein's formulation directly for numerical computations for aerodynamic flows with a stagnation point.

Atassi and Grzedzinski[28] have shown that it is possible to modify Goldstein's splitting of the unsteady velocity in such a way as to remove the singular and indeterminate character of the resulting airfoil and wake boundary condition for the unsteady potential. In their decomposition of the unsteady velocity, the vortical component is a known function of the upstream disturbance conditions and the Lagrangian coordinates of the mean potential flow, and has the remarkable property that its normal and streamwise velocity components vanish at the surface of the airfoil and in its wake. The unsteady potential satisfies Goldstein's convective wave equation with a modified source term.

For incompressible flows the governing convective wave equation reduces to a

Poisson equation. Atassi and Grzedzinski[29] used a Green's function formulation to study incompressible, vortical flows about isolated airfoils with arbitrary thickness, camber, and angle of attack. Their analysis assumed three-dimensional, periodic vortical disturbances imposed upstream of a two-dimensional airfoil of infinite span. Their results showed that the airfoil geometry and the upstream three-dimensional conditions of the vortical disturbances has a strong influence on the airfoil unsteady response.

For compressible flows, the governing convective wave equation of Goldstein as modified by Atassi and Grzedzinski has variable coefficients which are functions of the mean flow quantities. In this case it is not possible to formulate the problem in terms of an integral equation or to derive an analytical solution. Due to the effects of compressiblity, therefore, it is necessary to use a full numerical approach to obtain approximate solutions to the resulting boundary value problem.

The major purpose of the present work is to present a frequency domain numerical scheme which has been developed to implement this linearized approach in order to obtain solutions to periodic vortical flows around lifting airfoils of arbitrary thickness, camber, and angle of attack in compressible, subsonic flow. Previous papers[30,31] have presented details of the present approach for the special case of nonlifting airfoils.

The linearized unsteady aerodynamic analysis and solution method that are presented represent an alternative to the potential and primitive variable methods for the solution of unsteady aerodynamic flow problems. The present method offers the computational efficiency of potential methods, but at the same time accounts for the convection and distortion of the upstream vorticity by the nonuniform mean flow. Our approach is therefore equally well-suited to vortical flow problems as well as oscillating airfoil problems. In addition, since our linearization is about the nonuniform mean flow, the full nonlinear effects of the mean flow are accounted for. Only the unsteady part of the flow is linearized. These features, coupled with the

inherent efficiency of the linearized approach, make the present approach an ideal solution method for unsteady aerodynamic flow fields.

In addition to presenting the extension of our numerical scheme to lifting airfoils, another purpose of the present dissertation is to present numerical solutions for a wide range of flow conditions and airfoil geometries in order to assess the relative effects of Mach number, airfoil thickness, camber and angle of attack, and upstream disturbance conditions on the airfoil unsteady response (unsteady lift and moment). Our analysis will consider imposed upstream three-dimensional, vortical disturbances around two-dimensional airfoils of infinite span. We will assume that there are no incident acoustic waves or upstream entropy disturbances.

Although we will not directly concern ourselves with the acoustic radiation in the present dissertation, the method that we present can also give the far field unsteady pressure from which the acoustic radiation can be calculated. This avoids the use of Lighthill's analogy and the tedious calculation which may result from the refraction and scattering of the radiated acoustic waves by the spatially varying flow field. In a future paper, the present approach will be used to calculate the far field acoustic radiation for arbitrary lifting airfoils in subsonic flows. Dusey[32], and Atassi and Dusey[33], have carried out a similar calculation for flat plate airfoils.

In Chapter II we present the general aerodynamic theory and formulate the boundary value problem for the linearized treatment of potential mean flows with imposed upstream, periodic vortical disturbances. In Chapter III we provide the details of the general frequency domain numerical scheme which has been developed for lifting airfoils in subsonic flow. Finally, we present and discuss numerical results for a wide variety of flow conditions in Chapter IV.

CHAPTER II

AERODYNAMIC THEORY

2.1 <u>Linearized Euler Equations</u>

Consider an inviscid, compressible flow past an airfoil placed at nonzero incidence to a stream with uniform upstream velocity U_∞ in the x_1 direction. We shall assume in the present discussion that there are no shocks in the flow. Now if we also assume the fluid to be an ideal, non-heat conducting gas with constant specific heats, then the governing continuity, momentum, and entropy conservation equations can be written

$$\frac{D\rho}{Dt} + \rho\vec{\nabla}\cdot\vec{U} = 0 \tag{2.1}$$

$$\rho\frac{D\vec{U}}{Dt} = -\vec{\nabla}p \tag{2.2}$$

$$\frac{Ds}{Dt} = 0 \tag{2.3}$$

where $\frac{D}{Dt}$ is the material derivative, t denotes time, and ρ, $\vec{U}$, p and s denote the fluid density, velocity, pressure, and entropy, respectively. In addition, by ideal gas, we mean that the pressure p, density ρ, and temperature T are related through a gas constant R by the relation $p = \rho RT$.

In the absence of upstream flow disturbances, and assuming the airfoil to be rigid, there will be a steady flow $\vec{U}_0(\vec{x})$ about the airfoil such that $\vec{U}_0(\vec{x}) \to U_\infty\vec{i}$ as $x_1 \to -\infty$, where $\vec{i}$ is a unit vector in the x_1 direction. Let us suppose that far upstream a small amplitude, unsteady velocity disturbance, which we will denote by $\vec{u}_\infty$, is imposed on the flow. Then since $|\vec{u}_\infty|$ is small compared to U_∞, we assume that there will be small, unsteady perturbations in the physical properties of the otherwise steady flow. It is therefore reasonable to linearize the governing equations (2.1) - (2.3) about the mean flow state and to introduce perturbation quantities as follows:

$$\vec{U}(\vec{x}, t) = \vec{U}_0(\vec{x}) + \vec{u}(\vec{x}, t) \tag{2.4}$$

$$p(\vec{x}, t) = p_0(\vec{x}) + p'(\vec{x}, t) \tag{2.5}$$

$$\rho(\vec{x}, t) = \rho_0(\vec{x}) + \rho'(\vec{x}, t) \tag{2.6}$$

$$s(\vec{x}, t) = s_0 + s'(\vec{x}, t) \tag{2.7}$$

where 0 subscripts denote the steady mean flow quantities, the entropy s_0 is constant, and $\vec{u}$, p', ρ', and s' are the unsteady perturbation velocity, pressure, density and entropy, respectively.

Substituting relations (2.4) - (2.7) into equations (2.1) - (2.3) and neglecting products of small quantities, one obtains the linearized continuity, momentum, and entropy conservation equations

$$\frac{D_0 \rho'}{Dt} + \rho' \vec{\nabla} \cdot \vec{U}_0 + \vec{\nabla} \cdot (\rho_0 \vec{u}) = 0 \tag{2.8}$$

$$\rho_0 \left(\frac{D_0 \vec{u}}{Dt} + \vec{u} \cdot \vec{\nabla} \vec{U}_0 \right) + \rho' \vec{U}_0 \cdot \vec{\nabla} \vec{U}_0 = -\vec{\nabla} p' \tag{2.9}$$

$$\frac{D_0 s'}{Dt} = 0, \tag{2.10}$$

where $\frac{D_0}{Dt} = \frac{\partial}{\partial t} + \vec{U}_0 \cdot \vec{\nabla}$ is the material derivative associated with the mean flow.

Equations (2.8) - (2.10) are the governing partial differential equations for the unknown perturbation quantities $\vec{u}, p', \rho'$, and s' for the problem of small, unsteady disturbances to an otherwise steady flow. The upstream disturbance $\vec{u}_\infty$ is essentially a boundary condition which is imposed on the unsteady velocity $\vec{u}$. That is, we must have $\vec{u} \to \vec{u}_\infty$ as $x_1 \to -\infty$. We shall assume in the present paper that $\vec{u}_\infty$ is the only upstream disturbance imposed on the mean flow, i.e., there are no imposed entropy disturbances or incident acoustic waves.

Now from previous work concerning small amplitude velocity disturbances imposed on a uniform flow, it is known that the unsteady velocity can be decomposed into the sum of a vortical component which has zero divergence, is purely convected,

11

and is decoupled from the pressure and any thermodynamic property, and an irrotational component which is directly related to the pressure but produces no entropy fluctuations.[34,26] Then far upstream the total velocity $\vec{U}$ must be of the form

$$\vec{U} = U_\infty \vec{i} + \vec{u}_\infty (\vec{x} - \vec{i} U_\infty t) \tag{2.11}$$

where

$$\vec{\nabla} \cdot \vec{u}_\infty = 0. \tag{2.12}$$

To first order, there is no pressure associated with the velocity field $\vec{u}_\infty$. The unsteady velocity $\vec{u}$ must satisfy

$$\vec{u}(\vec{x}, t) \to \vec{u}_\infty (\vec{x} - \vec{i} U_\infty t) \quad \text{as} \quad x_1 \to -\infty, \tag{2.13}$$

and the pressure p' obeys

$$p'(\vec{x}, t) \to 0 \quad \text{as} \quad x_1 \to -\infty. \tag{2.14}$$

2.2 Goldstein's Approach

Goldstein[26] proposed a general approach for the analysis of potential mean flows with imposed upstream vortical and entropic disturbances which greatly simplifies the mathematical treatments of such flows. Under the conditions assumed on the flow in previous section, the mean flow can be expressed as the gradient of a potential,

$$\vec{U}_0(\vec{x}) = \vec{\nabla} \Phi_0. \tag{2.15}$$

In the present work we consider two-dimensional mean flow, so that $\vec{U}_0(\vec{x}) = (\frac{\partial \Phi_0}{\partial x_1}, \frac{\partial \Phi_0}{\partial x_2})$.

The simplest case of potential mean flow with imposed upstream disturbances is the thin airfoil problem where the potential flow is simply a uniform parallel flow. In this case it is advantageous to split the unsteady velocity into a vortical

12

component which is solenoidal, and an irrotational component which is expressed as the gradient of an unsteady potential. For the general problem of nonuniform flows around real airfoils, however, the splitting into solenoidal and irrotational components does not lead to any simplification of the mathematical formulation.

Goldstein proposed a new approach wherein the unsteady velocity is decomposed into the sum of a known vortical component $\vec{u}^{(I)}$ and an unknown potential component $\vec{\nabla}\phi$ so that

$$\vec{u}(\vec{x}, t) = \vec{u}^{(I)} + \vec{\nabla}\phi. \tag{2.16}$$

The vortical component $\vec{u}^{(I)}$ is essentially a function of the upstream disturbance $\vec{u}_\infty$ and the mean flow Lagrangian coordinates and their spatial gradients. The unsteady potential satisfies a nonconstant-coefficient, inhomogeneous, convective wave equation

$$\frac{D_0}{Dt}\left(\frac{1}{c_0{}^2}\frac{D_0\phi}{Dt}\right) - \frac{1}{\rho_0}\vec{\nabla}\cdot(\rho_0\vec{\nabla}\phi) = \frac{1}{\rho_0}\vec{\nabla}\cdot(\rho_0\vec{u}^{(I)}), \tag{2.17}$$

where $\frac{D_0}{Dt}$ is the convective derivative associated with the mean flow, and c_0 and ρ_0 are, respectively, the mean flow speed of sound and density. ϕ is related to the pressure by

$$p' = -\rho_0(\vec{x})\frac{D_0\phi}{Dt}. \tag{2.18}$$

The vortical component $\vec{u}^{(I)}$ is in general not solenoidal, but it does become solenoidal far upstream where the mean flow is uniform. For flows with no upstream entropy disturbances, $\vec{u}^{(I)}$ is given by

$$u_i^{(I)} = \vec{u}_\infty(\vec{X} - \vec{i}U_\infty t)\cdot\frac{\partial\vec{X}}{\partial x_i}. \tag{2.19}$$

The components of $(\vec{X} - \vec{i}U_\infty t)$, where $\vec{X} = (X_1, X_2, X_3)$, are essentially Lagrangian coordinates of the mean flow fluid particles. $X_2 = X_2(x_1, x_2, x_3)$ and $X_3 = X_3(x_1, x_2, x_3)$ are functionally independent integrals of the equations

$$\frac{dx_1}{U_1} = \frac{dx_2}{U_2} = \frac{dx_3}{U_3} \tag{2.20a}$$

13

such that

$$X_2 \to x_2 \quad \text{and} \quad X_3 \to x_3 \quad \text{as} \quad x_1 \to -\infty. \qquad (2.20\text{b})$$

For two-dimensional mean flow, we may take

$$X_2 = \frac{\Psi_0}{\rho_\infty U_\infty} \qquad (2.21)$$

and

$$X_3 = x_3, \qquad (2.22)$$

where Ψ_0 is the stream function of the mean flow and x_3 is the spatial coordinate in the spanwise direction. The component X_1 is defined by

$$X_1 = U_\infty \Delta, \qquad (2.23)$$

where Δ is the Lighthill "drift" function[35], which can be expressed in terms of Φ_0 and Ψ_0 as

$$\Delta = \frac{\Phi_0}{U_\infty{}^2} + \int_{-\infty}^{\Phi_0} \left(\frac{1}{U_0{}^2} - \frac{1}{U_\infty{}^2} \right) d\Phi_0, \qquad (2.24)$$

where the integration is carried out on $\Psi_0 = $ constant. The difference in Δ between two points on a streamline is the time it takes a mean flow fluid particle to traverse the distance between those two points.

To complete the formulation of the problem, it is necessary to specify boundary conditions for the unsteady potential ϕ. At the surface of the airfoil, the normal velocity component must vanish, so that ϕ must satisfy

$$(\vec{u}^{(I)} + \vec{\nabla}\phi) \cdot \vec{n} = 0 \qquad (2.25)$$

or

$$\frac{\partial \phi}{\partial n} = -\vec{u}^{(I)} \cdot \vec{n}, \qquad (2.26)$$

14

where $\vec{n}$ is the unit normal at the surface of the airfoil. In the wake, the pressure is continuous so that ϕ must obey

$$\frac{D_0}{Dt}(\Delta\phi) = 0, \tag{2.27}$$

where $\Delta\phi$ is the jump in ϕ across the vortex sheet behind the airfoil. Far upstream, ϕ must satisfy

$$\phi \to 0 \qquad \text{as} \qquad x_1 \to -\infty. \tag{2.28}$$

2.3 Atassi and Grzedzinski's Decomposition of the Unsteady Velocity

For most flows of practical aerodynamic interest, there will be a stagnation point near the leading edge of the airfoil where the mean velocity U_0 vanishes. At this point the drift function Δ has a logarithmic singularity, and the right hand side of (2.19) then has a nonintegrable reciprocal singularity. Since Δ is additive, the right hand side of (2.19) will remain undefined along the surface of the airfoil and in its wake. Equation (2.26) then shows that the boundary condition for ϕ is singular along the airfoil surface. Because of these difficulties we conclude that it is not possible to use Goldstein's approach directly for numerical computations of unsteady vortical flows around aerodynamic bodies with a stagnation point.

Atassi and Grzedzinski[28] have shown that it is possible to modify Goldstein's splitting of the unsteady velocity field in such a way as to remove the singular and indeterminate character of the resulting boundary condition for the unsteady potential at the airfoil surface. In their decomposition of the unsteady velocity, $\vec{u}$ is split into the sum of a known vortical component $\vec{u}^{(R)}$, which has zero normal and streamwise velocity components on the airfoil and in the wake, and an unkown potential component $\phi^\star$ that satisfies equation (2.17) with a modified source term, so that

$$\vec{u}(\vec{x}, t) = \vec{u}^{(R)} + \vec{\nabla}\phi^\star \tag{2.29}$$

15

where $\phi^\star$ satisfies

$$\frac{D_0}{Dt}\left(\frac{1}{c_0{}^2}\frac{D_0\phi^\star}{Dt}\right) - \frac{1}{\rho_0}\vec{\nabla}\cdot(\rho_0\vec{\nabla}\phi^\star) = \frac{1}{\rho_0}\vec{\nabla}\cdot(\rho_0\vec{u}^{(R)}) \tag{2.30}$$

The vortical component $\vec{u}^{(R)}$ is given by

$$\vec{u}^{(R)} = \vec{u}^{(I)} + \vec{\nabla}\tilde{\phi}, \tag{2.31}$$

where $\tilde{\phi}$ is a function that satisfies

$$\frac{D_0\tilde{\phi}}{Dt} = 0. \tag{2.32}$$

As shown in Reference 28, there is no pressure associated with the velocity $\vec{\nabla}\tilde{\phi}$, so that the vortical velocity $\vec{u}^{(R)}$ produces no pressure fluctuations. The pressure is determined entirely by $\phi^\star$ and is given by

$$p' = -\rho_0(\vec{x})\frac{D_0\phi^\star}{Dt}. \tag{2.33}$$

In order to choose a particular function $\tilde{\phi}$ that cancels the singular behavior of $\vec{u}^{(I)}$ along the surface of the airfoil and in its wake, the boundary condition

$$(\vec{u}^{(I)} + \vec{\nabla}\tilde{\phi})\cdot\vec{n} = 0 \tag{2.34}$$

is imposed at the airfoil surface and in the wake. Condition (2.34) should be understood as the limit as we move close to the airfoil and the wake. Details concerning the construction of the function $\tilde{\phi}$ can be found in Reference 28. For the important special case of incident harmonic velocity disturbances, specific formulas for $\tilde{\phi}$ are presented in Reference 28, and will be discussed later in the present dissertation.

The function $\vec{u}^{(R)}$ has zero normal and streamwise velocity components at the airfoil surface and in the wake, so that $\vec{u}^{(R)}$ satisfies

$$\vec{u}^{(R)}\cdot\vec{n} = 0, \tag{2.35}$$

and

$$\vec{u}^{(R)}\cdot\vec{\tau} = 0, \tag{2.36}$$

16

where $\vec{n}$ and $\vec{\tau}$ are the unit normal and tangent vectors. The airfoil boundary condition for ϕ^* is then

$$(\vec{u}^{(R)} + \vec{\nabla}\phi^*) \cdot \vec{n} = 0 \qquad (2.37)$$

which reduces to simply

$$\vec{\nabla}\phi^* \cdot \vec{n} = 0. \qquad (2.38)$$

In addition to satisfying the governing equation (2.30) and the airfoil boundary condition (2.38), the unsteady potential ϕ^* must also satisfy appropriate boundary conditions in the far field, in the wake, and at the airfoil trailing edge.

In the far field, equations (2.29) and (2.31) together with condition (2.13) imply that ϕ^* must satisfy

$$\vec{\nabla}\phi^* \to -\vec{\nabla}\tilde{\phi} \quad \text{as} \quad x_1 \to -\infty. \qquad (2.39)$$

In the wake of the airfoil, ϕ^* is not continuous but must satisfy a jump condition determined by the continuity of the unsteady pressure. Applying (2.33) on each side of the vortex sheet behind the airfoil leads to the condition

$$\frac{D_0}{Dt}(\Delta\phi^*) = 0 \qquad \text{wake} \qquad (2.40)$$

Finally, at the trailing edge point ϕ^* must be continuous in the streamwise direction to ensure satisfaction of the Kutta condition.

2.4 Upstream Disturbances

In a previous paper[30], it has been shown that the most general upstream vortical disturbances can be represented as the sum of three-dimensional, harmonic vorticity waves in the blade frame of reference. Because the governing equation (2.30) is linear, we can without loss of generality consider a single Fourier component of the incident disturbance, and obtain the solution to more general disturbances by superposition. We therefore consider incident velocity disturbances of the form

$$\vec{u}_\infty = \vec{a}e^{i\vec{k}\cdot(\vec{x}-\vec{i}U_\infty t)} \qquad (2.41)$$

where $|\vec{a}| \ll U_\infty$, $\vec{k}$ is the wave number vector which specifies the direction of propagation of the gust, and $\vec{a}$ and $\vec{k}$ must satisfy

$$\vec{a} \cdot \vec{k} = 0 \tag{2.42}$$

in order to ensure that $\vec{u}_\infty$ is solenoidal (satisfies the continuity equation).

Now condition (2.13) shows that the unsteady velocity $\vec{u}(\vec{x}, t)$ must satisfy

$$\vec{u}(\vec{x}, t) \rightarrow \vec{a} e^{i\vec{k} \cdot (\vec{x} - \vec{i} U_\infty t)} \qquad \text{as} \qquad x_1 \rightarrow -\infty. \tag{2.43}$$

Since $X_2 = \frac{\Psi_0}{\rho_\infty U_\infty}$ and Ψ_0 is the stream function of a two-dimensional mean flow,

$$X_2 \rightarrow x_2 + \frac{\Gamma}{2\pi U_\infty} \ln(x_1^2 + x_2^2) + \text{constant} \qquad \text{as} \qquad x_1 \rightarrow -\infty, \tag{2.44}$$

so that we do not have $X_2 \rightarrow x_2$ at upstream infinity, as required by condition (2.20b). Equations (2.29), (2.31), and (2.39) together with (2.19) then show that

$$\vec{u}(\vec{x}, t) \rightarrow \vec{a} e^{i\vec{k} \cdot (x_1 - U_\infty t, x_2 + \frac{\Gamma}{2\pi U_\infty} \ln(x_1^2 + x_2^2) + \text{constant}, x_3)} \qquad \text{as} \qquad x_1 \rightarrow -\infty, \tag{2.45}$$

so that (2.43) is not satisfied.

However, as discussed by Atassi[8], for a real airfoil of finite span, $X_2 \rightarrow x_2 +$ constant. The two-dimensional approximation is only valid then for distances that are small compared to the airfoil span, but large compared to the chord. Thus, (2.44) should be considered in this limit.

In order to avoid difficulties with upstream conditions, the imposed upstream disturbances should then take the general form

$$\vec{u}_\infty = \vec{a} e^{i\vec{k} \cdot (\vec{X} - \vec{i} U_\infty t)} \tag{2.46}$$

where $\vec{X}$ is defined by (2.21) - (2.23). Then with this definition of $\vec{u}_\infty$, equations (2.19) and (2.45) show that condition (2.13) will be satisfied.

2.5 The Boundary Value Problem

For convenience we now summarize the boundary value problem that has been developed in the first four sections of the present chapter. From this point on we drop the "$\star$" notation which was used to distinguish between the formulation of Atassi and Grzedzinski in Section 2.3 and the formulation of Goldstein in Section 2.2.

We consider a potential mean flow about a two-dimensional airfoil of infinite span with three-dimensional, rotational velocity disturbances of the form

$$\vec{u}_\infty = \vec{a}\, e^{i\vec{k}\cdot(\vec{X} - \vec{i}U_\infty t)} \tag{2.47}$$

imposed upstream. The amplitude $\vec{a}$ satisfies $|\vec{a}| \ll U_\infty$, and $\vec{X}$ is defined by equations (2.21) through (2.23).

The unsteady potential obeys the convective wave equation

$$\frac{D_0}{Dt}\left(\frac{1}{c_0{}^2}\frac{D_0\phi}{Dt}\right) - \frac{1}{\rho_0}\vec{\nabla}\cdot(\rho_0\vec{\nabla}\phi) = \frac{1}{\rho_0}\vec{\nabla}\cdot(\rho_0\vec{u}^{(R)}), \tag{2.48}$$

where the unsteady velocity is given by

$$\vec{u}(\vec{x},t) = \vec{u}^{(R)} + \vec{\nabla}\phi \tag{2.49}$$

and the unsteady pressure is determined from

$$p' = -\rho_0(\vec{x})\frac{D_0\phi}{Dt}. \tag{2.50}$$

In addition, ϕ must satisfy the boundary conditions

$$\vec{\nabla}\phi \cdot \vec{n} = 0 \qquad \text{airfoil surface} \tag{2.51}$$

$$\frac{D_0}{Dt}(\triangle\phi) = 0 \qquad \text{wake} \tag{2.52a}$$

$$\triangle[\vec{\nabla}\phi \cdot \vec{n}] = 0 \qquad \text{wake} \tag{2.52b}$$

19

$$\vec{\nabla}\phi \to -\vec{\nabla}\tilde{\phi} \quad \text{as} \quad x_1 \to -\infty, \tag{2.53}$$

and be continuous in the streamwise direction at the airfoil trailing edge. Note that for completeness we have also included boundary condition (2.52b), which imposes continuity of the normal velocity across the wake. For nonlifting airfoils this condition is automatically satisfied, since in that case ϕ is an odd function with respect to X_2. For lifting airfoils, however, ϕ is no longer an odd function and condition (2.52b) must be imposed.

To complete the mathematical formulation of the boundary value problem, the explicit expression of the function $\tilde{\phi}$ must be given. For a complete discussion of the derivation of $\tilde{\phi}$ for the general problem of arbitrary upstream disturbances, the reader should consult Reference 28. For the problem of periodic disturbances of the form (2.47) imposed upstream of a single obstacle which is two-dimensional (such as an isolated airfoil), it is shown in Reference 28 that $\tilde{\phi}$ is given by

$$\tilde{\phi} = \frac{i}{k_1}(a_1 + \frac{a_2 k_1 - a_1 k_2}{1 + i a_0 U_\infty k_1} \frac{1 - e^{-i k_2 X_2}}{k_2})e^{i\vec{k}\cdot(\vec{X} - \vec{i}U_\infty t)}, \tag{2.54}$$

where

$$\vec{a} = (a_1, a_2, a_3) \quad \text{and} \quad a_0 = -(\frac{\partial U_0}{\partial n})_S^{-1}. \tag{2.55}$$

Here n denotes the direction of the outward unit normal, S denotes the stagnation point near the airfoil leading edge, and $U_0 = |\vec{U_0}|$ is the magnitude of the mean velocity.

With this definition of $\tilde{\phi}$, and with the upstream velocity disturbances given by (2.47), the vortical velocity may then be written

$$\vec{u}^{(R)} = [\vec{\nabla}(\vec{a} \cdot \vec{X})]e^{i\vec{k}\cdot(\vec{X} - \vec{i}U_\infty t)} + \vec{\nabla}\tilde{\phi}. \tag{2.56}$$

This completes the linearized mathematical formulation for the general boundary value problem of unsteady vortical flow past a lifting airfoil.

20

CHAPTER III

NUMERICAL SCHEME

3.1 Reformulation and Nondimensionalization of the Boundary Value Problem

For numerical purposes it is necessary to reformulate the boundary value problem presented in the previous section into a form more suitable for numerical computations. Of particular concern is condition (2.53). In order to facilitate the implementation of the far field boundary condition, it is convenient to replace ϕ by a function whose gradient vanishes as $r \to \infty$, where r is the distance from the airfoil center.

To this end, we introduce the potential functions ϕ_1 and ϕ_2, where

$$\phi = \phi_1 - \phi_2 \tag{3.1}$$

and ϕ_2 is a known function which is constructed such that

$$|\phi_2 - \tilde{\phi}| \to 0 \qquad \text{as} \quad r \to \infty. \tag{3.2}$$

Equation (3.1) together with conditions (2.53) and (3.2) then show that the new potential function ϕ_1 will satisfy

$$\vec{\nabla}\phi_1 \to \vec{\nabla}\phi_2 - \vec{\nabla}\tilde{\phi} \to 0 \qquad \text{as} \quad r \to \infty. \tag{3.3}$$

The problem may then be reformulated in terms of the unknown potential ϕ_1.

To satisfy condition (3.2), the function ϕ_2 must take the form

$$\phi_2 = \frac{i}{k_1}\left(a_1 + \frac{a_2 k_1 - a_1 k_2}{1 + ia_0 U_\infty k_1} \frac{1 - e^{-ik_2 X_2}}{k_2}\right)e^{i\vec{k}\cdot(\vec{X}_e - \vec{\imath}U_\infty t)}, \tag{3.4}$$

where the vector $\vec{X}_e$ satisfies

$$|\vec{X}_e - \vec{X}| \to 0 \qquad \text{as} \quad r \to \infty. \tag{3.5}$$

To satisfy this condition for the general problem of vortical flows around lifting airfoils, we define $\vec{X}_e$ as follows:

$$X_{e,1} = \frac{\Phi_0}{U_\infty} - \frac{\Gamma}{\pi U_\infty}\text{sgn}(\Psi_0)\left[\frac{\pi}{2} + \text{sgn}(\Psi_0)\tan^{-1}(\frac{\rho_\infty \Phi_0}{\beta_\infty \Psi_0})\right]\left[1 - e^{-(\Phi_0^2 + \frac{\Psi_0^2}{\rho_\infty^2})(\frac{2}{cU_\infty})^2}\right]$$

(3.6)

$$X_{e,2} = X_2 \tag{3.7}$$

$$X_{e,3} = X_3. \tag{3.8}$$

The expression for $X_{e,1}$ is obtained by making a far field expansion of Lighthill's drift function Δ in terms of Φ_0 and Ψ_0. Note that the first term in the expansion is just $\frac{\Phi_0}{U_\infty}$, and that the second term arises due to the circulation around the airfoil. Since the second term vanishes for airfoils with zero circulation, it is clear that the formulation of the source term for nonlifting airfoils is much simpler than for lifting airfoils.

We also point out that the first factor in brackets on the right hand side of equation (3.6) is discontinuous and undefined at the points on the airfoil where $\Phi_0 = 0, \Psi_0 = 0^+$ and $\Phi_0 = 0, \Psi_0 = 0^-$. The second factor in brackets is not part of the expansion itself, but is included to remove the discontinuity which would occur due to the first factor. By including the second factor in brackets and defining $X_{e,1} = 0$ at $\Phi_0 = 0, \Psi_0 = 0$, we obtain an expression for $X_{e,1}$ which is everywhere continuous. It is important that $X_{e,1}$ be continuous along the airfoil surface, for if it were not, the potential function ϕ_1 would have to satisfy a discontinuous airfoil boundary condition. (See condition (3.10) below.) By defining $X_{e,1}$ as in (3.6), we obtain an expression for $\vec{X}_e$ which is everywhere continuous and also ensures that conditions (3.5) and (3.2) will be satisfied for both lifting and nonlifting airfoils.

Finally, c is the airfoil chord length, and the parameter β_∞, which is equal to $\sqrt{1 - M_\infty^2}$, where M_∞ is the free stream Mach number, arises due to a Gothert's rule correction on the mean velocity so that the expression for $X_{e,1}$ is valid for both compressible and incompressible flows.

22

Before presenting the reformulated boundary value problem in terms of the potential ϕ_1, we present the nondimensionalization of the problem. We normalize as follows:

$x_1, x_2, x_3, X_1, X_2, X_3, X_{e,1}$	by	$\frac{c}{2}$
Φ_0, Γ	by	$\frac{c}{2}U_\infty$
Ψ_0	by	$\frac{c}{2}\rho_\infty U_\infty$
U_0, c_0	by	U_∞
ρ_0	by	ρ_∞
p'	by	$\rho_\infty U_\infty |\vec{a}|$
t, Δ	by	$\frac{c}{2U_\infty}$
ω	by	$\frac{2U_\infty}{c}$
k_1, k_2, k_3	by	$\frac{2}{c}$
$\phi, \tilde{\phi}, \phi_1, \phi_2$	by	$\frac{c}{2}|\vec{a}|$
$\vec{a}$	by	$|\vec{a}|$

The normalized wave number $k_1 = \frac{\omega c}{2U_\infty}$, where ω and U_∞ are the dimensional angular frequency and free stream velocity, respectively, is called the reduced frequency.

We will assume throughout the remainder of the present chapter, unless stated otherwise, that all quantities are nondimensional.

The governing equation for ϕ_1 is then

$$\frac{D_0}{Dt}\left(\frac{1}{c_0{}^2}\frac{D_0\phi_1}{Dt}\right) - \frac{1}{\rho_0}\vec{\nabla}\cdot(\rho_0\vec{\nabla}\phi_1) = \frac{1}{\rho_0}\vec{\nabla}\cdot(\rho_0\vec{u}^{(R)})$$

$$+ \frac{D_0}{Dt}\left(\frac{1}{c_0{}^2}\frac{D_0\phi_2}{Dt}\right) - \frac{1}{\rho_0}\vec{\nabla}\cdot(\rho_0\vec{\nabla}\phi_2) \qquad (3.9)$$

and the boundary conditions are

$$\vec{\nabla}\phi_1\cdot\vec{n} = \vec{\nabla}\phi_2\cdot\vec{n} \qquad \text{airfoil surface} \qquad (3.10)$$

23

$$\frac{D_0}{Dt}[\Delta(\phi_1 - \phi_2)] = 0 \qquad \text{wake} \qquad (3.11a)$$

$$\Delta[\vec{\nabla}(\phi_1 - \phi_2) \cdot \vec{n}] = 0 \qquad \text{wake} \qquad (3.11b)$$

$$\vec{\nabla}\phi_1 \to 0 \quad \text{as} \quad x_1 \to -\infty. \qquad (3.12)$$

For completeness we also present the nondimensional expressions for the potential functions $\tilde{\phi}$ and ϕ_2, for the unsteady velocity and pressure, and for the upstream velocity disturbances.

$$\tilde{\phi} = \frac{i}{k_1}(a_1 + \frac{a_2 k_1 - a_1 k_2}{1 + i a_0 k_1} \frac{1 - e^{-ik_2 X_2}}{k_2})e^{i\vec{k}\cdot\vec{X} - ik_1 t} \qquad (3.13)$$

$$\phi_2 = \frac{i}{k_1}(a_1 + \frac{a_2 k_1 - a_1 k_2}{1 + i a_0 k_1} \frac{1 - e^{-ik_2 X_2}}{k_2})e^{i\vec{k}\cdot\vec{X}_e - ik_1 t}, \qquad (3.14)$$

where

$$X_1 = \Delta, \quad X_2 = X_{e,2} = \Psi_0, \quad X_3 = X_{e,3} = x_3 \qquad (3.15)$$

$$X_{e,1} = \Phi_0 - \frac{\Gamma}{\pi}\text{sgn}(\Psi_0)[\frac{\pi}{2} + \text{sgn}(\Psi_0)\tan^{-1}(\frac{\Phi_0}{\beta_\infty \Psi_0})][1 - e^{-(\Phi_0^2 + \Psi_0^2)}] \qquad (3.16)$$

$$\vec{u}(\vec{x}, t) = \vec{u}^{(R)} + \vec{\nabla}(\phi_1 - \phi_2) \qquad (3.17)$$

where

$$\vec{u}^{(R)} = [\vec{\nabla}(\vec{a} \cdot \vec{X})]e^{i\vec{k}\cdot\vec{X} - ik_1 t} + \vec{\nabla}\tilde{\phi}. \qquad (3.18)$$

$$p' = -\rho_0(\vec{x})\frac{D_0(\phi_1 - \phi_2)}{Dt}. \qquad (3.19)$$

$$\vec{u}_\infty = \vec{a}e^{i\vec{k}\cdot\vec{X} - ik_1 t} \qquad (3.20)$$

3.2 Determination of Mean Potential Flow

In order to obtain numerical solutions to equation (3.9) and its associated boundary conditions, one must first obtain the steady potential flow about the airfoil for the given flow conditions. This will in general require the use of a standard potential flow solver such as FLO36.[36]

However, an examination of equations (3.13) through (3.18) indicate that the most natural choice of independent variables in which to solve equation (3.9) are Φ_0 and Ψ_0, the mean flow potential and stream functions. Since standard potential flow codes solve the steady problem in terms of the spatial coordinates x_1 and x_2, there is some difficulty in obtaining the steady solution as a function of Φ_0 and Ψ_0.

Another difficulty arises due to the fact that the grids used by steady flow solvers are not suitable for the unsteady calculation. As reported in References 30 and 31, accurate solution of equation (3.9) over a large range of flow conditions requires using grids which are determined as a function of both the reduced frequency k_1 and the free stream Mach number M_∞. This means that in general it will be necessary to interpolate the solution from the steady grid onto the appropriate unsteady grid.

Because of the loss of accuracy that can result from such an interpolation process, and also because of the need to know the mean flow as a function of Φ_0 and Ψ_0, an analytical scheme that can obtain the compressible, subsonic flow about isolated airfoils was developed. The scheme is based on the idea that, except for a small inner region surrounding the airfoil, the flow gradients are not too large. Thus in the large outer region extending to infinity, the mean flow is essentially governed by a set of linear equations. As a result, one can use Gothert's Rule, whereby the compressible flow about a given airfoil can be obtained from the incompressible flow about a similar airfoil.

If we let α_C, θ_C, and γ_C denote the angle of attack, thickness ratio, and camber ratio of the given airfoil in a compressible flow, then the transformed airfoil for the

incompressible flow field has angle of attack, thickness ratio, and camber ratio given by

$$\left. \begin{array}{l} \alpha_I = \beta_\infty \, \alpha_C \\ \theta_I = \beta_\infty \, \theta_C \\ \gamma_I = \beta_\infty \, \gamma_C \end{array} \right\} \tag{3.21}$$

where I subscripts denote quantities from the incompressible flow field. Using dimensional quantities and denoting the compressible velocity by $(U_\infty + u_C, v_C)$ at the point (x, y) and the incompressible velocity by $(U_\infty + u_I, v_I)$ at the point (x_I, y_I), the spatial coordinates and velocity in the compressible and incompressible planes are related by

$$x = x_I \tag{3.22a}$$

$$y = \frac{y_I}{\beta_\infty} \tag{3.22b}$$

and

$$u_C = \frac{u_I}{\beta_\infty^2} \tag{3.23a}$$

$$v_C = \frac{v_I}{\beta_\infty}. \tag{3.23b}$$

It is assumed here that the free stream velocity U_∞ is aligned with the x axis, and that the angle of attack, thickness ratio, and camber ratio of the airfoil are such that the perturbation velocities are small compared to U_∞. The potential and stream functions of the compressible flow field are then related to the potential and stream functions of the incompressible flow field by

$$\Phi_0 - U_\infty x = \frac{1}{\beta_\infty^2}(\Phi_I - U_\infty x_I) \tag{3.24a}$$

$$\Psi_0 - U_\infty y = \frac{1}{\beta_\infty}(\Psi_I - U_\infty y_I) \tag{3.24b}$$

Using (3.22), and assuming that all quantities have been nondimensionalized as in the previous section, equations (3.24) can be rewritten

$$\Phi_I - M_\infty^2 x_I = \beta_\infty^2 \Phi_0 \tag{3.25a}$$

$$\Psi_I = \beta_\infty \Psi_0 \tag{3.25b}$$

The problem is then, given (Φ_0, Ψ_0), solve equations (3.25) for (Φ_I, Ψ_I) and then use relations (3.22) and (3.23) to determine the spatial coordinates (x, y) and velocity components (u_C, v_C) of the compressible flow field. If this can be done, then we have the compressible flow field determined as a function of (Φ_0, Ψ_0). Note that this assumes that we can determine (x_I, y_I) and (u_I, v_I) as functions of (Φ_I, Ψ_I). Since there is a one to one correspondence between (x_I, y_I) and (Φ_I, Ψ_I), and between (u_I, v_I) and (Φ_I, Ψ_I), this is not a difficulty. At the least, it can always be done numerically. For the special case of Joukowski airfoils, however, it is possible to express the complex potential (Φ_I, Ψ_I) in terms of the polar coordinates (r, θ), and then obtain (x_I, y_I) and (u_I, v_I) through known functional expressions of (r, θ).

For the case of incompressible flow around a Joukowski airfoil the complex potential is given by

$$\Phi_I + i\,\Psi_I = \zeta' e^{-i\alpha_I} + \frac{a^2 e^{i\alpha_I}}{\zeta'} + \frac{\Gamma_I}{2\pi i}\ln(\frac{\zeta'}{a}) + K \tag{3.26}$$

where K is an arbitrary constant and

$$\zeta' = \zeta - \zeta_{0'} = re^{i\theta}. \tag{3.27}$$

Here $\zeta_{0'} = -\epsilon + i\epsilon'$ is a complex constant, and the parameters a, ϵ, and ϵ' depend on the airfoil geometry. Γ_I is the steady circulation around the airfoil and is given by

$$\Gamma_I = -4\pi a \sin(\alpha_I + \mu) \tag{3.28}$$

where μ is defined by

$$\sin\mu = \frac{\epsilon'}{a}. \tag{3.29}$$

27

The spatial coordinates (x_I, y_I) are determined from r and θ through the Joukowski transformation

$$x_I + i\, y_I = \zeta + \frac{d^2}{\zeta} \qquad (3.30)$$

where the parameter d satisfies

$$(\epsilon + d)^2 + \epsilon'^2 = a^2. \qquad (3.31)$$

Finally, the velocity components (u_I, v_I) are given by

$$u_I - i\, v_I = \frac{\zeta^2[\zeta' + ae^{i(2\alpha_I + \mu)}]}{(\zeta + d)\zeta'^2} \quad - \quad 1. \qquad (3.32)$$

Using relations (3.26) through (3.30), equations (3.25) can be expressed in terms of r and θ as

$$(r + \frac{a^2}{r})\cos(\theta - \alpha_I) - [2a\sin(\alpha_I + \mu)]\theta + K$$

$$-M_\infty^2[r\cos\theta - \epsilon + \frac{d^2(r\cos\theta - \epsilon)}{(r\cos\theta - \epsilon)^2 + (r\sin\theta + \epsilon')^2}] = \beta_\infty^2 \Phi_0 \qquad (3.33a)$$

$$(r - \frac{a^2}{r})\sin(\theta - \alpha_I) + 2a\sin(\alpha_I + \mu)\ln(\frac{r}{a}) = \beta_\infty \Psi_0 \qquad (3.33b)$$

If for given Φ_0 and Ψ_0 we can solve equations (3.33) for r and θ, then equations (3.30) and (3.32) can be used to get (x_I, y_I) and (u_I, v_I), and equations (3.22) and (3.23) can be used to obtain (x, y) and (u_c, v_c). Once we have obtained (u_c, v_c), the other mean flow quantities can then be obtained from Bernoulli's law for polytropic gases.

We note that, while the system of equations (3.33) is highly nonlinear in the unknowns r and θ, it can be routinely solved by two-dimensional Newton iteration. Once a subroutine has been developed to solve equations (3.33), the compressible steady flow around any Joukowski airfoil can be very efficiently obtained. In addition, the mean flow is obtained for arbitrary Φ_0 and Ψ_0, so that there is no

restriction whatsoever on the particular grid that may be used for the unsteady calculation.

The only limitation in obtaining the mean potential flow by this particular approach is the underlying assumption that u_C and v_C must be small compared to U_∞. This means that the method will not give a good approximation in the inner region and particularly near the stagnation point where the perturbation velocities are of the same order of magnitude as U_∞. However, extensive testing of this particular approach and comparing with the steady potential flow solver FLO36 has shown that the region of inaccuracy is very small. Figures 1 through 4 show Mach number comparisons between the present approximate analytical scheme and FLO36. The comparison is made at grid points along fixed grid lines used by FLO36. It is seen that the agreement overall is quite good, with the exception of grid points on the airfoil surface that are near the stagnation point. Because of this inaccuracy, we use FLO36 to calculate the mean flow quantities along the airfoil surface itself, and use the approximate analytical scheme off the airfoil except in a small region just upstream of the stagnation point. In this region, for airfoils that have steady loading, the velocities are calculated using a Taylor series expansion. For airfoils without steady loading, the velocities are calculated from a local analytical solution which is patched to the outer solution.

3.3 Frequency Domain Formulation

An inspection of equations (3.13), (3.14), (3.18), and (3.20) indicates that the time dependence of the boundary value problem presented in Section 3.1 comes entirely through the harmonic term $e^{-ik_1 t}$. It is therefore possible to make a transformation from the time domain into the frequency domain by a simple change of dependent variable. By transforming the problem into the frequency domain, time is completely eliminated from the problem and it is possible to significantly simplify the mathematical formulation of the boundary value problem.

For the case of two-dimensional mean flow, we transform into the frequency domain by making the following change of dependent variable:

$$\phi_1 = \varphi e^{-ik_1 t + ik_3 x_3} \tag{3.34}$$

By including the $ik_3 x_3$ term in the transformation, the harmonic dependence on the spanwise component x_3 is also eliminated, since all of the $e^{ik_3 x_3}$ terms then factor out from each side of the equation. This is of course possible in view of (3.20) and (3.15).

Before presenting the governing equation in the new dependent variable φ, we introduce the linear operators $\mathcal{L}$ and $\mathcal{L}_0$ to simplify the notation.

$$\mathcal{L} = \frac{D_0}{Dt}\left(\frac{1}{c_0^2}\frac{D_0}{Dt}\right) - \frac{1}{\rho_0}\vec{\nabla}\cdot(\rho_0\vec{\nabla}) \tag{3.35}$$

and

$$\mathcal{L}_0 = M_\infty^2\frac{D_0^2}{Dt_0^2} - \left(\frac{\partial^2}{\partial\Phi_0^2} + \frac{\partial^2}{\partial\Psi_0^2} + \frac{\partial^2}{\partial x_3^2}\right) \tag{3.36}$$

where

$$\frac{D_0}{Dt_0} = \frac{\partial}{\partial t} + \frac{\partial}{\partial\Phi_0} \tag{3.37}$$

The governing equation then takes the form

$$\mathcal{L}\phi_1 = \frac{1}{\rho_0}\vec{\nabla}\cdot(\rho_0\vec{u}^{(R)}) + \mathcal{L}\phi_2 \tag{3.38}$$

The operator $\mathcal{L}_0$ is essentially the operator for the thin airfoil gust response problem. By writing the governing equation in the following equivalent form, the left hand side of the equation will exhibit the character of the thin airfoil operator in the far field since $\mathcal{L} \to \mathcal{L}_0$ there.

$$\mathcal{L}_0\phi_1 + (\mathcal{L} - \mathcal{L}_0)\phi_1 = \frac{1}{\rho_0}\vec{\nabla}\cdot(\rho_0\vec{u}^{(R)}) + \mathcal{L}\phi_2 \tag{3.39}$$

30

We then have in terms of φ

$$\mathcal{L}_0\phi_1 + (\mathcal{L} - \mathcal{L}_0)\phi_1 =$$

$$e^{-ik_1 t + ik_3 x_3}\left\{-[\beta_\infty^2\frac{\partial^2\varphi}{\partial\Phi_0^2} + \frac{\partial^2\varphi}{\partial\Psi_0^2} + 2ik_1 M_\infty^2\frac{\partial\varphi}{\partial\Phi_0} + (k_1^2 M_\infty^2 - k_3^2)\varphi]\right.$$

$$+ [k_1^2 M_\infty^2 - \frac{k_1^2 M^2}{U_0^2} - ik_1 U_0^2\frac{\partial}{\partial\Phi_0}(\frac{M^2}{U_0^2})]\varphi \qquad (3.40)$$

$$+ [M^2(\frac{\partial U_0^2}{\partial\Phi_0} - 2ik_1) + 2ik_1 M_\infty^2 + U_0^4\frac{\partial}{\partial\Phi_0}(\frac{M^2}{U_0^2}) - \frac{U_0^2}{\rho_0}\frac{\partial\rho_0}{\partial\Phi_0}]\frac{\partial\varphi}{\partial\Phi_0}$$

$$\left.+ (\beta_\infty^2 - \beta^2 U_0^2)\frac{\partial^2\varphi}{\partial\Phi_0^2} + (1 - U_0^2)\frac{\partial^2\varphi}{\partial\Psi_0^2} - \frac{U_0^2}{\rho_0}\frac{\partial\rho_0}{\partial\Psi_0}\frac{\partial\varphi}{\partial\Psi_0}\right\}$$

Equation (3.40) may be simplified further by making the following change of both dependent and independent variables:

$$\varphi = \psi e^{-iK_0\Phi} \qquad (3.41a)$$

where

$$K_0 = \frac{k_1 M_\infty^2}{\beta_\infty^2} \qquad (3.41b)$$

and

$$\Phi = \Phi_0 \qquad (3.42a)$$

$$\Psi = \beta_\infty\Psi_0 \qquad (3.42b)$$

Expressing equation (3.40) in terms of ψ and the new independent variables

31

Φ and Ψ, one gets

$$\mathcal{L}_0\phi_1 + (\mathcal{L} - \mathcal{L}_0)\phi_1 =$$

$$e^{-ik_1 t + ik_3 z_3} e^{-iK_0\Phi} \left\{ -\beta_\infty^2 \left[\frac{\partial^2 \psi}{\partial \Phi^2} + \frac{\partial^2 \psi}{\partial \Psi^2} + \left(\frac{k_1^2 M_\infty^2}{\beta_\infty^4} - \frac{k_3^2}{\beta_\infty^2} \right) \psi \right] \right. \qquad (3.43)$$

$$\left. + A_1 \psi + A_2 \frac{\partial \psi}{\partial \Phi} + A_3 \frac{\partial \psi}{\partial \Psi} + A_4 \frac{\partial^2 \psi}{\partial \Phi^2} + A_5 \frac{\partial^2 \psi}{\partial \Psi^2} \right\}$$

where $A_1...A_5$ are functions of (Φ, Ψ) defined by

$$A_1(\Phi, \Psi) = \frac{k_1^2 M_\infty^2}{\beta_\infty^2} - \frac{k_1^2 M^2}{U_0^2} - ik_1 U_0^2 \frac{\partial}{\partial \Phi}\left(\frac{M^2}{U_0^2}\right) \qquad (3.44a)$$

$$- iK_0 \left[M^2 \left(\frac{\partial U_0^2}{\partial \Phi} - 2ik_1 \right) + U_0^4 \frac{\partial}{\partial \Phi}\left(\frac{M^2}{U_0^2}\right) - \frac{U_0^2}{\rho_0} \frac{\partial \rho_0}{\partial \Phi} \right] + \frac{k_1^2 M_\infty^4}{\beta_\infty^4} \beta^2 U_0^2$$

$$A_2(\Phi, \Psi) = M^2 \left(\frac{\partial U_0^2}{\partial \Phi} - 2ik_1 \right) + U_0^4 \frac{\partial}{\partial \Phi}\left(\frac{M^2}{U_0^2}\right) - \frac{U_0^2}{\rho_0} \frac{\partial \rho_0}{\partial \Phi} + 2iK_0 \beta^2 U_0^2$$
$$\qquad (3.44b)$$

$$A_3(\Phi, \Psi) = -\beta_\infty \frac{U_0^2}{\rho_0} \frac{\partial \rho_0}{\partial \Psi} \qquad (3.44c)$$

$$A_4(\Phi, \Psi) = \beta_\infty^2 - \beta^2 U_0^2 \qquad (3.44d)$$

$$A_5(\Phi, \Psi) = 1 - U_0^2 \qquad (3.44e)$$

Note that in the far field the functions $A_1...A_5$ tend to zero so that the right hand side of (3.43) reduces to that of the linear thin airfoil theory.[4]

To complete the frequency domain formulation, it is necessary to present the right hand side of the governing equation (3.39). We will refer to the right hand side of (3.39) as the source term and denote it by $e^{-ik_1t+ik_3x_3}S$. To facilitate the presentation of the source term, we will write the governing equation as

$$\mathcal{L}_0\,\phi_1 + (\mathcal{L} - \mathcal{L}_0)\,\phi_1 = e^{-ik_1t+ik_3x_3}\;S \qquad (3.45a)$$

or

$$\mathcal{L}_0\,\phi_1 + (\mathcal{L} - \mathcal{L}_0)\,\phi_1 = e^{-ik_1t+ik_3x_3}\,(S_1 + S_2 + S_3 - S_4) \qquad (3.45b)$$

where

$$e^{-ik_1t+ik_3x_3}\;S_1 = \frac{\vec{\nabla}\rho_0}{\rho_0}\cdot\{[\vec{\nabla}(\vec{a}\cdot\vec{X})]e^{i\vec{k}\cdot\vec{X}-ik_1t} + \vec{\nabla}\tilde{\phi}\} \qquad (3.46a)$$

$$e^{-ik_1t+ik_3x_3}\;S_2 = \vec{\nabla}\cdot\{[\vec{\nabla}(\vec{a}\cdot\vec{X})]e^{i\vec{k}\cdot\vec{X}-ik_1t} + \vec{\nabla}\tilde{\phi}\} \qquad (3.46b)$$

$$e^{-ik_1t+ik_3x_3}\;S_3 = \frac{D_0}{Dt}\left(\frac{1}{c_0{}^2}\frac{D_0\phi_2}{Dt}\right) \qquad (3.46c)$$

$$e^{-ik_1t+ik_3x_3}\;S_4 = \frac{1}{\rho_0}\vec{\nabla}\cdot(\rho_0\vec{\nabla}\phi_2) \qquad (3.46d)$$

We also introduce $\tilde{\varphi}$ and φ_2 where

$$e^{-ik_1t+ik_3x_3}\;\tilde{\varphi} = \tilde{\phi} \qquad (3.47a)$$

$$e^{-ik_1t+ik_3x_3}\;\varphi_2 = \phi_2 \qquad (3.47b)$$

The expressions for $S_1...S_4$ are then

33

$$S_1 = [a_1 \frac{\partial \rho_0}{\partial \Phi_0} + U_0^2 \frac{\partial \rho_0}{\partial \Psi_0}(a_1 \frac{\partial X_1}{\partial \Psi_0} + a_2)] \frac{e^{i(k_1 X_1 + k_2 X_2)}}{\rho_0}$$
$$+ \frac{U_0^2}{\rho_0}\left(\frac{\partial \rho_0}{\partial \Phi_0} \frac{\partial \tilde{\varphi}}{\partial \Phi_0} + \frac{\partial \rho_0}{\partial \Psi_0} \frac{\partial \tilde{\varphi}}{\partial \Psi_0}\right) \tag{3.48a}$$

where

$$\frac{\partial \tilde{\varphi}}{\partial \Phi_0} = \frac{i k_1}{U_0^2} \tilde{\varphi} \tag{3.48b}$$

$$\frac{\partial \tilde{\varphi}}{\partial \Psi_0} = (i k_1 \frac{\partial X_1}{\partial \Psi_0} + i k_2) \tilde{\varphi} - \frac{a_2 k_1 - a_1 k_2}{k_1(1 + i a_0 k_1)} e^{i k_1 X_1} \tag{3.48c}$$

$$S_2 = [a_1\left(\frac{i k_1}{U_0^2} - \frac{1}{U_0^2} \frac{\partial U_0^2}{\partial \Phi_0}\right) + a_1 U_0^2 \frac{\partial^2 X_1}{\partial \Psi_0^2}$$
$$+ U_0^2(a_1 \frac{\partial X_1}{\partial \Psi_0} + a_2)(i k_1 \frac{\partial X_1}{\partial \Psi_0} + i k_2) + i a_3 k_3] e^{i(k_1 X_1 + k_2 X_2)}$$
$$+ U_0^2\left(\frac{\partial^2 \tilde{\varphi}}{\partial \Phi_0^2} + \frac{\partial^2 \tilde{\varphi}}{\partial \Psi_0^2}\right) - k_3^2 \tilde{\varphi} \tag{3.49a}$$

where

$$\frac{\partial^2 \tilde{\varphi}}{\partial \Phi_0^2} = \frac{i k_1}{U_0^4}\left(i k_1 - \frac{\partial U_0^2}{\partial \Phi_0}\right) \tilde{\varphi} \tag{3.49b}$$

$$\frac{\partial^2 \tilde{\varphi}}{\partial \Psi_0^2} = (i k_1 \frac{\partial X_1}{\partial \Psi_0} + i k_2)\frac{\partial \tilde{\varphi}}{\partial \Psi_0} + i k_1 \frac{\partial^2 X_1}{\partial \Psi_0^2} \tilde{\varphi}$$
$$- i \frac{a_2 k_1 - a_1 k_2}{1 + i a_0 k_1} \frac{\partial X_1}{\partial \Psi_0} e^{i k_1 X_1} \tag{3.49c}$$

$$S_3 = - \left[\frac{k_1^2 M^2}{U_0^2} + i k_1 U_0^2 \frac{\partial}{\partial \Phi_0} \left(\frac{M^2}{U_0^2} \right) \right] \varphi_2$$

$$+ \left[M^2 \left(\frac{\partial U_0^2}{\partial \Phi_0} - 2 i k_1 \right) + U_0^4 \frac{\partial}{\partial \Phi_0} \left(\frac{M^2}{U_0^2} \right) \right] \frac{\partial \varphi_2}{\partial \Phi_0} \qquad (3.50a)$$

$$+ M^2 U_0^2 \frac{\partial^2 \varphi_2}{\partial \Phi_0^2}$$

where

$$\frac{\partial \varphi_2}{\partial \Phi_0} = i k_1 \frac{\partial X_{e,1}}{\partial \Phi_0} \varphi_2 \qquad (3.50b)$$

$$\frac{\partial X_{e,1}}{\partial \Phi_0} = 1 - \frac{2\Gamma}{\pi} \operatorname{sgn}(\Psi_0) \Phi_0 e^{-(\Phi_0^2 + \Psi_0^2)} \left[\frac{\pi}{2} + \operatorname{sgn}(\Psi_0) \tan^{-1} \left(\frac{\Phi_0}{\beta_\infty \Psi_0} \right) \right]$$

$$- \frac{\Gamma}{\pi} \frac{\beta_\infty \Psi_0}{\Phi_0^2 + \beta_\infty^2 \Psi_0^2} \left[1 - e^{-(\Phi_0^2 + \Psi_0^2)} \right] \qquad (3.50c)$$

$$\frac{\partial^2 \varphi_2}{\partial \Phi_0^2} = i k_1 \frac{\partial^2 X_{e,1}}{\partial \Phi_0^2} \varphi_2 - k_1^2 \left(\frac{\partial X_{e,1}}{\partial \Phi_0} \right)^2 \varphi_2 \qquad (3.50d)$$

$$\frac{\partial^2 X_{e,1}}{\partial \Phi_0^2} = - \frac{\Gamma}{\pi} \left\{ 2 \operatorname{sgn}(\Psi_0)(1 - 2\Phi_0^2) e^{-(\Phi_0^2 + \Psi_0^2)} \left[\frac{\pi}{2} + \operatorname{sgn}(\Psi_0) \tan^{-1} \left(\frac{\Phi_0}{\beta_\infty \Psi_0} \right) \right] \right.$$

$$\left. + \frac{4\beta_\infty \Phi_0 \Psi_0}{\Phi_0^2 + \beta_\infty^2 \Psi_0^2} e^{-(\Phi_0^2 + \Psi_0^2)} - \frac{2\beta_\infty \Phi_0 \Psi_0}{(\Phi_0^2 + \beta_\infty^2 \Psi_0^2)^2} \left[1 - e^{-(\Phi_0^2 + \Psi_0^2)} \right] \right\} \qquad (3.50e)$$

$$S_4 = \frac{U_0^2}{\rho_0}\left(\frac{\partial \rho_0}{\partial \Phi_0}\frac{\partial \varphi_2}{\partial \Phi_0} + \frac{\partial \rho_0}{\partial \Psi_0}\frac{\partial \varphi_2}{\partial \Psi_0}\right) + U_0^2\left(\frac{\partial^2 \varphi_2}{\partial \Phi_0^2} + \frac{\partial^2 \varphi_2}{\partial \Psi_0^2}\right) - k_3^2 \varphi_2 \tag{3.51a}$$

where

$$\frac{\partial \varphi_2}{\partial \Psi_0} = (ik_1\frac{\partial X_{e,1}}{\partial \Psi_0} + ik_2)\varphi_2 - \frac{a_2 k_1 - a_1 k_2}{k_1(1+ia_0 k_1)}e^{ik_1 X_{e,1}} \tag{3.51b}$$

$$\frac{\partial X_{e,1}}{\partial \Psi_0} = -\frac{2\Gamma}{\pi}\mathrm{sgn}(\Psi_0)\Psi_0 e^{-(\Phi_0^2+\Psi_0^2)}[\frac{\pi}{2} + \mathrm{sgn}(\Psi_0)\tan^{-1}(\frac{\Phi_0}{\beta_\infty \Psi_0})]$$
$$+ \frac{\Gamma}{\pi}\frac{\beta_\infty \Phi_0}{\Phi_0^2 + \beta_\infty^2 \Psi_0^2}[1 - e^{-(\Phi_0^2+\Psi_0^2)}] \tag{3.51c}$$

$$\frac{\partial^2 \varphi_2}{\partial \Psi_0^2} = (ik_1\frac{\partial X_{e,1}}{\partial \Psi_0} + ik_2)\frac{\partial \varphi_2}{\partial \Psi_0} + ik_1\frac{\partial^2 X_{e,1}}{\partial \Psi_0^2}\varphi_2$$
$$- i\frac{a_2 k_1 - a_1 k_2}{1+ia_0 k_1}\frac{\partial X_{e,1}}{\partial \Psi_0}e^{ik_1 X_{e,1}} \tag{3.51d}$$

$$\frac{\partial^2 X_{e,1}}{\partial \Phi_0^2} = -\frac{\Gamma}{\pi}\left\{2\,\mathrm{sgn}(\Psi_0)(1-2\Psi_0^2)e^{-(\Phi_0^2+\Psi_0^2)}[\frac{\pi}{2} + \mathrm{sgn}(\Psi_0)\tan^{-1}(\frac{\Phi_0}{\beta_\infty \Psi_0})]\right.$$
$$- \frac{4\beta_\infty \Phi_0 \Psi_0}{\Phi_0^2+\beta_\infty^2 \Psi_0^2}e^{-(\Phi_0^2+\Psi_0^2)} + \frac{2\beta_\infty^3 \Phi_0 \Psi_0}{(\Phi_0^2+\beta_\infty^2 \Psi_0^2)^2}[1-e^{-(\Phi_0^2+\Psi_0^2)}]\left.\right\} \tag{3.51e}$$

The frequency domain governing equation is then given by

$$-\beta_\infty^2 \left[\frac{\partial^2 \psi}{\partial \Phi^2} + \frac{\partial^2 \psi}{\partial \Psi^2} + \left(\frac{k_1^2 M_\infty^2}{\beta_\infty^4} - \frac{k_3^2}{\beta_\infty^2} \right) \psi \right]$$

$$+ A_1 \psi + A_2 \frac{\partial \psi}{\partial \Phi} + A_3 \frac{\partial \psi}{\partial \Psi} + A_4 \frac{\partial^2 \psi}{\partial \Phi^2} + A_5 \frac{\partial^2 \psi}{\partial \Psi^2} \qquad (3.52)$$

$$= e^{iK_0 \Phi}(S_1 + S_2 + S_3 - S_4)$$

where $A_1...A_5$ are defined by equations (3.44) and $S_1...S_4$ are defined by equations (3.48), (3.49), (3.50), and (3.51). In the far field both the coefficients $A_1...A_5$ and the source term $S_1 + S_2 + S_3 - S_4$ tend to zero so that the equation reduces to a Helmholtz equation.

We conclude this section by presenting the frequency domain formulation of the airfoil and wake boundary conditions given by equations (3.10), (3.11a) and (3.11b). In terms of the new coordinates (Φ, Ψ) and the new dependent variable ψ, equation (3.10) for the airfoil boundary condition becomes

$$\frac{\partial \psi}{\partial \Psi} = -\frac{e^{iK_0 \Phi}}{\beta_\infty} \left[\frac{a_1 \beta_\infty \Gamma}{\pi} \frac{1 - e^{-\Phi^2}}{\Phi} + \frac{a_2 + ia_0 a_1 k_2}{1 + ia_0 k_1} \right] e^{ik_1 X_{e,1}}. \qquad (3.53)$$

The wake boundary condition (3.11a) becomes

$$\left(-ik_1 + U_0^2 \frac{\partial}{\partial \Phi} \right) [\Delta(\psi e^{-iK_0 \Phi} - \varphi_2)] = 0, \qquad (3.54a)$$

where $\Delta(\psi e^{-iK_0 \Phi} - \varphi_2)$ denotes the jump in the quantity $(\psi e^{-iK_0 \Phi} - \varphi_2)$ across the vortex sheet behind the airfoil. Finally, condition (3.11b) becomes

$$\Delta[\vec{\nabla}(\psi e^{-iK_0 \Phi} - \varphi_2) \cdot \vec{n}] = 0. \qquad (3.54b)$$

3.4 Transformation into Computational Coordinates and Formulation of the Numerical Boundary Value Problem

Our basic numerical approach to solving equation (3.52) is to use the method of finite difference approximations. By discretizing the flow field and employing finite differences at each grid point, a large linear system of equations is obtained which can be solved using a matrix solver.

Previous experience in solving equation (3.52) for the case of flat plate and symmetric airfoils has shown that the independent variables (Φ, Ψ) are not suitable computational coordinates for the gust response problem.[30,31] There are difficulties in obtaining consistently accurate results over a large range of Mach numbers and reduced frequencies, and also problems with the implementation of far field boundary conditions. A transformation of the independent variables is needed which not only provides an adequate distribution of grid points around the airfoil in the near field, but also provides a distribution of grid points in the far field which is suitable for acoustic wave propagation and the implementation of far field, radiation type boundary conditions.

In order to satisfy these requirements, we make a transformation into the elliptic coordinates (η, ξ) with the transformation

$$\Phi = a^* \cos(\pi\eta)\cosh(\pi\xi) \qquad (3.55a)$$

$$\Psi = a^* \sin(\pi\eta)\sinh(\pi\xi) \qquad (3.55b)$$

where a^* is an arbitrary constant which will be defined later. Note that in the far field the elliptic coordinates reduce essentially to cylindrical coordinates, and that the $\Phi - \Psi$ plane is mapped into a semi-infinite strip in the $\eta - \xi$ plane.

With this change of variables, the governing equation takes the following form:

38

$$
- \beta_\infty^2 \left[\frac{\partial^2 \psi}{\partial \eta^2} + \frac{\partial^2 \psi}{\partial \xi^2} + J(\eta,\xi) \left(\frac{k_1^2 M_\infty^2}{\beta_\infty^4} - \frac{k_3^2}{\beta_\infty^2} \right) \psi \right]
$$

$$
+ A_1 J(\eta,\xi) \psi + T_1 \frac{\partial \psi}{\partial \xi} + T_2 \frac{\partial \psi}{\partial \eta} + T_3 \frac{\partial^2 \psi}{\partial \xi^2} + T_4 \frac{\partial^2 \psi}{\partial \eta^2} + T_5 \frac{\partial^2 \psi}{\partial \eta \partial \xi}
$$

$$
= e^{iK_0 \Phi} (S_1 + S_2 + S_3 - S_4) J(\eta,\xi). \tag{3.56}
$$

Here $J(\eta,\xi)$ is the Jacobian of the transformation (3.55) and is given by

$$
J(\eta,\xi) = \pi^2 a^{*2} [\sin^2(\pi\eta) + \sinh^2(\pi\xi)], \tag{3.57}
$$

and $T_1 ... T_5$ are functions of (η,ξ) defined by

$$
T_1(\eta,\xi) = a^\star \pi \, A_2 C_3(\eta,\xi) + a^\star \pi \beta_\infty \, A_3 C_4(\eta,\xi)
$$

$$
+ a^{\star 2} \pi^2 \beta_\infty \frac{A_4 C_1(\eta,\xi)}{J(\eta,\xi)^2} + a^{\star 2} \pi^2 \beta_\infty^3 \frac{A_5 C_5(\eta,\xi)}{J(\eta,\xi)^2} \tag{3.58a}
$$

$$
T_2(\eta,\xi) = -a^\star \pi \, A_2 C_4(\eta,\xi) + a^\star \pi \beta_\infty \, A_3 C_3(\eta,\xi)
$$

$$
+ a^{\star 2} \pi^2 \beta_\infty \frac{A_4 C_2(\eta,\xi)}{J(\eta,\xi)^2} + a^{\star 2} \pi^2 \beta_\infty^3 \frac{A_5 C_6(\eta,\xi)}{J(\eta,\xi)^2} \tag{3.58b}
$$

$$
T_3(\eta,\xi) = a^{\star 2} \pi^2 \frac{A_4 C_3(\eta,\xi)^2}{J(\eta,\xi)} + a^{\star 2} \pi^2 \beta_\infty^2 \frac{A_5 C_4(\eta,\xi)^2}{J(\eta,\xi)} \tag{3.58c}
$$

$$
T_4(\eta,\xi) = a^{\star 2} \pi^2 \frac{A_4 C_4(\eta,\xi)^2}{J(\eta,\xi)} + a^{\star 2} \pi^2 \beta_\infty^2 \frac{A_5 C_3(\eta,\xi)^2}{J(\eta,\xi)} \tag{3.58d}
$$

39

$$T_5(\eta,\xi) = -2a^{*2}\pi^2 \frac{A_4 C_3(\eta,\xi)C_4(\eta,\xi)}{J(\eta,\xi)}$$

$$+ 2a^{*2}\pi^2\beta_\infty^2 \frac{A_5 C_3(\eta,\xi)C_4(\eta,\xi)}{J(\eta,\xi)} \tag{3.58e}$$

and where $C_1...C_6$ are functions of (η,ξ) given by

$$C_1(\eta,\xi) = \frac{\pi}{\beta_\infty}\sinh(\pi\xi)\cosh(\pi\xi)\Big\{J(\eta,\xi)$$

$$+ 2a^{*2}\pi^2[\sin^2(\pi\eta)\cos^2(\pi\eta) - \sinh^2(\pi\xi)\cos^2(\pi\eta)]\Big\} \tag{3.59a}$$

$$C_2(\eta,\xi) = \frac{\pi}{\beta_\infty}\sin(\pi\eta)\cos(\pi\eta)\Big\{J(\eta,\xi)$$

$$+ 2a^{*2}\pi^2[\sinh^2(\pi\xi)\cosh^2(\pi\xi) - \cosh^2(\pi\xi)\sin^2(\pi\eta)]\Big\} \tag{3.59b}$$

$$C_3(\eta,\xi) = \sinh(\pi\xi)\cos(\pi\eta) \tag{3.59c}$$

$$C_4(\eta,\xi) = \cosh(\pi\xi)\sin(\pi\eta) \tag{3.59d}$$

$$C_5(\eta,\xi) = \frac{\pi}{\beta_\infty}\cosh(\pi\xi)\sinh(\pi\xi)\Big\{J(\eta,\xi)$$

$$- 2a^{*2}\pi^2[\sin^2(\pi\eta)\cosh^2(\pi\xi) + \sin^2(\pi\eta)\cos^2(\pi\eta)]\Big\} \tag{3.59e}$$

$$C_6(\eta, \xi) = \frac{\pi}{\beta_\infty} \sin(\pi\eta) \cos(\pi\eta) \Big\{ J(\eta, \xi)$$

$$- 2a^{\star 2}\pi^2[\sinh^2(\pi\xi)\cosh^2(\pi\xi) + \sinh^2(\pi\xi)\cos^2(\pi\eta)] \Big\} \tag{3.59f}$$

As before, $A_1...A_5$ are defined by equations (3.44).

The airfoil boundary condition (3.53) has also been transformed through the change of variables (3.55). Expressing condition (3.53) in the variables (η, ξ), one gets

$$\frac{\partial \psi}{\partial \xi} = -a^\star \pi \, \sin(\pi\eta) \frac{e^{iK_0\Phi}}{\beta_\infty} \Big[\frac{a_1\beta_\infty\Gamma}{\pi} \frac{1 - e^{-\Phi^2}}{\Phi} + \frac{a_2 + ia_0 a_1 k_2}{1 + ia_0 k_1} \Big] e^{ik_1 X_{e,1}}. \tag{3.60}$$

We now proceed to discuss the remaining boundary conditions. First, the wake boundary condition (3.54a) may be integrated so that it becomes

$$\Delta(\psi e^{-iK_0\Phi}) = \Delta\varphi_2 + [\Delta(\psi e^{-iK_0\Phi})_{t.e.} - \Delta\varphi_{2\,t.e.}]e^{ik_1 \int_{\Phi_{t.e.}}^{\Phi} \frac{d\Phi}{v_0^2}}, \tag{3.61}$$

where the subscript $t.e.$ denotes quantities at the airfoil trailing edge. Note that, in general, both ψ and Φ are discontinuous across the wake, so that in evaluating $\Delta(\psi e^{-iK_0\Phi})$, it is necessary to take into account the jump in both ψ and Φ. This condition is imposed for grid points on the lower side of the wake.

On the upper side of the wake, we impose condition (3.54b), which specifies that the normal velocity component of the unsteady velocity is continuous across the wake. This may be written

$$\Big[U_0 \frac{\partial}{\partial \Psi}(\psi e^{-iK_0\Phi} - \varphi_2)\Big]^+ = \Big[U_0 \frac{\partial}{\partial \Psi}(\psi e^{-iK_0\Phi} - \varphi_2)\Big]^- \tag{3.62}$$

where "+" and "−" superscripts denote above and below the wake, respectively, and the derivatives in (3.62) are taken to be one-sided.

In order to proceed further in the development of the boundary conditions (3.61) and (3.62) in terms of the computational coordinates (η, ξ), it is necessary to first discuss in more detail the transformation (3.55). First, the constant $a^\star$ is determined from the condition that the airfoil trailing edge point on the suction side, where $\Phi = a^\star, \Psi = 0$, should map into the point $\eta = 0, \xi = 0$, and the stagnation point, where $\Phi = -a^\star, \Psi = 0$ should map into the point $\eta = 1, \xi = 0$. Then $a^\star$ must be determined from

$$a^\star = \frac{1}{2} \int_{t.e.}^{s.p.} U_0 ds \tag{3.63a}$$

where s denotes the arc length along the airfoil surface, $t.e.$ denotes the airfoil trailing edge, and $s.p.$ denotes the stagnation point. The steady solver FLO36 is used to locate the stagnation point, and the integration in (3.63a) is carried out using trapezoidal integration.

The suction surface of the airfoil, then, corresponds to the line segment on the η axis between 0 and 1, and the pressure surface corresponds to the line segment on the η axis between 1 and $\eta_{t.e.-}$, where $\eta_{t.e.-} < 2.0$ (See Figure 5.) The value of $\eta_{t.e.-}$ is determined from equations (3.55a) and (3.33a), and is given by

$$\eta_{t.e.-} = 2 - \frac{1}{\pi} \cos^{-1}\left\{ \frac{1}{a^\star \beta_\infty^2} \left[2a\Big(\cos(\alpha + \mu) - \sin(\alpha + \mu)(2\pi - \mu)\Big) + K \right.\right.$$
$$\left.\left. - M_\infty^2 \left(a\cos\mu - \epsilon + \frac{d^2(a\cos\mu - \epsilon)}{a^2 - 2a(\epsilon'\sin\mu + \epsilon\cos\mu) + \epsilon^2 + \epsilon'^2} \right) \right] \right\}, \tag{3.63b}$$

where the constant K is determined from (3.33a) and (3.63a) and is given by

$$K = a^\star \beta_\infty^2 - 2a\Big[\cos(\alpha + \mu) + \mu\sin(\alpha + \mu)\Big]$$
$$+ M_\infty^2 \left[a\cos\mu - \epsilon + \frac{d^2(a\cos\mu - \epsilon)}{a^2 - 2a(\epsilon'\sin\mu + \epsilon\cos\mu) + \epsilon^2 + \epsilon'^2} \right], \tag{3.63c}$$

and the parameters $a, d, \epsilon, \epsilon'$, and μ are as defined in Section 3.2.

The pressure side of the wake, then, corresponds to the line segments given by $\{\eta_{t.e.-} < \eta \le 2.0, \ \xi = 0\}$, and $\{\eta = 2.0, \ \xi > 0\}$. The suction side of the wake

corresponds to the positive ξ axis. The upper boundary of the $\eta - \xi$ grid, which is given by $\{\xi = \xi_{max}, \ 0 \leq \eta \leq 2\}$, corresponds to the far field boundary in the $\Phi - \Psi$ plane.

Because of the discontinuity in Φ across the wake grid line, the grid points on the upper and lower sides of the wake in the physical plane (the $x_1 - x_2$ plane) do not coincide. This presents some difficulty in the implementation of boundary conditions (3.61) and (3.62), inasmuch as these conditions both specify a relation that must be satisfied across the wake. The difficulty can be removed, however, by simply using a linear averaging of ψ at the two adjacent grid points to represent ψ at an arbitrary point in between. Using such a linear averaging, then, boundary condition (3.61), which is imposed for wake grid points on the pressure side, becomes

$$
\left[(\psi e^{-iK_0\Phi})\right]^{+}_{avg} - \left[(\psi e^{-iK_0\Phi})\right]^{-}
$$

$$
= \Delta\varphi_2 + [\Delta(\psi e^{-iK_0\Phi})_{t.e.} - \Delta\varphi_{2t.e.}]e^{ik_1 \int_{\Phi_{t.e.}}^{\Phi} \frac{d\Phi}{U_0^2}}. \tag{3.64}
$$

The discontinuity in Φ across the wake also leads to a shift in the location of the corresponding grid points in the physical plane on opposite sides of the wake. Because of this shift, the last several grid points on the pressure side in the physical plane extend past the last suction side wake grid point, so that the above averaging technique cannot be employed. (See Figure 5.) However, because these last few points are in the far field where the mean flow is nearly uniform, the function ψ behaves essentially as in the case of the thin airfoil problem, and is approximately an odd function of Ψ. By assuming ψ to be an odd function with respect to Ψ in the far field, condition (3.61) becomes

$$
\left[(\psi e^{-iK_0\Phi})\right]^{-} = -\frac{1}{2}\Delta\varphi_2 - \frac{1}{2}[\Delta(\psi e^{-iK_0\Phi})_{t.e.} - \Delta\varphi_{2t.e.}]e^{ik_1 \int_{\Phi_{t.e.}}^{\Phi} \frac{d\Phi}{U_0^2}} \tag{3.65}
$$

43

for extra far field wake grid points on the pressure side.

For wake grid points on the suction side, the linear averaging technique can be used for all points, and condition (3.62) becomes

$$\left[U_0 \frac{\partial}{\partial \Psi}(\psi e^{-iK_0\Phi} - \varphi_2) \right]^+ = \left[U_0 \frac{\partial}{\partial \Psi}(\psi e^{-iK_0\Phi} - \varphi_2) \right]^-_{avg}. \tag{3.66}$$

Expressing this in η and ξ, one gets

$$\left[e^{-iK_0\Phi} \frac{U_0}{\sinh(\pi\xi)} \frac{\partial \psi}{\partial \eta} \right]^+ - \left[e^{-iK_0\Phi} \frac{U_0}{\sin(\pi\eta)} \frac{\partial \psi}{\partial \xi} \right]^-_{avg}$$

$$= U_0^+ \left(\frac{\partial \varphi_2^+}{\partial \Psi} - \frac{\partial \varphi_2^-}{\partial \Psi} \right) \tag{3.67}$$

when the averaged values of ψ lie on the η axis. When the averaged values of ψ lie on the right hand boundary of the $\eta - \xi$ grid $\{\eta = 2.0,\ \xi > 0\}$, (3.66) becomes

$$\left[e^{-iK_0\Phi} \frac{U_0}{\sinh(\pi\xi)} \frac{\partial \psi}{\partial \eta} \right]^+ - \left[e^{-iK_0\Phi} \frac{U_0}{\sinh(\pi\xi)} \frac{\partial \psi}{\partial \eta} \right]^-_{avg}$$

$$= U_0^+ \left(\frac{\partial \varphi_2^+}{\partial \Psi} - \frac{\partial \varphi_2^-}{\partial \Psi} \right) \tag{3.68}$$

In order to complete the formulation of the boundary conditions, it is only necessary to specify conditions at the airfoil trailing edge and in the far field. At the trailing edge, there are two grid points that coincide, one corresponding to the suction side of the airfoil and one corresponding to the pressure side. It is therefore necessary to impose two conditions at the trailing edge point. At the point on the suction side, which corresponds to $(\eta, \xi) = (0, 0)$, the Jacobian of the coordinate transformation (3.55) vanishes. Since the Kutta condition requires that the velocity at the trailing edge be finite, we are led to the requirement that

$$\frac{\partial \psi}{\partial \eta} = 0 \quad \text{at} \quad (\eta, \xi) = (0, 0). \tag{3.69}$$

At the pressure side trailing edge point, we impose the condition that the unsteady pressure is continuous,

$$p'_{t.e.+} = p'_{t.e.-} \quad \text{at} \quad (\eta, \xi) = (\eta_{t.e.-}, 0). \tag{3.70}$$

We point out that since the Jacobian vanishes at the suction side trailing edge point, it is not possible to directly calculate the pressure in the (η, ξ) coordinates at that point. However, it can be calculated using a Taylor series expansion from neighboring points. By using this approach, condition (3.70) can be satisfied.

In presenting the far field boundary condition, we first comment that while condition (3.12) expresses the mathematical requirement that $\vec{\nabla}\phi_1 \to 0$ at upstream infinity, this condition cannot be imposed throughout the far field on a boundary at a finite distance from the airfoil. To implement such a condition would impose a reflecting boundary condition which can lead to large errors in the solution.

To correctly model the physics of the present unsteady boundary value problem requires that the far field boundary condition be such that it allows outgoing acoustic waves to leave the solution domain without being reflected back into the computational grid. This can be accomplished, for example, by using separation of variables along with a series expansion for the far field solution ψ and only accepting those terms in the series which represent outgoing waves. The difficulty with this approach, however, is that it leads to a matrix which requires pivoting and therefore longer solution times. In addition, since ψ is not continuous across the wake, but the series expansion for ψ is continuous everywhere, there is an incompatibility near the wake which can lead to a poor solution in the far field.

An alternative to the series expansion approach is to use a Sommerfield radiation condition on the unsteady pressure. This approach avoids both the difficulties associated with the series expansion method and is also easier to implement. The Sommerfield radiation condition for the pressure is the approach used in the present

work, and may be written in operator notation as

$$\left[\frac{\partial}{\partial R} - i\sqrt{(\frac{k_1 M_\infty}{\beta_\infty^2})^2 - (\frac{k_3}{\beta_\infty})^2}\right](\frac{\partial}{\partial \Phi} - i\frac{k_1}{\beta_\infty^2})\,\psi = 0 \qquad (3.71)$$

where

$$\Phi = R\cos\Theta \qquad (3.72a)$$

$$\Psi = R\sin\Theta. \qquad (3.72b)$$

Neglecting $\frac{1}{R}\frac{\partial}{\partial\Theta}$ terms, this reduces to

$$\cos\Theta\frac{\partial^2\psi}{\partial R^2} - i\left[\sqrt{(\frac{k_1 M_\infty}{\beta_\infty^2})^2 - (\frac{k_3}{\beta_\infty})^2}\cos\Theta + \frac{k_1}{\beta_\infty^2}\right]\frac{\partial\psi}{\partial R}$$

$$- \frac{k_1}{\beta_\infty^2}\left[\sqrt{(\frac{k_1 M_\infty}{\beta_\infty^2})^2 - (\frac{k_3}{\beta_\infty})^2}\right]\psi = 0 \qquad (3.73)$$

This condition is applied for all grid points such that $0 < \eta < 2$, $\xi = \xi_{max}$.

3.5 Numerical Method

In the previous section we presented the transformation into computational coordinates and the development of the numerical boundary value problem. The problem to be solved numerically consists of the governing equation (3.56), and the boundary conditions (3.60), (3.64), (3.65), (3.67), (3.68), (3.69), (3.70) and (3.73). As mentioned previously, our basic numerical approach is to use the method of finite difference approximations, and then to solve the resulting linear system of equations using a matrix solver.

The first step in obtaining numerical solutions to equation (3.56) and its associated boundary conditions for a given flow configuration is to calculate the source term S and the coefficient functions $A_1...A_5$. This requires the evaluation of Lighthill's drift function and its first and second partial derivatives with respect

46

to Ψ, and the evaluation of the mean flow quantities and their partial derivatives with respect to Φ and Ψ at each interior grid point. The mean flow quantities are obtained through the scheme presented in Section 3.2, and their derivatives are calculated using four point differencing.

It should be emphasized that accurate evaluation of the source term is essential if accurate solutions to equation (3.56) are to be obtained, and this in turn depends largley upon the accurate calculation of the drift function. If the drift function is not calculated accurately, then the source term will not tend to zero in the far field and the numerical scheme will become unstable. One of the major advantages of using the analytical scheme outlined in Section 3.2 to obtain the mean flow is that it can determine the mean velocities at arbitrary (Φ, Ψ). This means that for fixed Ψ, i.e. on a given streamline, we can determine the mean velocities for arbitrary Φ. Since evaluation of the drift function requires the integration of the expression $(\frac{1}{U_0^2} - \frac{1}{U_\infty^2})$ with respect to Φ on a fixed streamline, it is very easy to do the numerical integrations necessary to accurately evaluate the drift function Δ. In the actual calculations, we evaluate Δ at a given grid point as the sum of an analytically determined part and a numerically determined part. The analytical part comes from a far field expansion for Δ which is given by

$$\Delta = \Phi_0 - \frac{\Gamma}{\pi} \text{sgn}(\Psi_0) \left[\frac{\pi}{2} + \text{sgn}(\Psi_0) \tan^{-1}(\frac{\Phi_0}{\beta_\infty \Psi_0}) \right] \qquad (3.74)$$

This expression can be used to accurately calculate Δ at some point far upstream, and then since Δ is additive, the remaining portion of the integration can be done numerically from the upstream location to the given grid point. The numerical integration is done using the trapezoid rule with variable spacing in Φ to ensure accurate resolution near the airfoil. The first and second partial derivatives of Δ are approximated using four point differencing.

Once S and $A_1...A_5$ have been calculated, they can be stored separately and passed to the subroutine which sets up the matrix equation to be solved.

We now proceed to discuss the differencing used for the governing equation and boundary conditions. To represent equation (3.56) we use the standard nine-point, central difference computational molecule which is second order accurate in η and ξ. (Nine points are required due to the mixed derivative term.) We assume in general that the spacing in each direction is nonuniform. Details of the grid spacing will be discussed momentarily. Each of the boundary conditions (3.60), (3.69), (3.70), and (3.73) are implemented using four-point, one-sided differencing which is third order accurate for (3.60), (3.69), and (3.70), and second order accurate for (3.73). Boundary conditions (3.67) and (3.68) are both implemented using three-point, one-sided differencing which is second order accurate.

Obtaining a numerical solution to the finite difference equations representing the governing equation (3.56) and its associated boundary conditions requires solving a large matrix equation whose size is equal to twice the number of grid points. There are difficulties in solving this linear system of equations because the matrix is not block tridiagonal and does not have a regular block structure which can be exploited. In addition, iterative solvers have convergence problems because the diagonal dominance of the matrix changes as the parameters M_∞, k_1, and k_3 are varied.

Because of these difficulties, a general purpose sparse matrix solver was developed which stores only the nonzero entries of the matrix and can solve an arbitrary sparse matrix equation using Gaussian elimination. The solver basically works by using an ordered list to represent the nonzero entries of each row in the matrix, and then inserts and deletes new entries in the rows of the matrix as multiples of each row are added to other rows to carry out the elimination process. The only requirement for the solver to work is that the matrix must be arranged such that it remains reasonably sparse during the elimination procedure.

The sparse solver has both a pivoting and non-pivoting feature. However, as pivoting during the elimination process proved to be unnecessary, the pivoting

feature was not used. By not pivoting during the elimination, it was possible to increase the storage efficiency of the solver and thereby solve larger systems of equations. The increased storage efficiency was gained by using a mapping function to map sub-blocks of the rectangular two-dimensional arrays containing the nonzero entries of the matrix and their associated column numbers into singly dimensioned arrays which contained less unused storage. By using this technique, the storage efficiency of the solver was increased by about 25 percent.

The final issue to be discussed in regard to our numerical scheme is the method of grid determination. As reported previously[30,31], it is not possible to use a single grid and obtain accurate solutions to the gust response problem for a large range of reduced frequencies. Rather, the unsteady grid must be determined as a function of both the mean flow Mach number and the reduced frequency.

This requirement is dictated by both the accuracy of the far field boundary condition (3.73), and the need to adequately model the airfoil boundary condition (3.63) and the wake boundary conditions (3.64) and (3.65). The accuracy of the far field boundary condition depends on the reduced frequency k_1 and free stream Mach number M_∞ in such a way that the parameter $\frac{k_1 M_\infty}{\beta_\infty^2} R$, where R is the distance to the far field boundary, should remain at least $O(1)$. This shows that the location of the outer boundary of the grid must be determined as a function of k_1 and M_∞. In addition, there should be enough grid points per wavelength to accurately represent the airfoil and wake boundary conditions. Due to the harmonic terms containing the parameters K_0 and k_1, this shows that the η and ξ spacing have to be determined as a function of k_1 and M_∞.

The spacing in the η direction is constant for $0 \leq \eta \leq 1$, and then changes slightly but constant again for $1 \leq \eta \leq \eta_{t.e.-}$, and finally constant again, but slightly different from the two previous intervals, for $\eta_{t.e.-} \leq \eta \leq 2$. The spacing on $0 \leq \eta \leq \eta_{t.e.-}$ determines the spacing on the airfoil surface. Normally the number of grid points in the η direction varies from 40 for the low frequencies up to about

70 for reduced frequencies of 4.

An optimal spacing of the grid points in the wake (the ζ direction) turns out to be more difficult to achieve than the spacing on the airfoil. Numerical studies of the thin airfoil gust response problem showed that the optimal choice of spacing was 12 uniformly spaced grid points per wavelength. For the case of the thin airfoil, the wake boundary condition analogous to condition (3.64) is much simpler, and it is possible to choose the spacing of the ζ grid points such that they are uniformly spaced along the waves. However, for the general problem of nonuniform mean flows, the waves in the wake are distorted due to the $e^{ik_1 \int_{*_{t.e.}}^{*} \frac{d\xi}{v_0^*}}$ term, and it is no longer possible to determine the grid point spacing such that they are uniformly spaced along the waves. This does not prove to be a difficulty, however, because in the far field the general problem of vortical flows past a lifting airfoil reduces essentially to a linear problem as the mean flow tends to become uniform. So we may determine the wake spacing as in the case of the flat plate airfoil, and in the far field the grid points will be nearly uniformly spaced along the waves.

For a flat plate airfoil, the wake boundary condition which imposes the continuity of the pressure is given, corresponding to the transformation (3.55), by

$$\psi_{wake,j} = \psi_{t.e.} e^{i \frac{k_1}{\beta_\infty^2}[a^* \cosh(\pi \xi_j) - a^*]}. \tag{3.75}$$

In order to have uniformly spaced grid points along the waves in the wake, the argument of the exponential function should vary by equal fractional increments of π. To place 12 grid points per wavelength, we are then led to the requirement that the location of the $j th$ ζ grid point be determined from the relation

$$\frac{k_1}{\beta_\infty^2}[a^* \cosh(\pi \xi_j) - a^*] = j \frac{2\pi}{12}. \tag{3.76}$$

Solving for ξ_j, we get

$$\xi_j = \frac{1}{\pi} \cosh^{-1}\left(j \frac{\pi \beta_\infty^2}{6 a^* k_1} + 1\right). \tag{3.77}$$

This is the method for determining the ζ spacing in the far field. Near the airfoil the above procedure leads to a spacing which is too coarse to be used. So near the

50

airfoil we use uniform ξ spacing which remains constant at some value $\triangle \xi$, until a point is reached such that the ξ_j determined from (3.77) satisfy $\xi_{j+1} - \xi_j \leq \triangle \xi$. From that point on, the spacing of the ξ grid points is determined from (3.77).

CHAPTER IV

NUMERICAL RESULTS AND DISCUSSION

4.1 Code Validation

Extensive efforts were taken to validate the computer codes which were developed to implement the numerical solution procedure which was outlined in the previous chapter. The validation process consisted of a combination of comparing numerical results with known analytical solutions to the classical thin airfoil gust response problems, comparing with the second order theory of Goldstein and Atassi[7] and Atassi,[8] comparing with the first order numerical results of Atassi and Grzedzinski,[29] and calculating solutions to limiting case problems i.e., as Mach number, thickness, angle of attack, or camber go to zero.

Sample computation times for the results presented varied considerably, depending on the reduced frequency, Mach number, and airfoil loading. For thin, unloaded airfoils, with low reduced frequency gusts, typical solution times were about 20 seconds per frequency on the Cray X-MP at the NASA Lewis Research Center. The higher frequencies for these airfoils required on the order of 60 CPU seconds per frequency, with slightly higher solution times for the higher Mach number cases. For symmetric, unloaded airfoils with nonzero thickness, the solution times ranged from about 40 seconds for the lower frequencies up to about 150 seconds for the highest frequencies. Finally, for loaded airfoils, the solution times ranged from about 250 seconds for the low frequencies up to around 1200 seconds for the highest reduced frequencies. No effort was made to optimize the computational efficiency of the scheme, as our main purpose was to validate its accuracy.

In the results that follow, comparisons are made for one-dimensional (transverse) gusts, two-dimensional (transverse and longitudinal) gusts, and fully three-dimensional gusts. See Figures 6, 7, and 8.

52

The first step in the validation process was to compare numerical results with known solutions to the classical thin airfoil gust response problems. In Figures 9 and 10 we present comparisons between numerical and analytical results for the normalized unsteady lift for vortical flows past flat plate airfoils. The normalized unsteady lift, commonly called the response function, is defined by

$$R_L(k_1, k_3, M_\infty) = \frac{L'}{\pi \rho_\infty c U_\infty |\vec{a}| e^{i\omega t}} \tag{4.1}$$

where L' is the unsteady lift. Figure 9.a shows a comparison between numerical results and the Sears solution[2] for the case of a one-dimensional (transverse) gust in incompressible flow, and Figures 9.b and 9.c compare numerical results and analytical results obtained from a Possio solver for a one-dimensional gust at Mach numbers of .5 and .8. The reduced frequency values at which the comparisons are made range from 0 to 4.0, and are shown below the plots. The point on the real axis and furthest to the right corresponds to $k_1 = 0$, and the other points along the curve correspond in order to the other reduced frequency values. Figures 10.a through 10.c compare numerical results and analytical results from a Possio solver for three-dimensional gusts for Mach numbers of .1, .5, and .8. The conditions on the gust wave number parameters are shown below the plots. As can be readily seen, there is excellent agreement between the numerical and analytical results. The only loss of accuracy occurs when both the Mach number and reduced frequency become large.

In order to assess the accuracy of the present numerical scheme for vortical flows around thin airfoils in which the mean flow is not uniform, we compare with the second order theory of Goldstein and Atassi [7] and Atassi.[8] The results given by Atassi assume a zero thickness airfoil, but account for the effects of camber and angle of attack on the airfoil unsteady response. In Figure 11, we compare the numerically computed response function with the second order theory for an incompressible flow with a two-dimensional gust about an airfoil with an angle of attack of two degrees and a camber ratio of .05. The numerically computed response function is for a 6%

thick Joukowski airfoil, while the second order theory does not take into account the airfoil thickness. The reduced frequency values used for the comparison are shown below the plot. As can be seen, the numerical results for the 6% thick airfoil show a slightly larger lift at the low frequencies, but a slightly smaller lift at the higher frequencies for k_1 up to about 3.0. As will be seen later in the discussion on the effects of airfoil thickness, this effect can be attributed entirely to the thickness of the airfoil, so that the agreement is very good for reduced frequencies ranging from 0 up to about 3.0. For the frequencies higher than 3.0, it is not possible to make any firm conclusion on the accuracy of the numerical results.

It should be mentioned at this point that the numerical results in the present work assume that the origin of the imposed upstream gust is at the center of the airfoil. Due to the representation of the gust given by (2.47), the gust will not appear to be centered at the airfoil center and there will be a corresponding phase change in the unsteady lift and moment. For a Joukowski airfoil with an imposed upstream gust of the form (2.47), it can be shown that the unsteady lift and moment should be multiplied by the phase correction factor P_c given by

$$P_c = e^{i[k_1(\frac{\Gamma}{2\pi} - W_{o,r} - x_c') + k_2(\frac{\Gamma}{2\pi}\ln 2 - W_{o,i} - y_c')]}$$
(4.2a)

in order for the gust to be referenced with respect to the airfoil center. Here $W_{o,r} + i\, W_{o,i}$ is the complex constant associated with the complex potential for the incompressible flow around the transformed Joukowski airfoil, and x_c' and y_c' are the coordinates of the airfoil center rotated through the angle of attack α. These parameters are given by

$$W_{o,r} = \epsilon \cos \alpha - \epsilon' \sin \alpha + K$$
(4.2b)

$$W_{o,i} = -\epsilon \sin \alpha - \epsilon' \cos \alpha - \frac{\Gamma}{2\pi} \ln a$$
(4.2c)

and

$$x_c' = x_c \cos \alpha + y_c \sin \alpha$$
(4.2d)

$$y_c' = y_c \cos \alpha - x_c \sin \alpha \qquad (4.2e)$$

where

$$x_c = 2d - 1 \qquad (4.2f)$$

$$y_c = \frac{2 d \epsilon'}{d + \epsilon} \qquad (4.2g)$$

and the chord length of the airfoil is 2. The parameters ϵ, ϵ', a and d are as defined in Section 3.2 and the constant K is given by equation (3.63c). Note that for airfoils with zero thickness and zero mean loading, the phase correction factor P_c reduces to just 1.

In the results given in Figure 11, the second order theory assumed a zero thickness airfoil. In order to to validate the numerical scheme for airfoils with thickness, we compare with the first order results of Atassi and Grzedzinski.[29] In Figure 12, we show comparisons for one-, two-, and three-dimensional gusts for incompressible flows around a 12% thick Joukowski airfoil with zero degrees angle of attack and zero camber ratio. The reduced frequency values for the comparison range from .2 to 2.5 and are shown below the plots. We limit the comparison to this range of k_1, since this is roughly the range of validity of the Green's function approach of Atassi and Grzedzinski. The agreement between the two sets of results is good in general.

The final step in the validation process was to calculate the solutions to various limiting case problems. The limiting case of $M_\infty \to 0$, i.e., the incompressible case, was covered above where the numerical results were compared to the Sears solution. We now present results for the limiting cases of airfoil thickness, angle of attack, and camber.

In Figures 13 through 16, we compare numerical results for the unsteady lift and moment about the airfoil center of a 3% thick, symmetric Joukowski airfoil with that of a flat plate airfoil with zero thickness. Analogous to the response function R_L for the unsteady lift, we define the response function R_M for the unsteady

moment by

$$R_M(k_1, k_3, M_\infty) = \frac{M'}{\frac{\pi}{2}\rho_\infty c^2 U_\infty |\vec{a}| e^{i\omega t}} \qquad (4.3)$$

where M' is the unsteady moment about the airfoil center. Figures 13 and 14 present results for $M_\infty = .1$, and Figures 15 and 16 present results for $M_\infty = .6$. For both Mach numbers, it is seen that the small airfoil thickness has little effect on the unsteady response, except for high reduced frequencies in the two-dimensional gust case, where the magnitude of the unsteady lift is reduced by 15 - 20 percent. It would appear from these results that thickness effects become more important at the higher frequencies for the case of the two-dimensional gust.

Figures 17 and 18 present comparisons between results for a 12% thick symmetric Joukowski airfoil at zero degrees angle of attack and one degree angle of attack. All plots are for a free stream Mach number of .1. As in the case of airfoil thickness, the strongest effect is seen in the two-dimensional gust case. However, here there is a significant effect both for the low and high reduced frequencies. At the low frequency end, the effect is primarily a reduction in the magnitude of the unsteady lift, while at the high end it is primarily a change in phase of the unsteady lift. We also point out that, in agreement with the theoretical results of Atassi,[8] for the transverse gust case in which the gust has only an upwash component, the steady loading on the airfoil has virtually no effect on the unsteady lift.

Finally, in Figures 19 through 20, we compare results for a 12% thick Joukowski airfoil with no camber with a 12% thick Joukowski airfoil with a camber ratio of .02. The free stream Mach number for all plots is .1 and the angle of attack is zero degrees. The effect of the small airfoil camber here is exactly analogous to the effect of small angle of attack above, except that here the effect is stronger due to the increased steady loading on the airfoil. For the airfoil with one degree angle of attack, the steady lift coefficient was .12, while for the 2% cambered airfoil the steady lift coefficient was .27. In each case, the reduction of the quasi-steady lift $(k_1 \to 0, \ k_2 \to 0)$ for the two-dimensional gust is directly proportional to the steady

56

loading on the airfoil with a proportionality constant of 0.26. Using the theoretical results of Atassi reported in Reference 8, it can be shown that for zero thickness airfoils in a two-dimensional gust in incompressible flow, the reduction in the quasi-steady lift for airfoils with small camber and angle of attack is proportional to the steady lift coefficient with a proportionality constant of $\frac{1}{\pi}\frac{k_2}{|k|} = .23$. The difference between the numerical and theoretical values of the proportionality constant can be accounted for by the fact that the theoretical result does not account for the thickness of the airfoil.

Before concluding the present section, the author would like to emphasize the significance of the method of grid determination which was outlined in Section 3.5. In Figure 21 we present numerical results which demonstrate the kinds of errors that can occur as a result of using an inappropriate grid. The results shown in these figures were generated without determining the grid as a function of the reduced frequency. For each case shown, the same grid was used for all frequencies in the calculation. The grid used for each Mach number was the one normally used only for the highest reduced frequency. By using the grid for the highest frequency, it was assured that there would be sufficient grid resolution to resolve the waves for the lower frequencies. But as can be seen, the agreement is not nearly as good as when the grid is determined as a function of both the Mach number and reduced frequency. These results show the effect of keeping the outer boundary fixed, and not varying it with the reduced frequency in order to ensure that the representation of the far field boundary condition is sufficiently accurate.

The results in Figure 22 show the kinds of errors that can occur when the grid points are not suitably spaced in the far field. The grids used for the results in Figure 22 used an exponentially decreasing spacing which was varied to ensure that there were enough grid points per wavelength to adequately model the wavelike structure of the solution. In addition, the location of the far field boundary was also varied to ensure that the far field boundary condition would be sufficiently accurate.

However, as the results show, there are large errors in the response function curves. This is due to the fact that exponential spacing is not suitable for this kind of wave propagation problem.

4.2 Discussion of Numerical Results

Our major purpose in the presentation and discussion of numerical results is to demonstrate the effects of airfoil thickness, angle of attack, camber, and Mach number on the airfoil unsteady response to imposed upstream rotational velocity disturbances (gusts). We will examine in detail the effects of each of these parameters on the unsteady lift and moment of airfoils subjected to one-, two-, and three-dimensional gusts. First we will examine the effects of airfoil thickness, then the effects of mean loading through both angle of attack and camber, and finally the effects of Mach number.

Before presenting the unsteady results, we show plots of the mean flow Mach number at the airfoil surface for the various flow configurations that were considered in the present work. These plots are shown in Figures 23 through 43. Plots of the airfoils used for these calculations are shown in Figures 44 and 45. We also present sample computational grids used for the unsteady calculations in Figures 46 through 61. Since for each airfoil geometry a different grid was used for every Mach number and reduced frequency, these represent only a very small fraction of the unsteady grids used to generate the results that follow.

4.2.1 Effects of Airfoil Thickness
on the Unsteady Response Functions

In Figures 62 through 82, we present results that demonstrate the effects of airfoil thickness on the unsteady response functions. Figures 62 through 68 show results for the one-dimensional gust case, Figures 69 through 75 show results for the two-dimensional gust case, and Figures 76 through 82 show results for the three-dimensional gust case. For each of the three cases, we begin by comparing results

for unloaded flat plate airfoils versus results for unloaded, symmetric airfoils with a thickness ratio of .12. Comparisons are made at Mach numbers of .1, .5, .6, and .7. At a Mach number of .8, there is a strong shock on the 12% thick airfoil, and so for this case we compare the flat plate results with results for a 6% thick airfoil. The comparisons for the unloaded airfoils are followed by comparisons for airfoils with mean loading. Here we compare results between airfoils with thickness ratios of .06 and .12. Each airfoil has an angle of attack of $2°$ and camber ratio of .05. We compare results at Mach numbers of .1 and .5.

An examination of the results indicates that there is a significant difference in the effects of airfoil thickness on the unsteady response functions depending on whether the gust is one-, two-, or three-dimensional, and also depending on the Mach number. We will discuss the one-dimensional gust case first, then the two-dimensional case, and finally the three-dimensional case.

For the one-dimensional gust, it is seen that the effects of thickness at the lower frequencies, i.e., for k_1 ranging from 0 up to about .2, is primarily to increase the magnitude of the unsteady response, while the phase is only slightly altered. The results for the unsteady moment show that for this range of frequencies the effects of thickness are essentially the same irrespective of the Mach number. For the unsteady lift, however, the effects of airfoil thickness becomes stronger with increasing Mach number. At a Mach number of .1, for example, there is an increase in the quasi-steady lift ($k_1 \to 0$) from the flat plate to the 12% thick airfoil of 9.1%. At the .5 Mach number, however, there is a 10.9% increase, and at the .6 and .7 Mach numbers, there is a 12.5% and 15.7% increase, respectively. As the reduced frequency increases above about .2, the airfoil thickness has a significant effect on both the magnitude and phase of the unsteady response. The plots for the unsteady lift show that the change in phase at the highest frequencies depends strongly upon the Mach number. At a Mach number of .1, the phase of the unsteady lift for the thick airfoil lags the corresponding phase for the flat plate, but at a Mach number

of .5, the phases are about the same, and for higher Mach numbers, the phase of the lift for the thick airfoil leads the phase of the flat plate airfoil by an amount that increases as the Mach number becomes higher. This is in contrast to the effect of thickness on the phase of the high frequencies of the unsteady moment, where the phase of the thick airfoil always lags the phase of the flat plate airfoil, irrespective of Mach number. We also note that the magnitude of the unsteady moment at the higher frequencies is strongly affected by the airfoil thickness as the Mach number increases.

The above results are all for symmetric airfoils without mean loading. In Figures 67 and 68, we present results demonstrating the effects of airfoil thickness on the unsteady response for airfoils that have steady loading. As mentioned previously, the results in these figures are for 6% thick versus 12% thick airfoils, with a camber ratio of .05 and angle of attack of 2°. Results are shown for Mach numbers of .1 and .5. It is seen that the unsteady lift for the loaded airfoils in the one-dimensional gust case is affected by airfoil thickness in an analogous way to the unloaded airfoils. The general trend is for the magnitude of the unsteady lift of the thicker airfoil to be increased at the lower frequencies, while at the higher frequencies the magnitude is reduced and the phase is also altered. The results for the unsteady moment show little change with increased airfoil thickness for the airfoil configurations used in these figures.

We now turn to discuss thickness effects for the case of the two-dimensional gust, i.e. a transverse and longitudinal gust. We begin our discussion with the comparison between the flat plate results versus the thick symmetric airfoil results in which there is no mean loading on the airfoil (See Figures 69 - 73.) There are noticeable differences in the effects of airfoil thickness between the one- and two-dimensional gust cases.

At a free stream Mach number of .1, it is seen that the effect of thickness is to increase the magnitude of the unsteady lift at the lowest frequencies by about

9%, while at the highest frequencies the magnitude is reduced by nearly 40% and the phase has been shifted by about -90°. Remarkably, there is a range of reduced frequencies, roughly $0.45 \leq k_1 \leq 1.6$, where the thickness has virtually no effect on the unsteady lift and moment.

It is interesting to note that as the Mach number increases, the effect of airfoil thickness at the lowest frequencies actually decreases. The reason for this unexpected result is not known at the present time. Recall that for the one-dimensional gust case, the effects of airfoil thickness became stronger for the low reduced frequencies as the Mach number increased.

Figures 74 and 75 show the effects of airfoil thickness for the two-dimensional gust case for the two loaded airfoil configurations that were described earlier. For the unsteady lift, the general trend at both Mach numbers is for the magnitude of the unsteady response function for the thicker airfoil to be increased at the low frequency end and decreased at the high frequency end. The unsteady moment plots show almost no thickness effects. These results are essentially analogous to the previous results for the unloaded airfoil case, except that the previous results showed a stronger effect due to the fact that the comparison was between a 0% thick and 12% thick airfoil, rather than 6% and 12% thick airfoils.

We conclude our discussion of airfoil thickness effects by looking at the results for the case of three-dimensional gusts (See Figures 76 - 82). We note first that the effects of thickness for three-dimensional gusts are noticeably different than for one- and two-dimensional gusts. There are two main differences which are apparent.

First, for the low reduced frequencies, airfoil thickness does not lead to an increase in the magnitude of the unsteady response functions when the gust is three-dimensional. For Mach numbers up to .6, there is no significant difference in the response function magnitude on the low frequency end. However, for the .7 and .8 Mach numbers, the results show that the magnitude of both the unsteady lift and moment are noticeably reduced for the thick airfoil for reduced frequencies ranging

from 0 up to about .2. This is in direct contrast to the one- and two-dimensional gust cases where the magnitude of the unsteady response was in general increased for the thicker airfoil for this range of reduced frequencies.

The second major difference in the effects of thickness for the three-dimensional gust case versus the one- and two-dimensional cases is that there is a strong effect on both the magnitude and phase of the unsteady response functions in the mid-frequency range, i.e., for k_1 roughly between .3 and 1.0. The results show that for this range of reduced frequencies, especially for the higher Mach numbers, the magnitude of the unsteady lift and moment is significantly increased for the thicker airfoil. In the one- and two-dimensional gust cases, the effects of airfoil thickness were strongest at the low and high reduced frequencies, rather than for the middle range of frequencies.

Finally, we note that for the high reduced frequencies at all Mach numbers shown, the magnitude of the unsteady lift and moment is significantly reduced for the thicker airfoil. This is the main respect in which the three-dimensional gust results for thickness effects resemble the one- and two-dimensional gust results.

4.2.2 Effects of Mean Airfoil Loading
on the Unsteady Response Functions

Figures 83 through 112 present results which show the effects of mean loading on the unsteady response functions. All of the plots in these figures compare response functions for a 12% thick airfoil with no steady loading versus a 12% thick airfoil with steady loading due to either angle of attack or camber or both. Comparisons are made at Mach numbers of .1, .5, and .6. At a Mach number of .1, the loaded airfoils for which the comparison is made have the following configurations: $\alpha = 3^o$, camber $= 0$; $\alpha = 5^o$, camber $= 0$; $\alpha = 0^o$, camber $= .05$; $\alpha = 2^o$, camber $= .05$; and finally $\alpha = 0^o$, camber $= .10$. At a Mach number of .5, the loaded airfoil configurations are: $\alpha = 5^o$, camber $= 0$; $\alpha = 0^o$, camber $= .05$; $\alpha = 2^o$, camber $=$

.05; and $\alpha = 0°$, camber = .10. At a .6 Mach number, the only comparison made is for an airfoil with $\alpha = 3°$ and camber = 0. The choice of the airfoil configurations was limited by the necessity that the mean flow be free of shocks. The configurations that were chosen enable us to look at loading effects due to angle of attack alone, camber alone, and angle of attack and camber together.

It is evident from the results that the effects that steady airfoil loading has on the unsteady response functions varies considerably, depending upon whether the gust is one-, two-, or three-dimensional. It is also evident that the effect on the unsteady moment differs in significant ways from the effect on the unsteady lift.

The results for the one-dimensional gust case (Figures 83 - 92) show that there is not much effect on the response functions due to the airfoil loading unless the airfoil is substantially loaded. For the results presented, only the 10% cambered airfoil shows a strong effect on the unsteady lift and moment. At both the .1 and .5 Mach numbers, the effect on the unsteady lift for the 10% cambered airfoil is to produce a spike in the response function curve which occurs at about $k_1 = 3.0$. The results for the unsteady moment also show a spike in the response function curve for the .5 Mach number case. The spike here occurs at $k_1 = 2.0$, and is followed by a portion of the curve that is concave up rather than concave down. It is interesting to note that these features for both the unsteady lift and moment can be seen in their formative stages in the plots for the .5 Mach number airfoil with 5% camber and $2°$ angle of attack (See Figure 90). We conclude that for the one-dimensional gust case, small amounts of mean airfoil loading have a negligible effect on the unsteady response functions, but as the loading increases, there eventually develops a spike that appears in the response function curve at the higher frequencies. The spike point is then followed by a portion of the curve which is markedly different from the corresponding curve for the unloaded airfoil case.

In contrast to the results for the one-dimensional gust case, the two-dimensional gust results (Figures 93 - 102) show a strong effect due to airfoil mean loading, even

for only lightly loaded airfoils. The effect on the unsteady lift is seen to be much stronger than on the unsteady moment.

For airfoils with small loading, the effect on the unsteady lift at the low reduced frequencies is primarily to shift the response function in the direction of the negative real axis without changing the basic shape of the curve. The amount that the curve is shifted is given by the change in the quasi-steady lift ($k_1 \rightarrow 0$, $k_2 \rightarrow 0$) from the unloaded airfoil to the loaded airfoil.

For airfoils that are more heavily loaded, the response function for the unsteady lift is both shifted to the left and distorted. As the steady loading on the airfoil increases, the distortion of the curve becomes very strong until a point is reached such that the response function doubles back and crosses itself and the whole character of the curve changes. This can be seen in the results in Figure 101.a. Note that the evolution of the curves leading up to this marked change in the character of the unsteady lift response function can be seen in Figures 99.a and 100.a.

In Section 4.1, it was mentioned that for airfoils with small angle of attack and camber, the reduction in the quasi-steady lift due to airfoil loading is proportional to the steady lift coefficient C_L. It is interesting to note that this result also holds approximately for airfoils that are more substantially loaded. Denoting the change in the quasi-steady lift by $\Delta C'_L$ and the proportionality constant by $-K$, we have approximately $\Delta C'_L = -K\, C_L$, where $K = .25$. This compares with a value of $K = .26$ for lightly loaded airfoils. As a general rule of thumb, then, the two-dimensional quasi-steady lift for an airfoil with steady loading is reduced over that of an unloaded airfoil of the same thickness by about 25% of the value of the steady lift coefficient. This is true irregardless of whether the induced loading is due to airfoil angle of attack or camber or both. We conclude, then, that for a two-dimensional gust, mean loading on the airfoil leads to a significant reduction in the magnitude of the unsteady lift at the lowest reduced frequencies.

Unlike the results for the unsteady lift, the results for the unsteady moment

64

show that there is a marked difference in the effects of mean airfoil loading on the unsteady moment response function depending on whether the induced loading is due to airfoil angle of attack or camber. The results indicate that when the steady loading on the airfoil is induced by angle of attack, there is a reduction in the magnitude of the unsteady moment for the reduced frequencies up to about .5. The reduction in the quasi-steady moment is significant, being about 19% for a 12% thick airfoil at a Mach number of .1 and angle of attack of 5°, and 17% for the same airfoil at a .5 Mach number. However, when the steady loading is induced by airfoil camber, there is not much effect on the unsteady moment unless the airfoil is substantially loaded. For example, the plots for the airfoils with 5% camber and no angle of attack show almost no difference between the unsteady moment for the loaded and unloaded airfoils (See Figures 95.b and 99.b). Only when the camber ratio is .10 and the Mach number is .5 do the unsteady moment plots show much effect due to the airfoil loading, and here it is limited to the higher reduced frequencies beginning around 1.3. Our conclusion is that induced loading due to angle of attack significantly reduces the magnitude of the unsteady moment for the quasi-steady case and the lower reduced frequencies up to about .5, but induced loading due to airfoil camber has little effect on the unsteady moment for the two-dimensional gust case.

In looking at the three-dimensional gust results (Figures 103 - 112), it is evident that there are both similarities and differences in the effects of mean loading on the unsteady lift and moment of airfoils subjected to 2-D and 3-D gusts.

First, the effects are similar in that the unsteady lift for the three-dimensional gust case is also sensitive to small changes in mean airfoil loading. This is particularly true for the quasi-steady lift and the lift at the lower reduced frequencies. It turns out that the reduction in the quasi-steady lift from the unloaded airfoil to the loaded airfoil, $\Delta C'_L$, is again approximately proportional to the steady lift coefficient C_L. The proportionality constant for the 3-D results shown in Figures

103 - 112 is about .10, as opposed to .25 for the previously described 2-D results. It should be pointed out that for all of the three-dimensional results shown in these figures, the value of the spanwise wave number, k_3, was fixed at .4. We can therefore make no conclusion as to how general this value of the proportionality constant is for three-dimensional gust results, or as to how the proportionality constant for the 3-D case might be effected by a change in k_3.

The second main similarity between the 2-D and 3-D results is that in both cases the unsteady moment responds differently to airfoil steady loading depending on whether the loading is due to angle of attack or camber. For the 2-D case, the unsteady moment decreased significantly for the low reduced frequencies when the mean loading was due to angle of attack, but showed almost no change when the loading was due to airfoil camber. For the 3-D case, the low frequency unsteady moment again decreases in response to airfoil steady loading which is induced by angle of attack. However, when the mean loading is induced by airfoil camber, the unsteady moment for the low reduced frequencies actually increases rather than decreasing or showing no change at all. For example, at a Mach number of .1, the airfoil with $5°$ angle of attack and no camber shows a decrease in the quasi-steady moment of 12% over the same airfoil with no angle of attack. On the other hand, an airfoil with the same thickness ratio and Mach number that has no angle of attack but has a camber ratio of .05 shows a 7% increase in the quasi-steady moment. (See Figures 104.b and 105.b.) At a Mach number of .5, the same comparison between the two airfoils shows an 11% decrease in the quasi-steady moment for the airfoil with angle of attack but no camber, but an 8% increase for the airfoil with no angle of attack but 5% camber. (See Figures 108.b and 109.b.)

So the two main similarities between the 2-D and 3-D results are that in each case the unsteady lift is sensitive to small changes in mean loading, and in each case the unsteady moment responds differently to airfoil loading induced by angle of attack and airfoil loading induced by camber.

The biggest difference between the 2-D and 3-D results is that for the 3-D case, mean loading does not have much effect on the results for the higher reduced frequencies. This is in contrast to the 2-D case, where the entire range of reduced frequencies showed a strong sensitivity to changes in mean airfoil loading.

4.2.3 Effects of Airfoil Mach Number on the Unsteady Response Functions

We conclude our discussion of the numerical results by looking at the effects of Mach number on the unsteady response functions. Figures 113 through 136 show comparisons of the unsteady response functions for various airfoils at different Mach numbers. All of the results are for 12% thick airfoils. The 1-D gust results are shown in Figures 113 - 120, the 2-D gust results in Figures 121 - 128, and the 3-D gust results in Figures 129 - 136.

An analysis of the results would seem to indicate that there are two main effects on the unsteady response functions due to an increase in airfoil Mach number.

First, the magnitude of the unsteady lift and moment are significantly increased for the low reduced frequencies ranging from 0 up to about .2 or .3, and then significantly decreased for reduced frequencies above about 2.0. For reduced frequencies ranging from about .3 up to 2.0, the effect of the higher Mach number on the unsteady response functions is mainly a change in phase. These trends essentially hold for one-, two-, and three-dimensional gusts, particularly for airfoils without mean loading. For airfoils that have mean loading, the trends do not hold quite so strongly for the three-dimensional gust case, where there is little effect on the magnitude of the unsteady response for the low frequency cases. The strength of the Mach number effects on the two-dimensional gust results is also somewhat reduced for the loaded airfoil case. For example, for an unloaded 12% thick airfoil, the two-dimensional quasi-steady lift increases by 12.6% when the Mach number is increased from .1 to .5. However, for a 12% thick airfoil with 2° angle of attack and

camber ratio of .05, the two-dimensional quasi-steady lift increases by only 7.1% when the Mach number is increased from .1 to .5 (See Figures 121.a and 126.a). The one-dimensional gust results show essentially the same trends with increasing Mach number, irrespective of whether the airfoil has mean loading or not.

The second major effect that an increase in airfoil Mach number has on the unsteady response functions is that it intensifies the distortion of the response function curves that occurs due to mean loading. This can be seen very clearly in Figures 125, 126, and 127, where the response functions for the higher Mach number cases are much more distorted than those for the lower Mach number cases. Because the gradients in the mean flow are stronger at the higher Mach number, the imposed gust undergoes a stronger distortion with increasing Mach number, and there is a corresponding greater distortion of the unsteady response functions.

CHAPTER V

CONCLUSION

We conclude on the basis of the numerical results presented in the previous chapter that the frequency domain numerical scheme developed in the present work can be used to solve a wide variety of unsteady vortical flow problems for a large range of Mach numbers and reduced frequencies. The results presented demonstrated the effects of airfoil thickness, camber, angle of attack, and Mach number on the unsteady lift and moment of Joukowski airfoils in subsonic vortical flows. It was seen that the effects of these parameters on the unsteady response functions varied considerably, depending on both the magnitude of the reduced frequency and the dimensionality of the imposed upstream gust. In addition, the results have shown that the distortion by the nonuniform mean flow of the convected upstream disturbances can have a very strong effect on the unsteady airfoil response. The results presented have thus demonstrated the importance of having a numerical scheme which can handle mean flow distortion effects as well as three-dimensional gusts for a large range of reduced frequencies.

Another contribution of the present work is that it presents a set of benchmark solutions for realistic flow configurations on which unsteady computational fluid dynamics codes can be validated. In addition, it lays the foundation for the numerical implementation of the linearized aerodynamic approach for the analysis of unsteady vortical flows around airfoils used in real applications. Although we have considered only Joukowski airfoil geometries in the present work, we point out that since any airfoil geometry can be represented using complex variables and conformal mapping techniques, the present method can be straightforwardly extended to other airfoils. The current work has therefore illuminated many of the important issues to be resolved in the development of such a general numerical implementation.

We conclude, then, that the present approach represents an alternative to the

potential and primitive variable methods for the efficient and accurate solution of unsteady aerodynamic flow problems. The key features of the present frequency domain numerical scheme are the transformation into elliptical coordinates, the method of grid determination, the far field radiation condition, the formulation and method of evaluation of the source term, and the direct sparse matrix solver.

Finally, it is hoped that the present theoretical study of unsteady vortical flows around lifting airfoils will help pave the way for the development of robust, highly-efficient computer codes which can be used in the engineering analysis of unsteady aerodynamic flow fields.

FIGURES
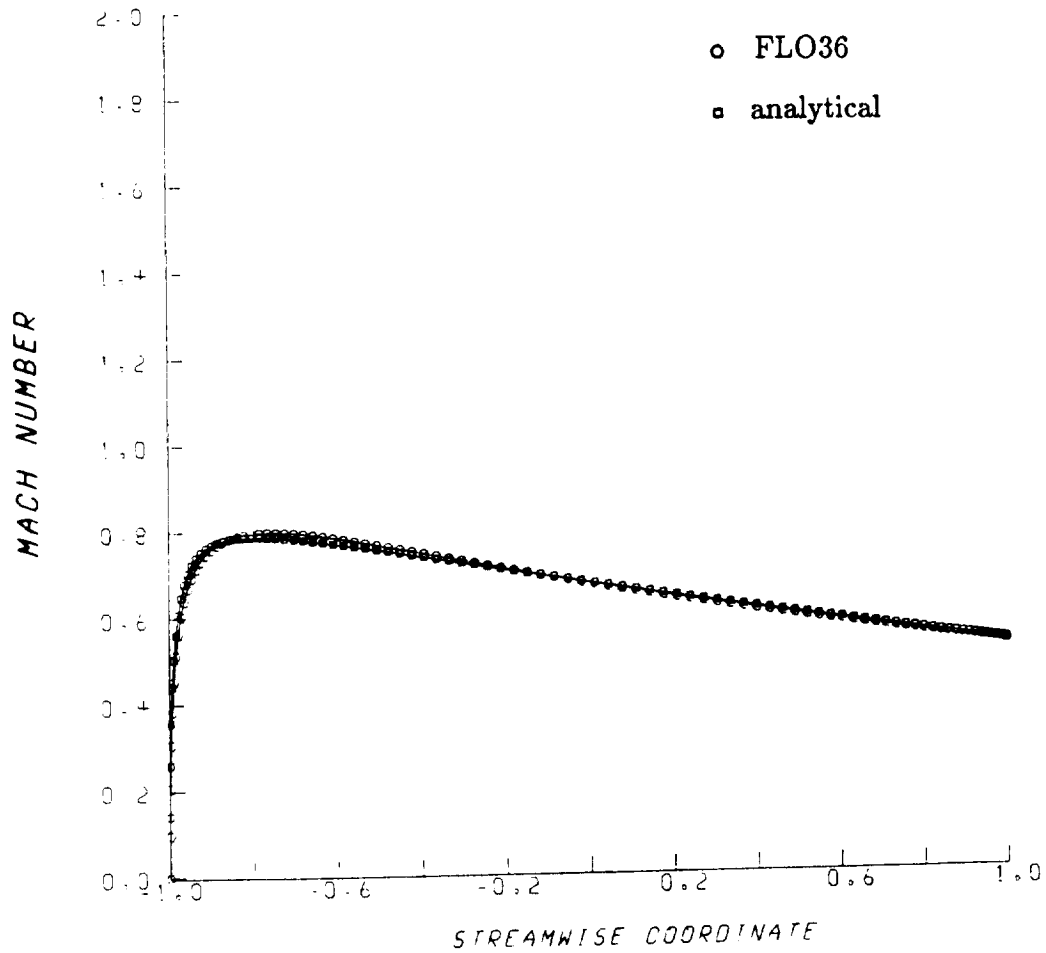
Figure 1. Comparison of Mach number at the airfoil surface between FLO36 and the present analytical scheme. $M_\infty = .6$, $\alpha = 0^o$, camber = 0, thickness = .12.
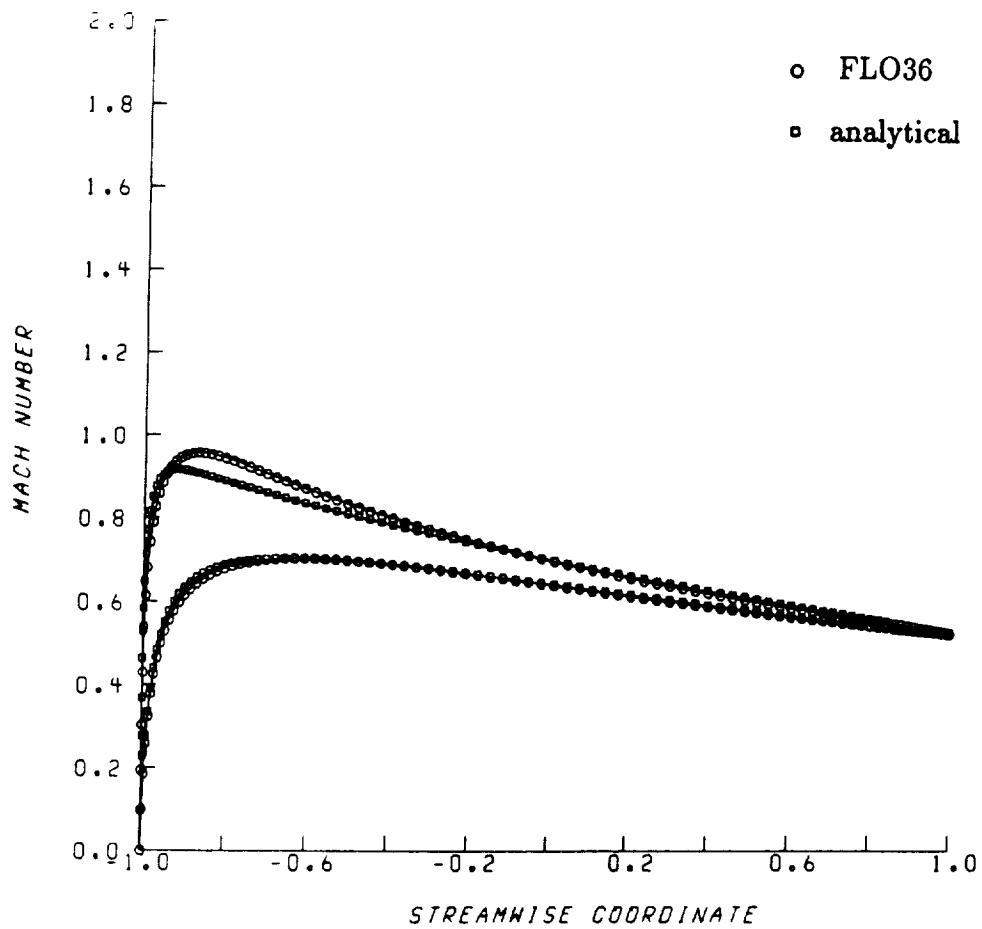
Figure 2. Comparison of Mach number at the airfoil surface between FLO36 and the present analytical scheme. $M_\infty = .6$, $\alpha = 2^o$, camber = 0, thickness = .12.
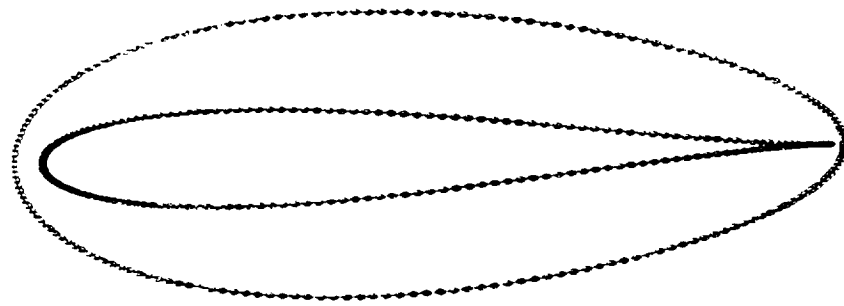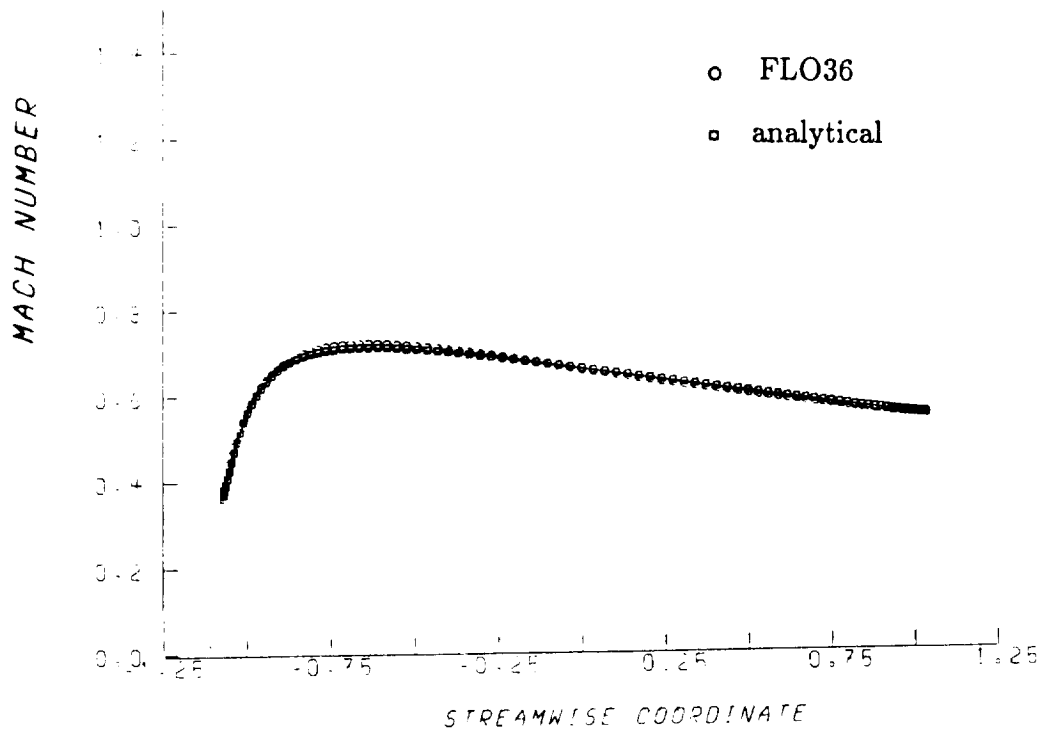
Figure 3.   Comparison of Mach number along a FLO36 grid line which
wraps around the airfoil. $M_\infty = .6$, $\alpha = 0^o$,   camber $= 0$,
thickness $= .12$.

73
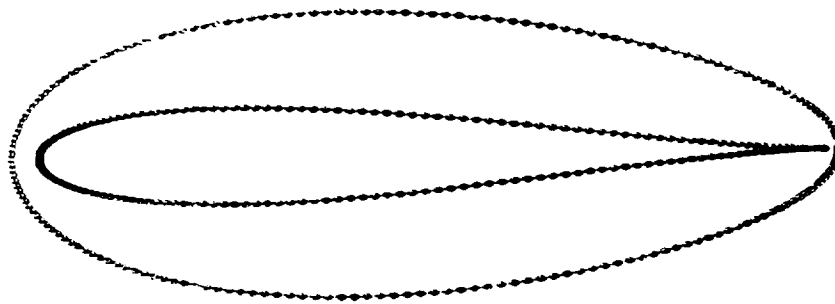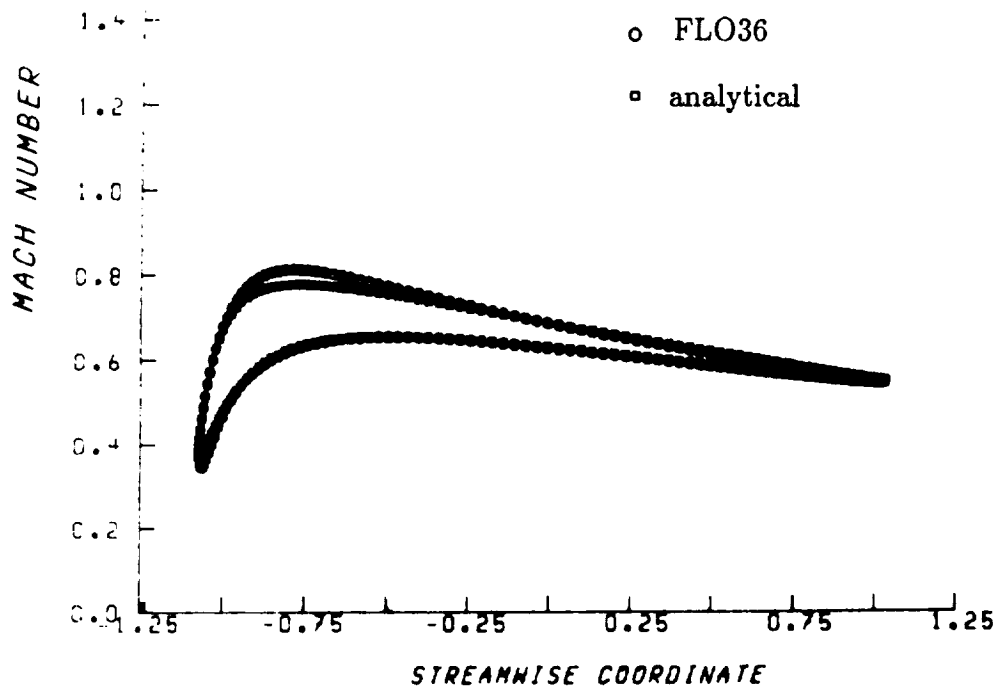
Figure 4. Comparison of Mach number along a FLO36 grid line which wraps around the airfoil. $M_\infty = .6$, $\alpha = 2^o$, camber = 0, thickness = .12.
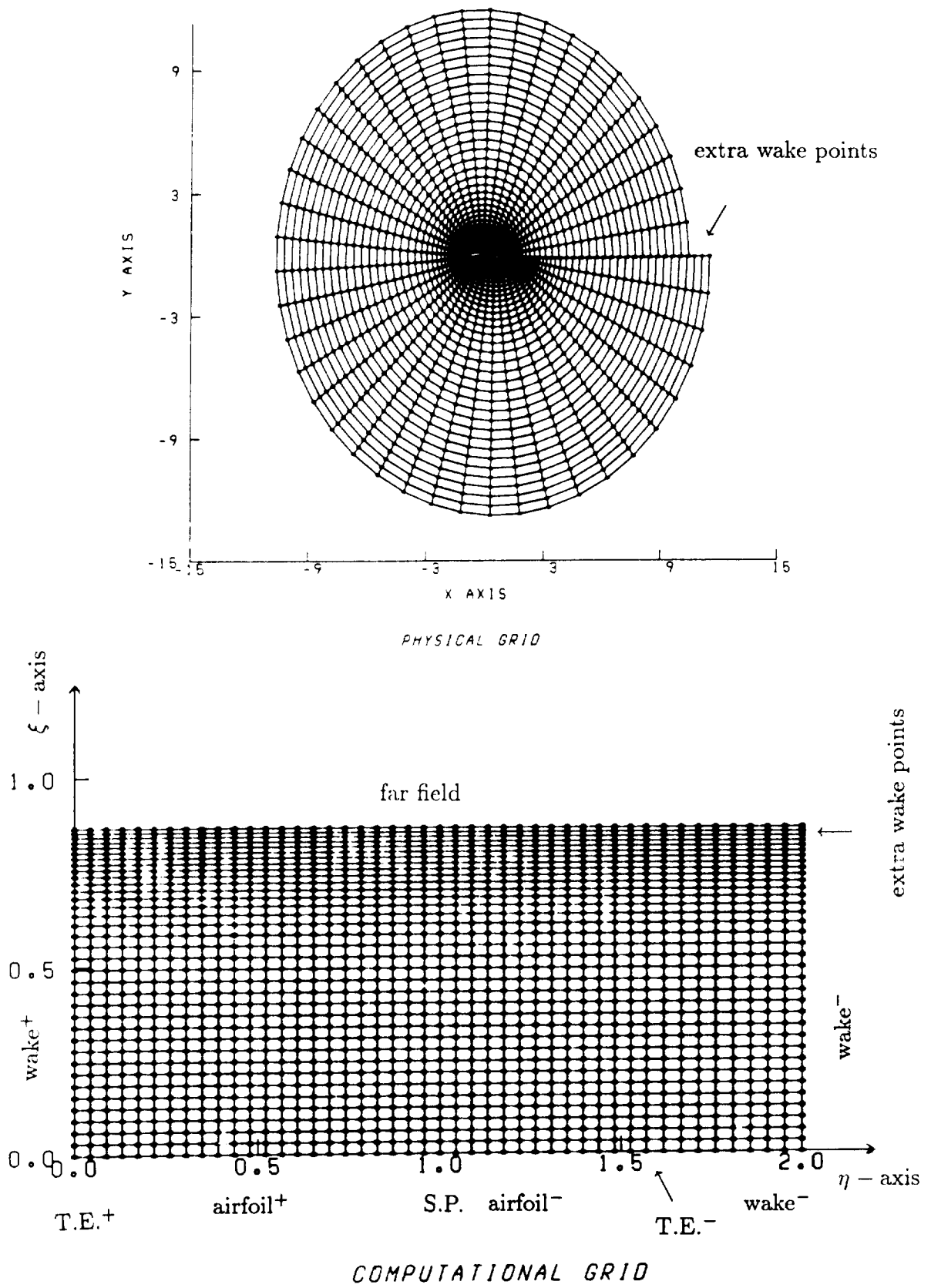
Figure 5. Computational and physical grids.
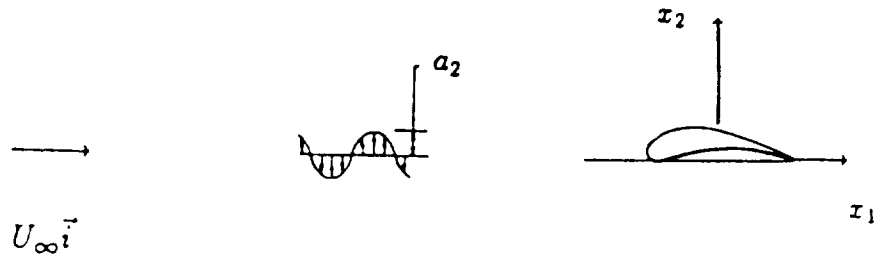
Figure 6.   Airfoil in a transverse gust.
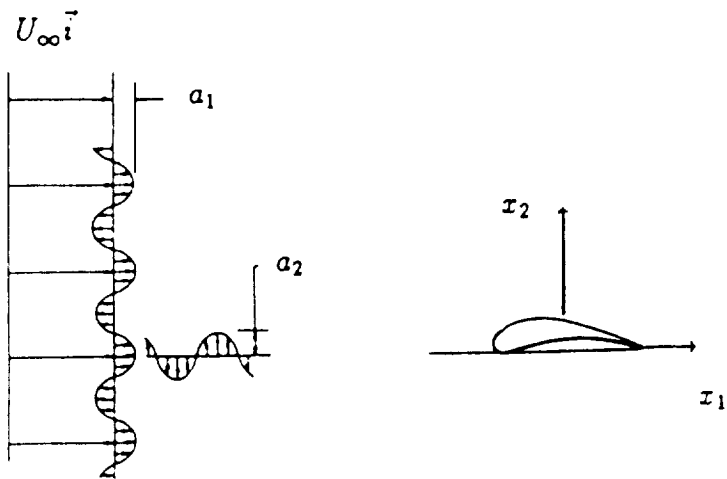
Figure 7.   Airfoil in a transverse and longitudinal gust.
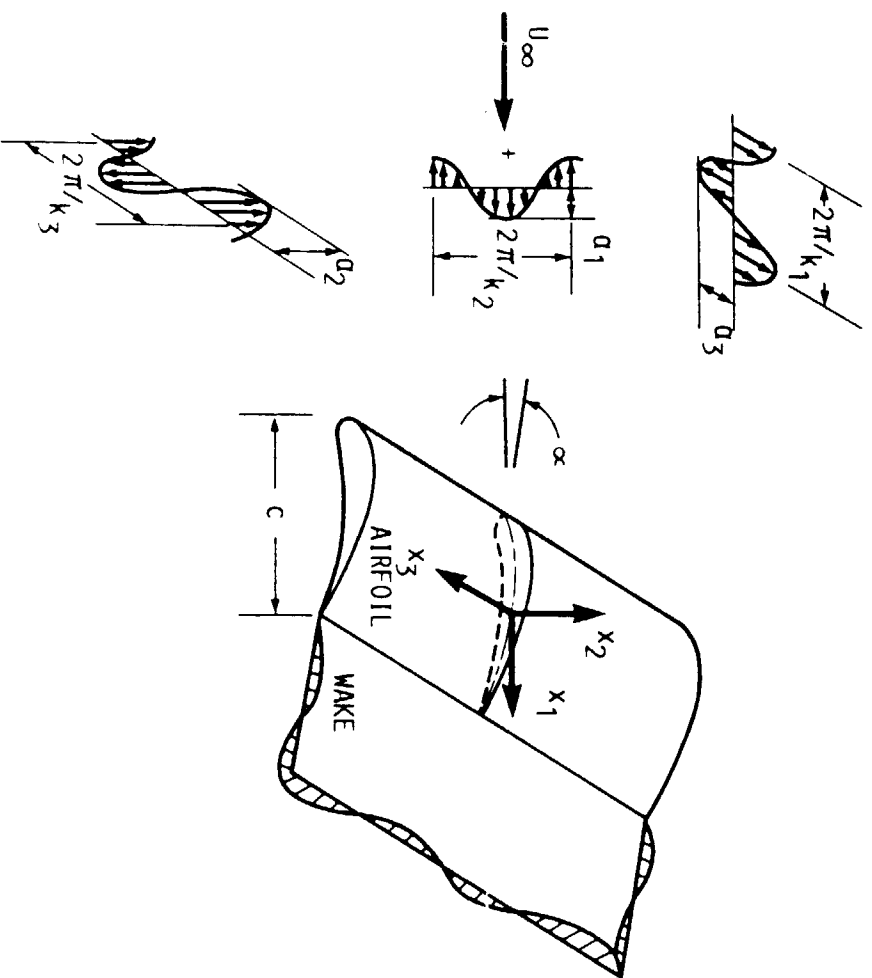
Figure 8.   Airfoil in a three-dimensional gust.

77
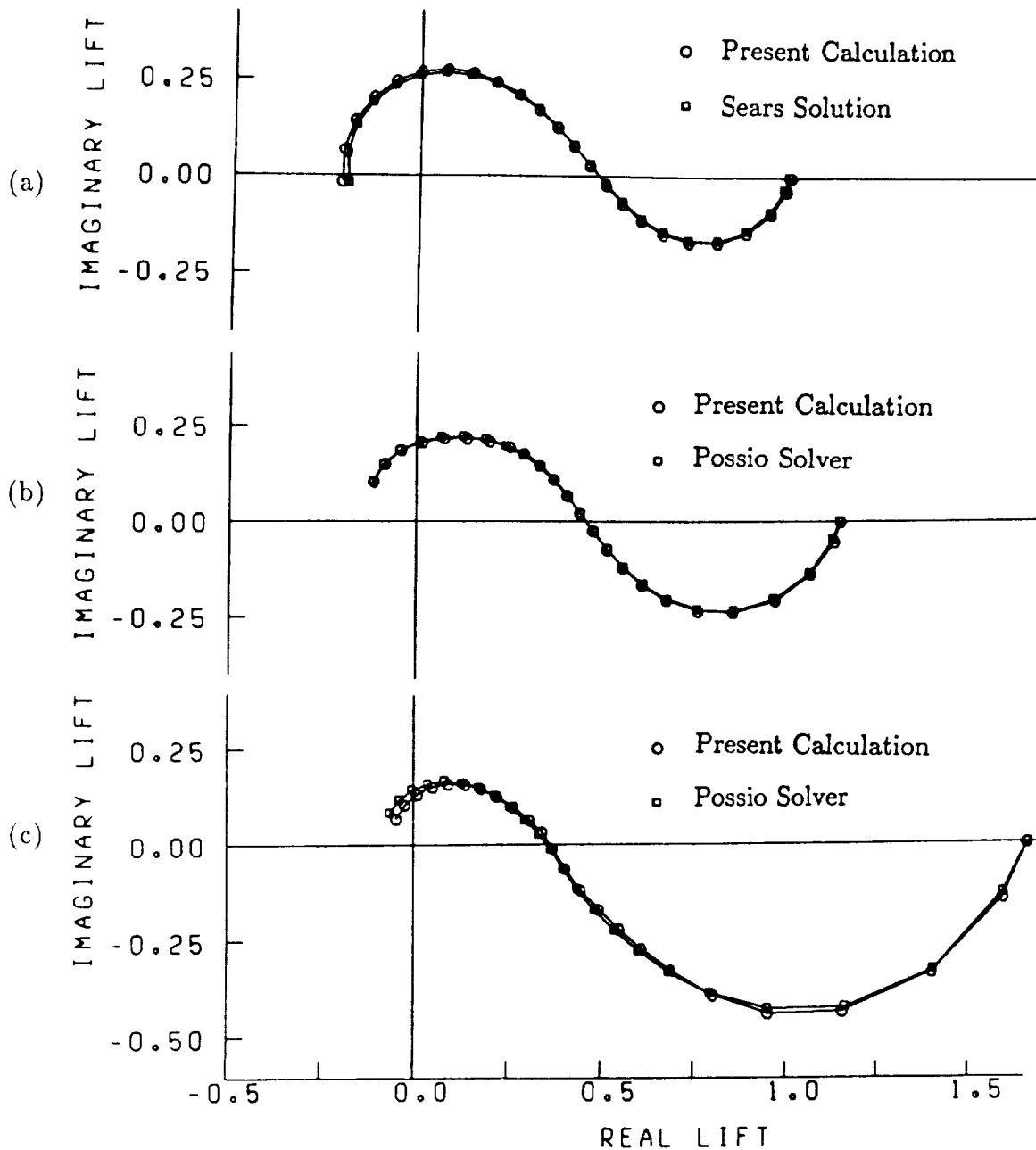
Figure 9. Comparison between the numerically computed unsteady lift and
analytical results for a flat plate airfoil in a transverse gust at
(a) $M = 0.1$, (b) $M = 0.5$, and (c) $M = 0.8$; $k_1 = 0.0$, 0.007,
0.027, 0.062, 0.110, 0.172, 0.248, 0.338, 0.442, 0.561, 0.694, 0.842,
1.01, 1.18, 1.38, 1.59, 1.82, 2.07, 2.33, 2.62, 2.93, 3.26, 3.62, 4.01.
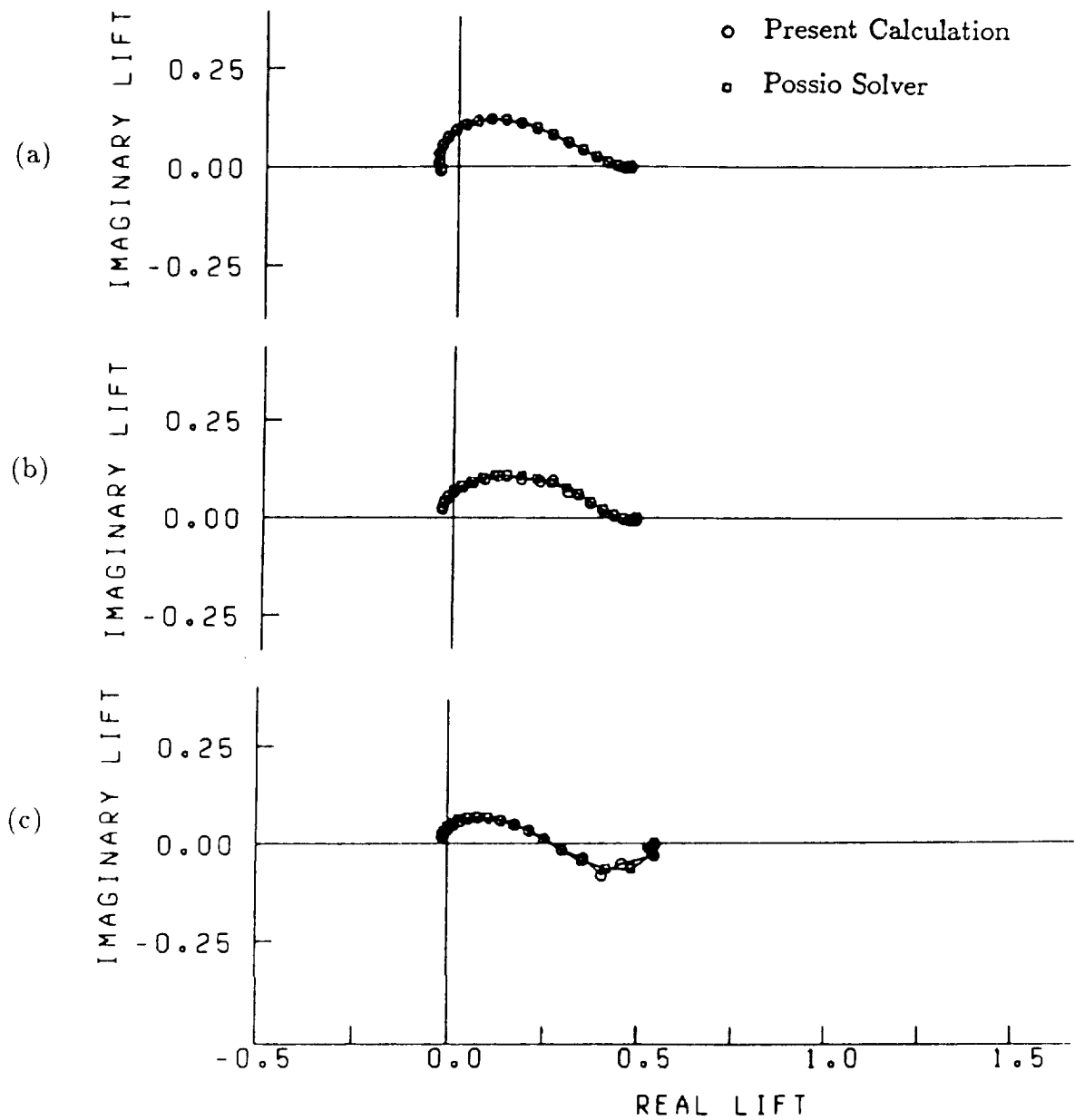
Figure 10. Comparison between the numerically computed unsteady lift and analytical results for a flat plate airfoil in a three-dimensional gust at (a) $M = 0.1$, (b) $M = 0.5$, and (c) $M = 0.8$; $k_1 = 0.0$, 0.007, 0.027, 0.062, 0.110, 0.172, 0.248, 0.338, 0.442, 0.561, 0.694, 0.842, 1.01, 1.18, 1.38, 1.59, 1.82, 2.07, 2.33, 2.62, 2.93, 3.26, 3.62, 4.01; $k_3 = 0.442$, $|\vec{a}| = 1$, $\frac{a_2}{a_1} = -\frac{7}{4}$, $k_1 = k_2$, $\vec{a} \cdot \vec{k} = 0$, $a_2 > 0$.
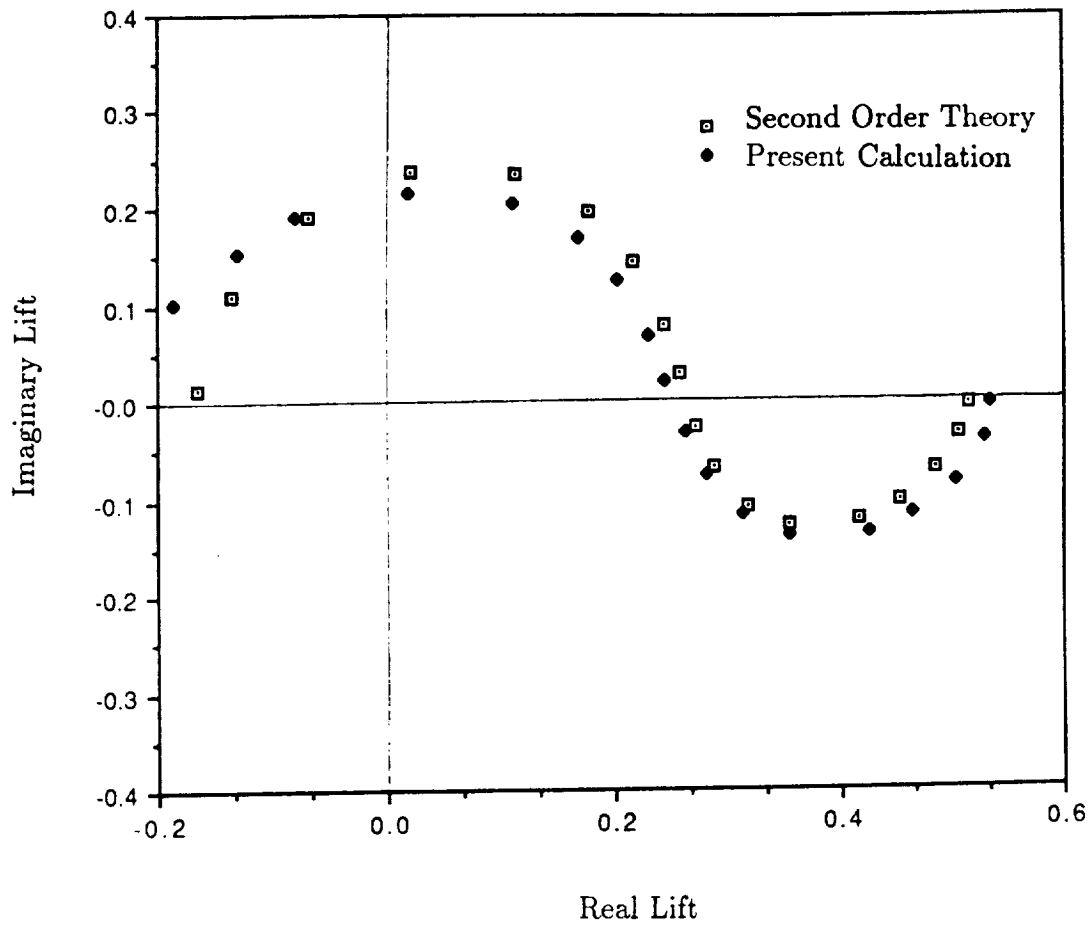
Figure 11. Comparison between the numerically computed unsteady lift
and the second order theory for an airfoil in a transverse
and longitudinal gust. The second order theory does not account for
the thickness of the airfoil. $M_\infty = .1$, $\alpha = 2^o$, camber $= .05$,
thickness ratio $= .06$. $-a_1 = a_2 = .7071$, $k_1 = k_2$, $a_3 = k_3 = 0$,
$k_1 = 0.0, 0.01, 0.03, 0.06, 0.1, 0.2, 0.3, 0.45, 0.6, 0.8, 1.0, 1.3$,
$1.6, 2.0, 2.5, 3.0, 3.5, 4.0$.
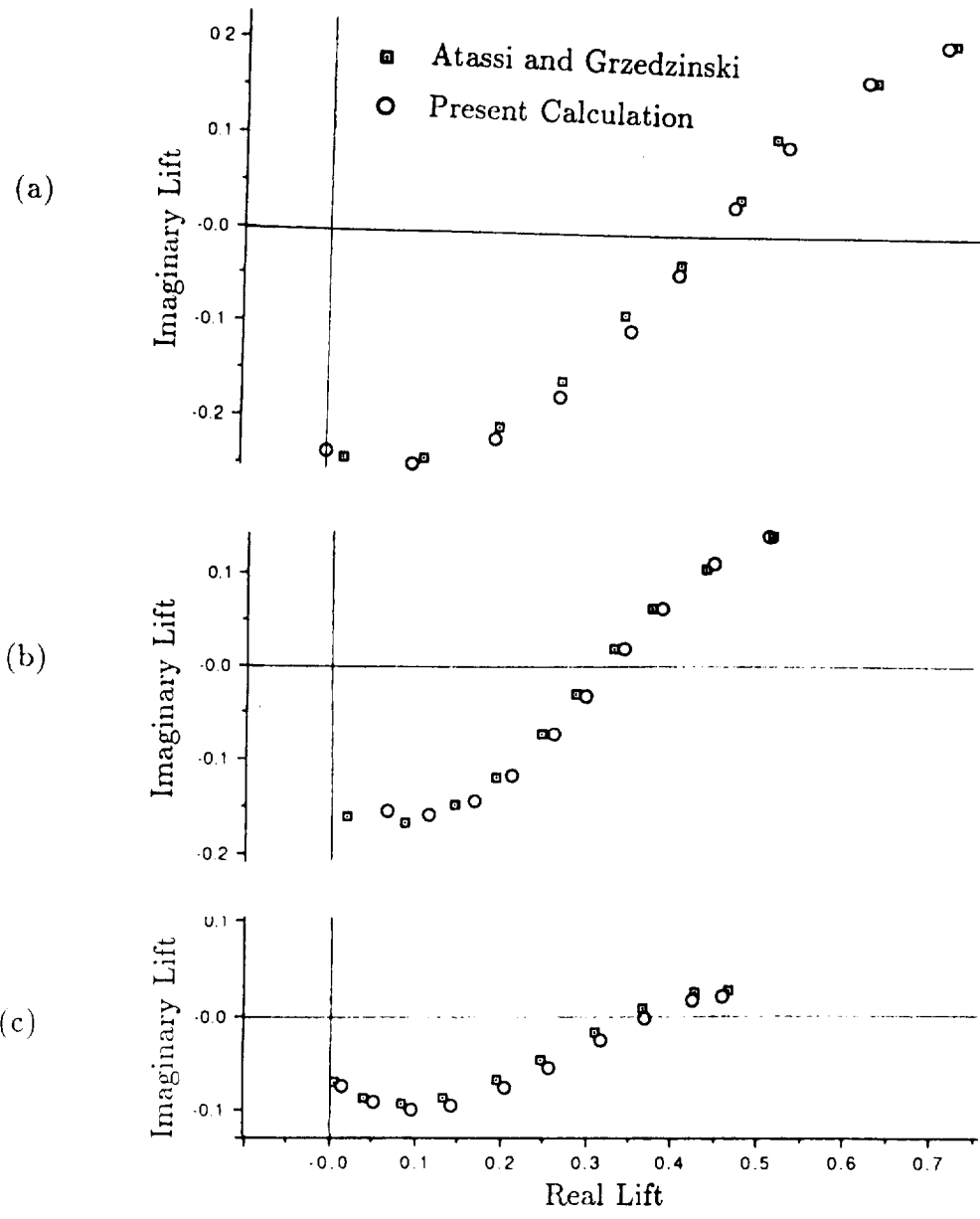
Figure 12. Comparison between the numerically computed unsteady lift and the first order results of Atassi and Grzedzinski for a (a) transverse gust, (b) transverse and longitudinal gust with $-a_1 = a_2 = .7071$, $k_1 = k_2$, $a_3 = k_3 = 0$, and (c) a three-dimensional gust with $k_3 = 0.4$, $|\vec{a}| = 1$, $\frac{a_2}{a_1} = -\frac{7}{4}$, $k_1 = k_2$, $\vec{a} \cdot \vec{k} = 0$, $a_2 > 0$. $M_\infty = .1$, $\alpha = 0^\circ$, camber $= 0$, thickness ratio $= .12$. Results shown are the complex conjugate values of the unsteady lift. $k_1 = 0.2, 0.3, 0.45, 0.6, 0.8, 1.0, 1.3, 1.6, 2.0, 2.5$.
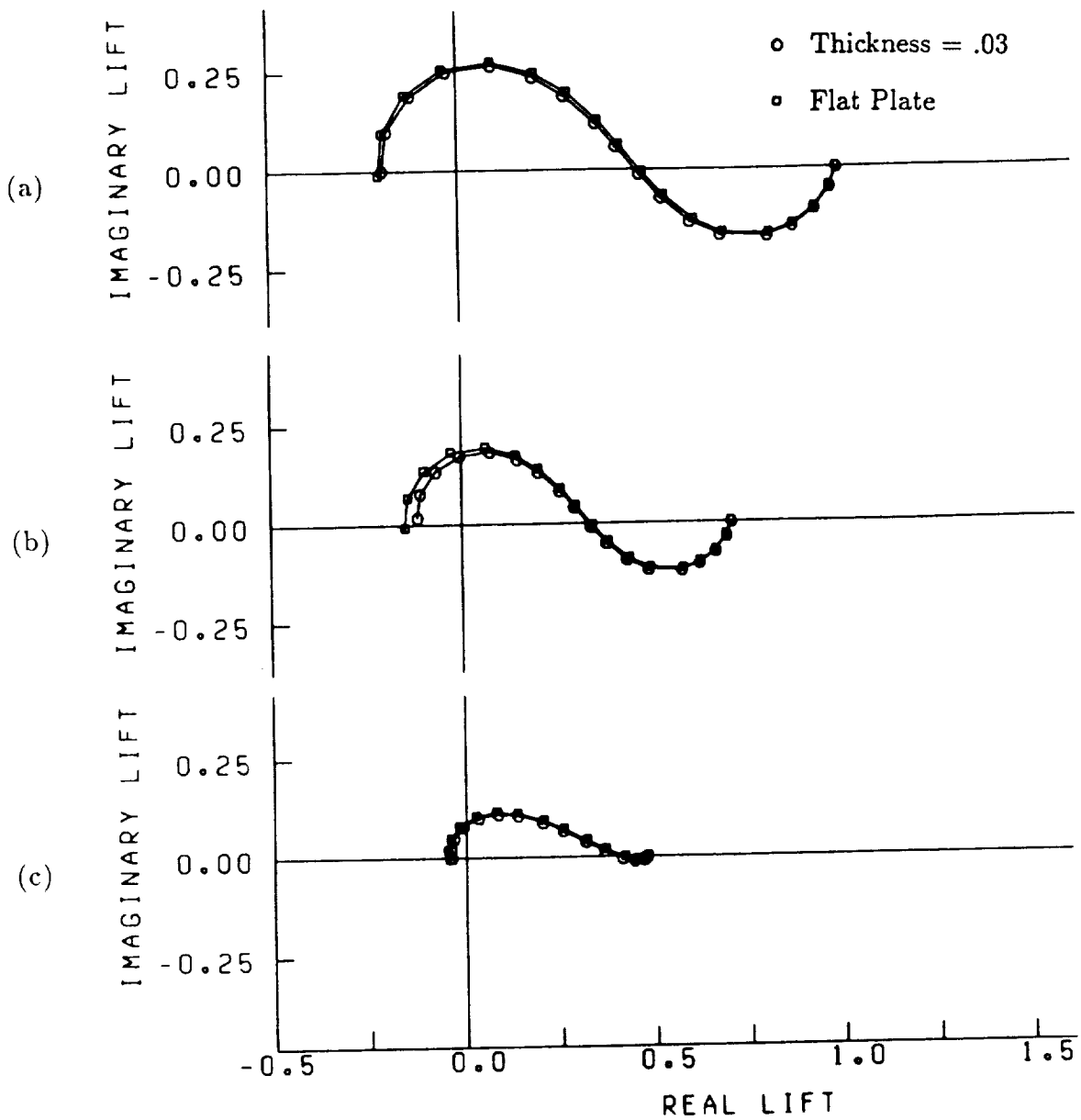
Figure 13. Comparison between the unsteady lift of a flat plate airfoil and a
3 percent thick Joukowski airfoil in a (a) transverse gust,
(b) transverse and longitudinal gust with $-a_1 = a_2 = .7071$, $k_1 = k_2$,
$a_3 = k_3 = 0$, and (c) a three-dimensional gust with $k_3 = 0.4$, $|\vec{a}| = 1$,
$\frac{a_2}{a_1} = -\frac{7}{4}$, $k_1 = k_2$, $\vec{a} \cdot \vec{k} = 0$, $a_2 > 0$. $M_\infty = .1$, $\alpha = 0°$, camber $= 0$.
$k_1 = 0.0$, 0.01, 0.03, 0.06, 0.1, 0.2, 0.3, 0.45, 0.6, 0.8, 1.0,
1.3, 1.6, 2.0, 2.5, 3.0, 3.5, 4.0.
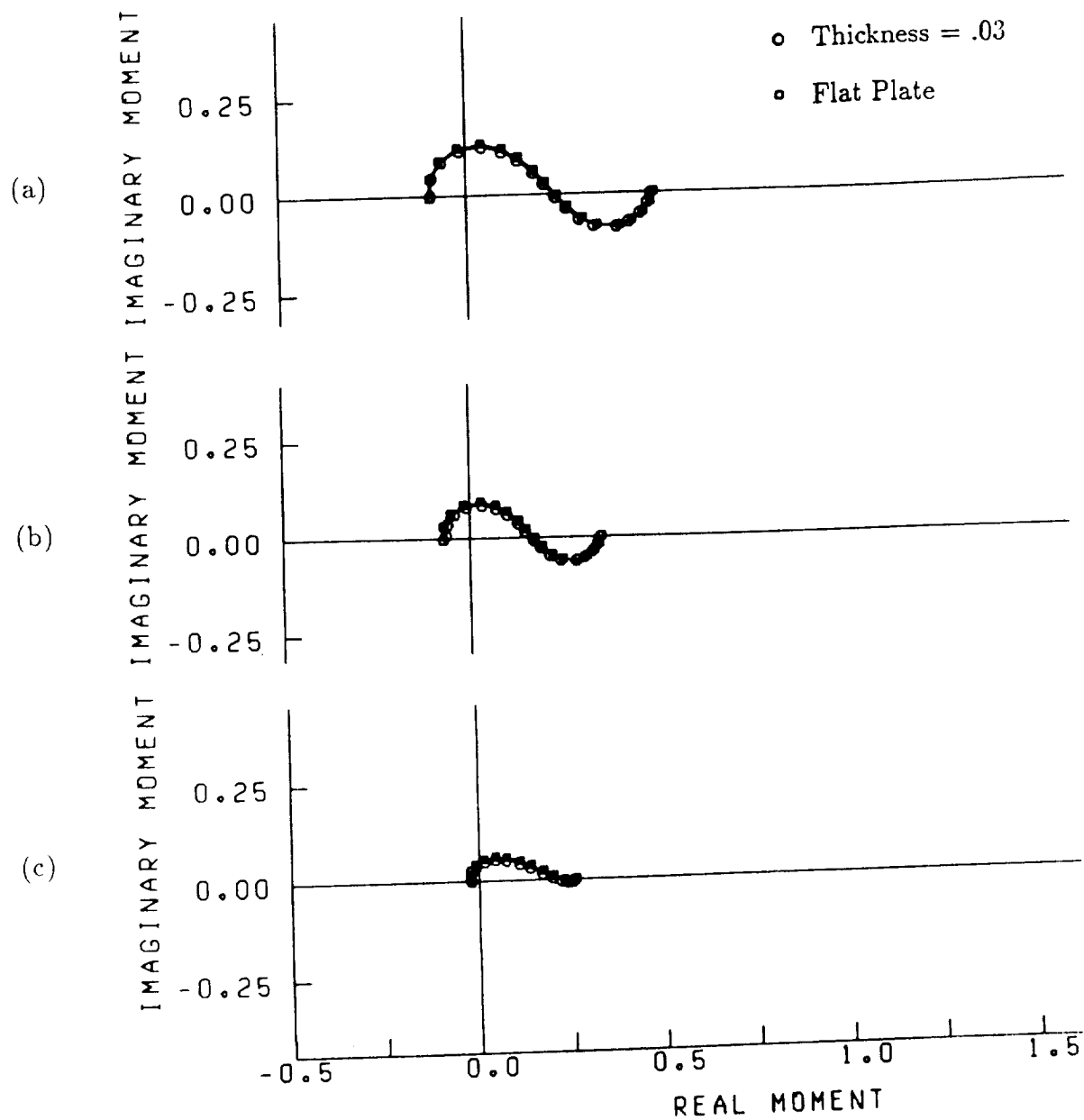
Figure 14. Comparison between the unsteady moment of a flat plate airfoil and a 3 percent thick Joukowski airfoil in a (a) transverse gust, (b) transverse and longitudinal gust with $-a_1 = a_2 = .7071$, $k_1 = k_2$, $a_3 = k_3 = 0$, and (c) a three-dimensional gust with $k_3 = 0.4$, $|\vec{a}| = 1$, $\frac{a_2}{a_1} = -\frac{7}{4}$, $k_1 = k_2$, $\vec{a} \cdot \vec{k} = 0$, $a_2 > 0$. $M_\infty = .1$, $\alpha = 0°$, camber $= 0$ $k_1 = 0.0, 0.01, 0.03, 0.06, 0.1, 0.2, 0.3, 0.45, 0.6, 0.8, 1.0,$ 1.3, 1.6, 2.0, 2.5, 3.0, 3.5, 4.0.
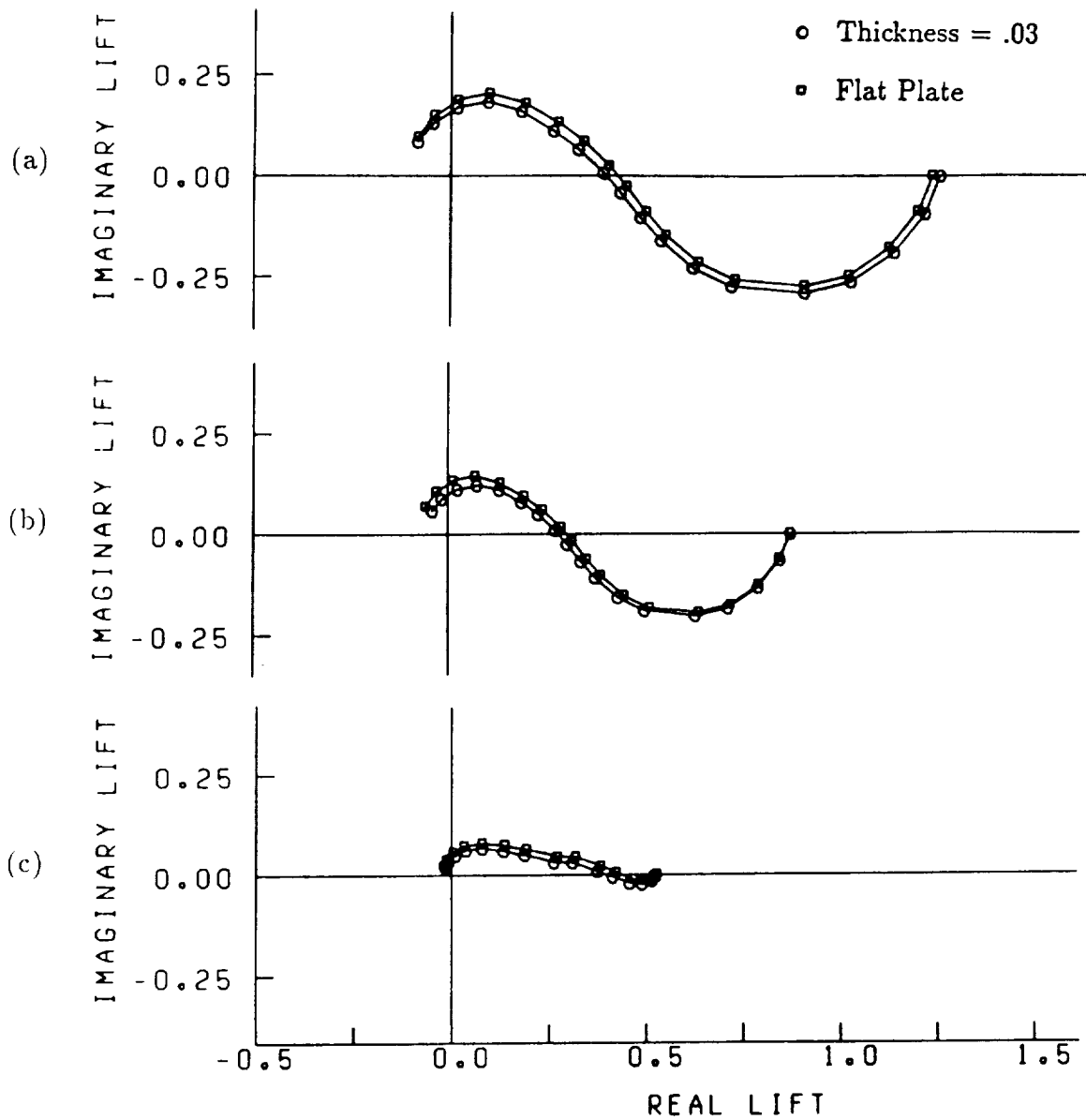
Figure 15.   Comparison between the unsteady lift of a flat plate airfoil and a
3 percent thick Joukowski airfoil in a (a) transverse gust,
(b) transverse and longitudinal gust with $-a_1 = a_2 = .7071$, $k_1 = k_2$,
$a_3 = k_3 = 0$, and (c) a three-dimensional gust with $k_3 = 0.4$, $|\vec{a}| = 1$,
$\frac{a_2}{a_1} = -\frac{7}{4}$, $k_1 = k_2$, $\vec{a} \cdot \vec{k} = 0$, $a_2 > 0$. $M_\infty = .6$, $\alpha = 0°$, camber = 0.
$k_1 = 0.0$, 0.01, 0.03, 0.06, 0.1, 0.2, 0.3, 0.45, 0.6, 0.8, 1.0,
1.3, 1.6, 2.0, 2.5, 3.0, 3.5, 4.0.
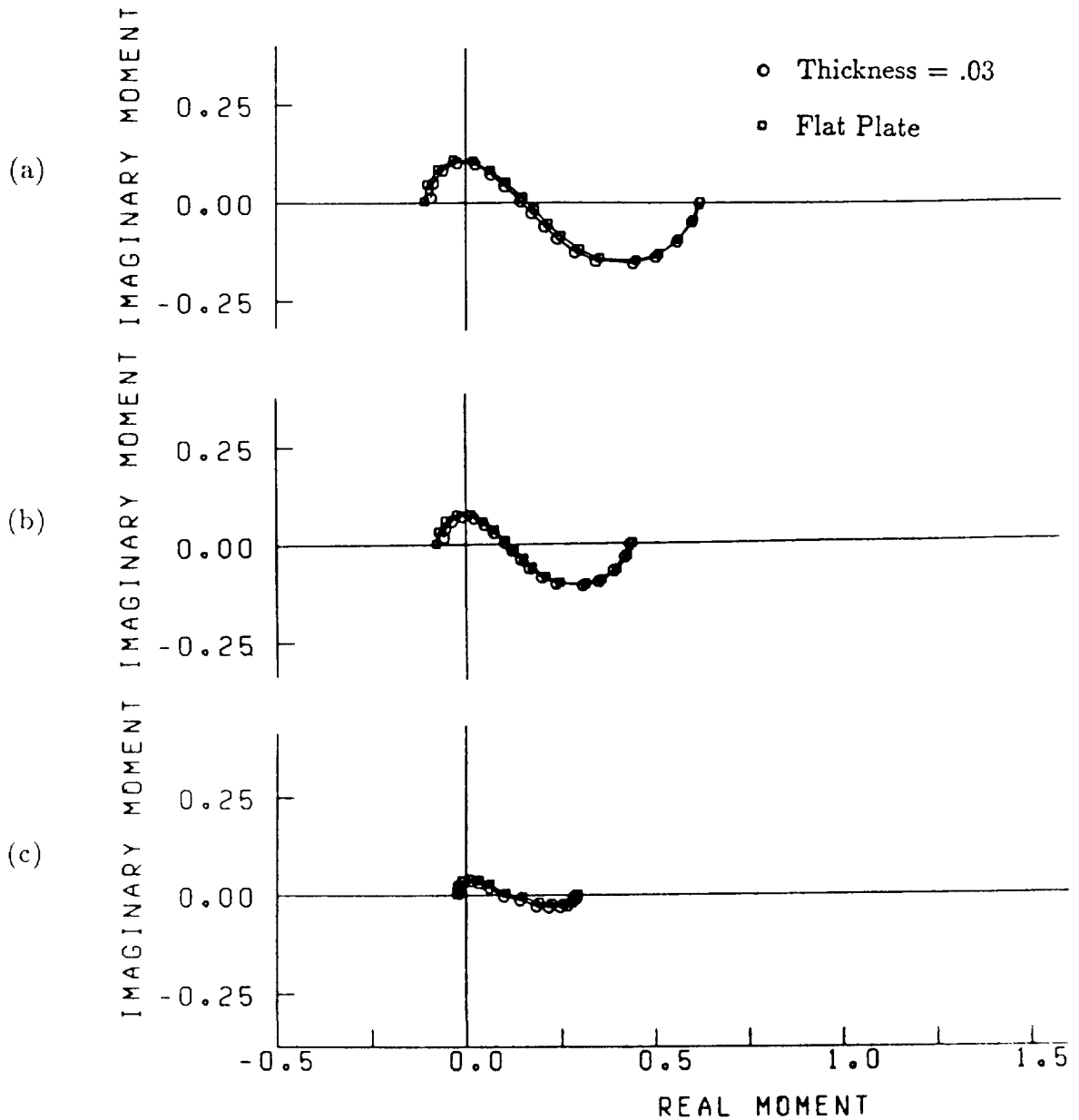
Figure 16. Comparison between the unsteady moment of a flat plate airfoil and a 3 percent thick Joukowski airfoil in a (a) transverse gust, (b) transverse and longitudinal gust with $-a_1 = a_2 = .7071$, $k_1 = k_2$, $a_3 = k_3 = 0$, and (c) a three-dimensional gust with $k_3 = 0.4$, $|\vec{a}| = 1$, $\frac{a_2}{a_1} = -\frac{7}{4}$, $k_1 = k_2$, $\vec{a} \cdot \vec{k} = 0$, $a_2 > 0$. $M_\infty = .6$, $\alpha = 0^\circ$, camber $= 0$. $k_1 = 0.0$, 0.01, 0.03, 0.06, 0.1, 0.2, 0.3, 0.45, 0.6, 0.8, 1.0, 1.3, 1.6, 2.0, 2.5, 3.0, 3.5, 4.0.
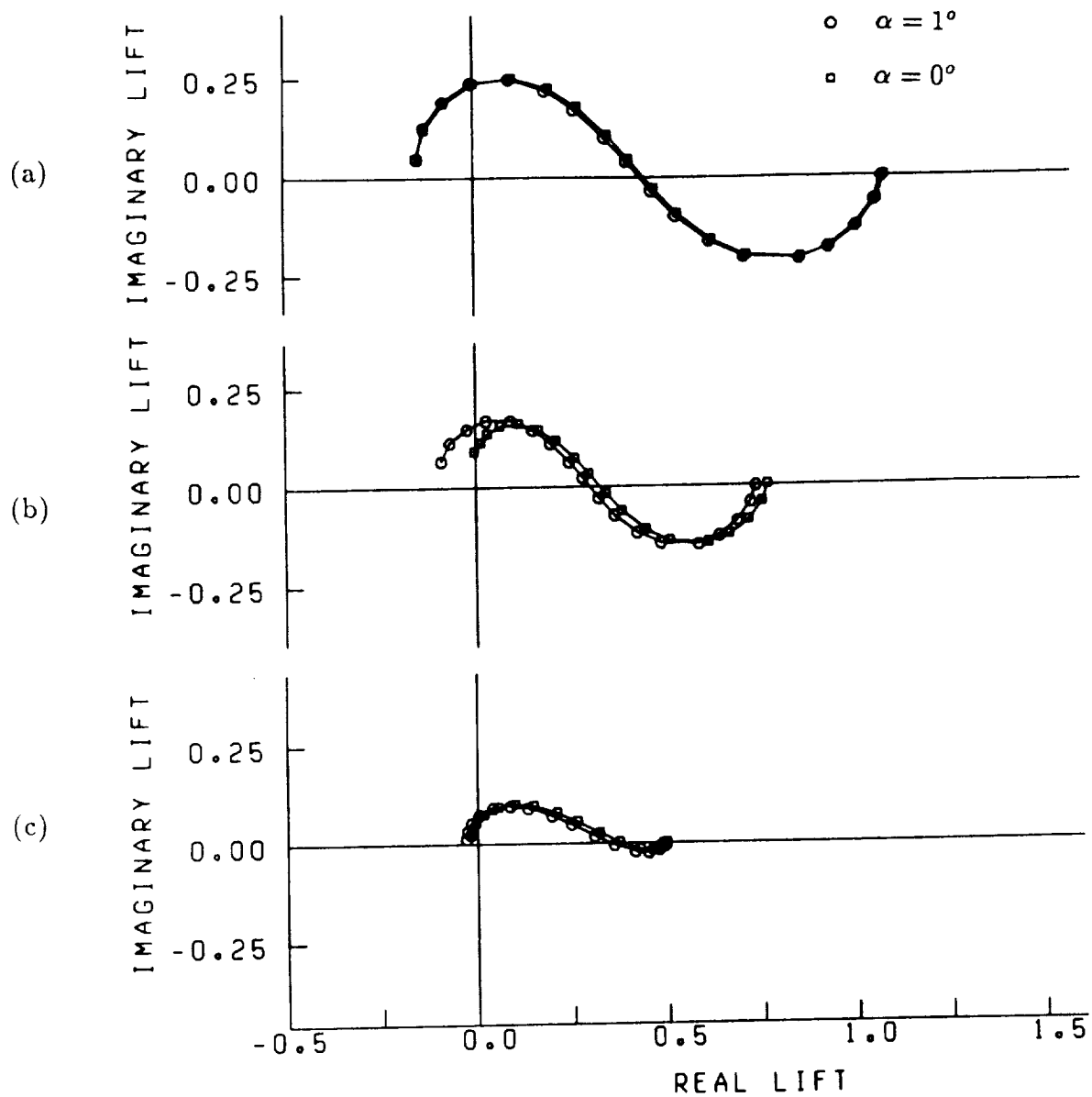
Figure 17. Comparison between the unsteady lift of a 12 percent thick, Joukowski airfoil at $0°$ angle of attack and $1°$ angle of attack for a (a) transverse gust, (b) transverse and longitudinal gust with $-a_1 = a_2 = .7071$, $k_1 = k_2$, $a_3 = k_3 = 0$, and (c) a three-dimensional gust with $k_3 = 0.4$, $|\vec{a}| = 1$, $\frac{a_2}{a_1} = -\frac{7}{4}$, $k_1 = k_2$, $\vec{a} \cdot \vec{k} = 0$, $a_2 > 0$. $M_\infty = .1$, camber = 0, thickness ratio = .12. $k_1 = 0.0, 0.01, 0.03, 0.06, 0.1, 0.2, 0.3, 0.45, 0.6, 0.8, 1.0, 1.3, 1.6, 2.0, 2.5, 3.0, 3.5, 4.0$.
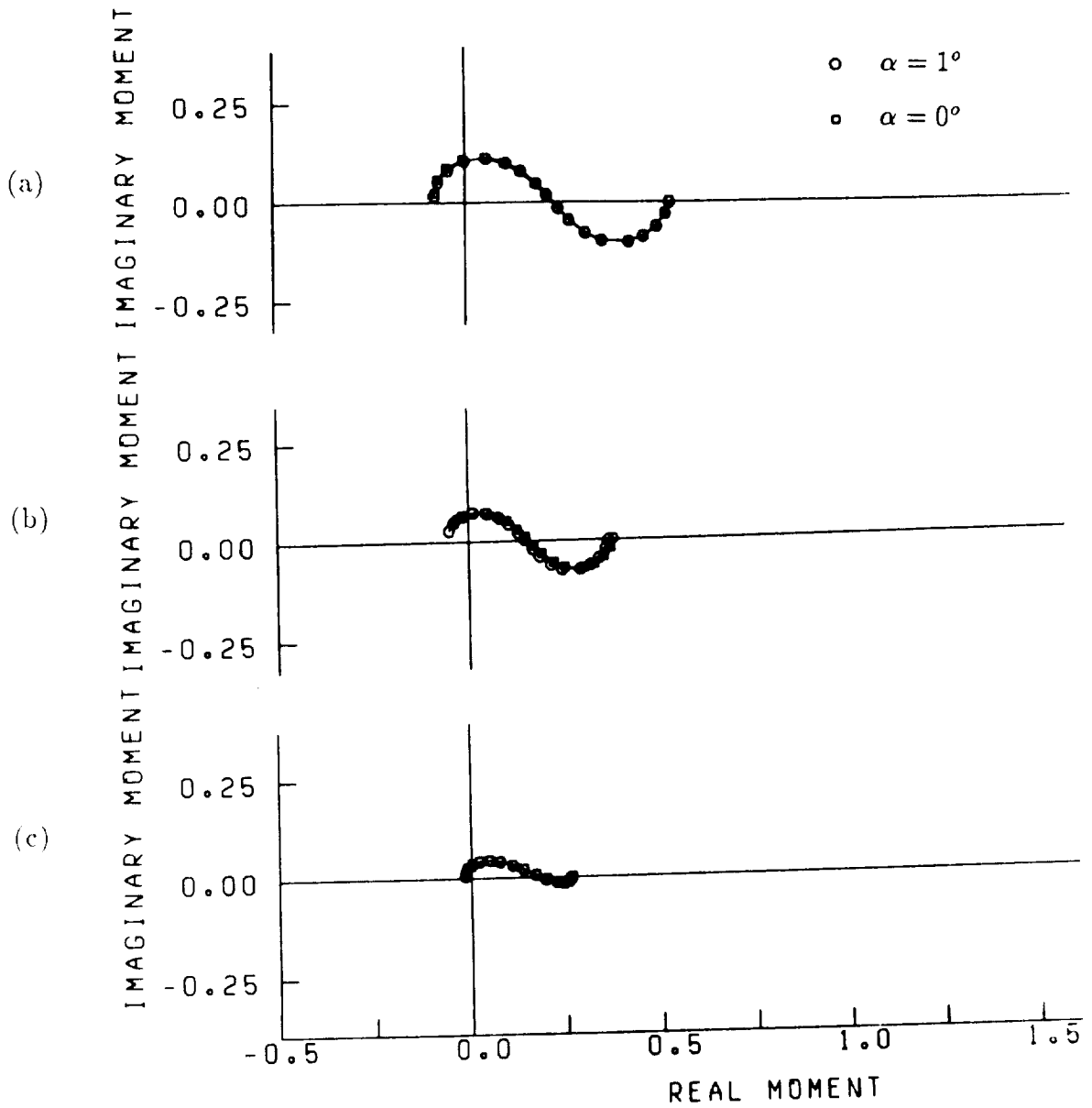
Figure 18. Comparison between the unsteady moment of a 12 percent thick, Joukowski airfoil at 0° angle of attack and 1° angle of attack for a (a) transverse gust, (b) transverse and longitudinal gust with $-a_1 = a_2 = .7071$, $k_1 = k_2$, $a_3 = k_3 = 0$, and (c) a three-dimensional gust with $k_3 = 0.4$, $|\vec{a}| = 1$, $\frac{a_2}{a_1} = -\frac{7}{4}$, $k_1 = k_2$, $\vec{a} \cdot \vec{k} = 0$, $a_2 > 0$. $M_\infty = .1$, camber $= 0$, thickness ratio $= .12$. $k_1 = 0.0, 0.01, 0.03, 0.06, 0.1, 0.2, 0.3, 0.45, 0.6, 0.8, 1.0, 1.3, 1.6, 2.0, 2.5, 3.0, 3.5, 4.0$.
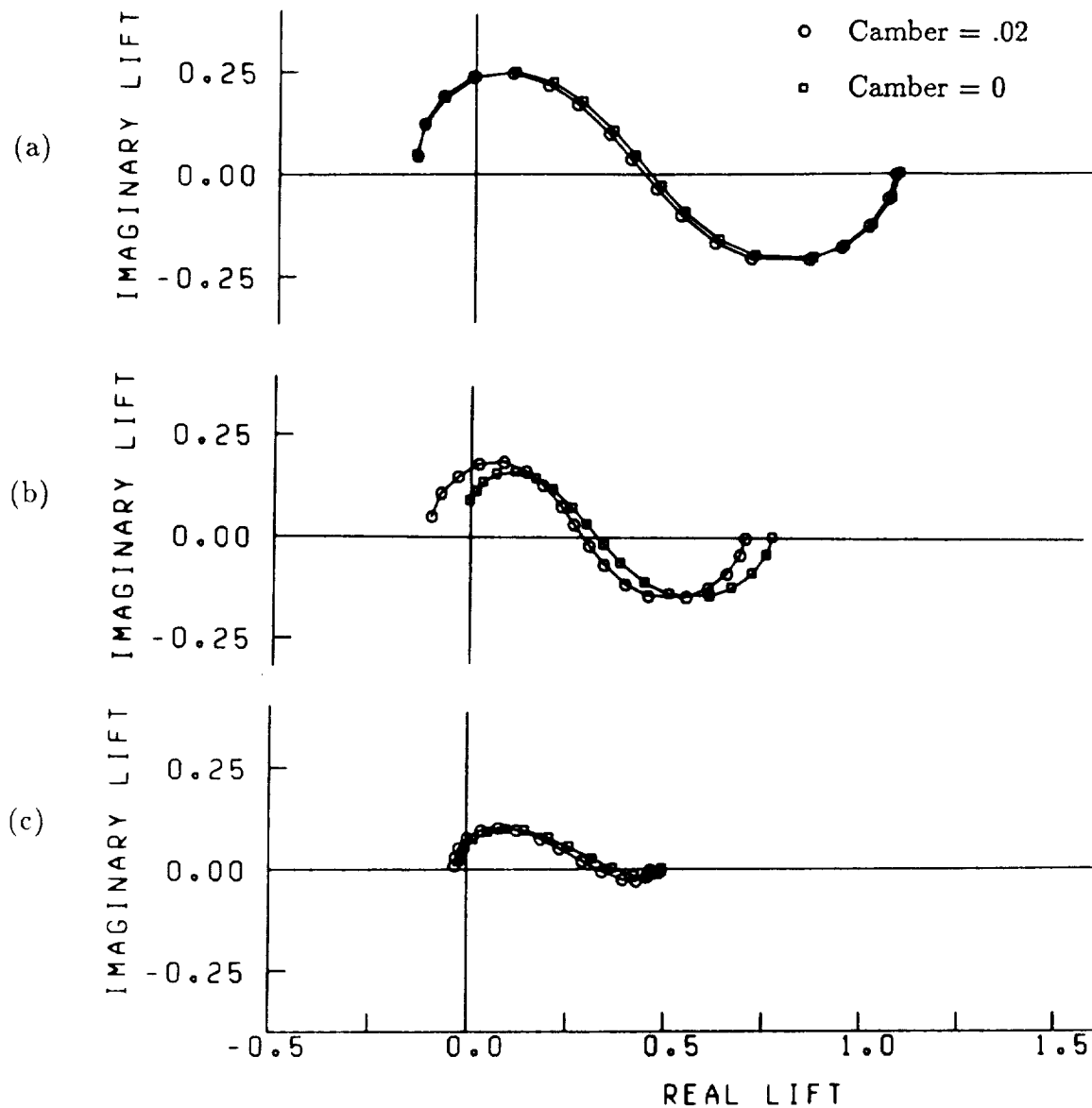
Figure 19. Comparison between the unsteady lift of an uncambered Joukowski airfoil and an airfoil with camber ratio of .02 for a (a) transverse gust, (b) transverse and longitudinal gust with $-a_1 = a_2 = .7071$, $k_1 = k_2$, $a_3 = k_3 = 0$, and (c) a three-dimensional gust with $k_3 = 0.4$, $|\vec{a}| = 1$, $\frac{a_2}{a_1} = -\frac{7}{4}$, $k_1 = k_2$, $\vec{a} \cdot \vec{k} = 0$, $a_2 > 0$. $M_\infty = .1$, $\alpha = 0°$, thickness ratio = .12. $k_1 = 0.0, 0.01, 0.03, 0.06, 0.1, 0.2, 0.3, 0.45, 0.6, 0.8, 1.0,$ 1.3, 1.6, 2.0, 2.5, 3.0, 3.5, 4.0.
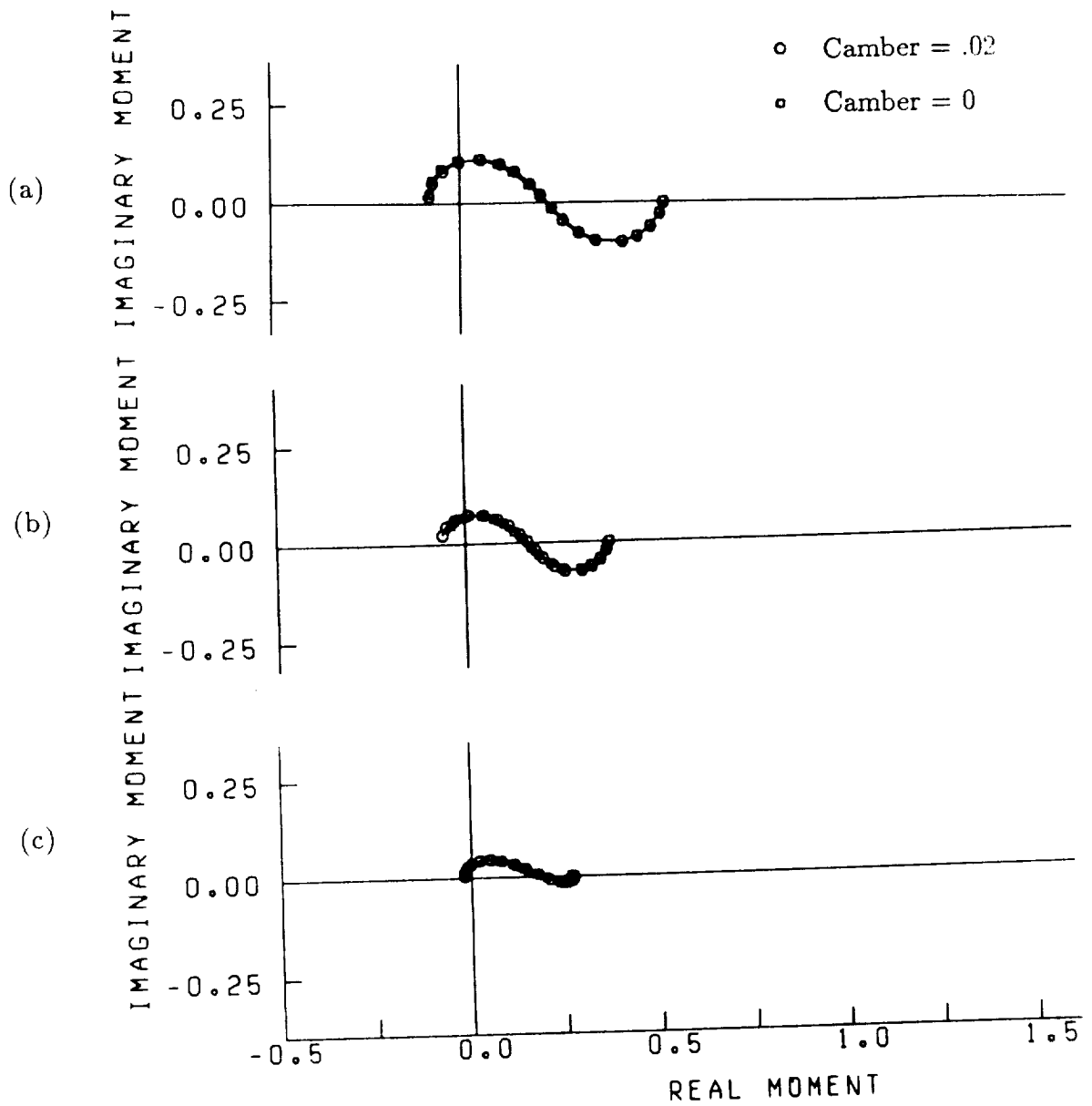
Figure 20. Comparison between the unsteady moment of an uncambered Joukowski airfoil and an airfoil with camber ratio of .02 for a (a) transverse gust, (b) transverse and longitudinal gust with $-a_1 = a_2 = .7071$, $k_1 = k_2$, $a_3 = k_3 = 0$, and (c) a three-dimensional gust with $k_3 = 0.4$, $|\vec{a}| = 1$, $\frac{a_2}{a_1} = -\frac{7}{4}$, $k_1 = k_2$, $\vec{a} \cdot \vec{k} = 0$, $a_2 > 0$. $M_\infty = .1$, $\alpha = 0°$, thickness ratio = .12. $k_1 = 0.0, 0.01, 0.03, 0.06, 0.1, 0.2, 0.3, 0.45, 0.6, 0.8, 1.0, 1.3, 1.6, 2.0, 2.5, 3.0, 3.5, 4.0$.
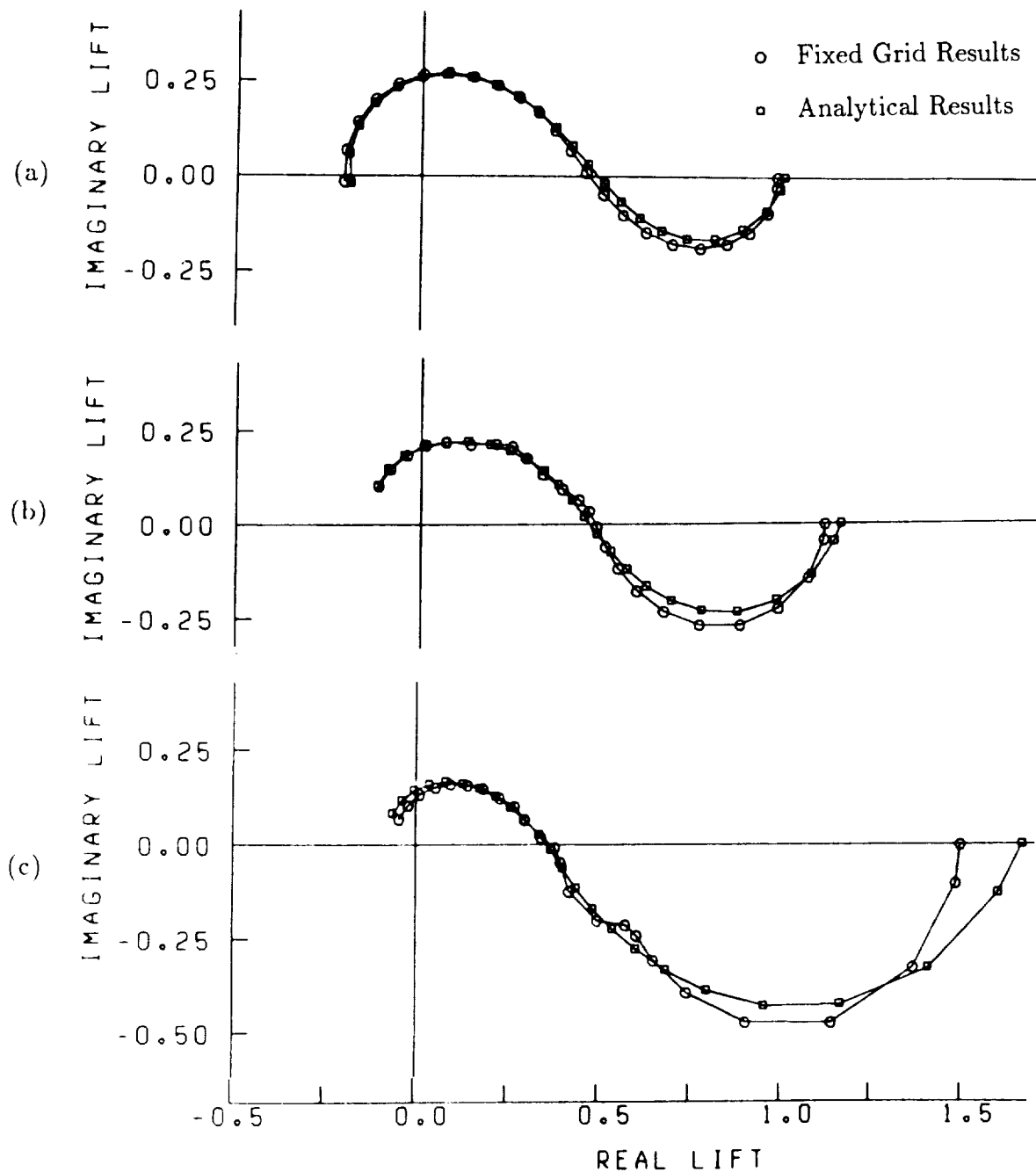
Figure 21. Comparison between numerical results generated on a fixed grid and analytical results for a flat plate airfoil in a transverse gust at (a) $M = 0.1$, (b) $M = 0.5$, and (c) $M = 0.8$; $k_1 = 0.0$, 0.007, 0.027, 0.062, 0.110, 0.172, 0.248, 0.338, 0.442, 0.561, 0.694, 0.842, 1.01, 1.18, 1.38, 1.59, 1.82, 2.07, 2.33, 2.62, 2.93, 3.26, 3.62, 4.01.
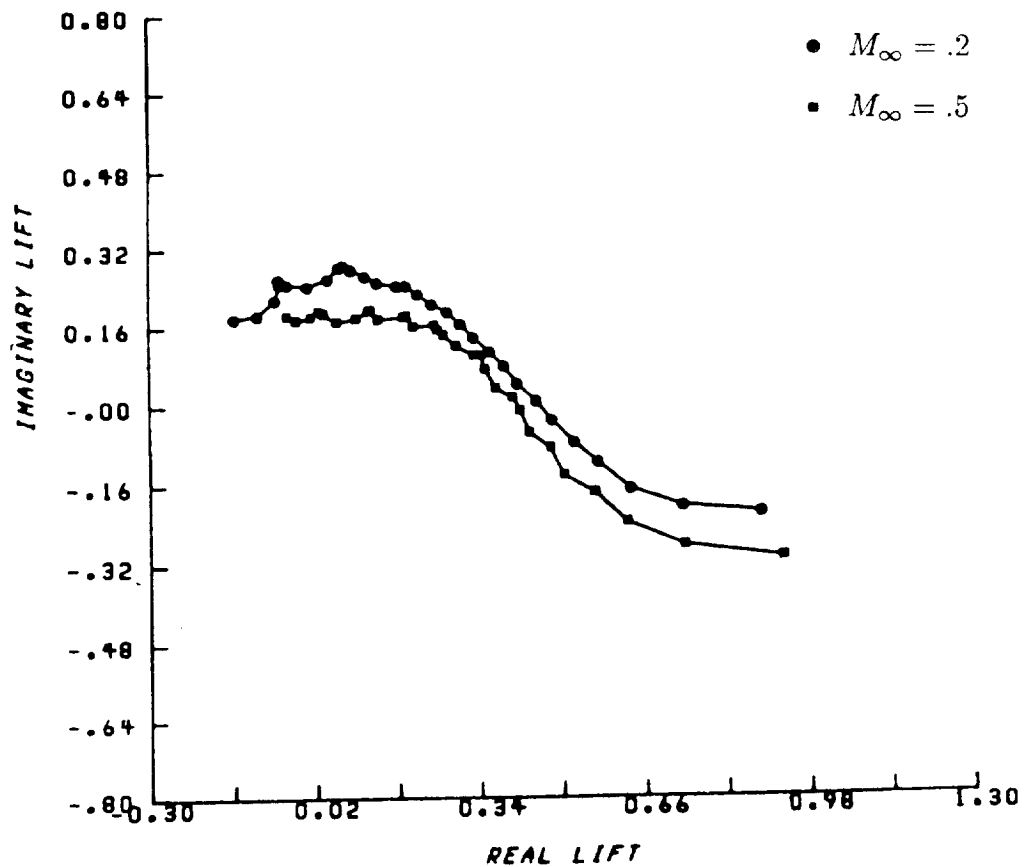
Figure 22. Numerical results for the unsteady lift of a 12 percent thick, symmetric Joukowski airfoil in a transverse gust. Results show grid dependent errors due to exponentially decreasing spacing in the ξ direction which was used in place of condition (3.70). $k_1 = 0.1, 0.2,$ 0.3, 0.4, 0.5, 0.6, 0.7, 0.8, 0.9, 1.0, 1.1, 1.2, 1.3, 1.4, 1.5, 1.6, 1.7, 1.8, 1.9, 2.0, 2.1, 2.2, 2.3, 2.4, 2.5, 2.6, 2.7, 2.8, 2.9, 3.0.
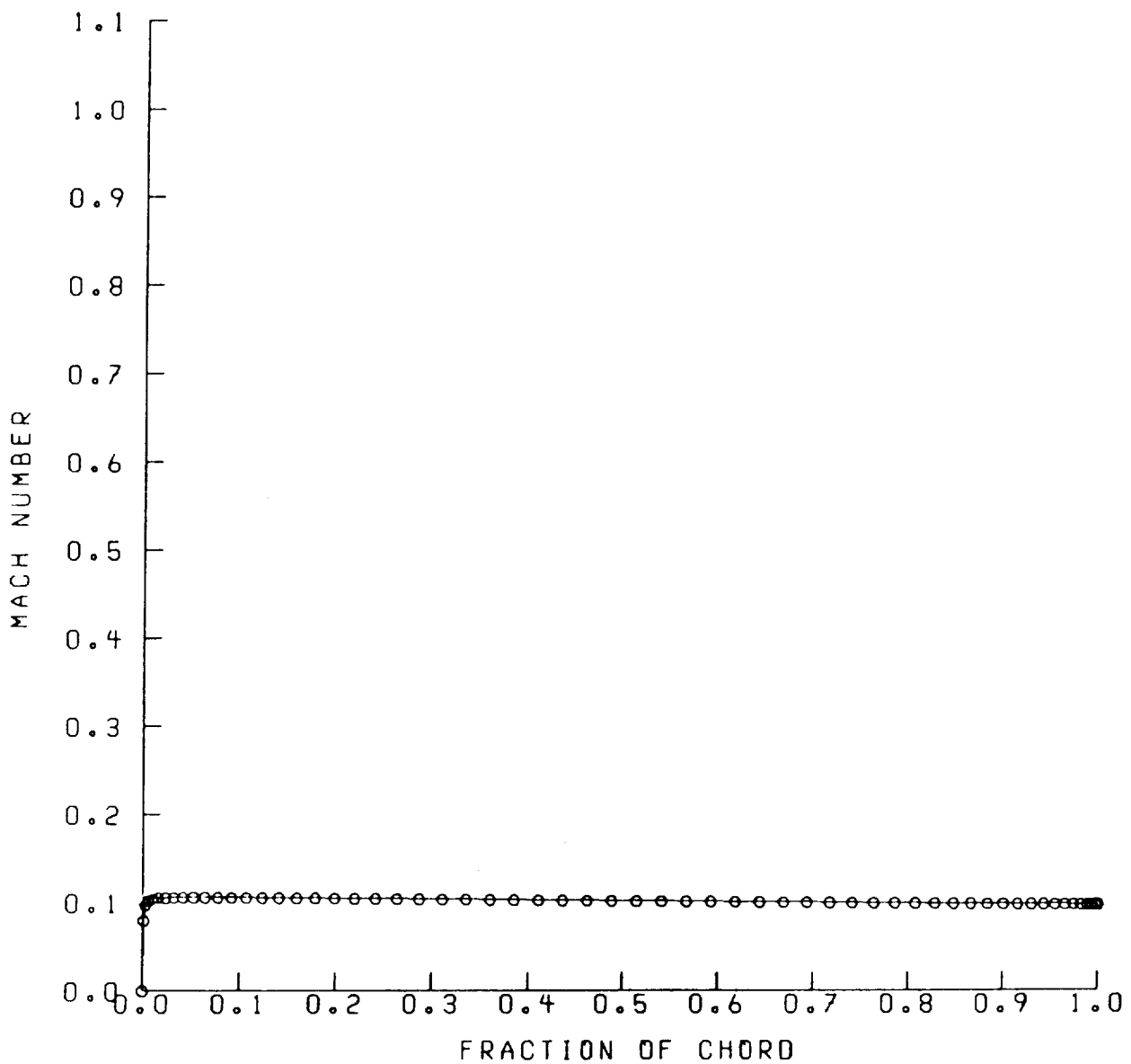
Figure 23. Mean flow Mach number at the airfoil surface for a 3 percent thick Joukowski airfoil with $M_\infty = .1, \alpha = 0°$, and camber ratio = 0.
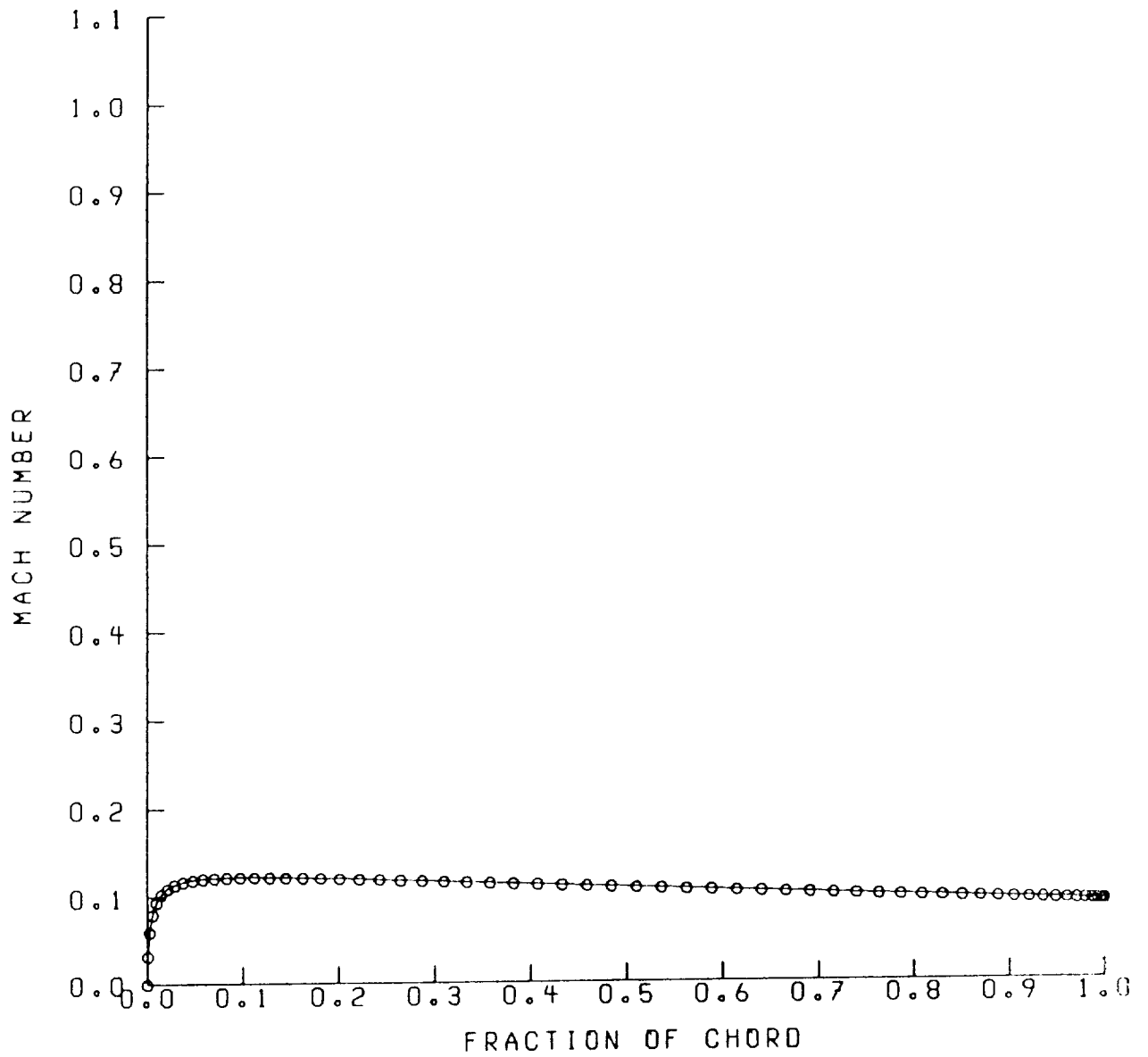
Figure 24.   Mean flow Mach number at the airfoil surface for a 12 percent thick Joukowski airfoil with $M_\infty = .1, \alpha = 0°$, and camber ratio = 0.

C 2
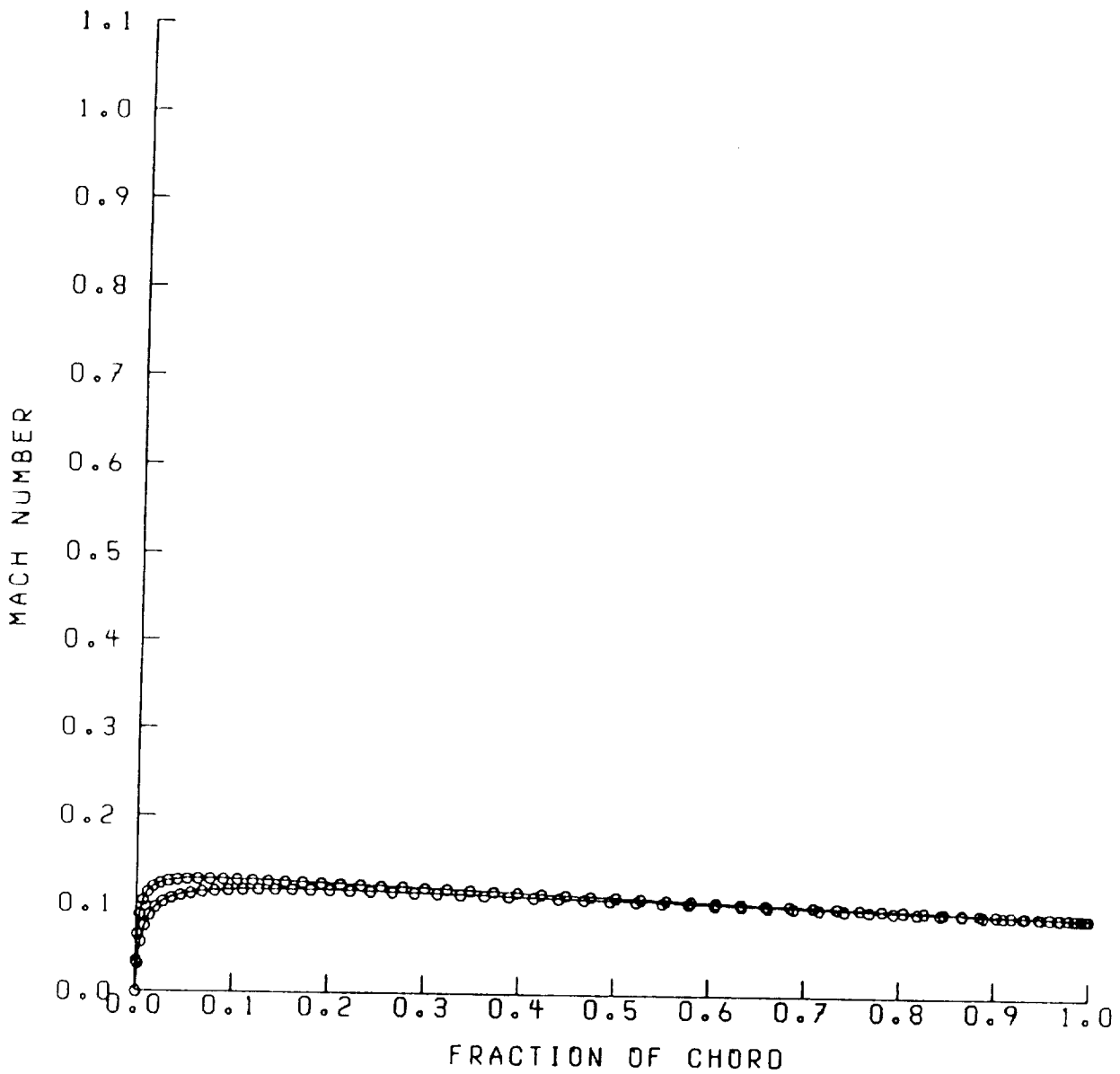
Figure 25. Mean flow Mach number at the airfoil surface for a 12 percent thick Joukowski airfoil with $M_\infty = .1, \alpha = 1^\circ$, and camber ratio = 0.
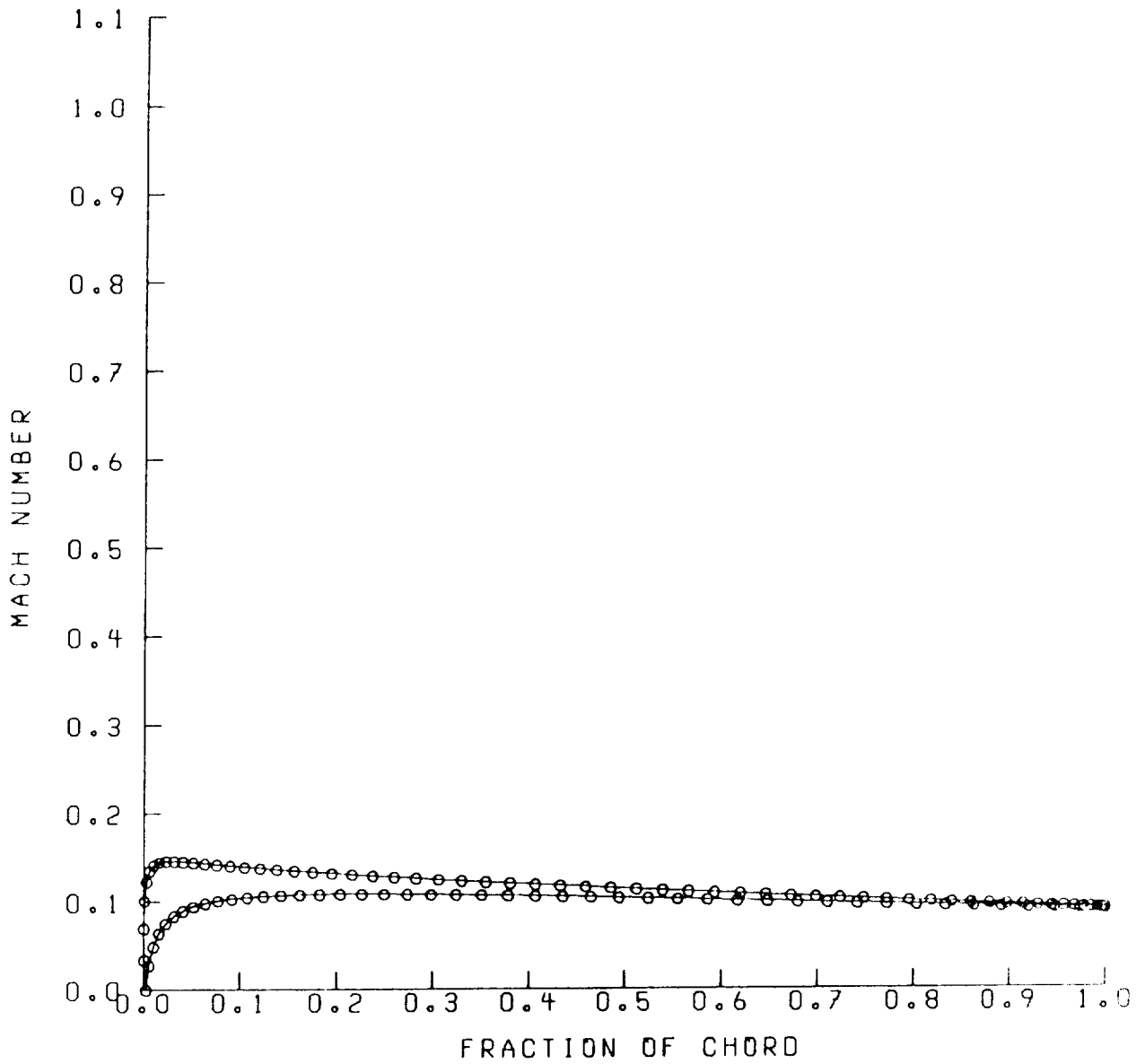
Figure 26.   Mean flow Mach number at the airfoil surface for a 12 percent
thick Joukowski airfoil with $M_\infty = .1, \alpha = 3^o$, and camber
ratio = 0.
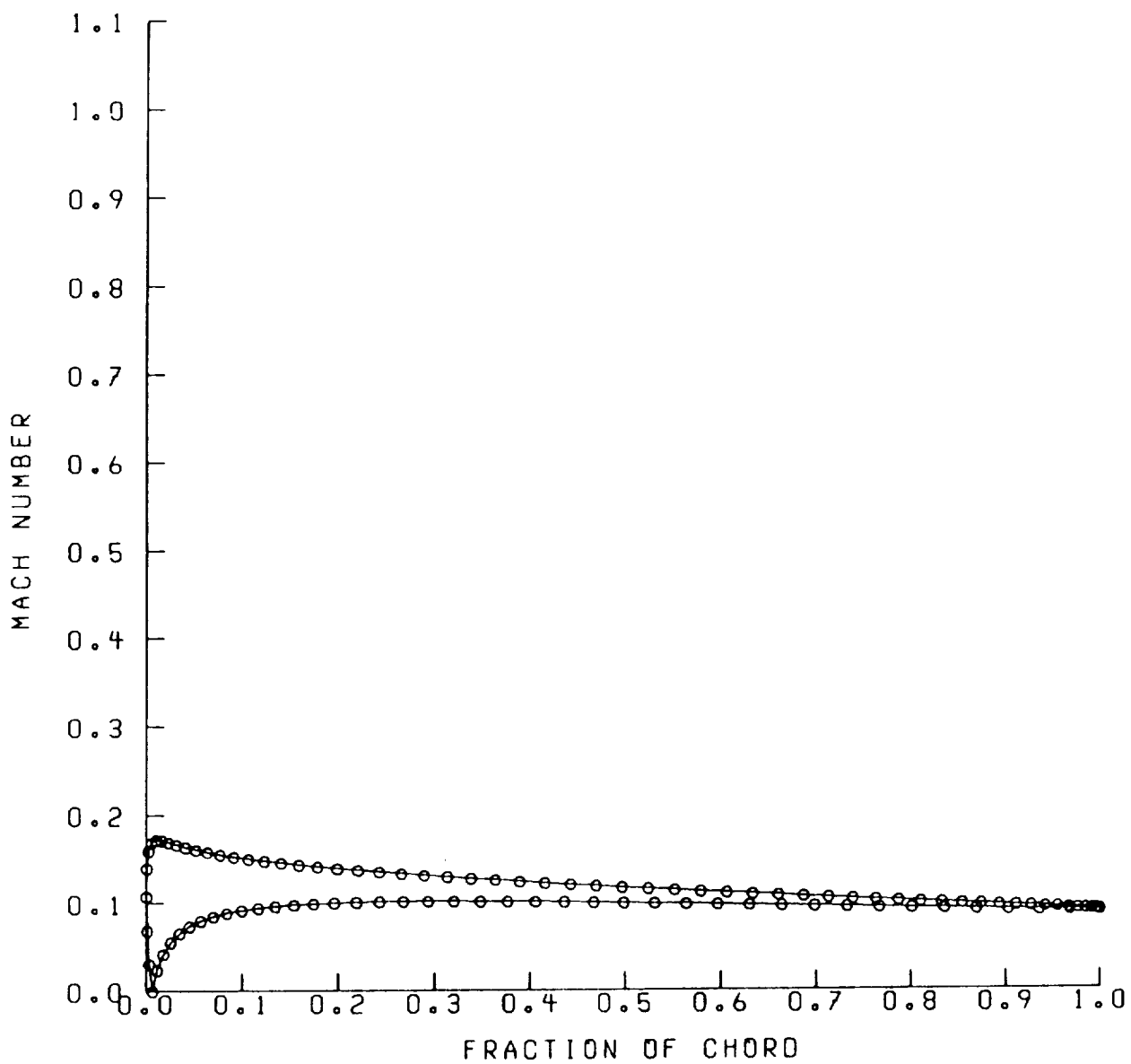
Figure 27.   Mean flow Mach number at the airfoil surface for a 12 percent
thick Joukowski airfoil with $M_\infty = .1, \alpha = 5^o$, and camber
ratio = 0.
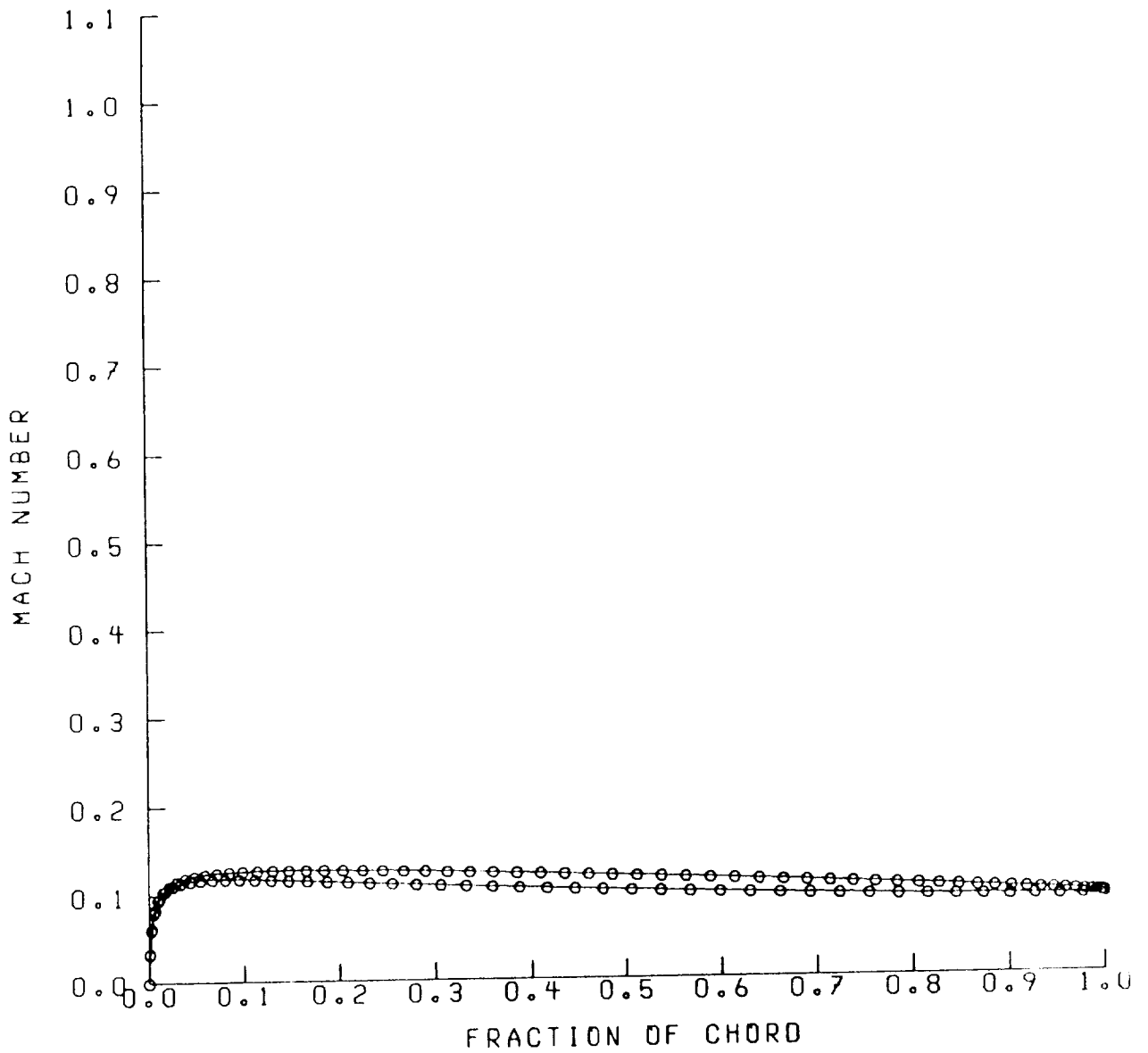
Figure 28.   Mean flow Mach number at the airfoil surface for a 12 percent thick Joukowski airfoil with $M_\infty = .1, \alpha = 0^o$, and camber ratio = .02.
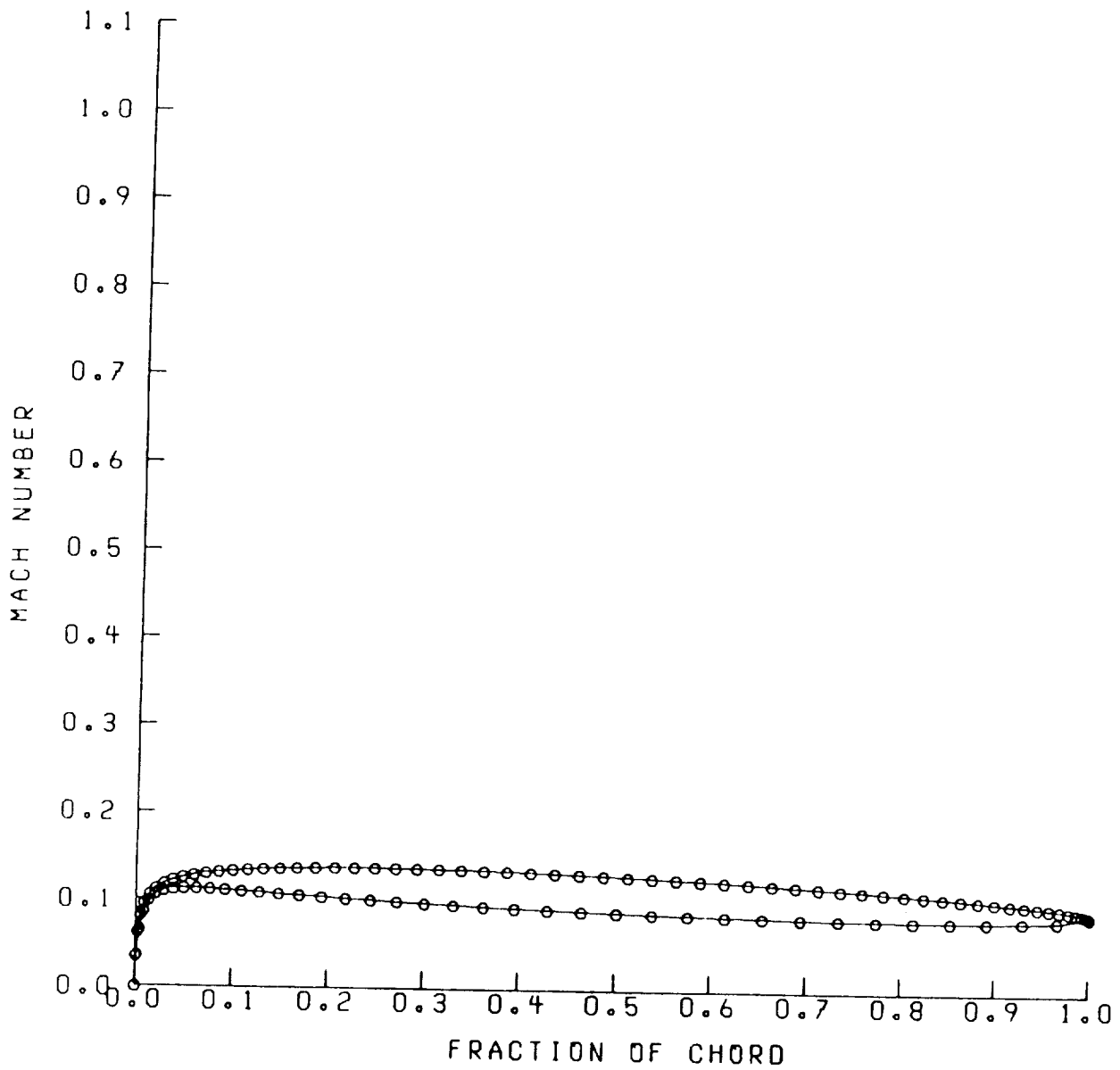
Figure 29.   Mean flow Mach number at the airfoil surface for a 12 percent
thick Joukowski airfoil with $M_\infty = .1, \alpha = 0°$, and camber
ratio = .05.
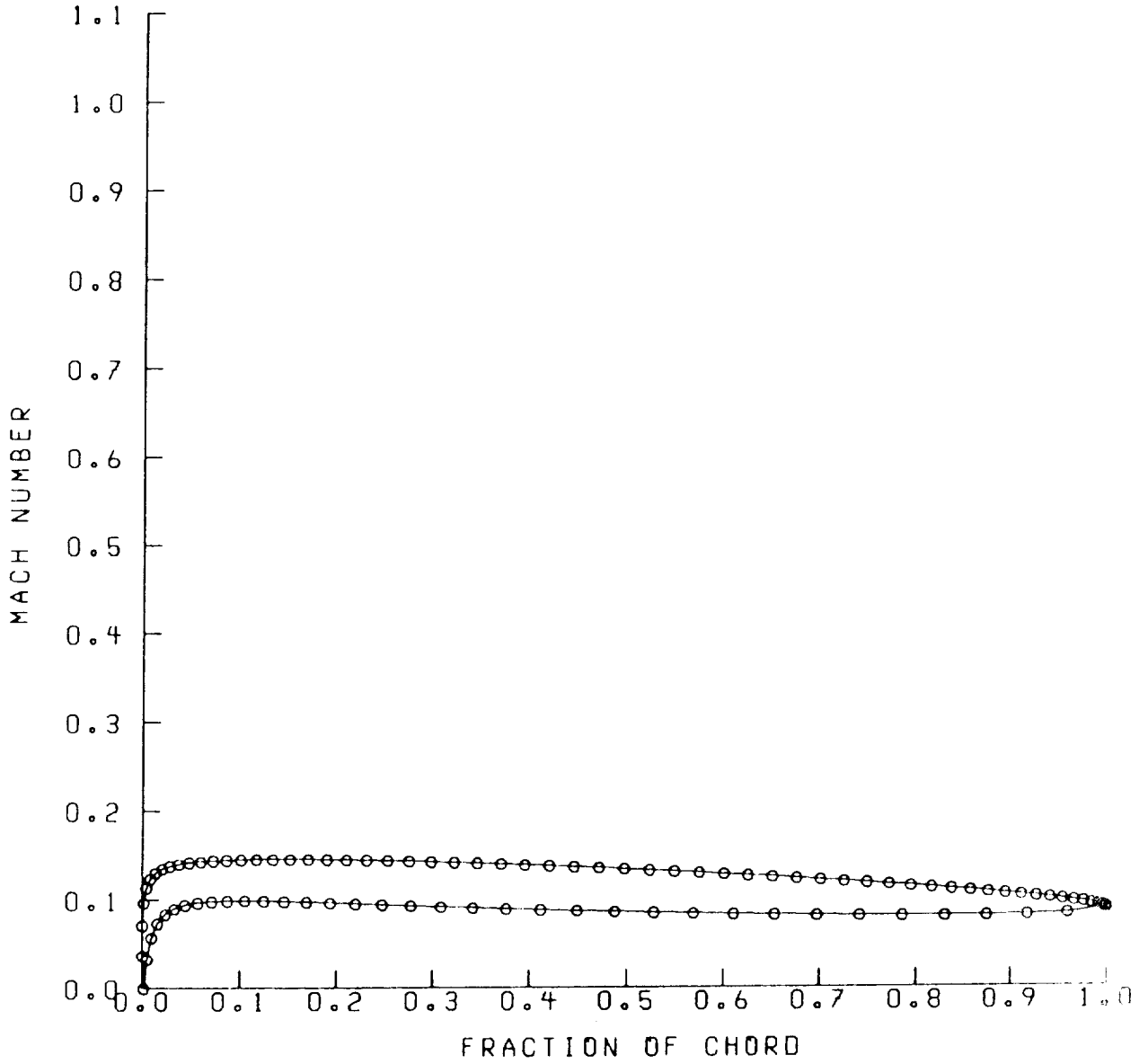
Figure 30.   Mean flow Mach number at the airfoil surface for a 12 percent thick Joukowski airfoil with $M_\infty = .1, \alpha = 2^o$, and camber ratio = .05.
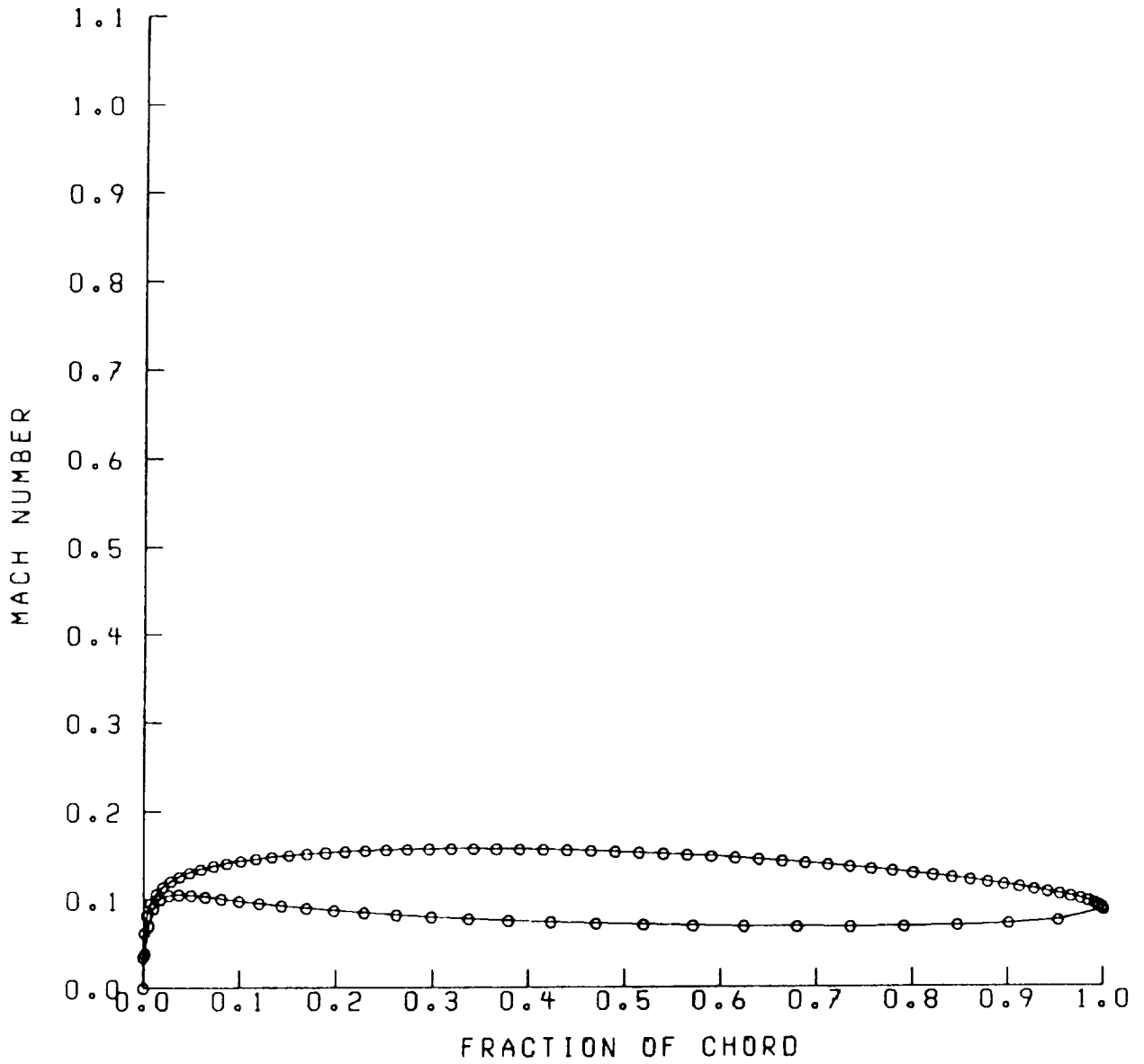
Figure 31.   Mean flow Mach number at the airfoil surface for a 12 percent thick Joukowski airfoil with $M_\infty = .1, \alpha = 0°$, and camber ratio = .10.

100
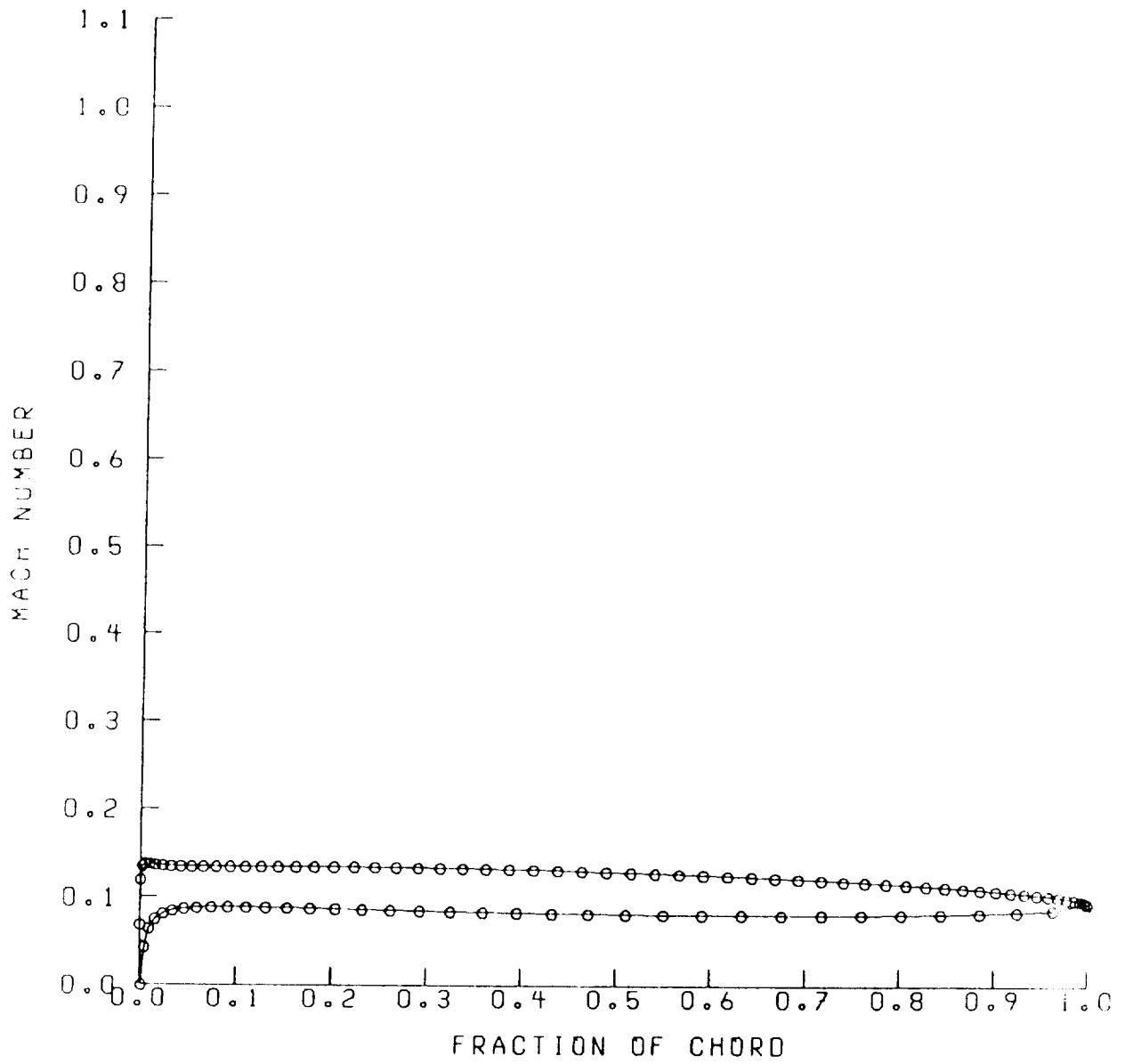
Figure 32.   Mean flow Mach number at the airfoil surface for a 6 percent thick Joukowski airfoil with $M_\infty = .1, \alpha = 2^o$, and camber ratio $= .05$.
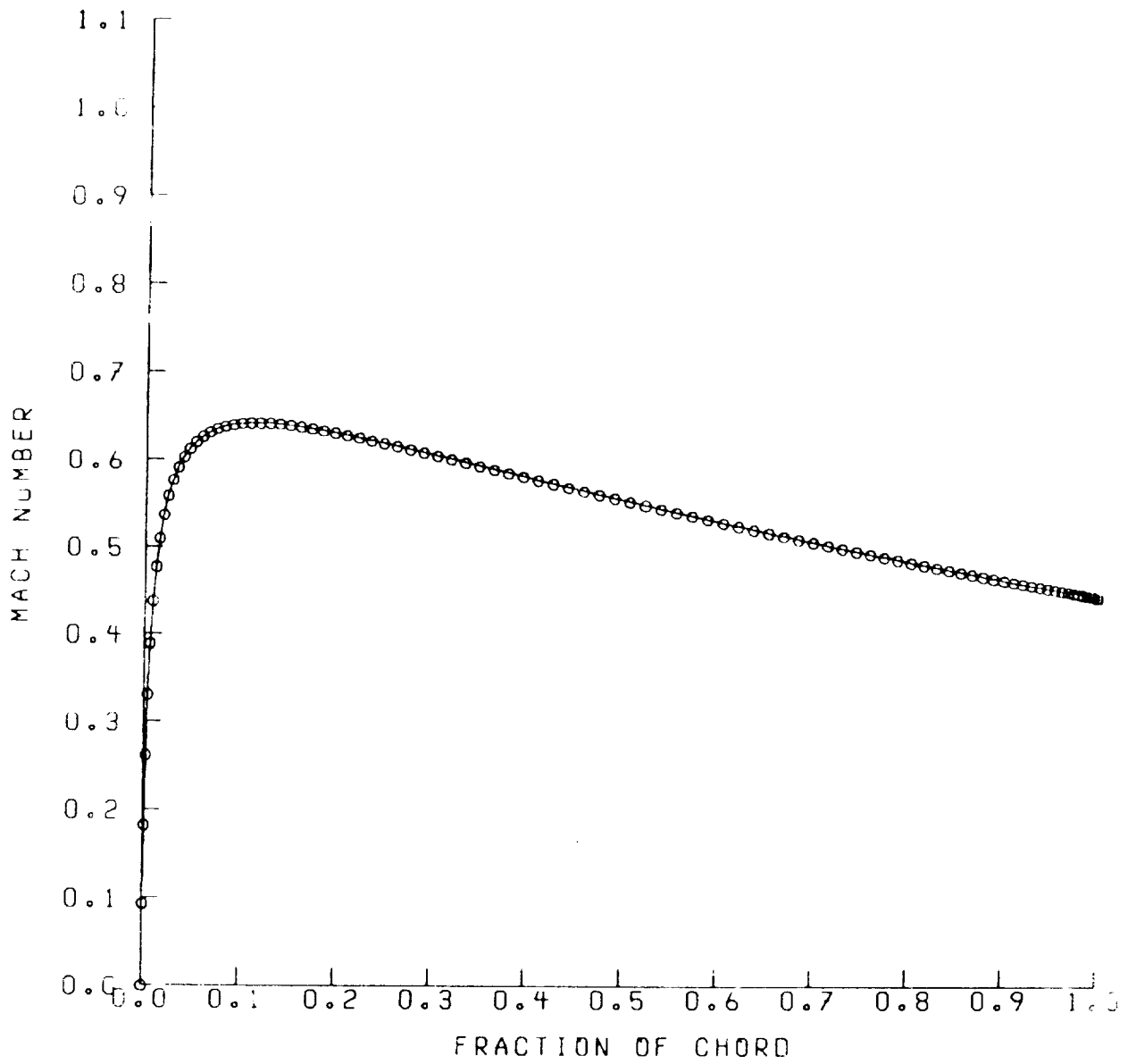
Figure 33.   Mean flow Mach number at the airfoil surface for a 12 percent
thick Joukowski airfoil with $M_\infty = .5, \alpha = 0^o$, and camber
ratio = 0. Calculation by FLO36.

Figure 34. Mean flow Mach number at the airfoil surface for a 12 percent thick Joukowski airfoil with $M_\infty = .5, \alpha = 5^\circ$, and camber ratio = 0. Calculation by FLO36.
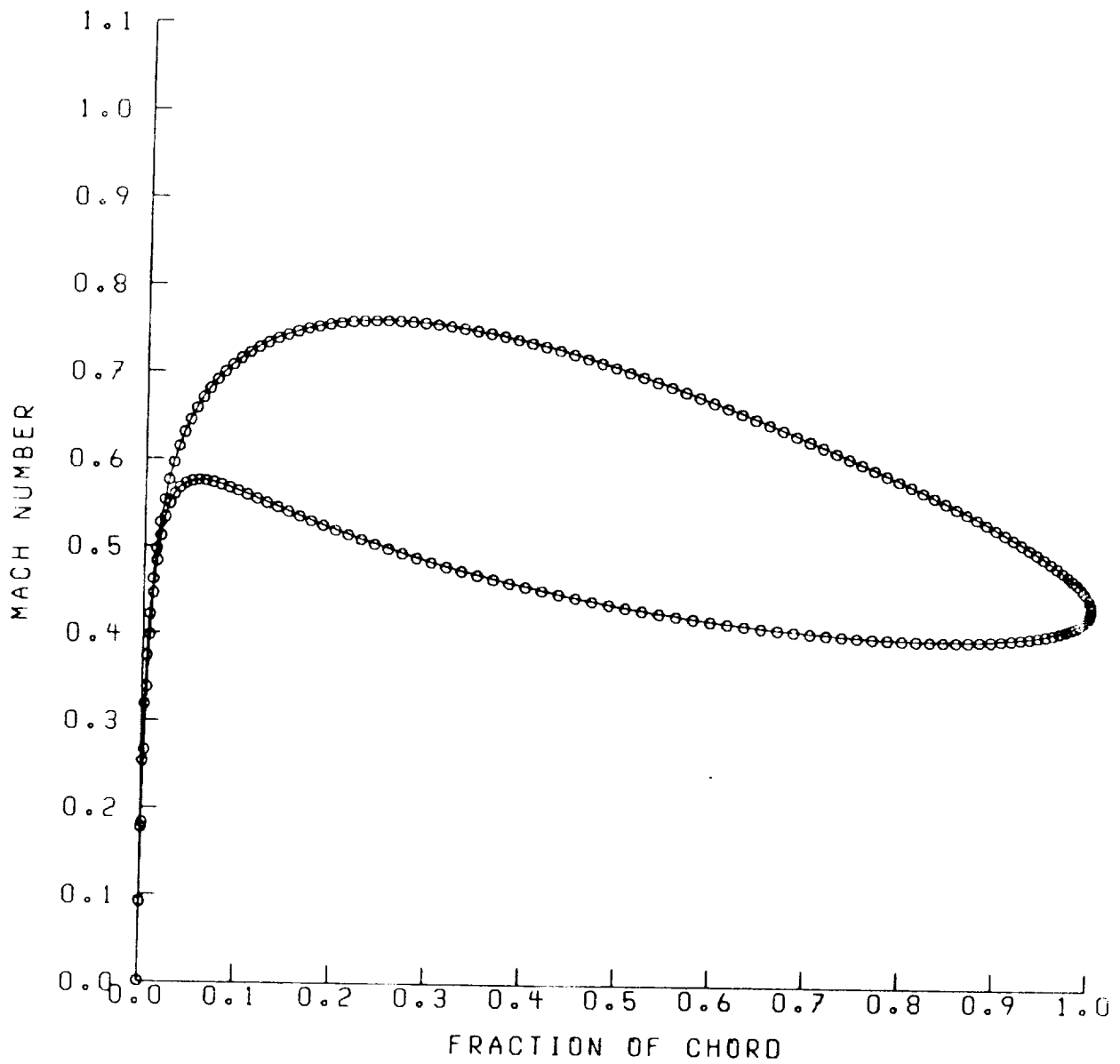
Figure 35.   Mean flow Mach number at the airfoil surface for a 12 percent
thick Joukowski airfoil with $M_\infty = .5, \alpha = 0^\circ$, and camber
ratio $= .05$. Calculation by FLO36.
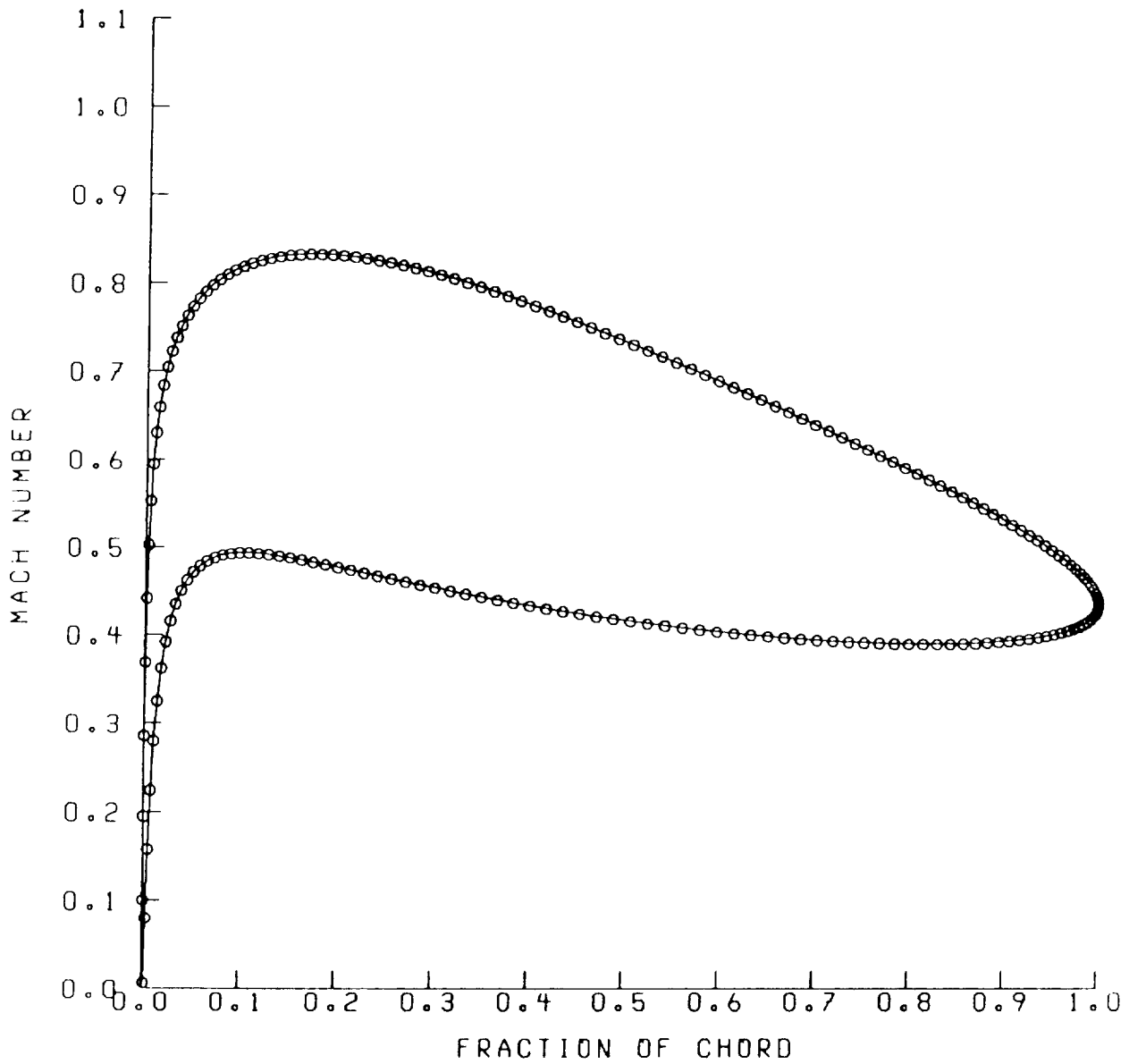
Figure 36. Mean flow Mach number at the airfoil surface for a 12 percent thick Joukowski airfoil with $M_\infty = .5, \alpha = 2^o$, and camber ratio $= .05$. Calculation by FLO36.

Figure 37. Mean flow Mach number at the airfoil surface for a 6 percent thick Joukowski airfoil with $M_\infty = .5, \alpha = 2°$, and camber ratio = .05. Calculation by FLO36.

106
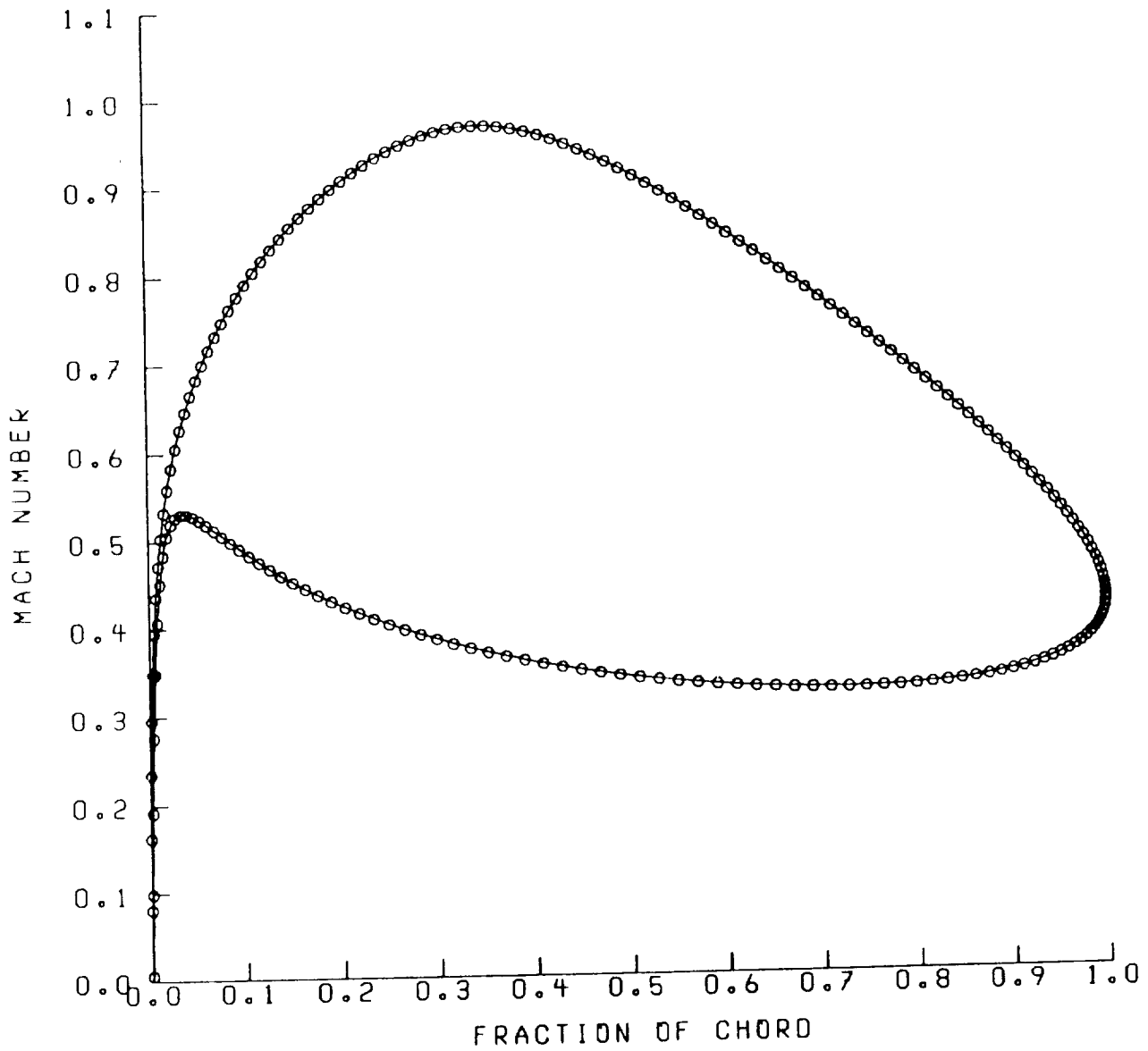
Figure 38.   Mean flow Mach number at the airfoil surface for a 12 percent thick Joukowski airfoil with $M_\infty = .5, \alpha = 0^o$, and camber ratio $= .10$. Calculation by FLO36.
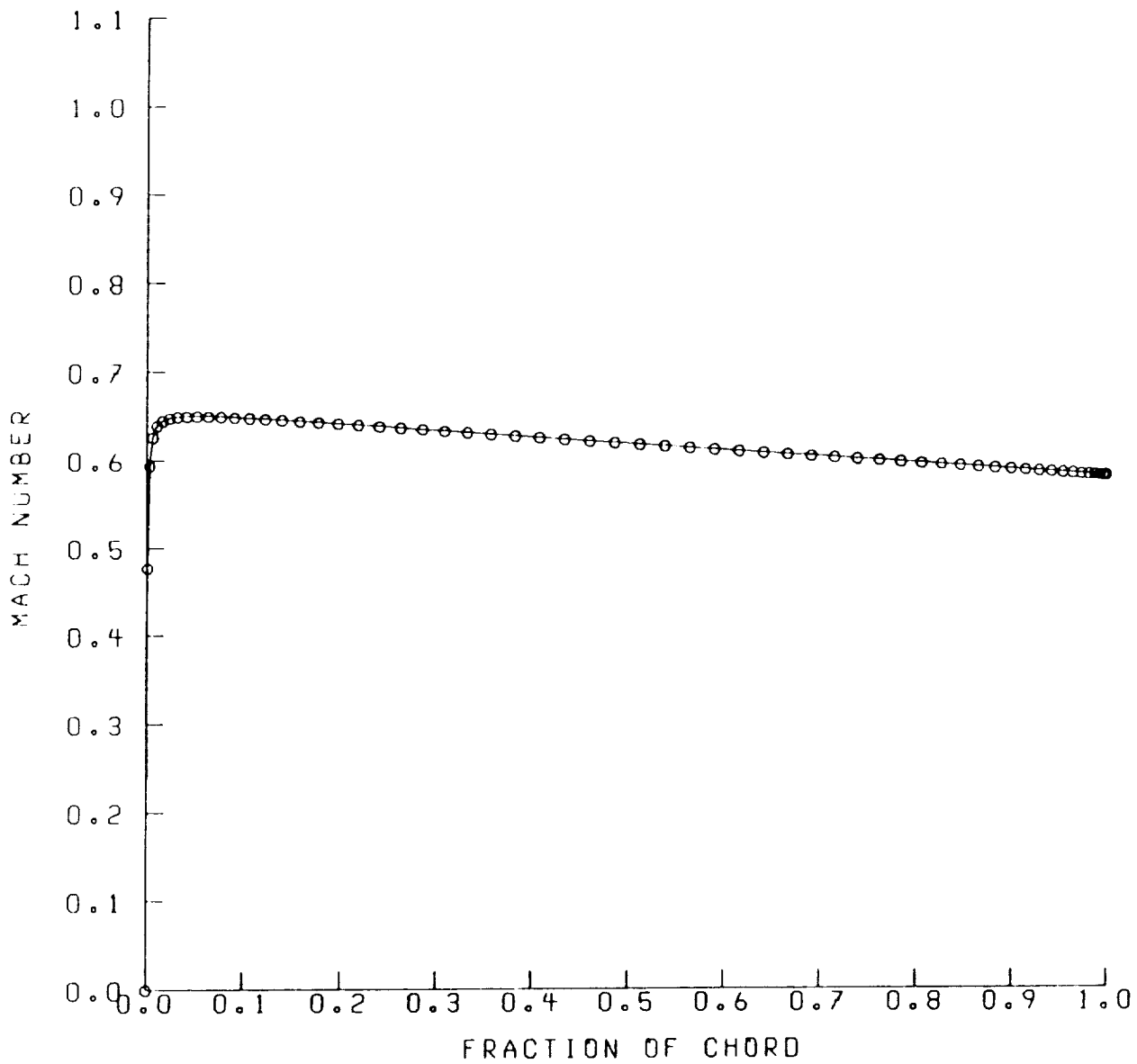
Figure 39. Mean flow Mach number at the airfoil surface for a 3 percent
thick Joukowski airfoil with $M_\infty = .6, \alpha = 0^o$, and camber
ratio = 0. Calculation by FLO36.
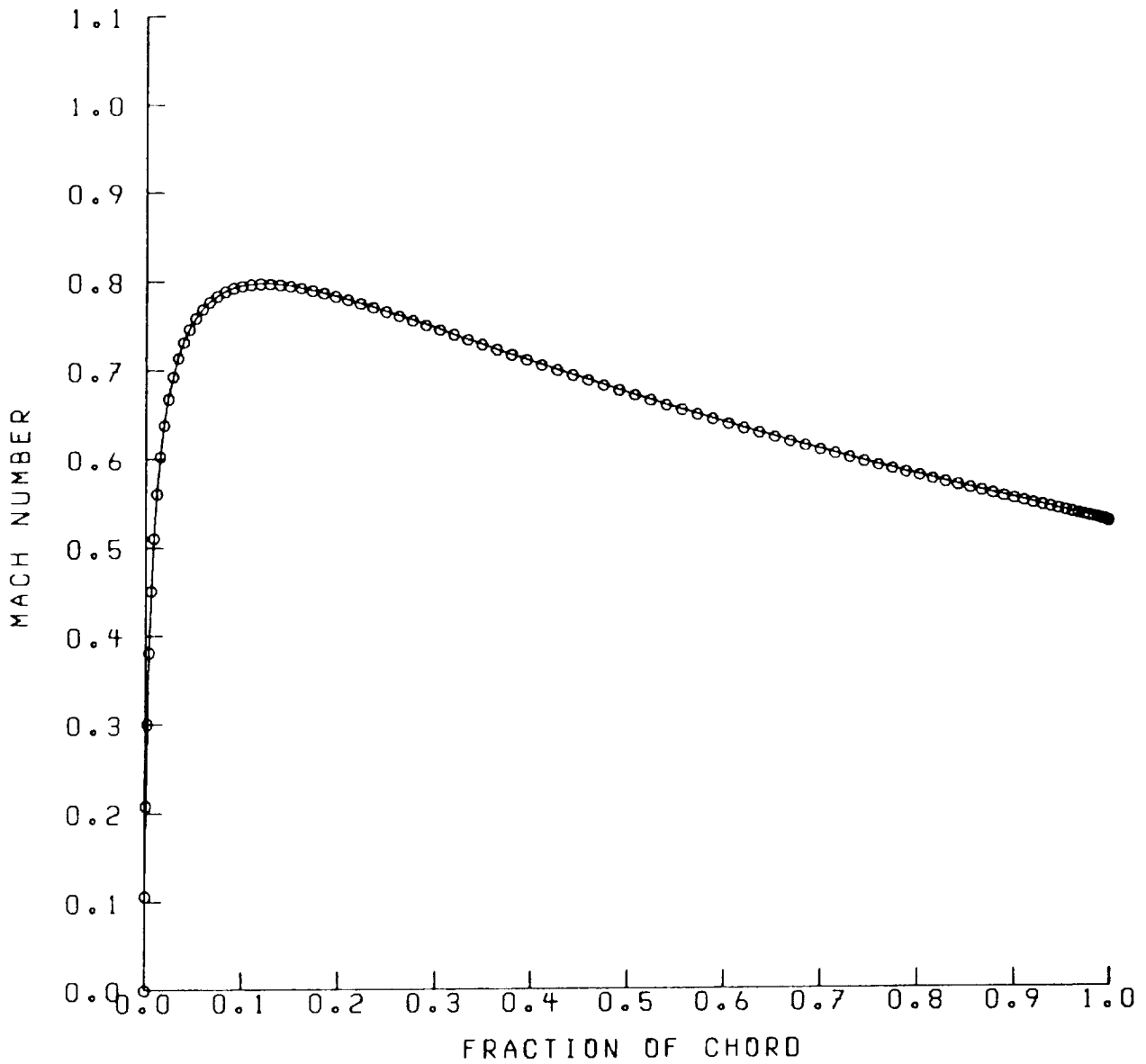
Figure 40. Mean flow Mach number at the airfoil surface for a 12 percent
thick Joukowski airfoil with $M_\infty = .6, \alpha = 0^o$, and camber
ratio $= 0$. Calculation by FLO36.
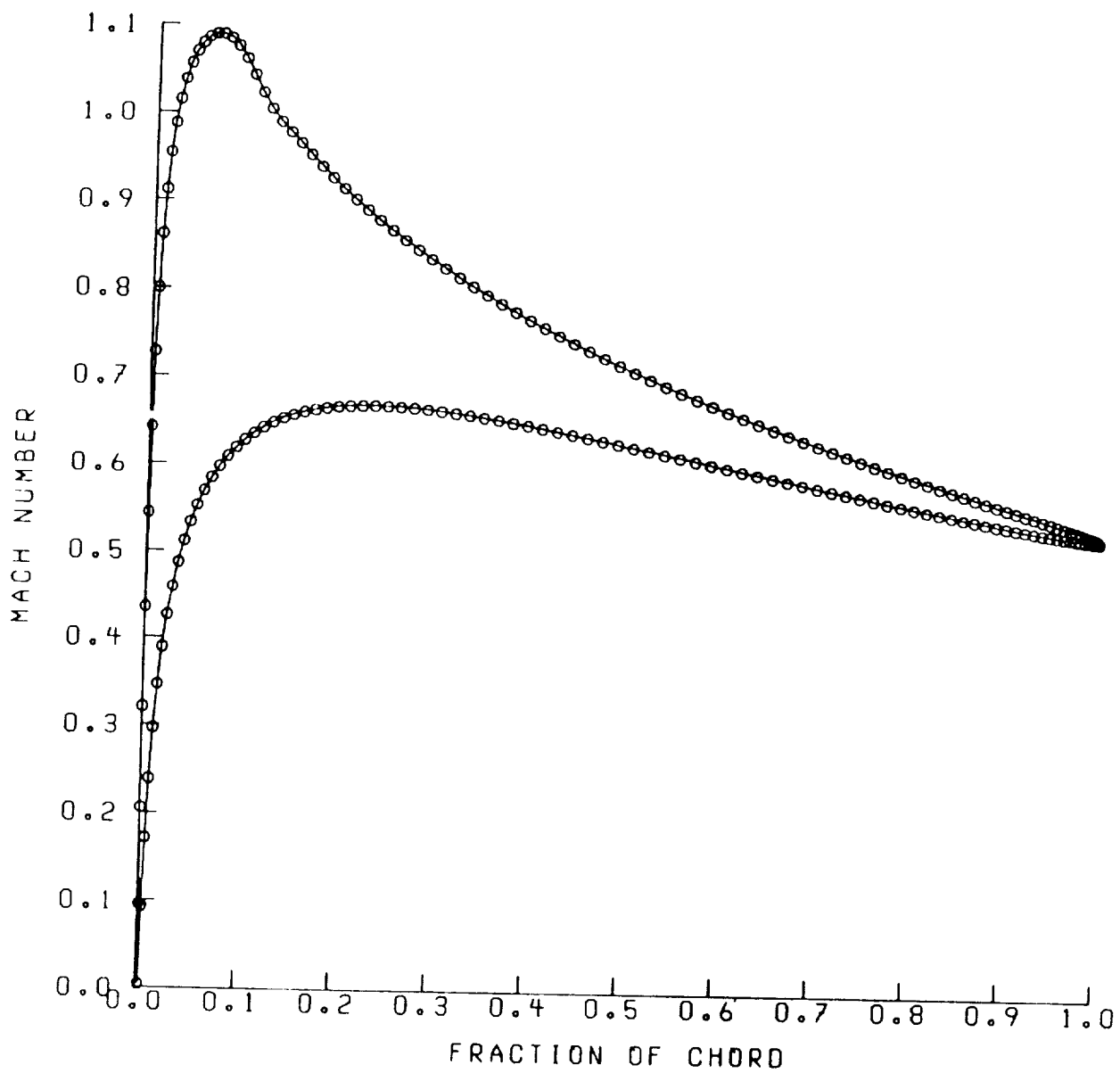
Figure 41.   Mean flow Mach number at the airfoil surface for a 12 percent
thick Joukowski airfoil with $M_\infty = .6, \alpha = 3°$, and camber
ratio $= 0$. Calculation by FLO36.

110
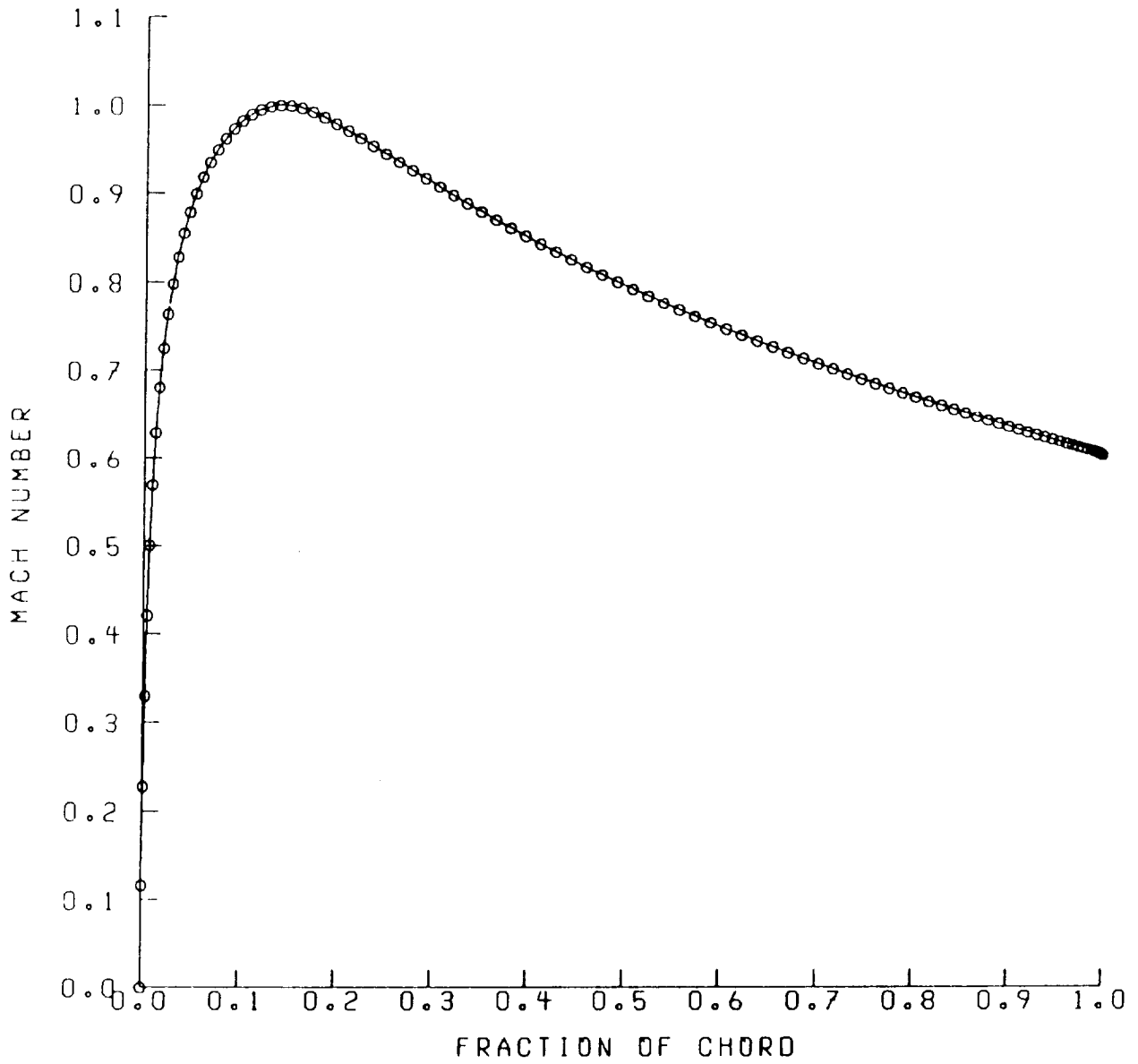
Figure 42.   Mean flow Mach number at the airfoil surface for a 12 percent
thick Joukowski airfoil with $M_\infty = .7, \alpha = 0^o$, and camber
ratio $= 0$. Calculation by FLO36.

111
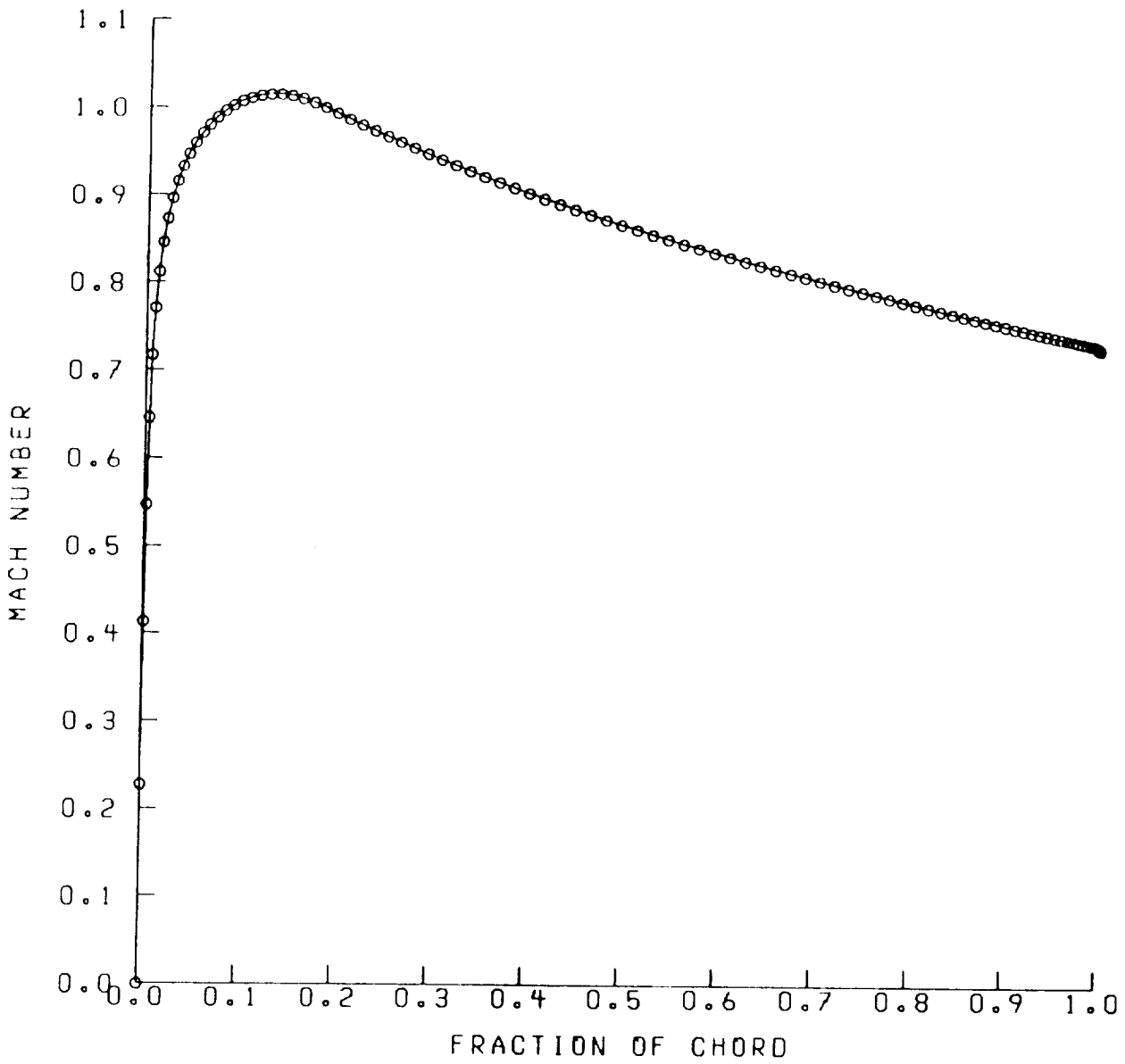
Figure 43. Mean flow Mach number at the airfoil surface for a 6 percent thick Joukowski airfoil with $M_\infty = .8, \alpha = 0^o$, and camber ratio $= 0$. Calculation by FLO36.

112

(a)

(b)

(c)

(d)
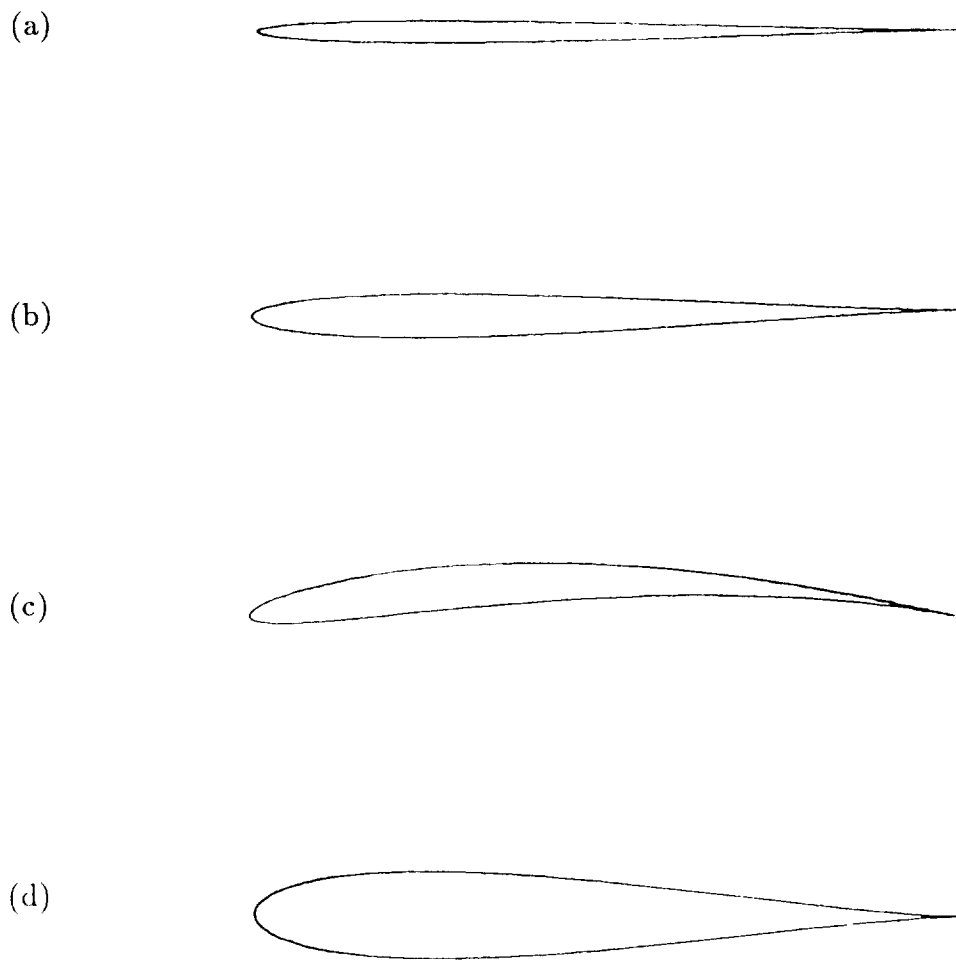
Figure 44. Joukowski airfoil geometries considered in the present work.
(a) thickness ratio = .03, camber = 0; (b) thickness ratio = .06,
camber = 0; (c) thickness ratio = .06, camber = .05;
(d) thickness ratio = .12, camber = 0.

(a)

(b)

(c)
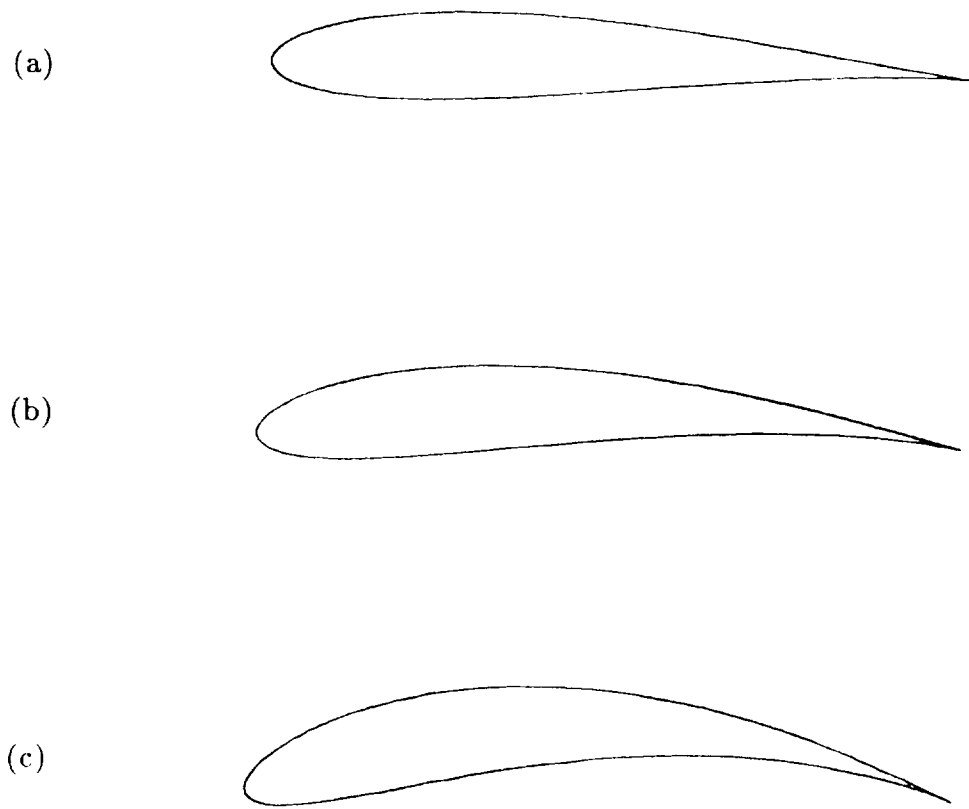
Figure 45.   Joukowski airfoil geometries considered in the present work.
(a) thickness ratio = .12, camber = .02; (b) thickness ratio = .12,
camber = .05; (c) thickness ratio = .12, camber = .10.

Figure 46. Computational grid in the transformed plane for a 12 percent thick Joukowski airfoil with $M_\infty = .1$, $\alpha = 5°$, camber = 0, and $k_1 = .1$.
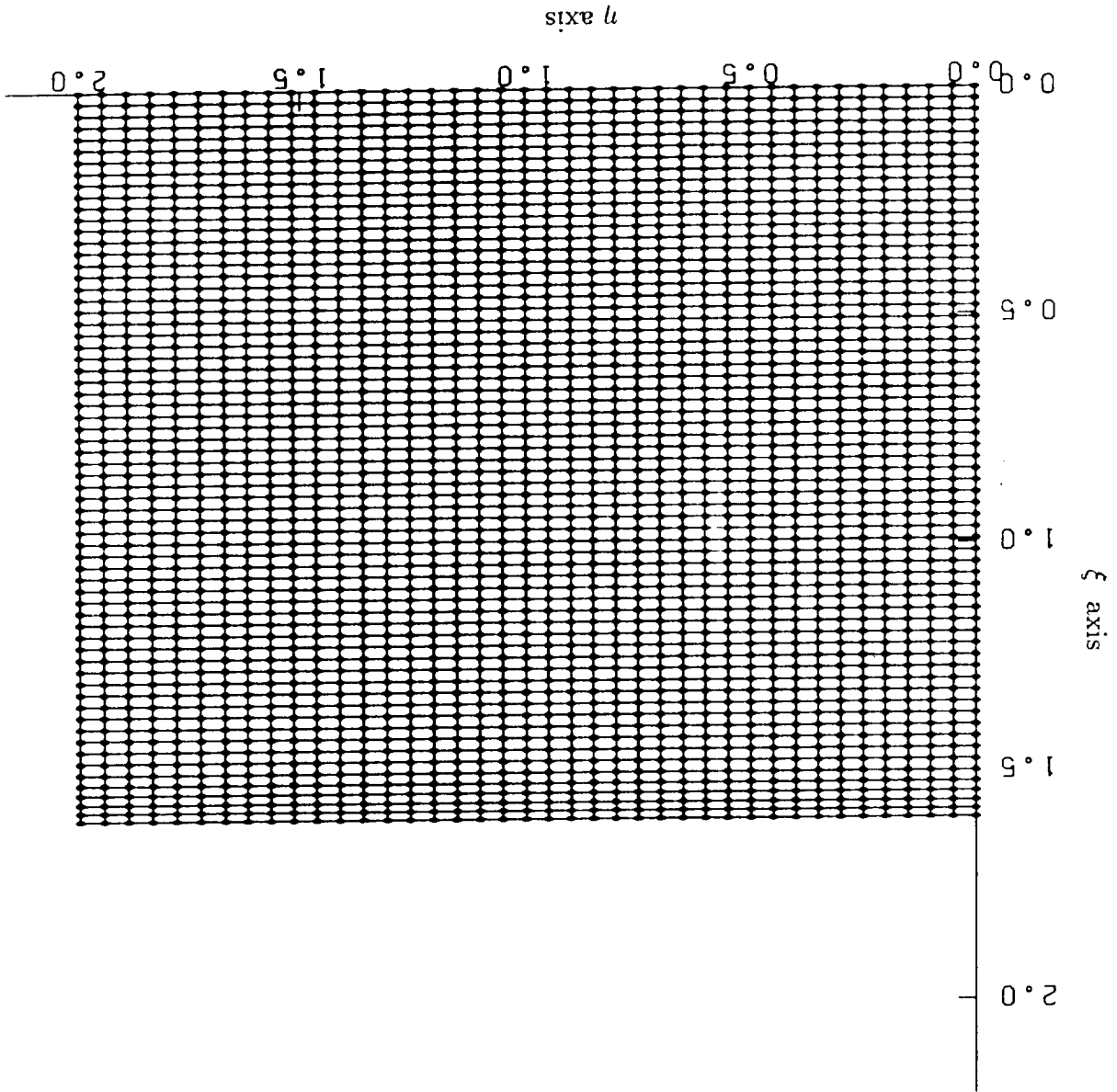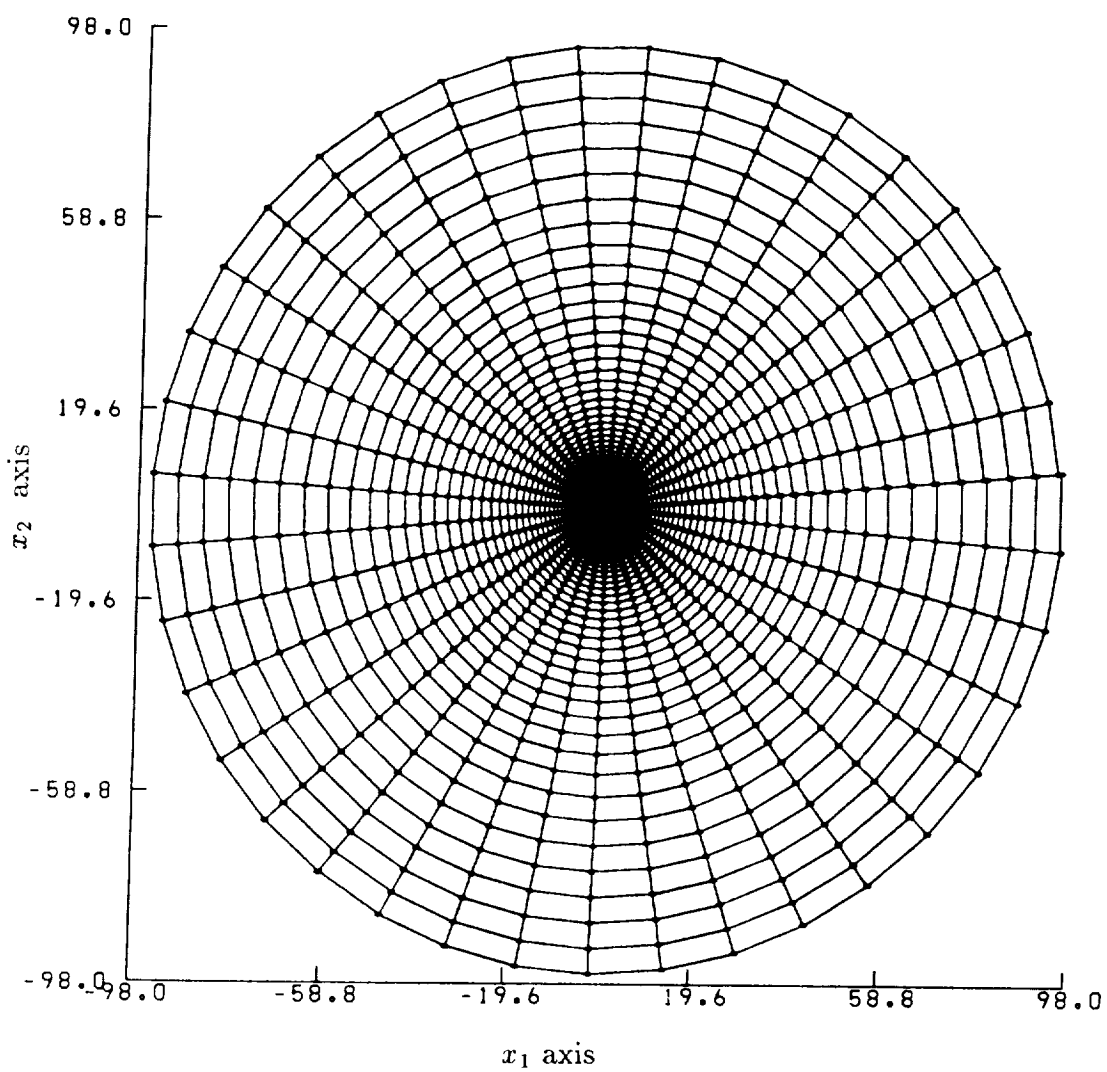
Figure 47. Computational grid in the physical plane for a 12 percent thick Joukowski airfoil with $M_\infty = .1$, $\alpha = 5^o$, camber = 0, and $k_1 = .1$.

116
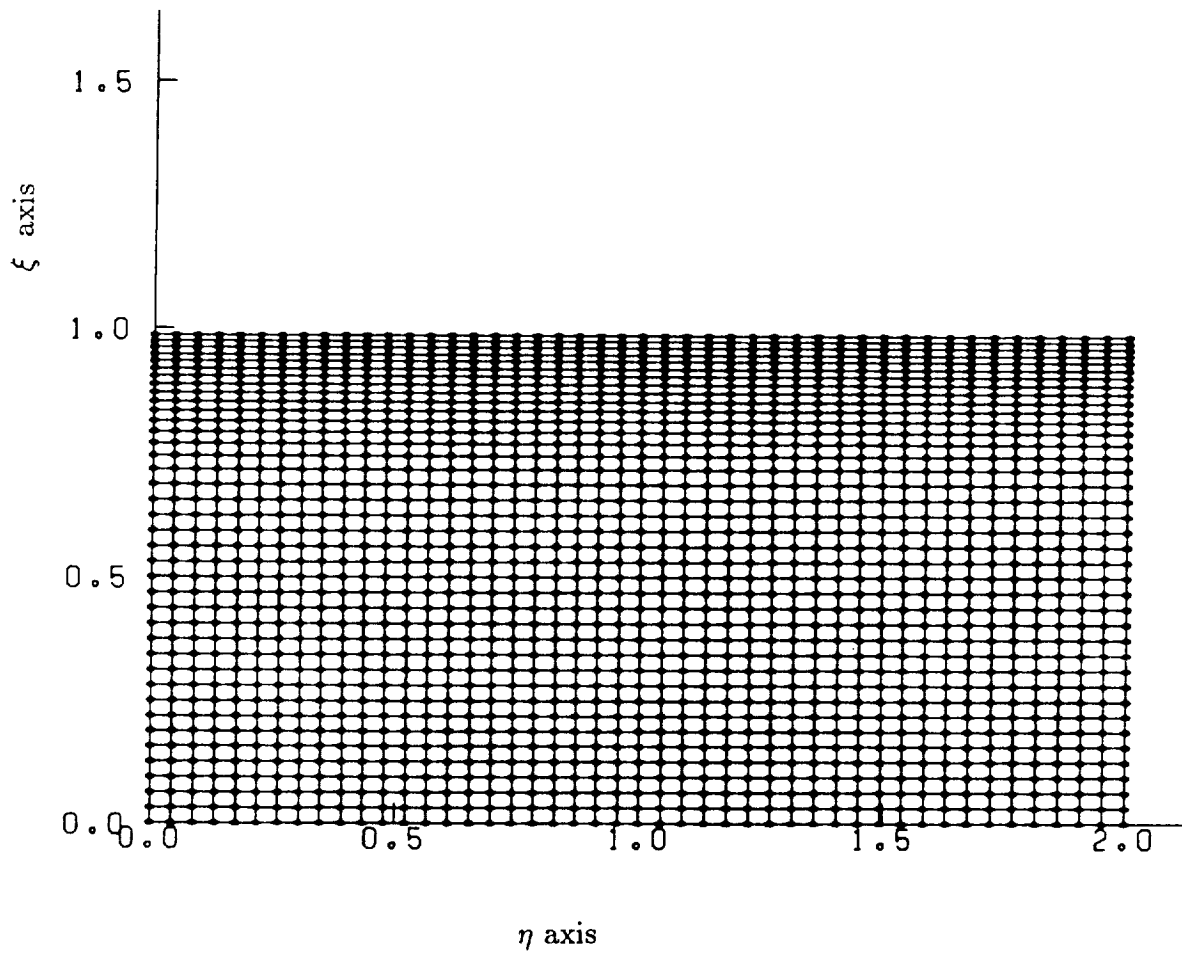
Figure 48. Computational grid in the transformed plane for a 12 percent thick Joukowski airfoil with $M_\infty = .1$, $\alpha = 5^\circ$, camber = 0, and $k_1 = 1.0$.
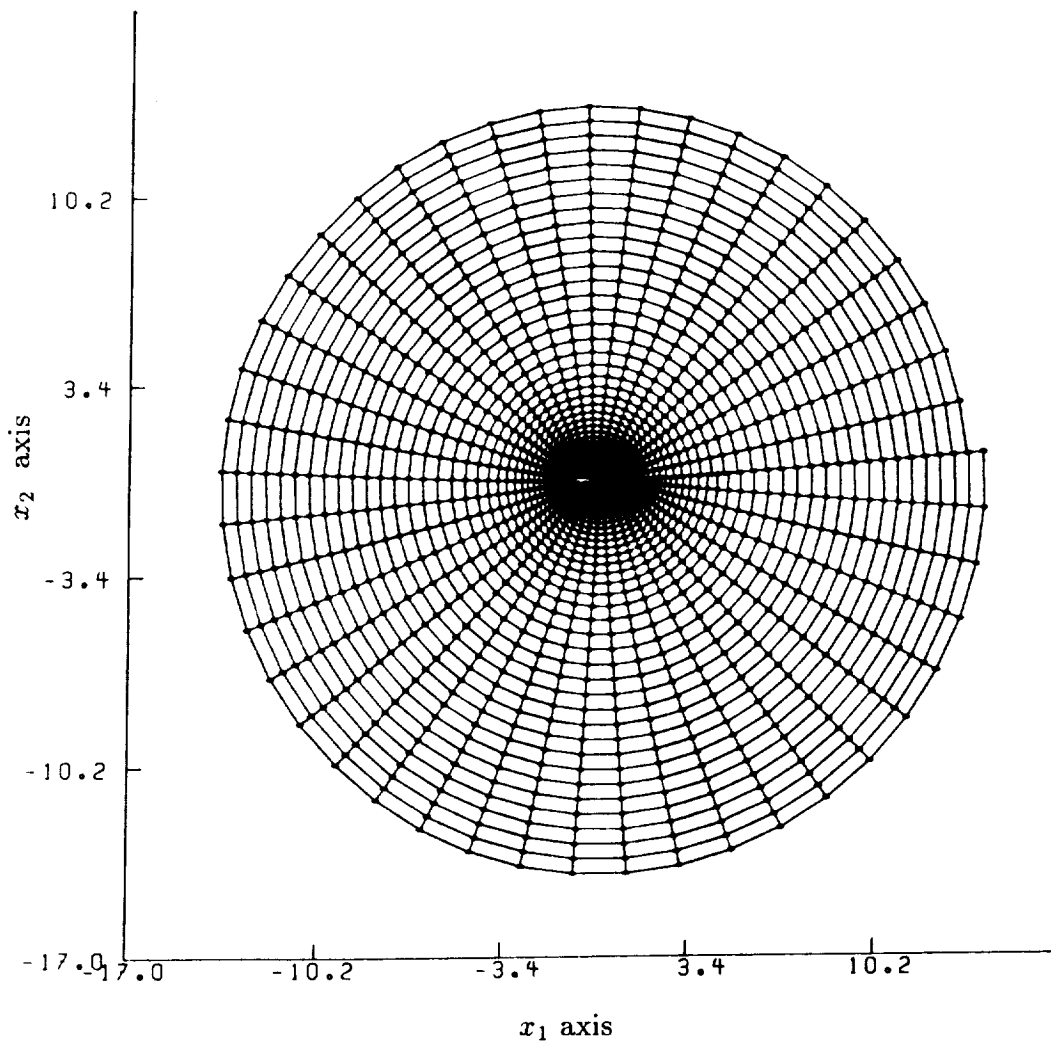
Figure 49.   Computational grid in the physical plane for a 12 percent
             thick Joukowski airfoil with $M_\infty = .1$, $\alpha = 5^o$, camber $= 0$,
             and $k_1 = 1.0$.

118
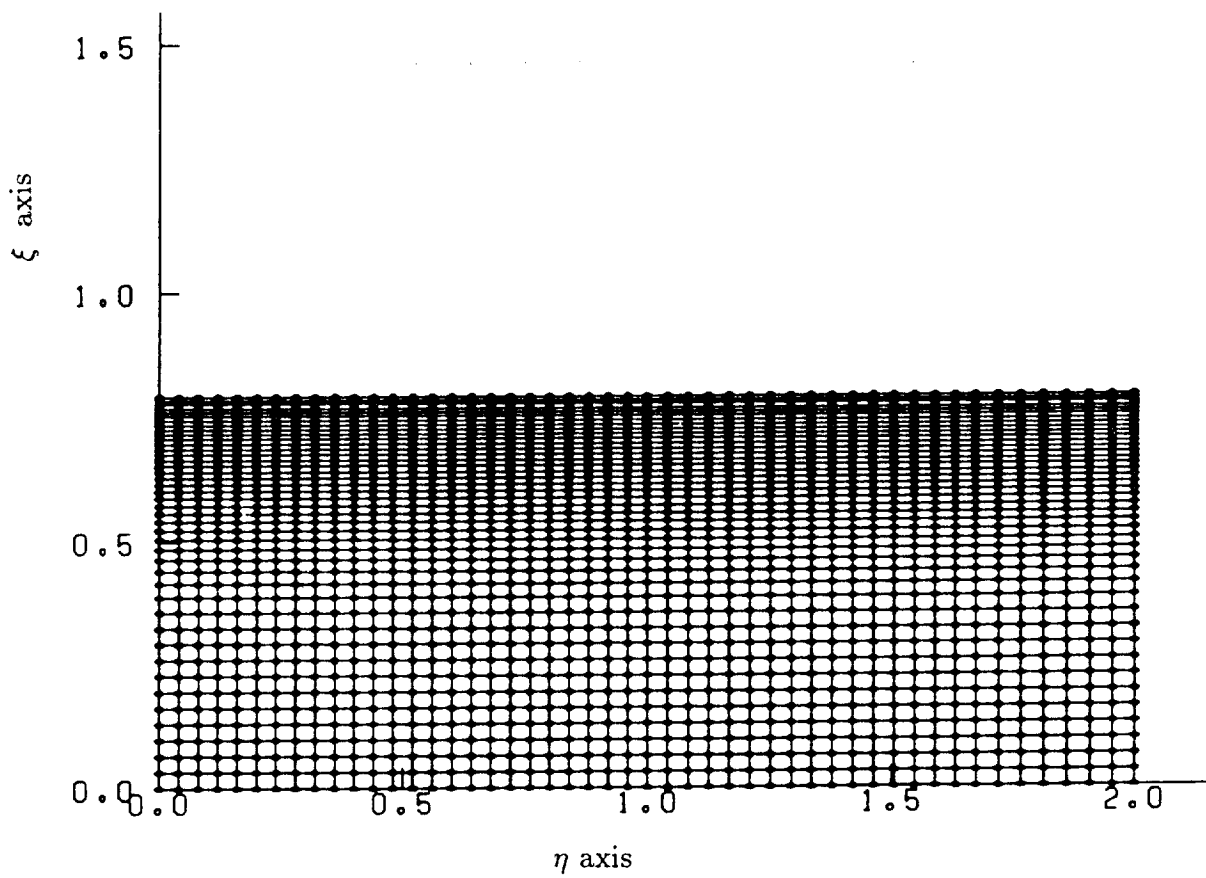
Figure 50.   Computational grid in the transformed plane for a 12 percent
thick Joukowski airfoil with $M_\infty = .1$, $\alpha = 5^o$, camber $= 0$,
and $k_1 = 3.0$.
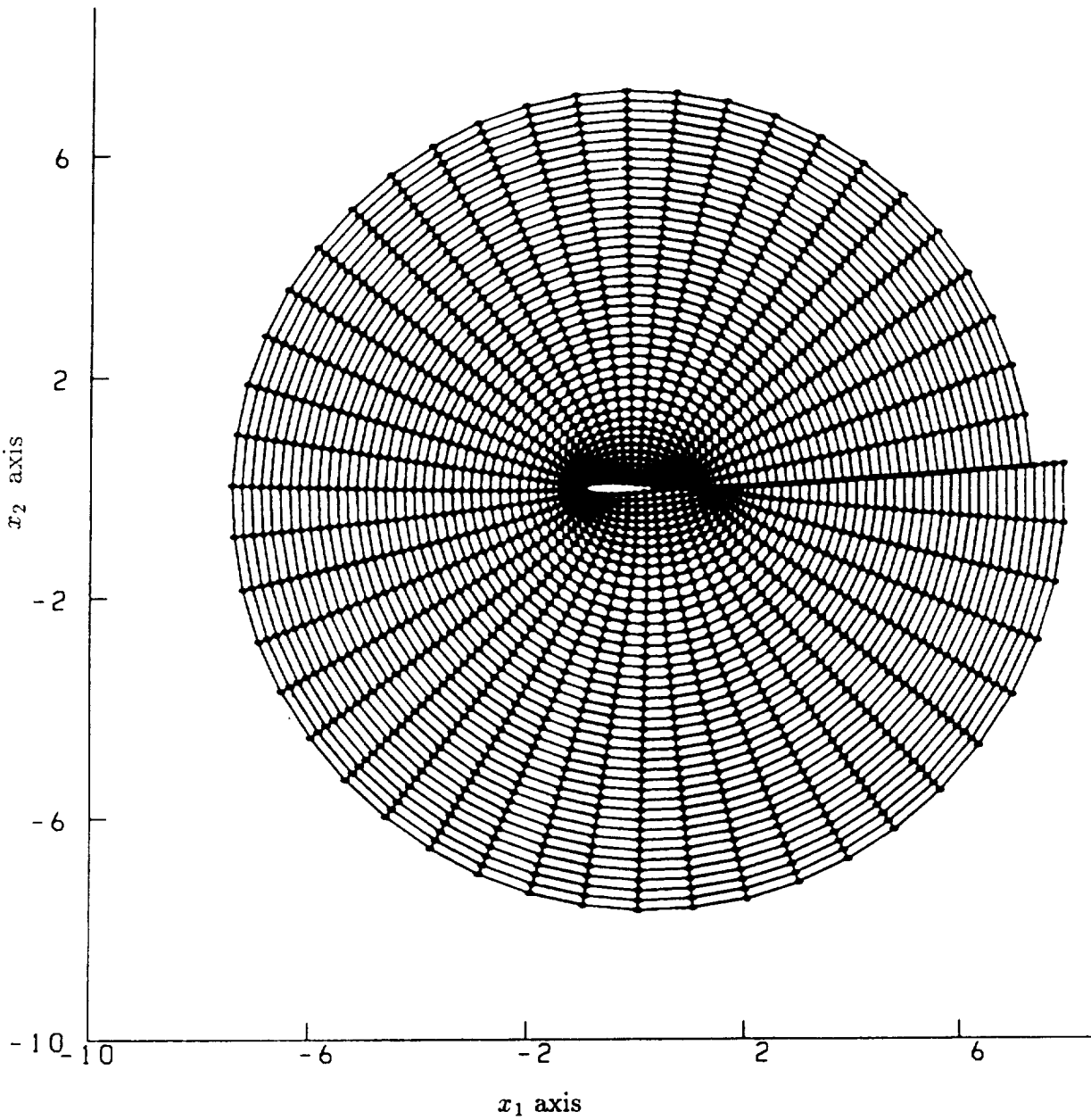
Figure 51.   Computational grid in the physical plane for a 12 percent
             thick Joukowski airfoil with $M_\infty = .1$, $\alpha = 5^\circ$, camber = 0,
             and $k_1 = 3.0$.
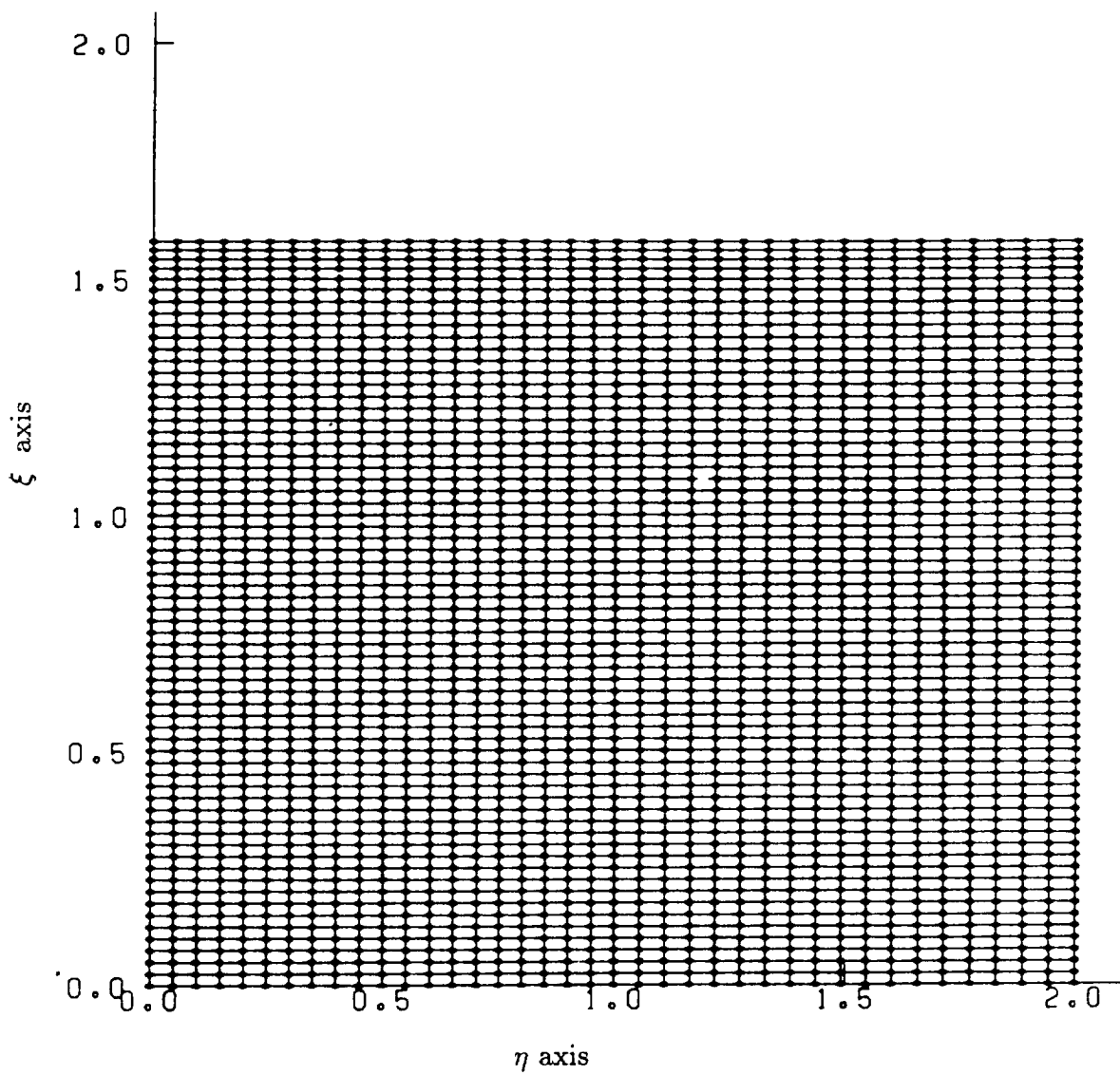
Figure 52. Computational grid in the transformed plane for a 12 percent thick Joukowski airfoil with $M_\infty = .1$, $\alpha = 2^o$, camber $= .05$, and $k_1 = .1$.
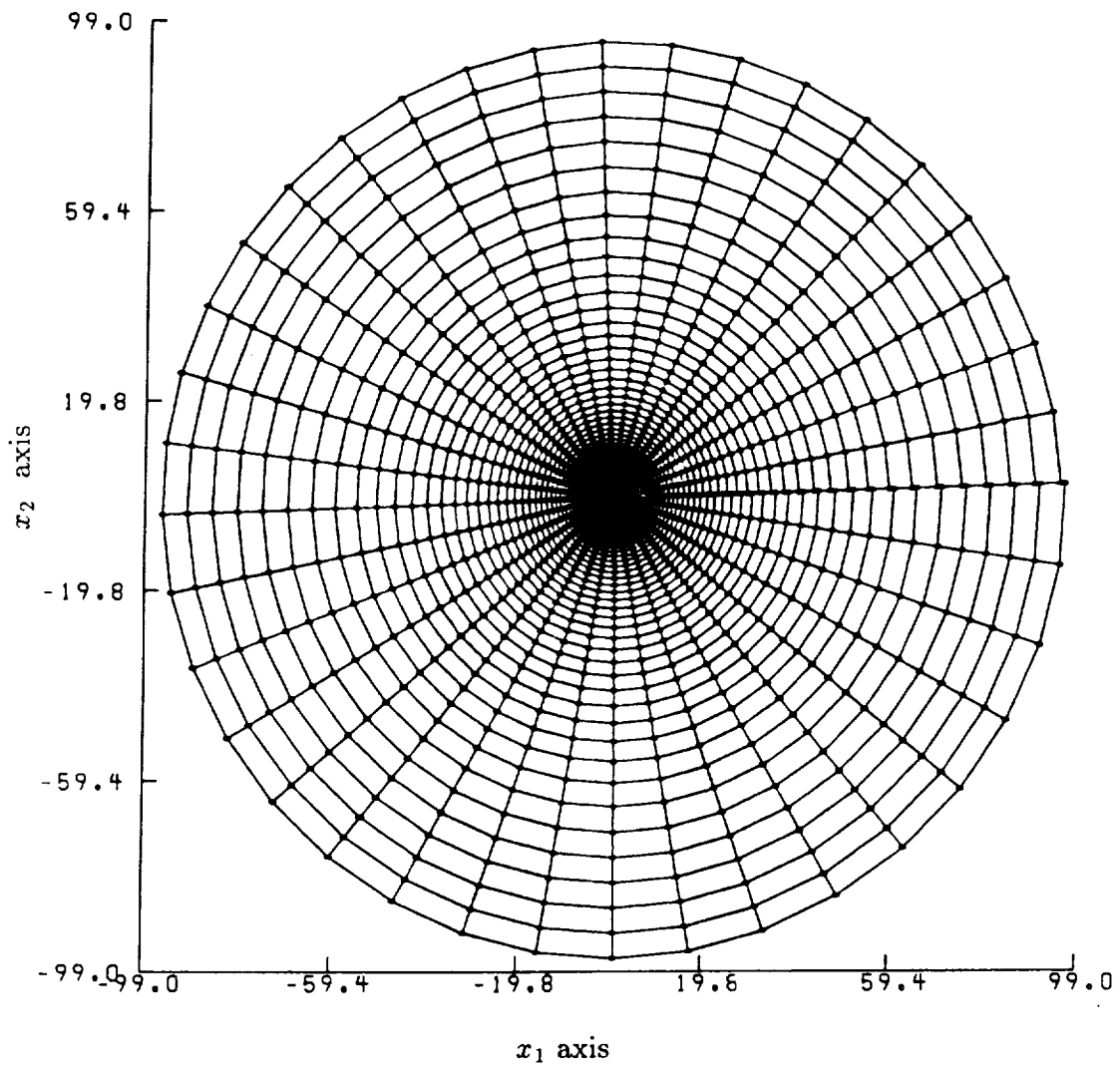
Figure 53.   Computational grid in the transformed plane for a 12 percent
thick Joukowski airfoil with $M_\infty = .1$, $\alpha = 2^o$, camber $= .05$,
and $k_1 = .1$.

122
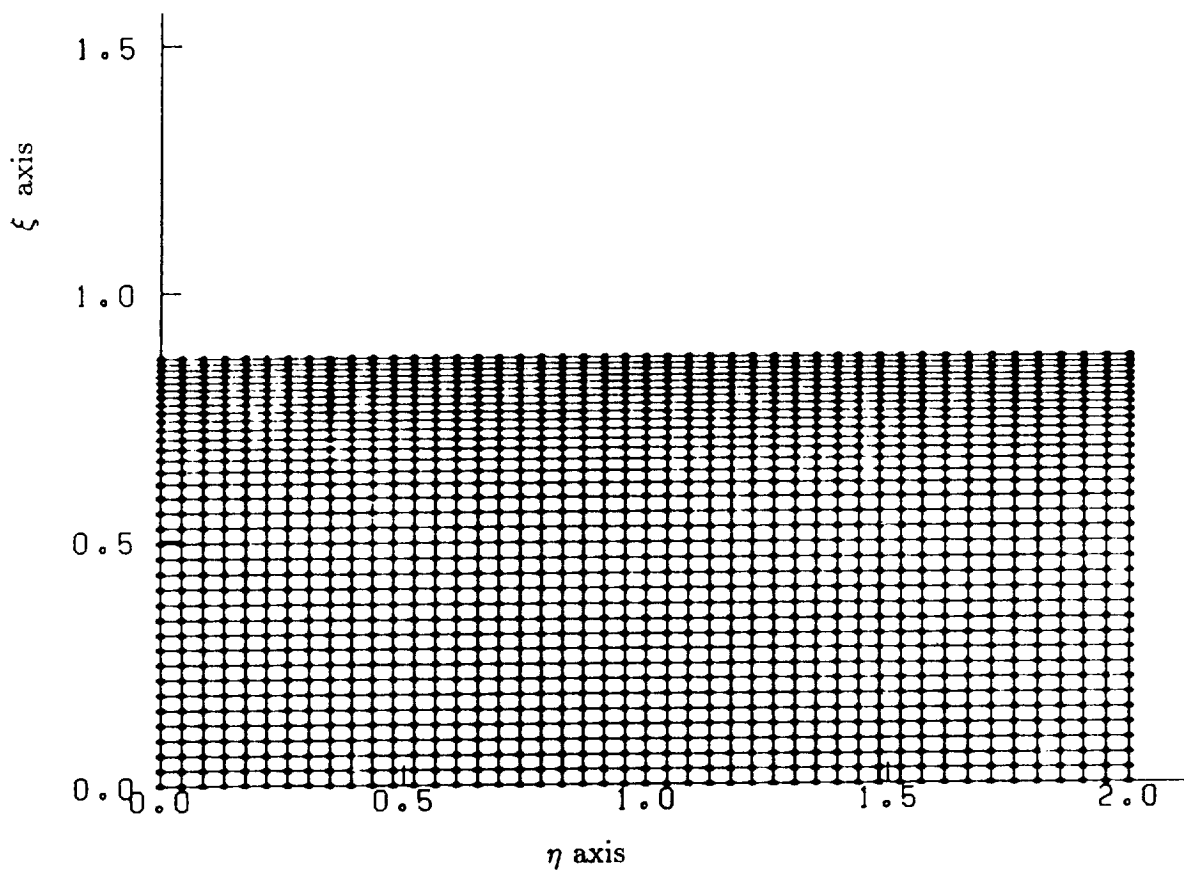
Figure 54. Computational grid in the transformed plane for a 12 percent thick Joukowski airfoil with $M_\infty = .5$, $\alpha = 2^o$, camber $= .05$, and $k_1 = 1.0$.

Figure 55.   Computational grid in the physical plane for a 12 percent
             thick Joukowski airfoil with $M_\infty = .5$, $\alpha = 2^o$, camber = .05,
             and $k_1 = 1.0$.

Figure 56.   Computational grid in the transformed plane for a 12 percent thick Joukowski airfoil with $M_\infty = .5$, $\alpha = 2^o$, camber $= .05$, and $k_1 = 3.0$.

Figure 57.   Computational grid in the physical plane for a 12 percent
thick Joukowski airfoil with $M_\infty = .5$, $\alpha = 2°$, camber = .05,
and $k_1 = 3.0$.
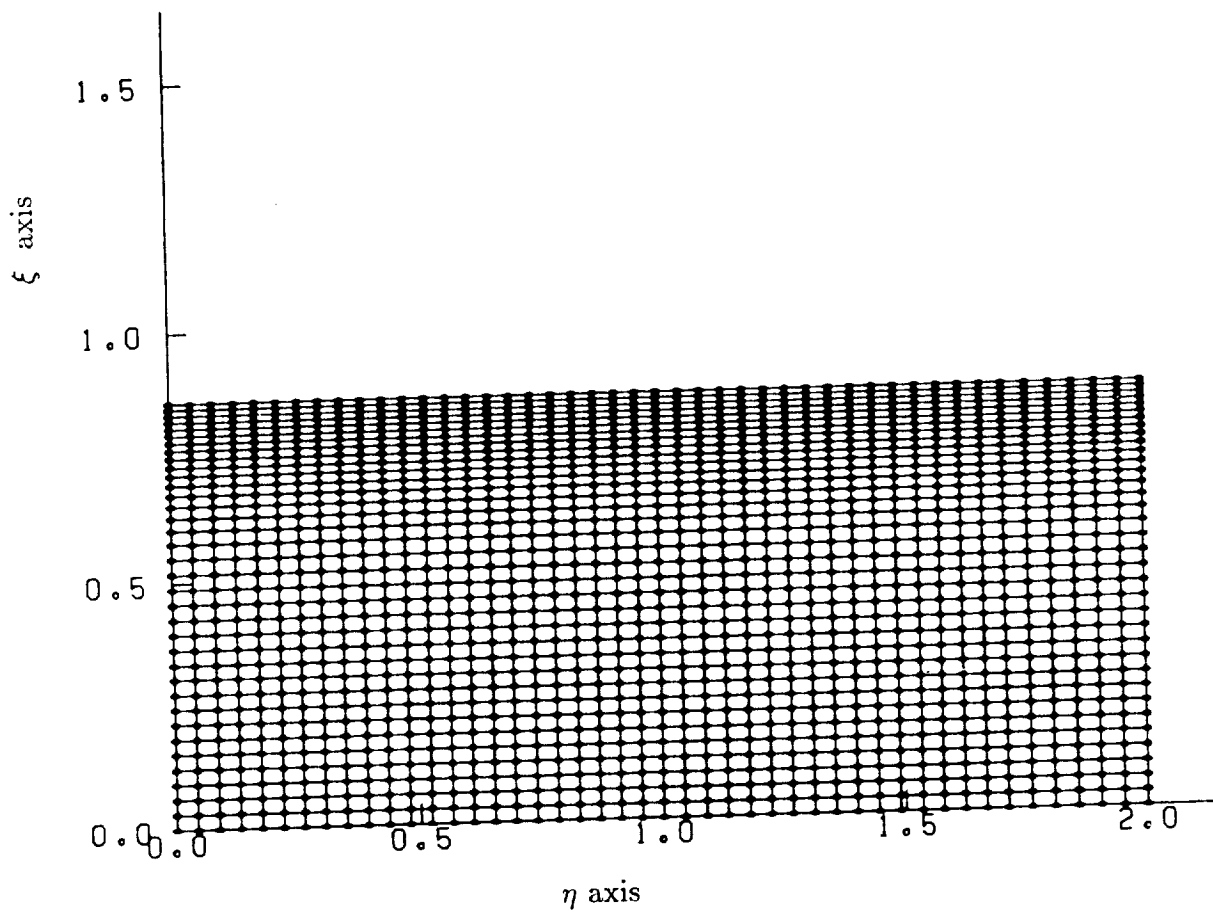
Figure 58. Computational grid in the transformed plane for a 12 percent thick Joukowski airfoil with $M_\infty = .6$, $\alpha = 3^o$, camber = 0, and $k_1 = 1.0$.
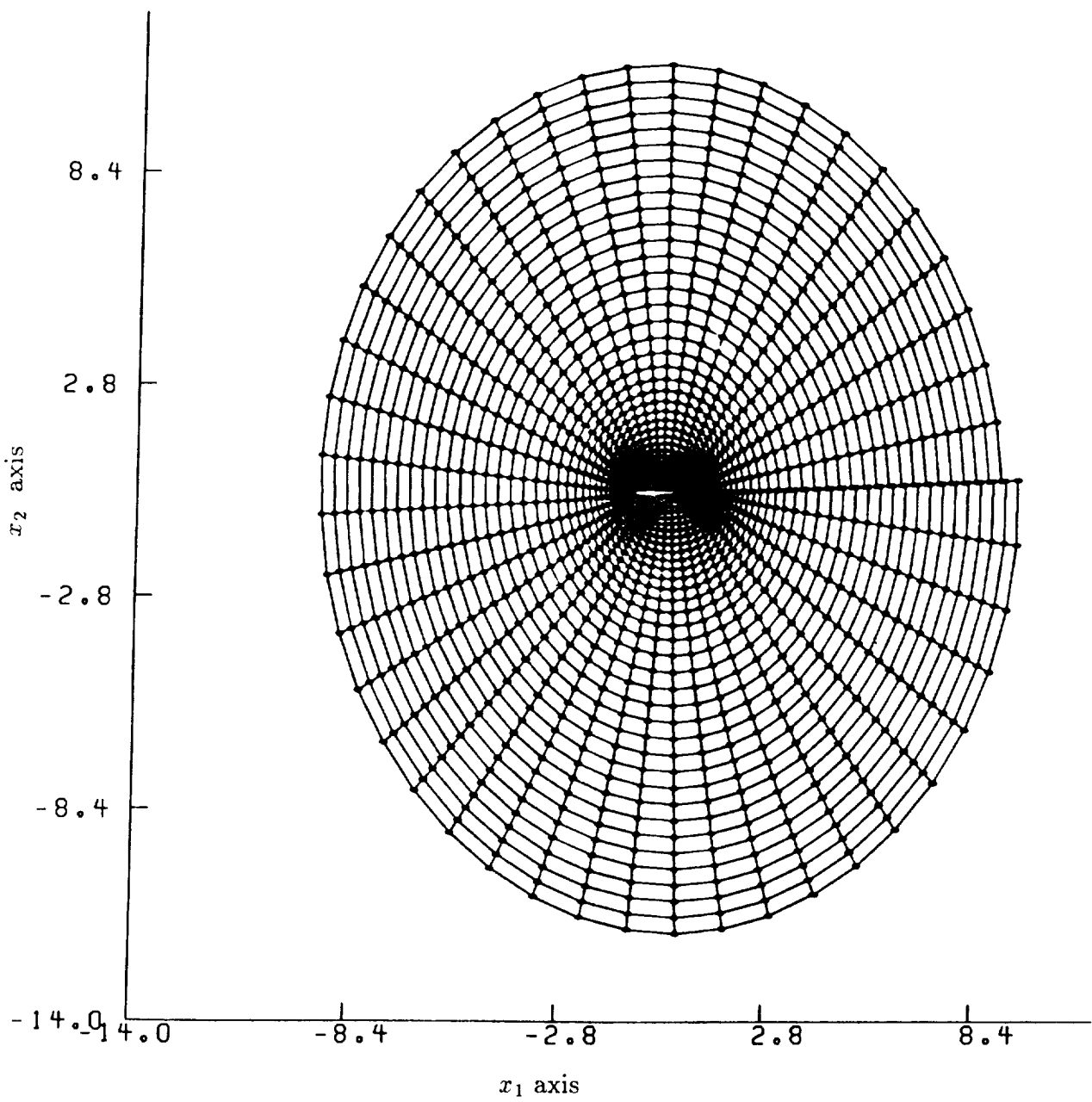
Figure 59.   Computational grid in the physical plane for a 12 percent
thick Joukowski airfoil with $M_\infty = .6$, $\alpha = 3^o$, camber $= 0$,
and $k_1 = 1.0$.
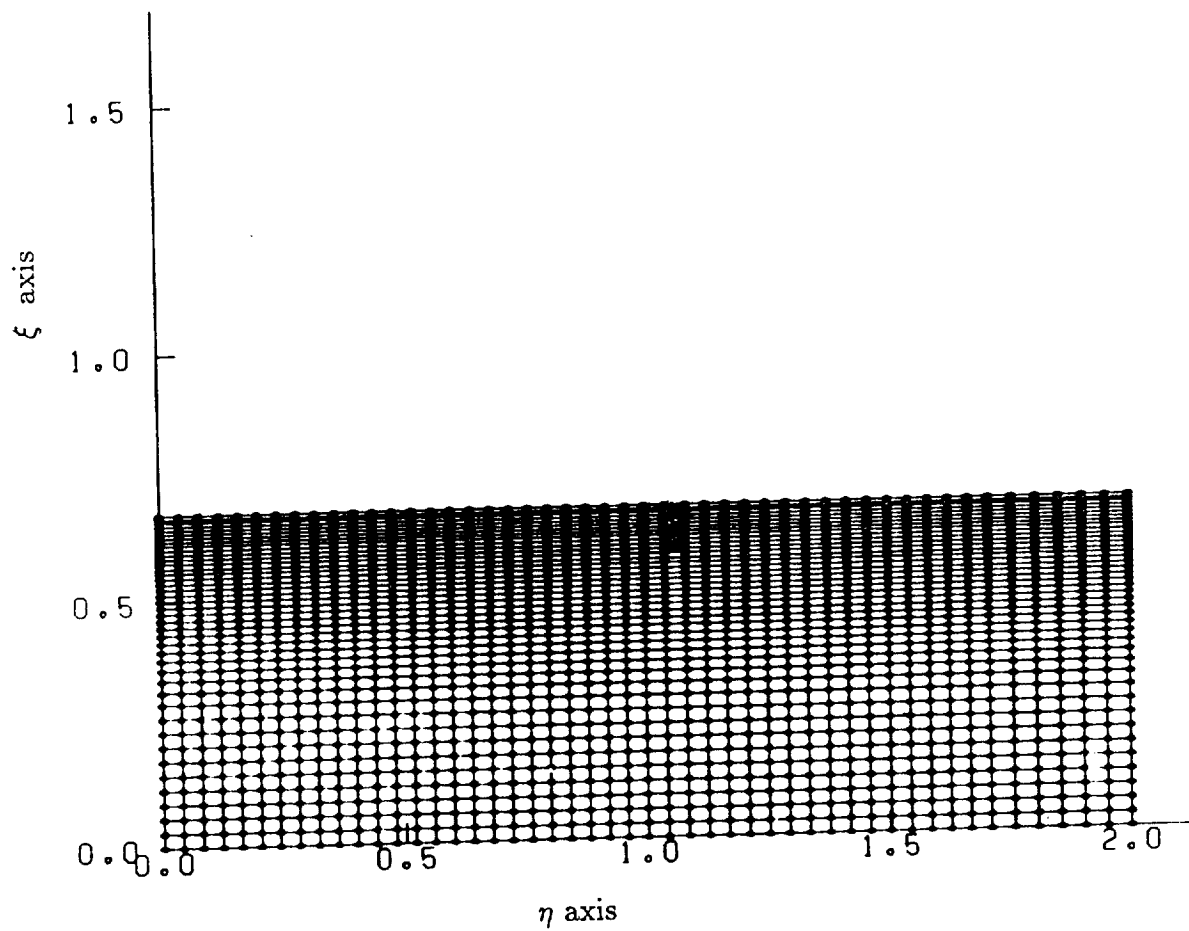
Figure 60.   Computational grid in the transformed plane for a 12 percent thick Joukowski airfoil with $M_\infty = .6$, $\alpha = 3°$, camber $= 0$, and $k_1 = 3.0$.
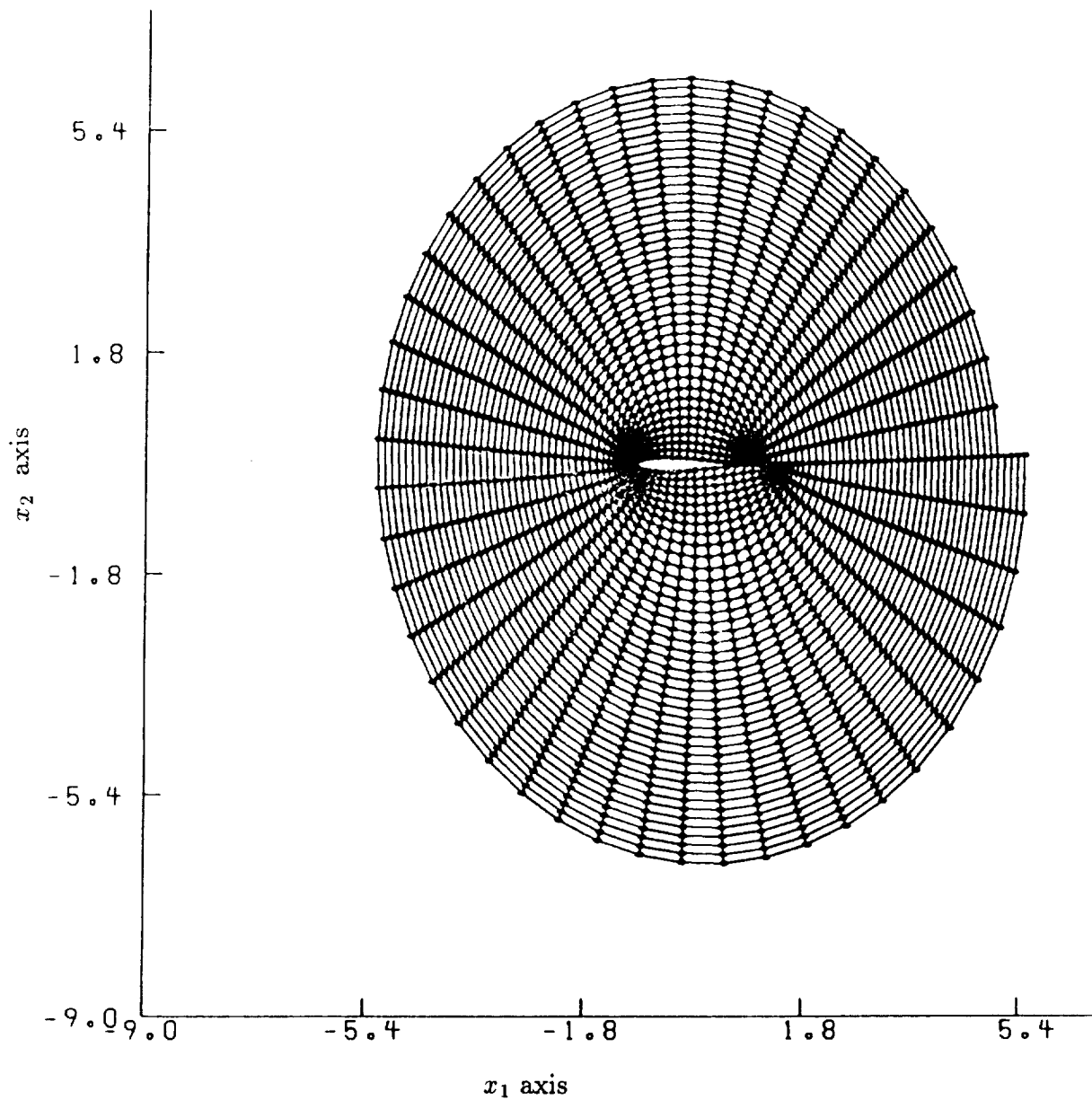
Figure 61.   Computational grid in the physical plane for a 12 percent
thick Joukowski airfoil with $M_\infty = .6$, $\alpha = 3°$, camber $= 0$,
and $k_1 = 3.0$.

130
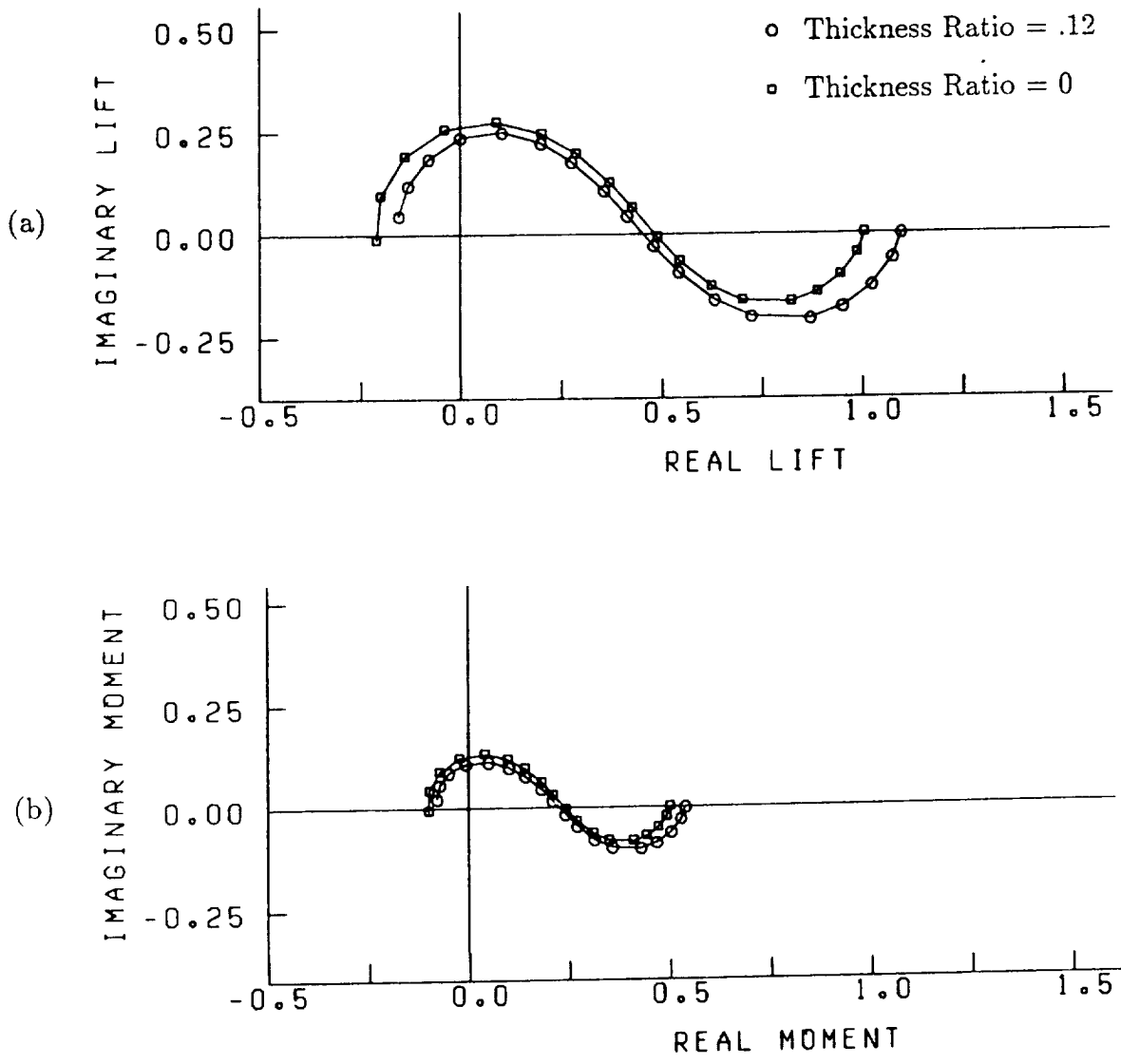
Figure 62. Effect of airfoil thickness on (a) the unsteady lift and (b) the unsteady moment of a Joukowski airfoil in a transverse gust. $M_\infty = .1$, $\alpha = 0^o$, camber $= 0$. $k_1 = 0.0$, 0.01, 0.03, 0.06, 0.1, 0.2, 0.3, 0.45, 0.6, 0.8, 1.0, 1.3, 1.6, 2.0, 2.5, 3.0, 3.5, 4.0.

131
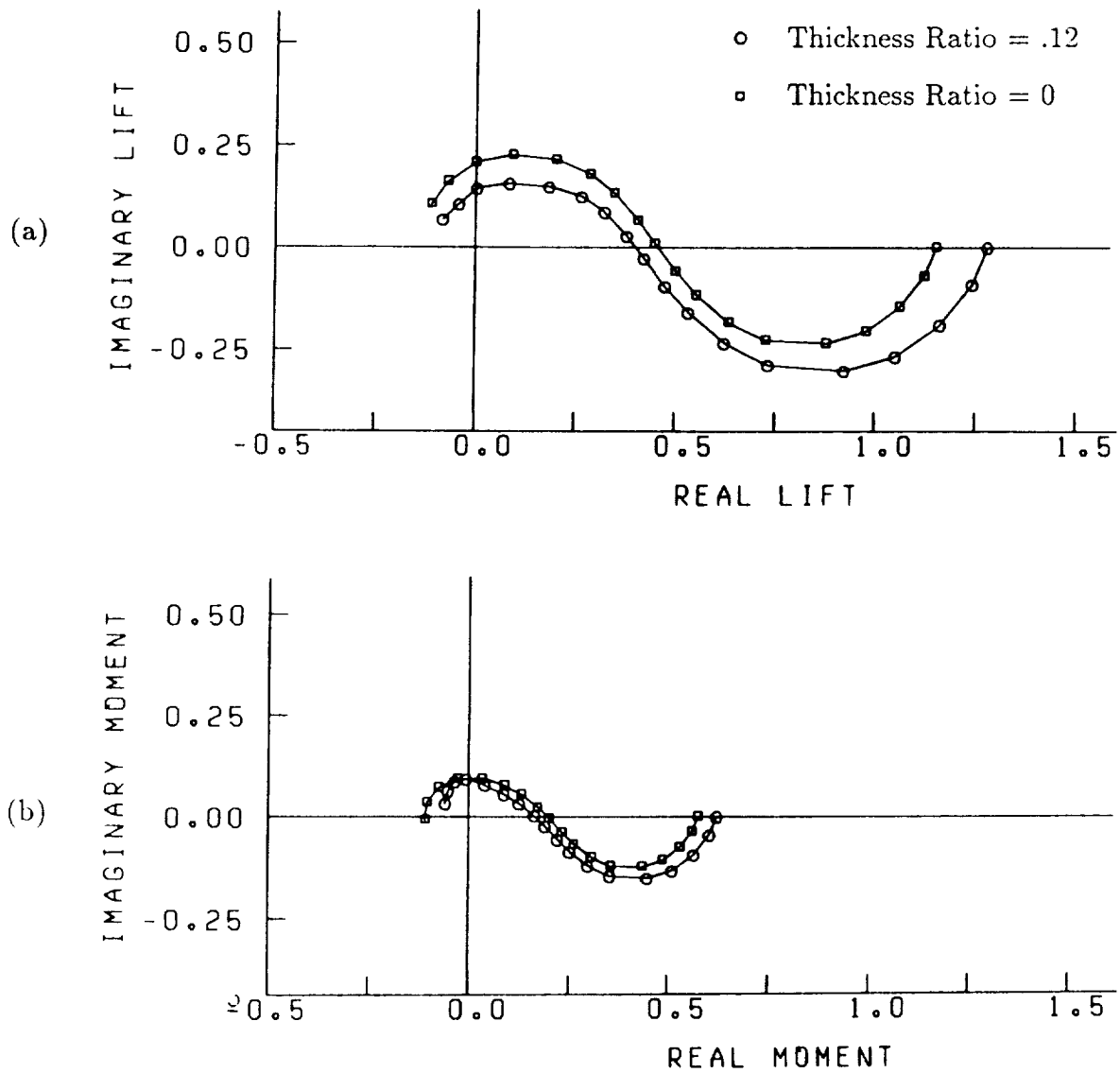
Figure 63. Effect of airfoil thickness on (a) the unsteady lift and (b) the unsteady moment of a Joukowski airfoil in a transverse gust. $M_\infty = .5$, $\alpha = 0°$, camber $= 0$. $k_1 = 0.0$, 0.01, 0.03, 0.06, 0.1, 0.2, 0.3, 0.45, 0.6, 0.8, 1.0, 1.3, 1.6, 2.0, 2.5, 3.0, 3.5, 4.0.

132
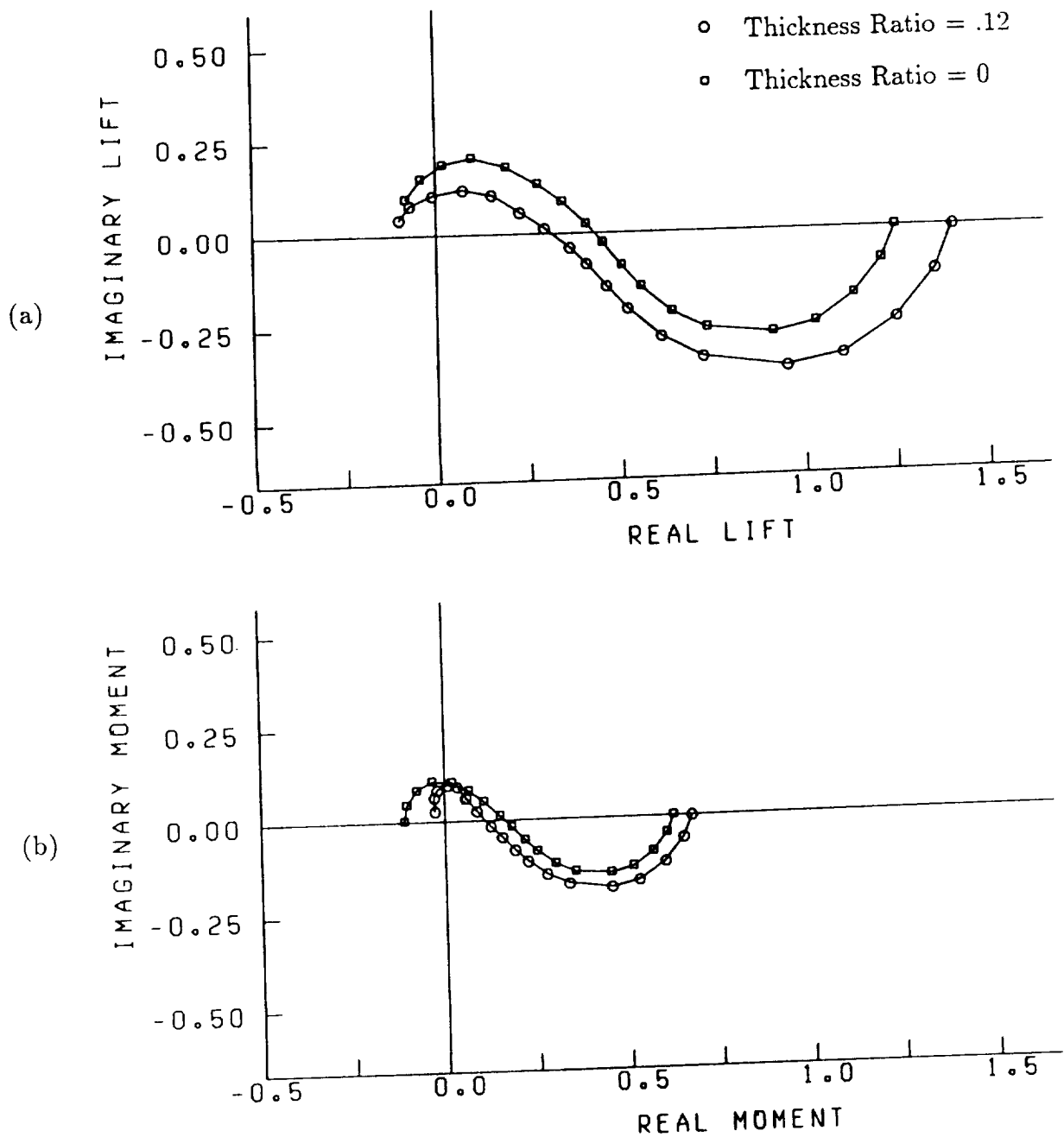
Figure 64.   Effect of airfoil thickness on (a) the unsteady lift and (b) the unsteady moment of a Joukowski airfoil in a transverse gust. $M_\infty = .6$, $\alpha = 0^o$, camber = 0. $k_1 = 0.0$, 0.01, 0.03, 0.06, 0.1, 0.2, 0.3, 0.45, 0.6, 0.8, 1.0, 1.3, 1.6, 2.0, 2.5, 3.0, 3.5, 4.0.
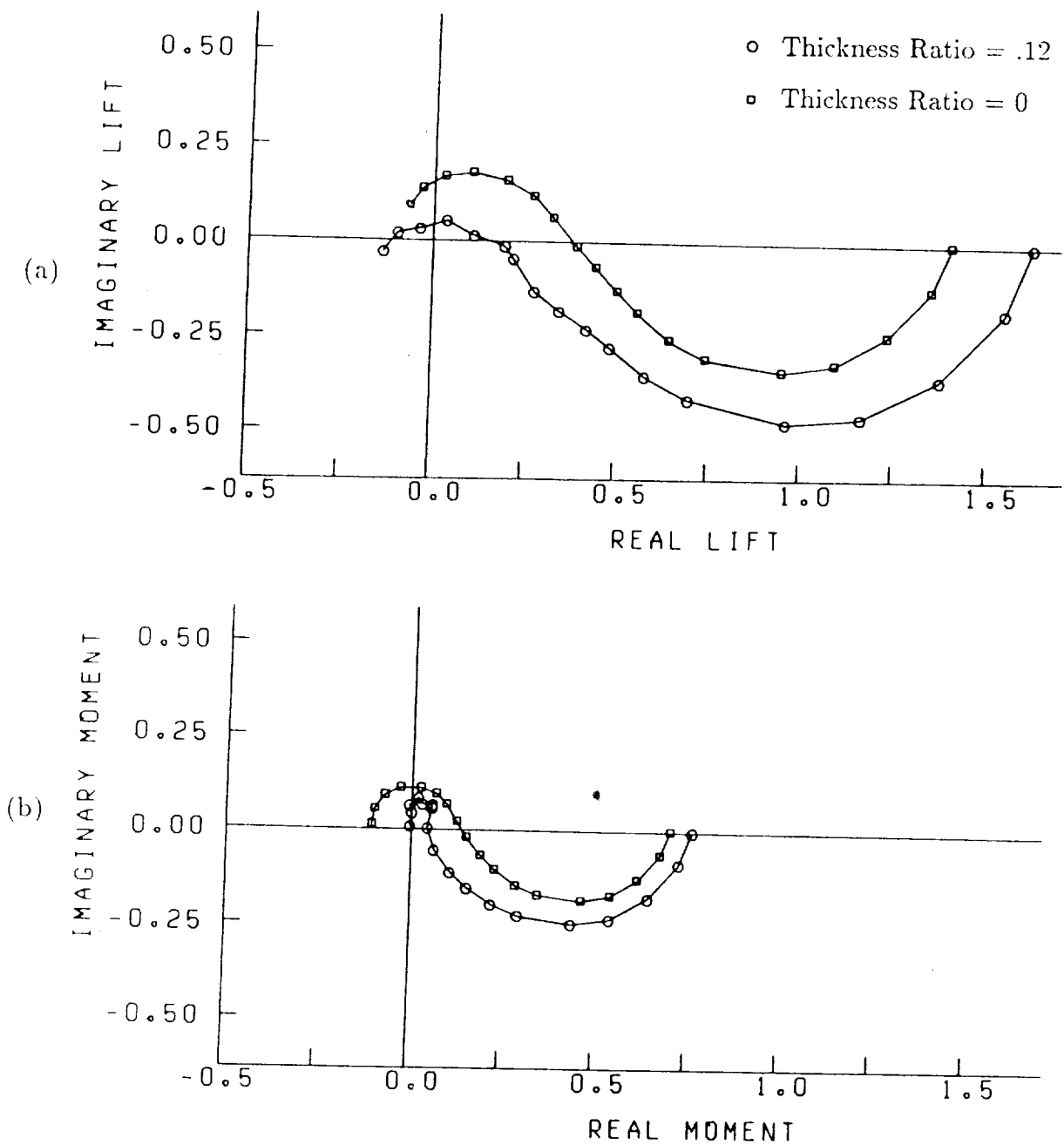
Figure 65.   Effect of airfoil thickness on (a) the unsteady lift and (b) the
unsteady moment of a Joukowski airfoil in a transverse gust.
$M_\infty = .7$, $\alpha = 0°$, camber = 0. $k_1 = 0.0, 0.01, 0.03, 0.06,$
0.1, 0.2, 0.3, 0.45, 0.6, 0.8, 1.0, 1.3, 1.6, 2.0, 2.5, 3.0, 3.5, 4.0.
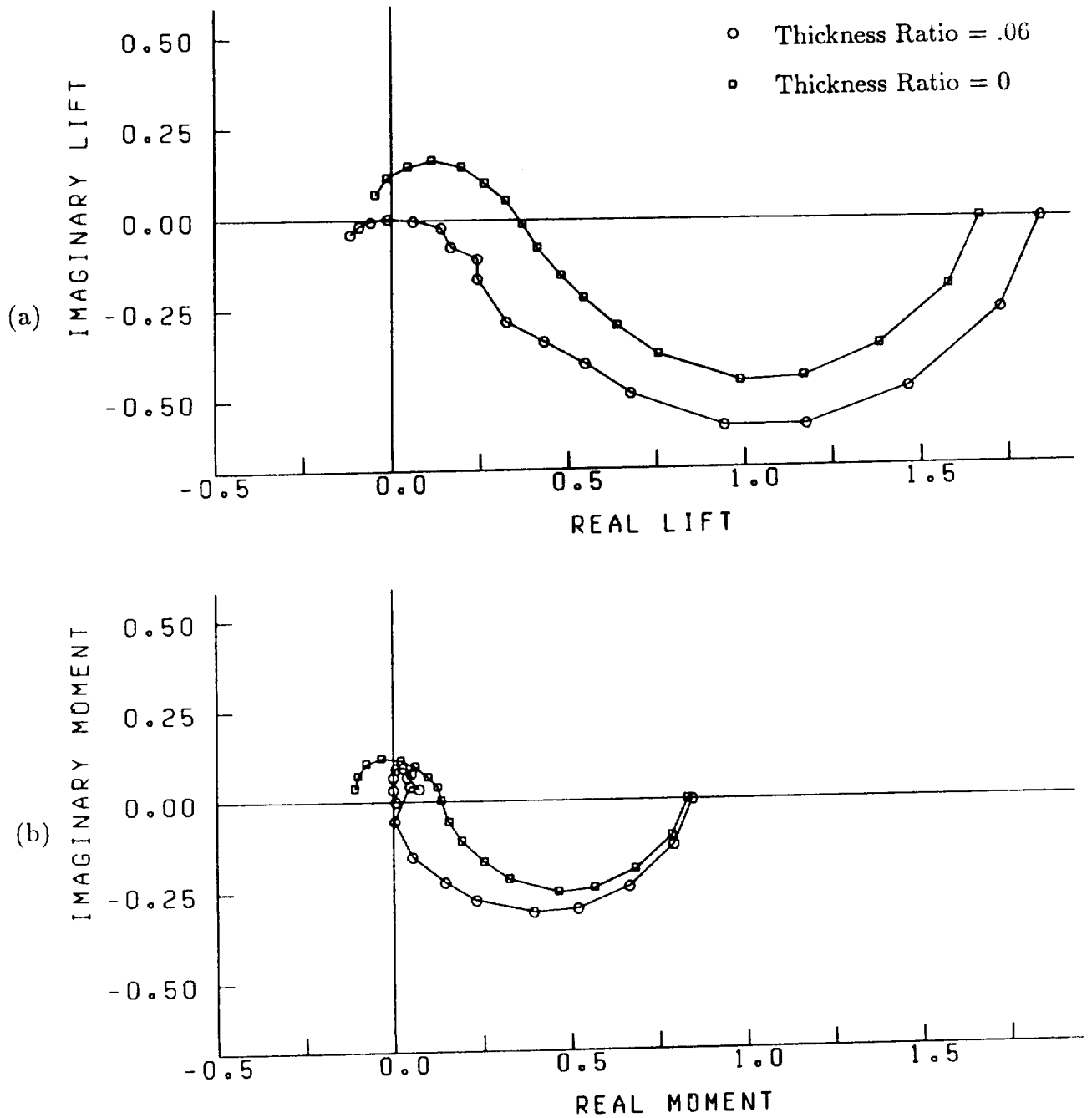
Figure 66. Effect of airfoil thickness on (a) the unsteady lift and (b) the unsteady moment of a Joukowski airfoil in a transverse gust. $M_\infty = .8$, $\alpha = 0°$, camber = 0. $k_1 = 0.0, 0.01, 0.03, 0.06,$ 0.1, 0.2, 0.3, 0.45, 0.6, 0.8, 1.0, 1.3, 1.6, 2.0, 2.5, 3.0, 3.5, 4.0.

135
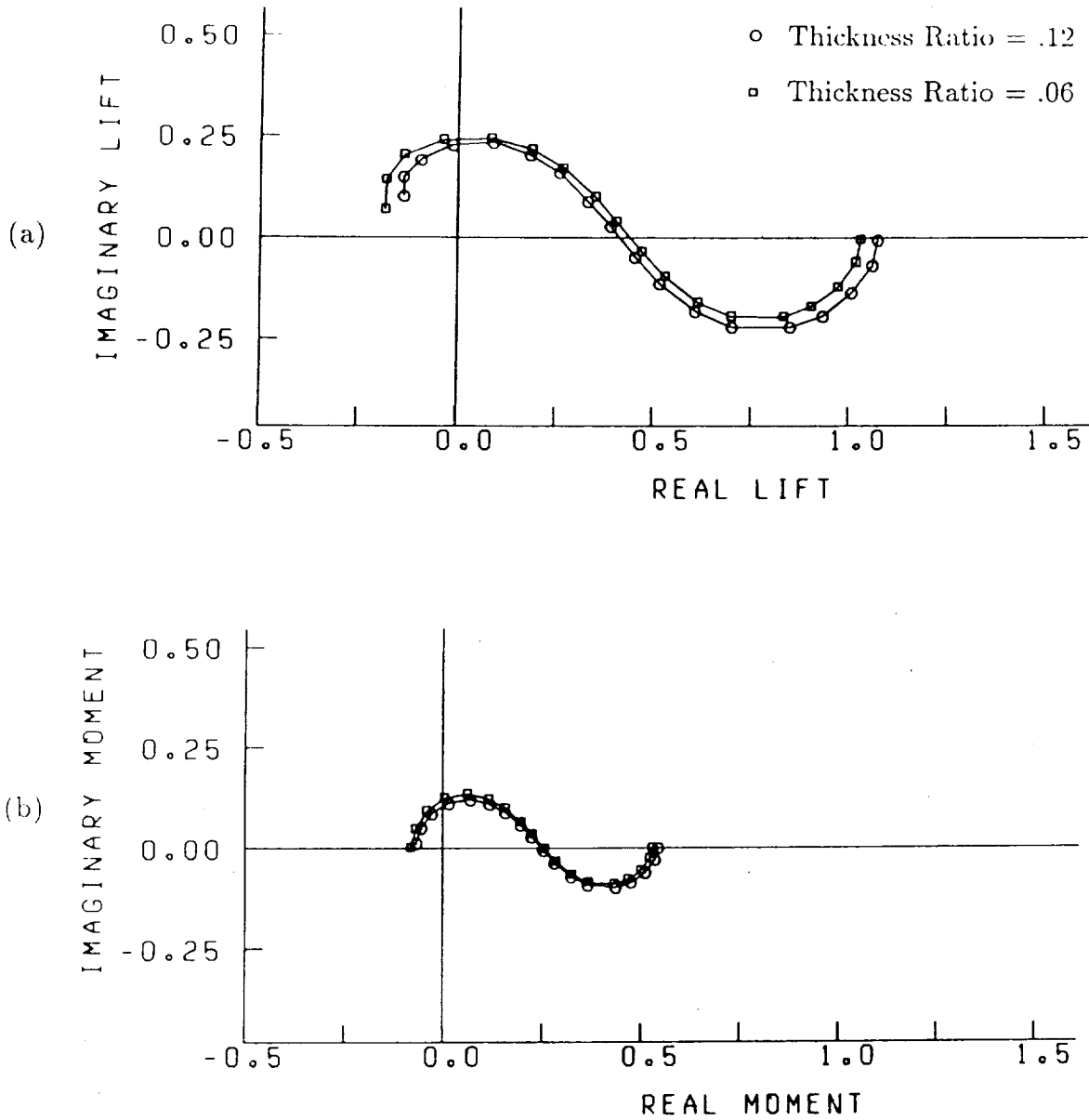
Figure 67. Effect of airfoil thickness on (a) the unsteady lift and (b) the unsteady moment of a Joukowski airfoil in a transverse gust. $M_\infty = .1$, $\alpha = 2^\circ$, camber $= .05$. $k_1 = 0.0, 0.01, 0.03, 0.06,$ 0.1, 0.2, 0.3, 0.45, 0.6, 0.8, 1.0, 1.3, 1.6, 2.0, 2.5, 3.0, 3.5, 4.0.
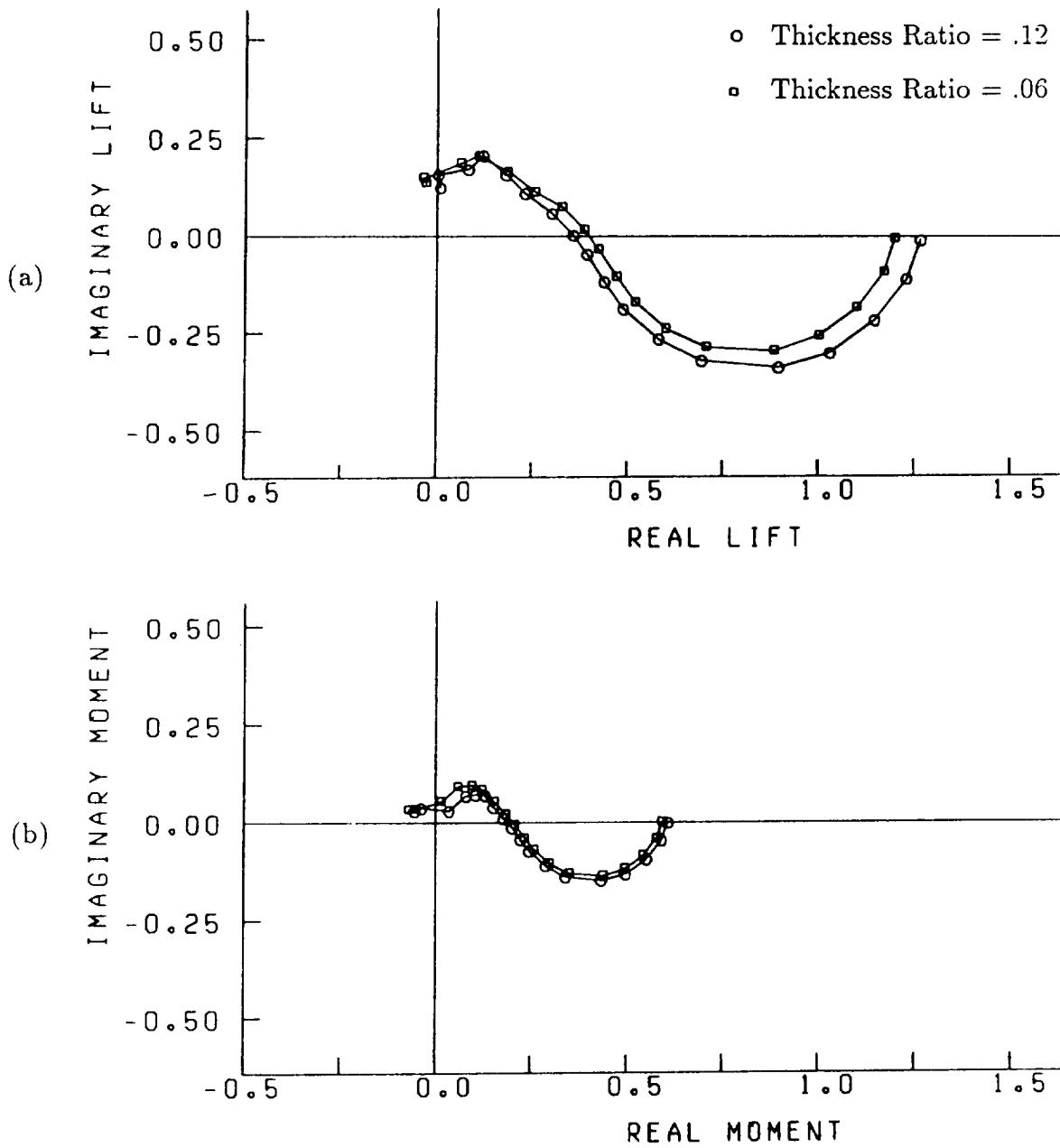
Figure 68. Effect of airfoil thickness on (a) the unsteady lift and (b) the unsteady moment of a Joukowski airfoil in a transverse gust. $M_\infty = .5$, $\alpha = 2^o$, camber $= .05$. $k_1 = 0.0, 0.01, 0.03, 0.06, 0.1, 0.2, 0.3, 0.45, 0.6, 0.8, 1.0, 1.3, 1.6, 2.0, 2.5, 3.0, 3.5, 4.0$.
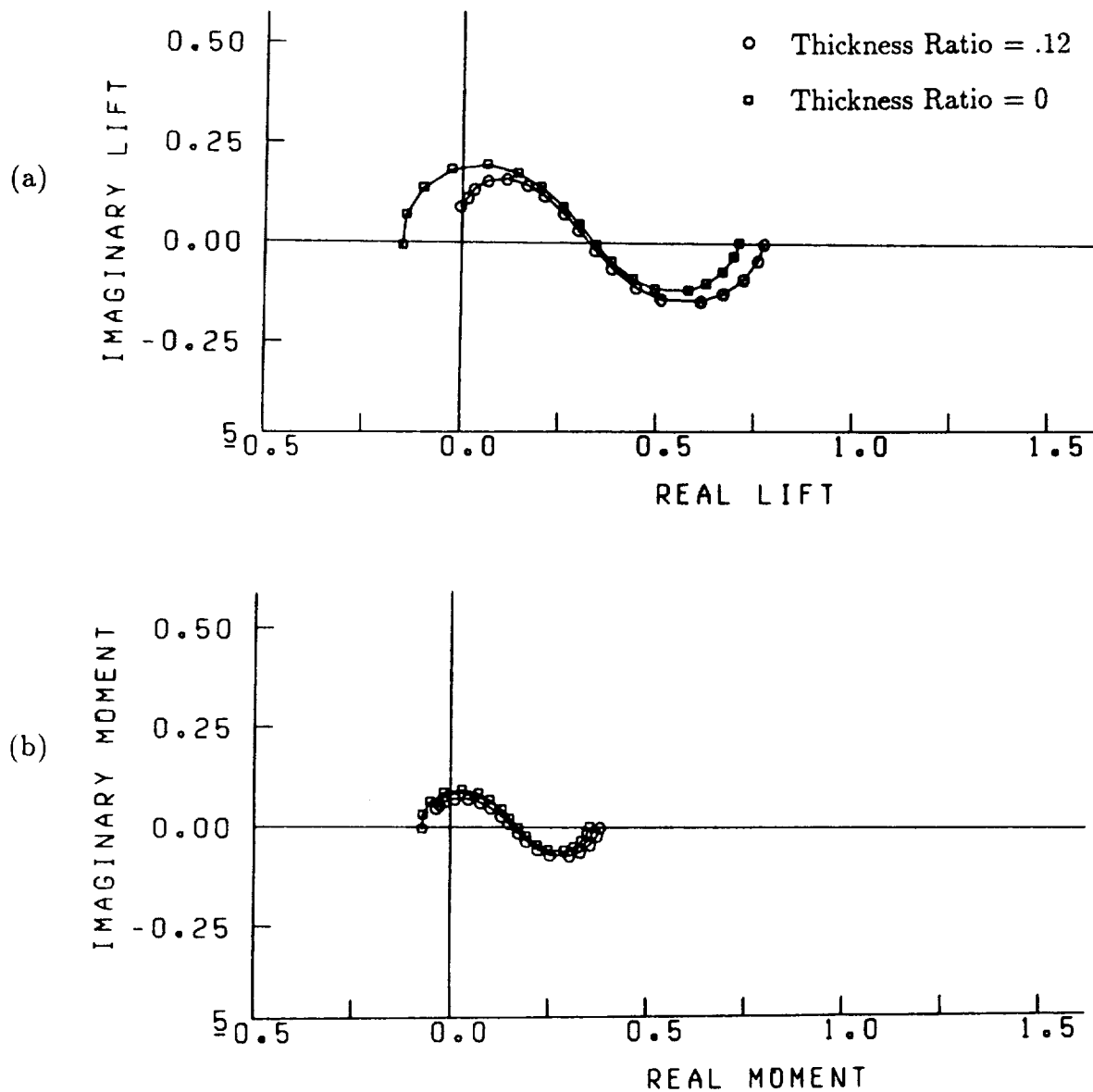
Figure 69. Effect of airfoil thickness on (a) the unsteady lift and (b) the
unsteady moment of a Joukowski airfoil in a transverse and
longitudinal gust. $M_\infty = .1$, $\alpha = 0°$, camber $= 0$. $k_1 = 0.0$,
0.01, 0.03, 0.06, 0.1, 0.2, 0.3, 0.45, 0.6, 0.8, 1.0, 1.3, 1.6, 2.0,
2.5, 3.0, 3.5, 4.0. $-a_1 = a_2 = .7071$, $k_1 = k_2$, $a_3 = k_3 = 0$.
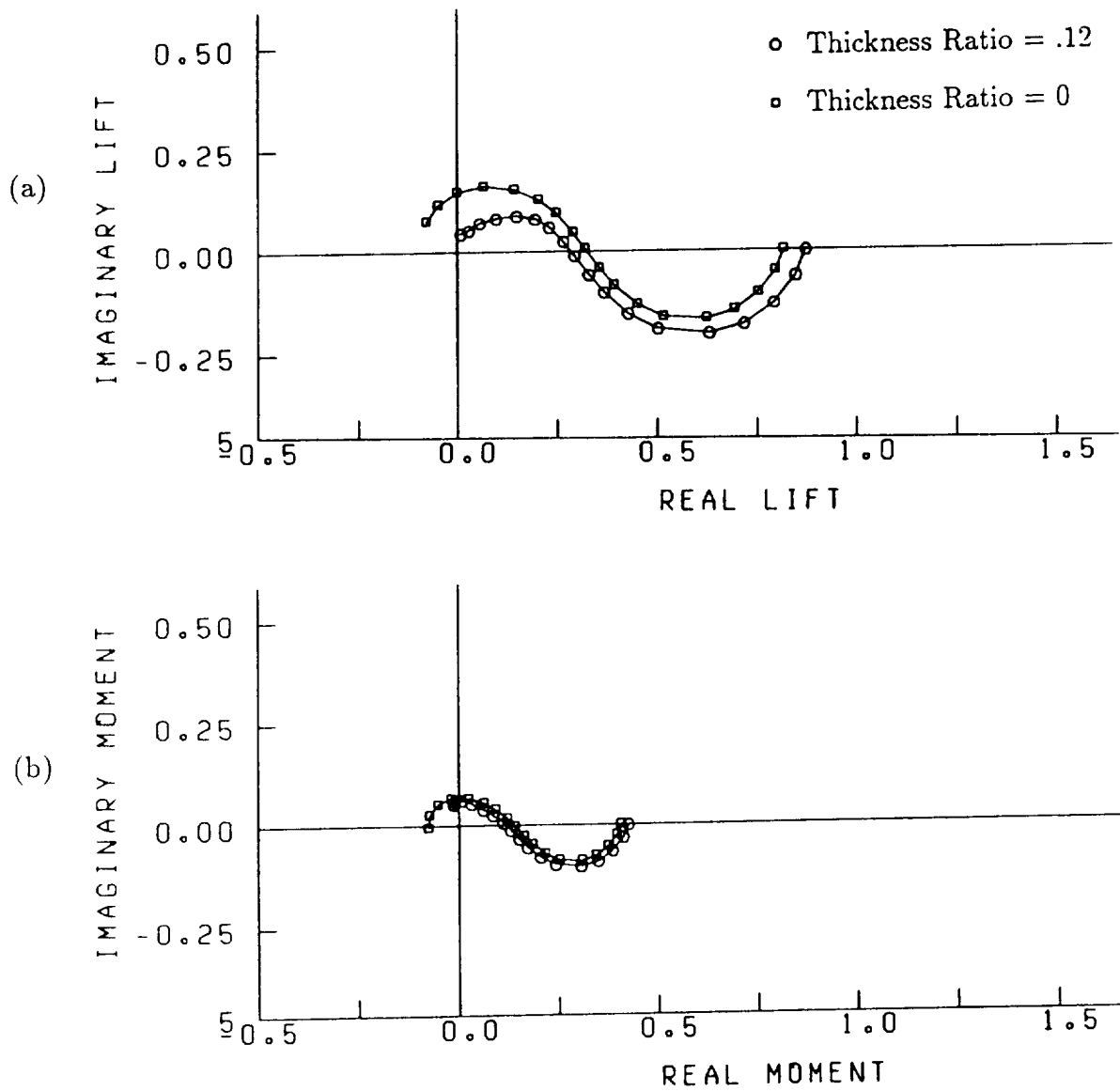
Figure 70. Effect of airfoil thickness on (a) the unsteady lift and (b) the unsteady moment of a Joukowski airfoil in a transverse and longitudinal gust. $M_\infty = .5$, $\alpha = 0°$, camber $= 0$. $k_1 = 0.0$, 0.01, 0.03, 0.06, 0.1, 0.2, 0.3, 0.45, 0.6, 0.8, 1.0, 1.3, 1.6, 2.0, 2.5, 3.0, 3.5, 4.0. $-a_1 = a_2 = .7071$, $k_1 = k_2$, $a_3 = k_3 = 0$.
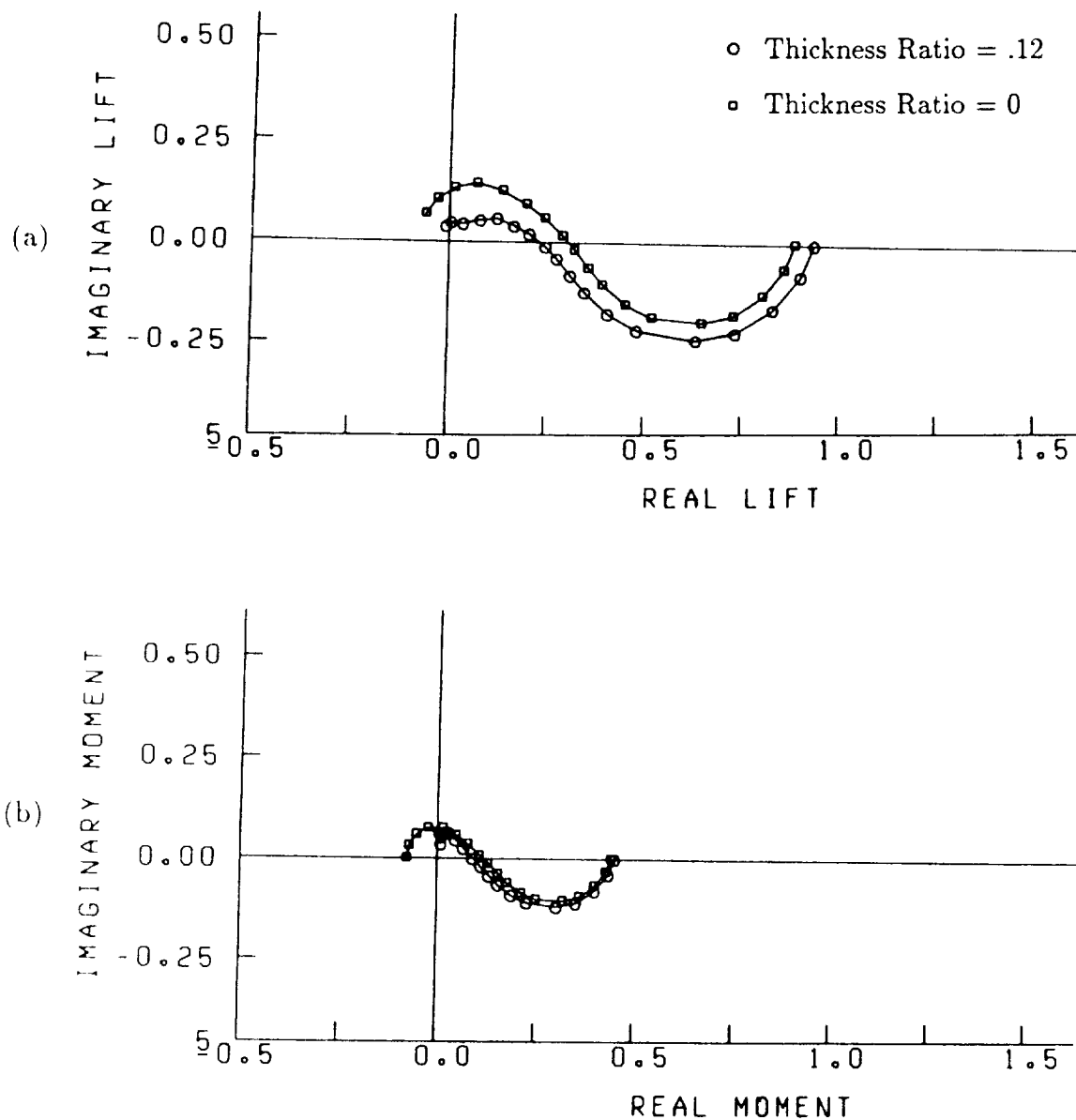
Figure 71.   Effect of airfoil thickness on (a) the unsteady lift and (b) the unsteady moment of a Joukowski airfoil in a transverse and longitudinal gust. $M_\infty = .6$, $\alpha = 0^\circ$, camber $= 0$. $k_1 = 0.0$, 0.01, 0.03, 0.06, 0.1, 0.2, 0.3, 0.45, 0.6, 0.8, 1.0, 1.3, 1.6, 2.0, 2.5, 3.0, 3.5, 4.0. $-a_1 = a_2 = .7071$, $k_1 = k_2$, $a_3 = k_3 = 0$.
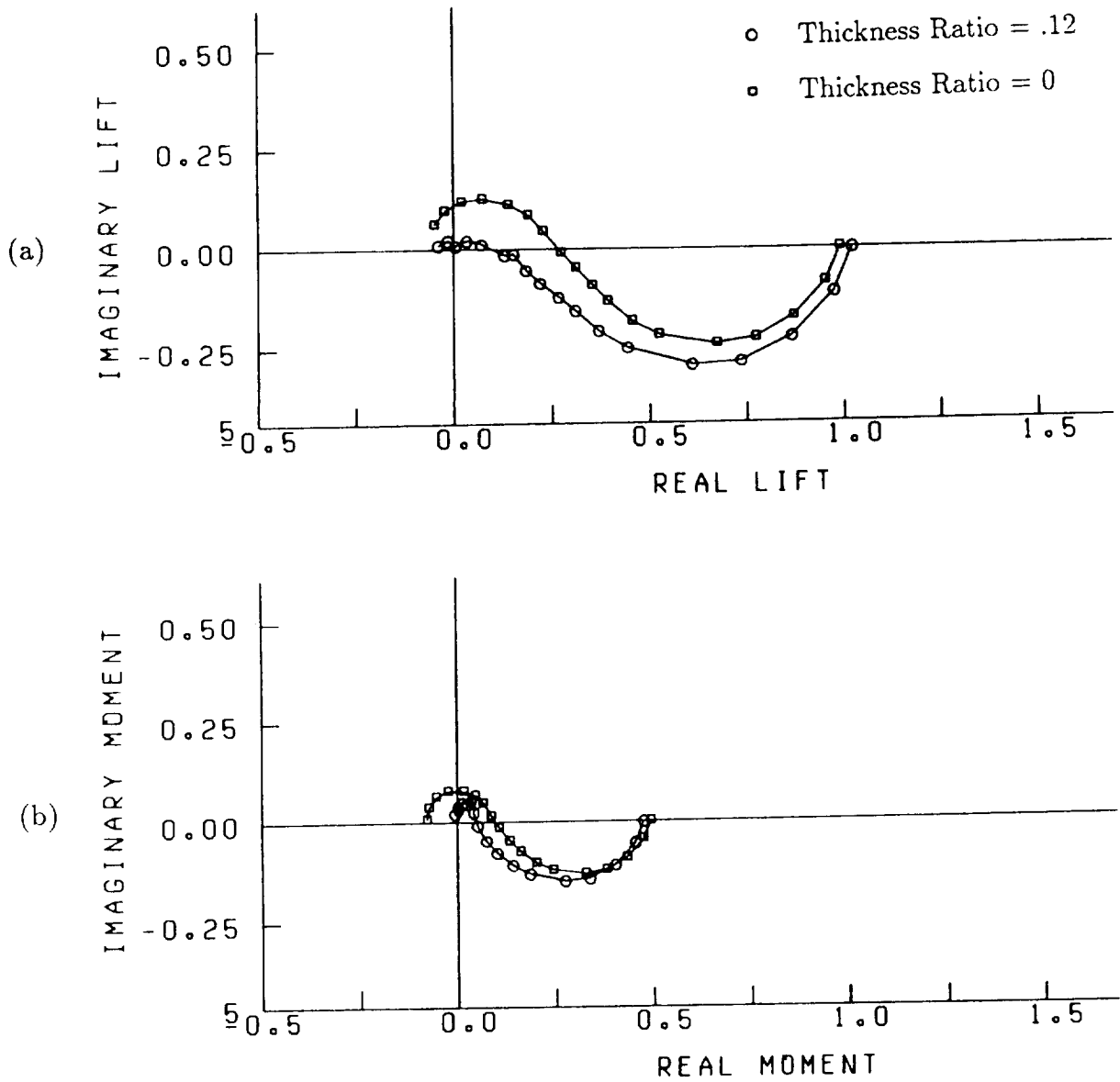
Figure 72. Effect of airfoil thickness on (a) the unsteady lift and (b) the unsteady moment of a Joukowski airfoil in a transverse and longitudinal gust. $M_\infty = .7$, $\alpha = 0^o$, camber = 0. $k_1 = 0.0$, 0.01, 0.03, 0.06, 0.1, 0.2, 0.3, 0.45, 0.6, 0.8, 1.0, 1.3, 1.6, 2.0, 2.5, 3.0, 3.5, 4.0. $-a_1 = a_2 = .7071$, $k_1 = k_2$, $a_3 = k_3 = 0$.

141

Figure 73. Effect of airfoil thickness on (a) the unsteady lift and (b) the
unsteady moment of a Joukowski airfoil in a transverse and
longitudinal gust. $M_\infty = .8$, $\alpha = 0^o$, camber $= 0$. $k_1 = 0.0$,
0.01, 0.03, 0.06, 0.1, 0.2, 0.3, 0.45, 0.6, 0.8, 1.0, 1.3, 1.6, 2.0,
2.5, 3.0, 3.5, 4.0. $-a_1 = a_2 = .7071$, $k_1 = k_2$, $a_3 = k_3 = 0$.

Figure 74.   Effect of airfoil thickness on (a) the unsteady lift and (b) the
unsteady moment of a Joukowski airfoil in a transverse and
longitudinal gust. $M_\infty = .1$, $\alpha = 2^o$, camber $= .05$. $k_1 = 0.0$,
0.01, 0.03, 0.06, 0.1, 0.2, 0.3, 0.45, 0.6, 0.8, 1.0, 1.3, 1.6, 2.0,
2.5, 3.0, 3.5, 4.0. $-a_1 = a_2 = .7071$, $k_1 = k_2$, $a_3 = k_3 = 0$.
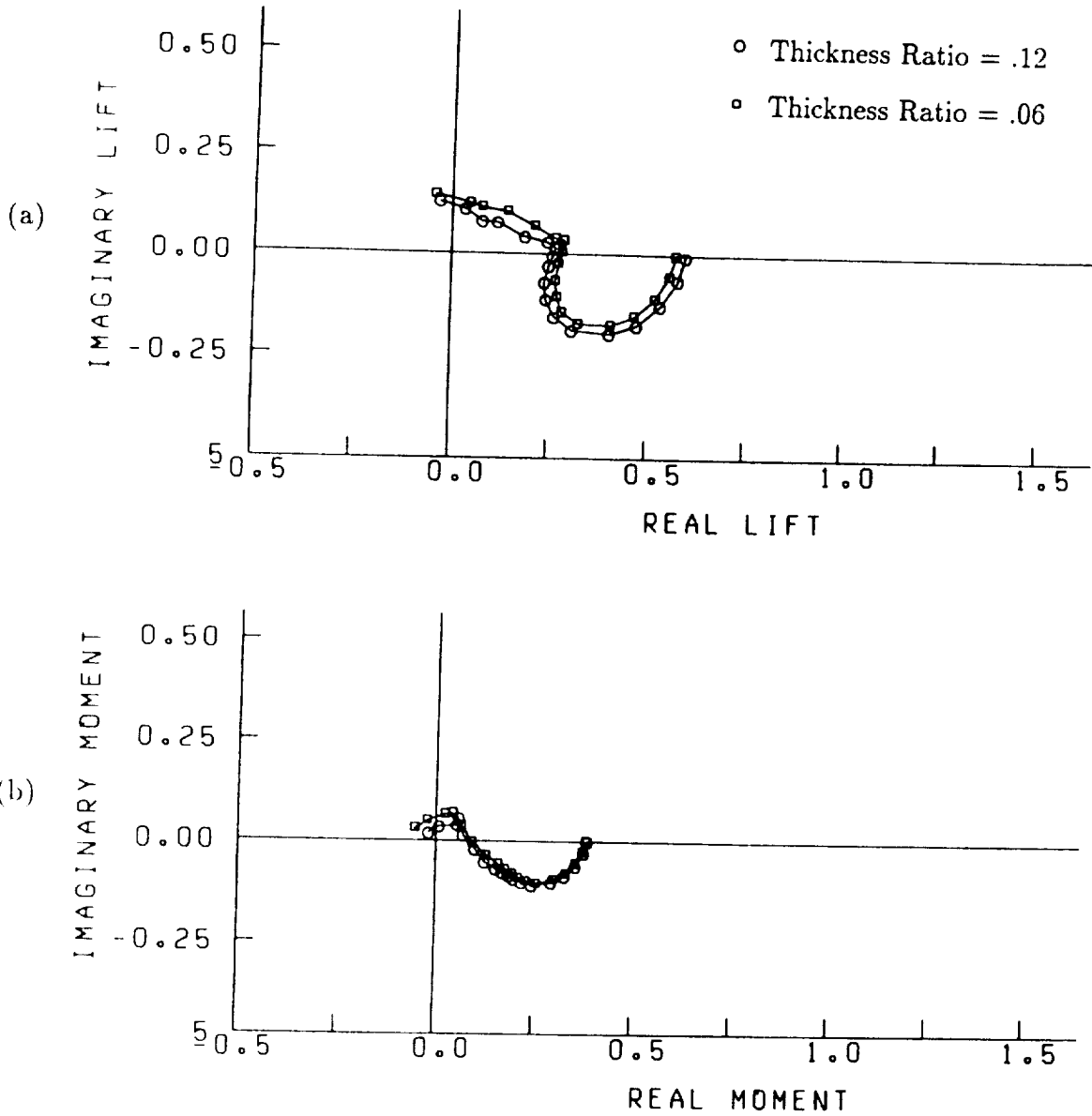
Figure 75.   Effect of airfoil thickness on (a) the unsteady lift and (b) the
unsteady moment of a Joukowski airfoil in a transverse and
longitudinal gust. $M_\infty = .5$, $\alpha = 2^o$, camber $= .05$. $k_1 = 0.0$,
0.01, 0.03, 0.06, 0.1, 0.2, 0.3, 0.45, 0.6, 0.8, 1.0, 1.3, 1.6, 2.0,
2.5, 3.0, 3.5, 4.0. $-a_1 = a_2 = .7071$, $k_1 = k_2$, $a_3 = k_3 = 0$.
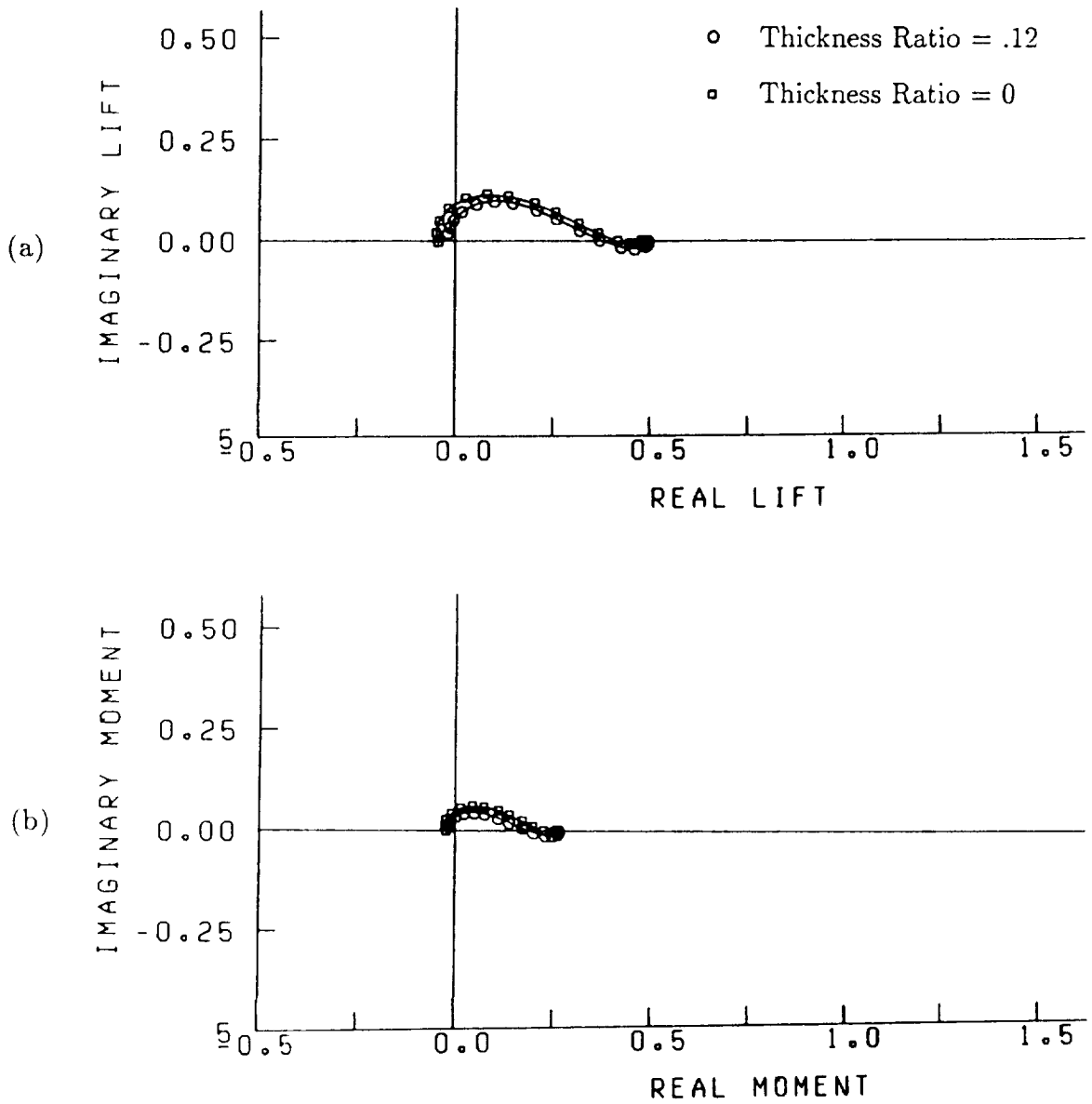
Figure 76. Effect of airfoil thickness on (a) the unsteady lift and (b) the unsteady moment of a Joukowski airfoil in a three-dimensional gust. $M_\infty = .1$, $\alpha = 0^o$, camber $= 0$. $k_1 = 0.0$, 0.01, 0.03, 0.06, 0.1, 0.2, 0.3, 0.45, 0.6, 0.8, 1.0, 1.3, 1.6, 2.0, 2.5, 3.0, 3.5, 4.0. $k_3 = 0.4$, $|\vec{a}| = 1$, $\frac{a_2}{a_1} = -\frac{7}{4}$, $k_1 = k_2$, $\vec{a} \cdot \vec{k} = 0$, $a_2 > 0$.

Figure 77. Effect of airfoil thickness on (a) the unsteady lift and (b) the unsteady moment of a Joukowski airfoil in a three-dimensional gust. $M_\infty = .5$, $\alpha = 0^o$, camber = 0. $k_1 = 0.0$, 0.01, 0.03, 0.06, 0.1, 0.2, 0.3, 0.45, 0.6, 0.8, 1.0, 1.3, 1.6, 2.0, 2.5, 3.0, 3.5, 4.0. $k_3 = 0.4$, $|\vec{a}| = 1$, $\frac{a_2}{a_1} = -\frac{7}{4}$, $k_1 = k_2$, $\vec{a} \cdot \vec{k} = 0$, $a_2 > 0$.
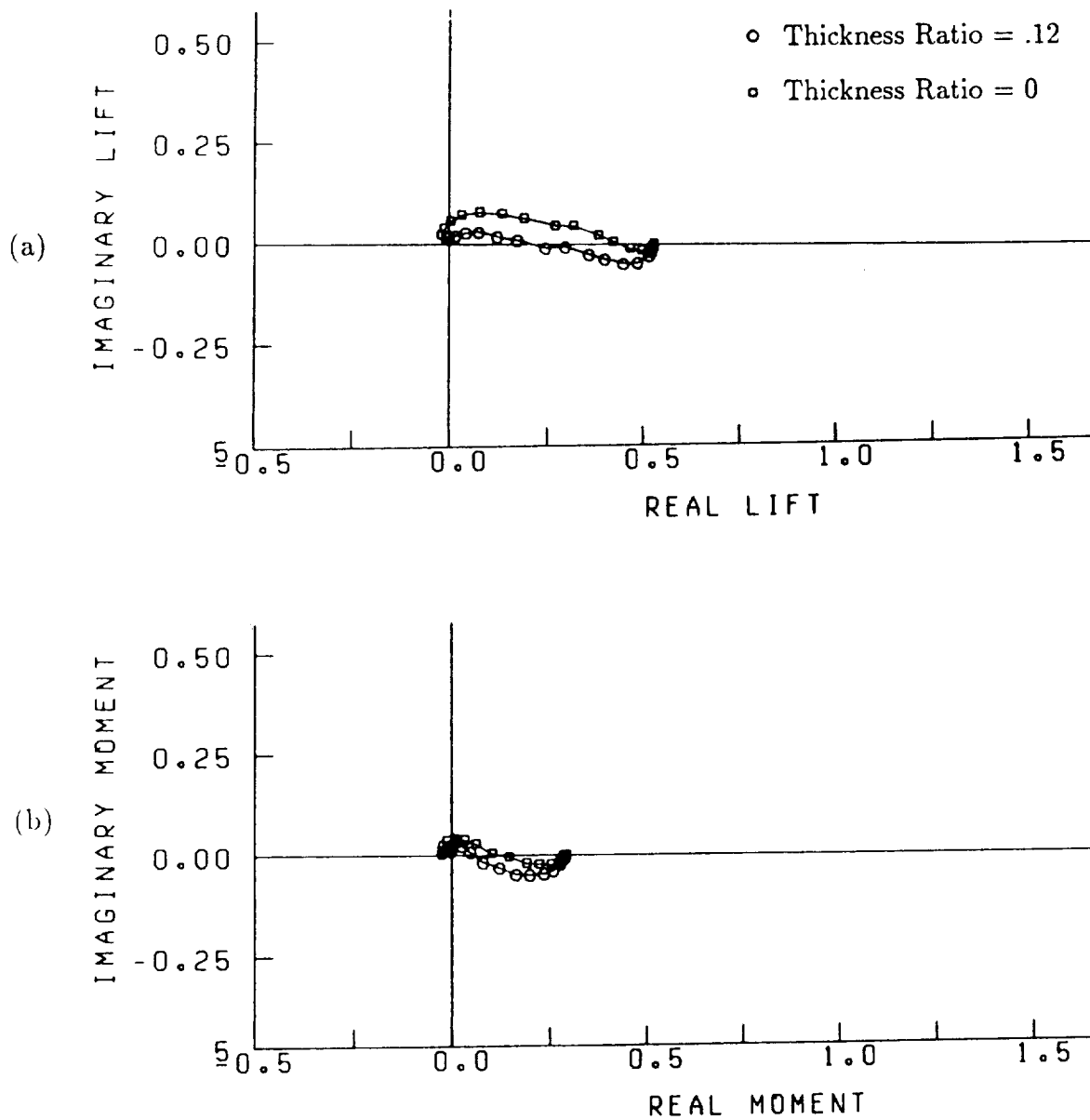
Figure 78. Effect of airfoil thickness on (a) the unsteady lift and (b) the unsteady moment of a Joukowski airfoil in a three-dimensional gust. $M_\infty = .6$, $\alpha = 0°$, camber = 0. $k_1 = 0.0$, 0.01, 0.03, 0.06, 0.1, 0.2, 0.3, 0.45, 0.6, 0.8, 1.0, 1.3, 1.6, 2.0, 2.5, 3.0, 3.5, 4.0. $k_3 = 0.4$, $|\vec{a}| = 1$, $\frac{a_2}{a_1} = -\frac{7}{4}$, $k_1 = k_2$, $\vec{a} \cdot \vec{k} = 0$, $a_2 > 0$.
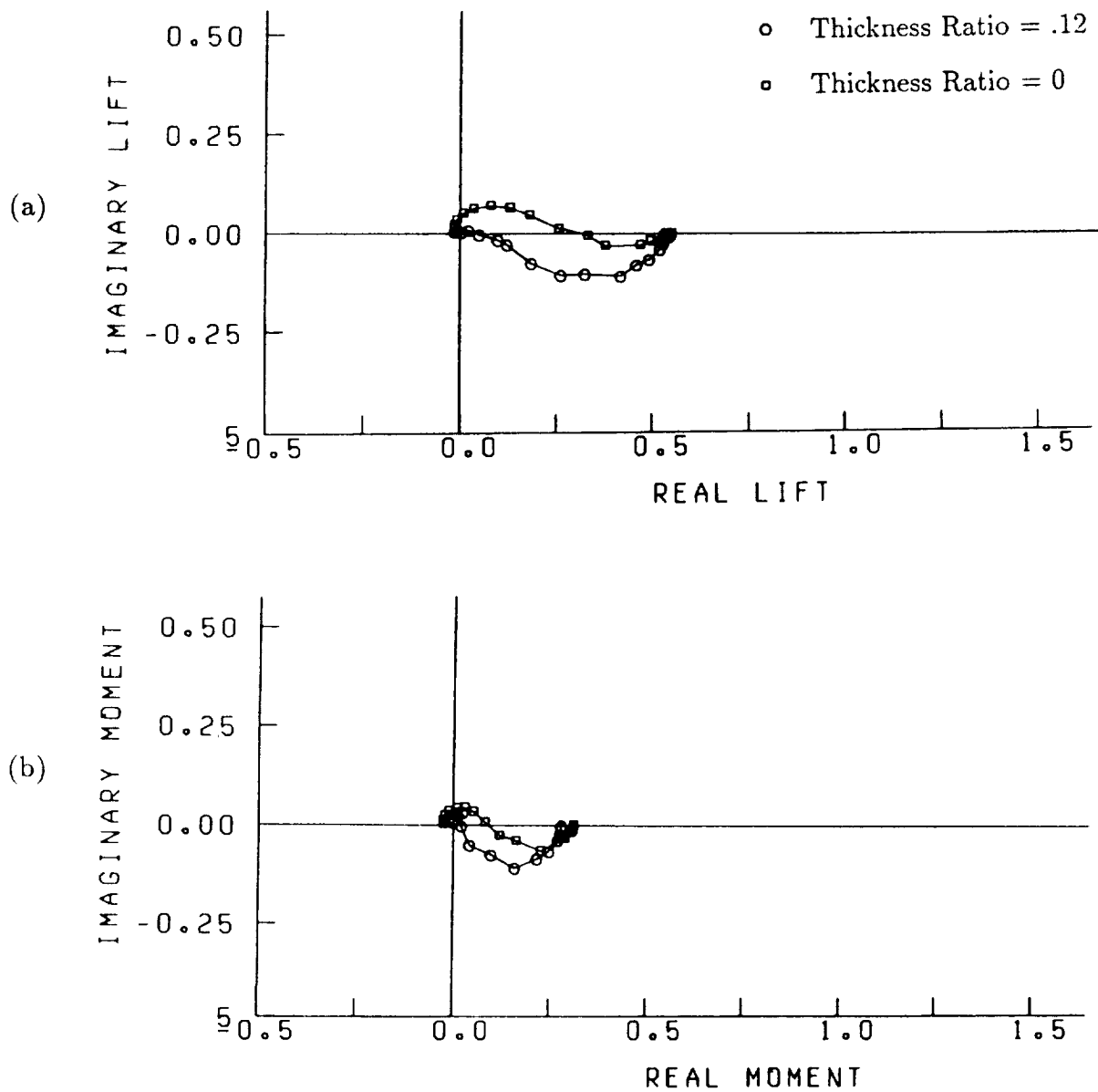
Figure 79. Effect of airfoil thickness on (a) the unsteady lift and (b) the unsteady moment of a Joukowski airfoil in a three-dimensional gust. $M_\infty = .7$, $\alpha = 0^o$, camber $= 0$. $k_1 = 0.0$, $0.01, 0.03, 0.06, 0.1, 0.2, 0.3, 0.45, 0.6, 0.8, 1.0, 1.3, 1.6, 2.0$, $2.5, 3.0, 3.5, 4.0$. $k_3 = 0.4$, $|\vec{a}| = 1$, $\frac{a_2}{a_1} = -\frac{7}{4}$, $k_1 = k_2$, $\vec{a} \cdot \vec{k} = 0$, $a_2 > 0$.
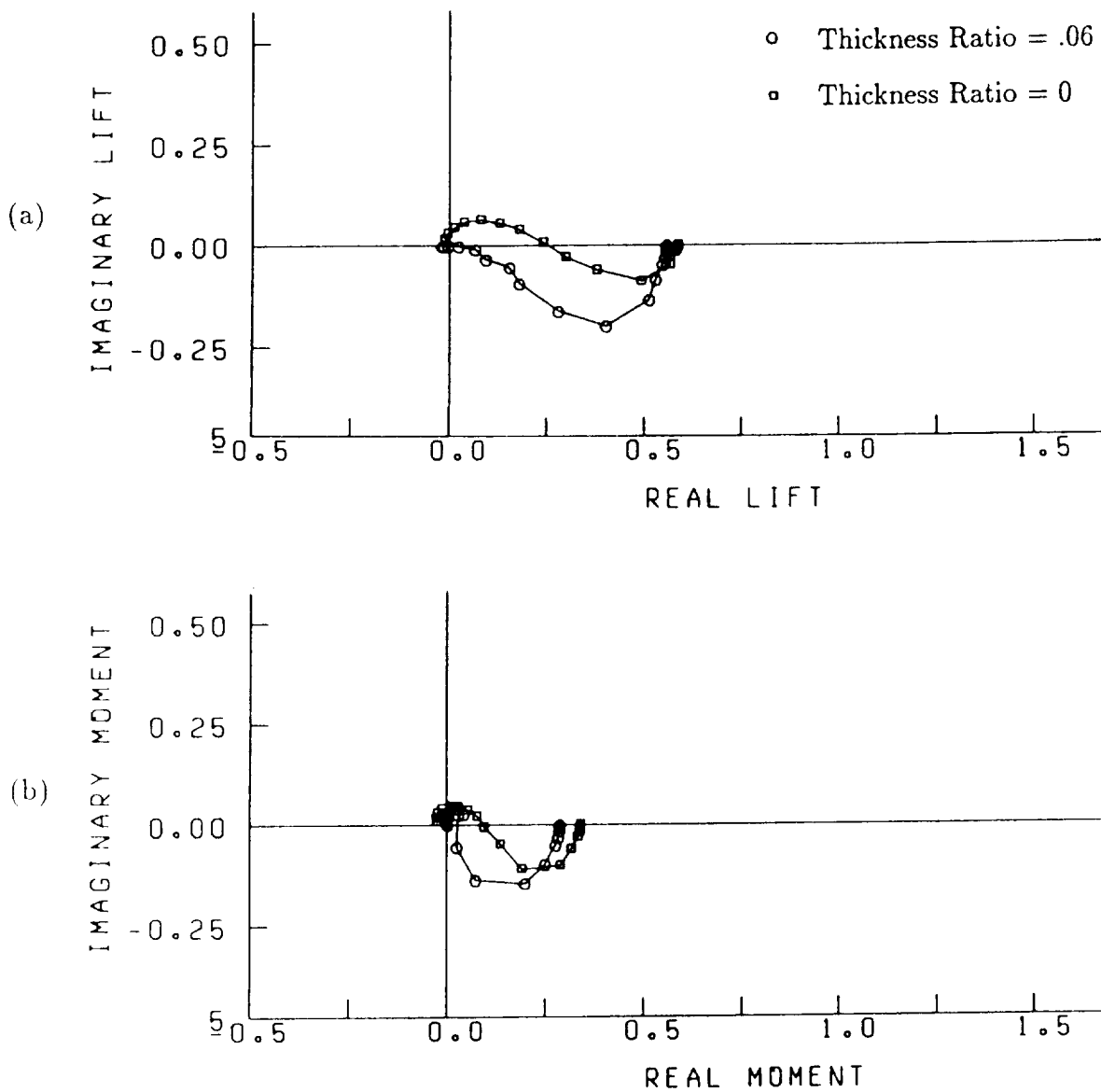
Figure 80. Effect of airfoil thickness on (a) the unsteady lift and (b) the unsteady moment of a Joukowski airfoil in a three-dimensional gust. $M_\infty = .8$, $\alpha = 0^o$, camber = 0. $k_1 = 0.0$, 0.01, 0.03, 0.06, 0.1, 0.2, 0.3, 0.45, 0.6, 0.8, 1.0, 1.3, 1.6, 2.0, 2.5, 3.0, 3.5, 4.0. $k_3 = 0.4$, $|\vec{a}| = 1$, $\frac{a_2}{a_1} = -\frac{7}{4}$, $k_1 = k_2$, $\vec{a} \cdot \vec{k} = 0$, $a_2 > 0$.

149
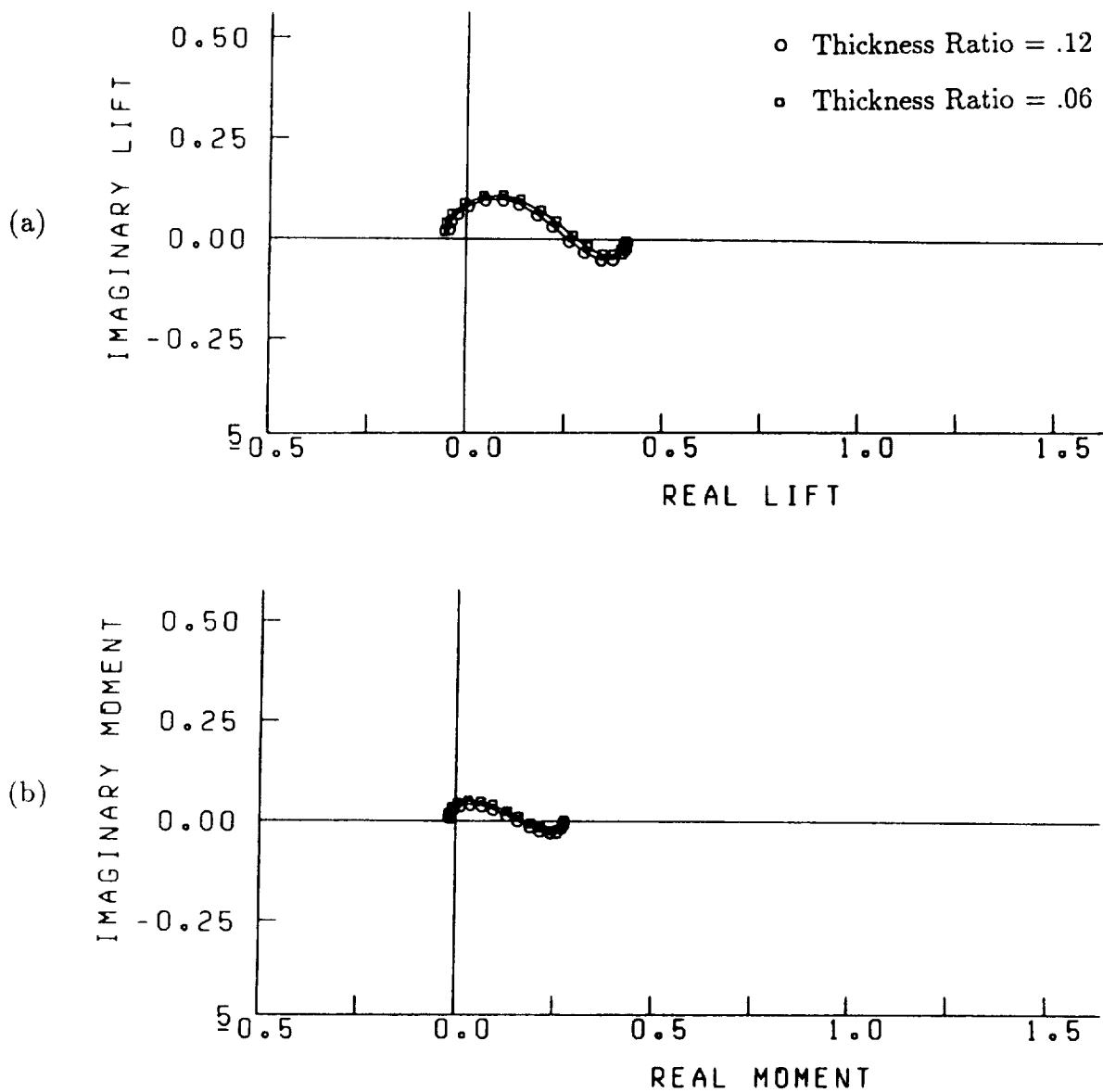
Figure 81. Effect of airfoil thickness on (a) the unsteady lift and (b) the unsteady moment of a Joukowski airfoil in a three-dimensional gust. $M_\infty = .1$, $\alpha = 2^o$, camber $= .05$. $k_1 = 0.0, 0.01, 0.03, 0.06,$ 0.1, 0.2, 0.3, 0.45, 0.6, 0.8, 1.0, 1.3, 1.6, 2.0, 2.5, 3.0, 3.5, 4.0. $k_3 = 0.4$, $|\vec{a}| = 1$, $\frac{a_2}{a_1} = -\frac{7}{4}$, $k_1 = k_2$, $\vec{a} \cdot \vec{k} = 0$, $a_2 > 0$.
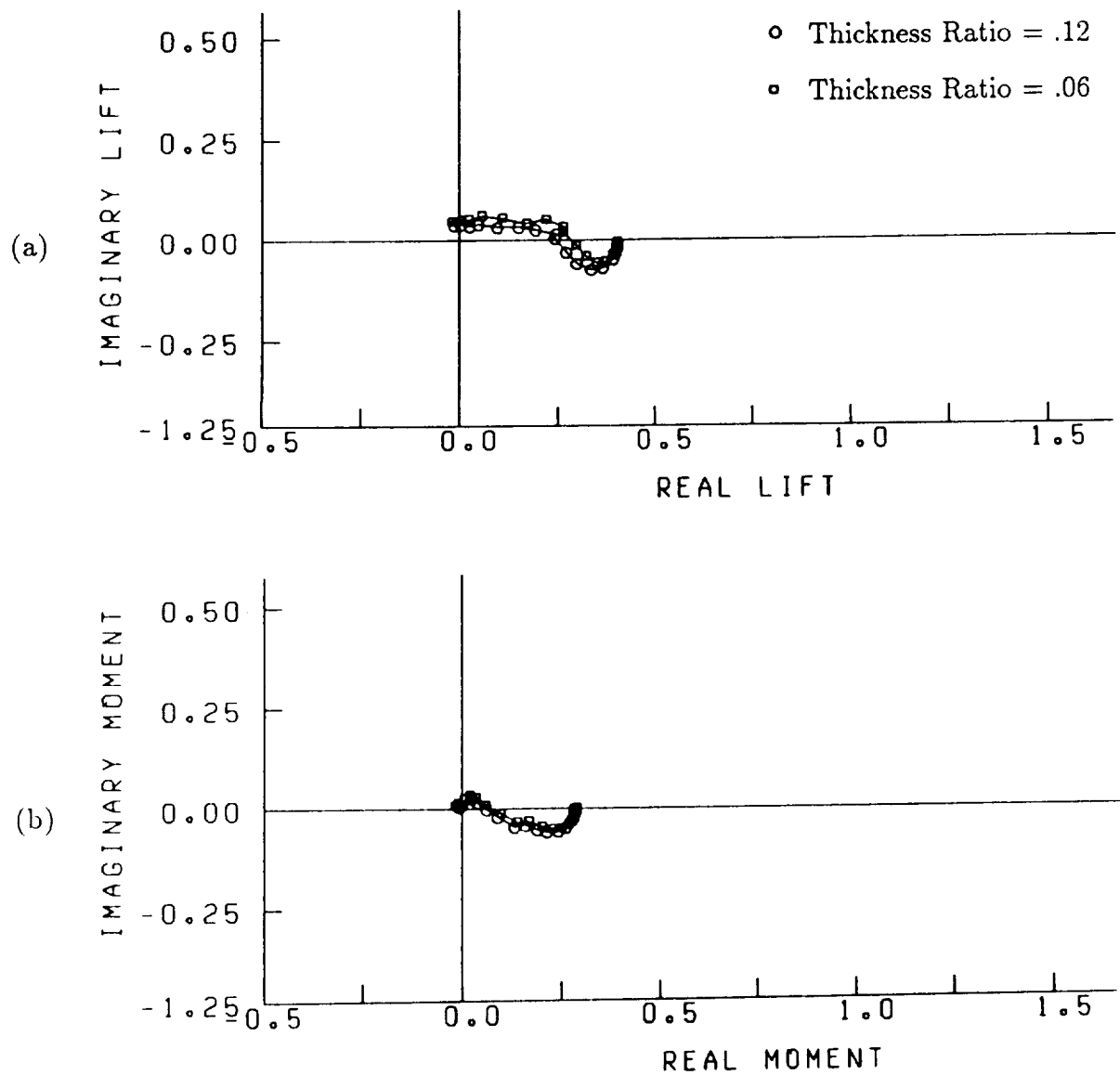
Figure 82. Effect of airfoil thickness on (a) the unsteady lift and (b) the unsteady moment of a Joukowski airfoil in a three-dimensional gust. $M_\infty = .5$, $\alpha = 2^o$, camber $= .05$. $k_1 = 0.0, 0.01, 0.03, 0.06, 0.1, 0.2, 0.3, 0.45, 0.6, 0.8, 1.0, 1.3, 1.6, 2.0, 2.5, 3.0, 3.5, 4.0$. $k_3 = 0.4$, $|\vec{a}| = 1$, $\frac{a_2}{a_1} = -\frac{7}{4}$, $k_1 = k_2$, $\vec{a} \cdot \vec{k} = 0$, $a_2 > 0$.
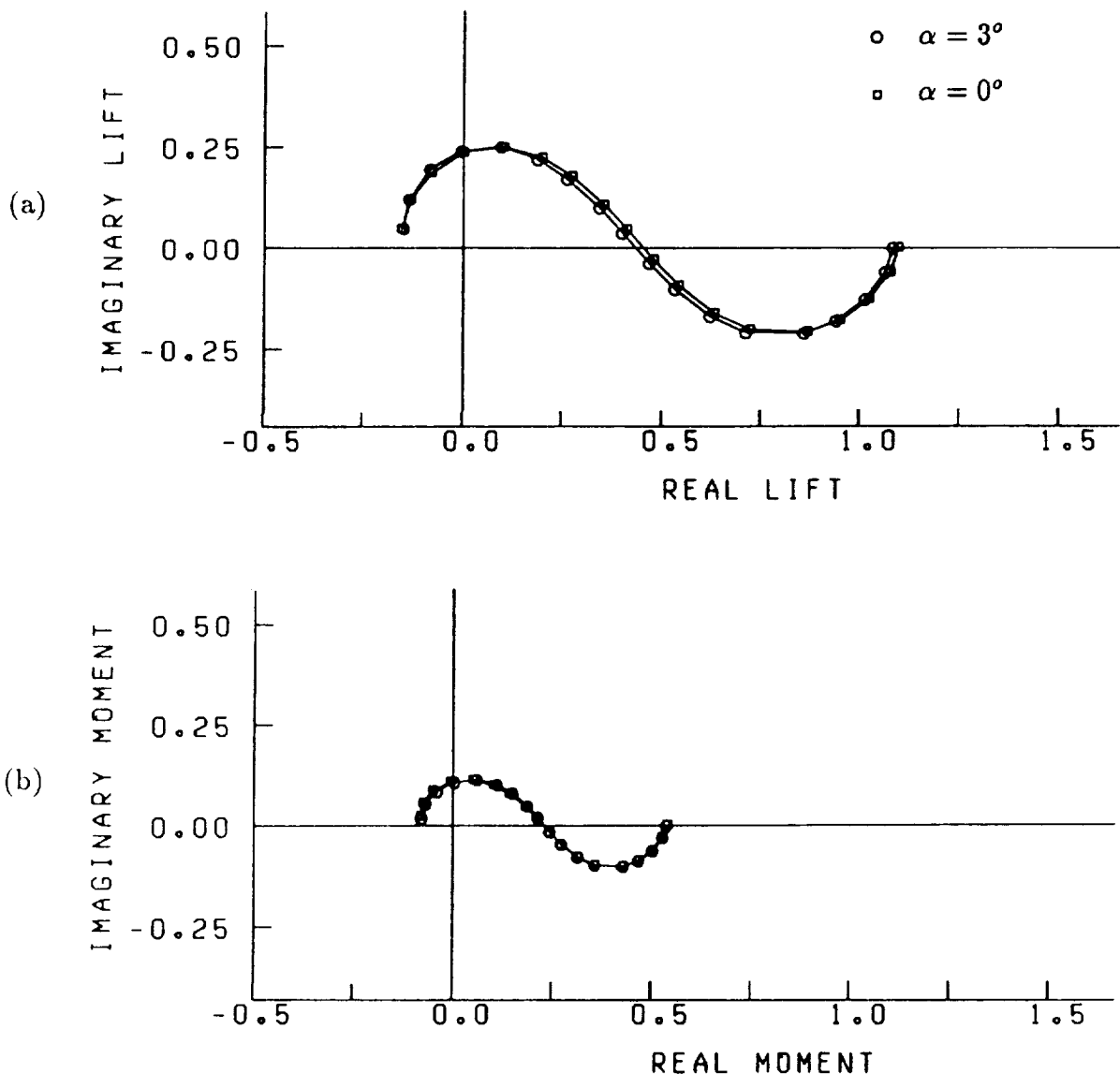
Figure 83. Effect of mean airfoil loading on (a) the unsteady lift and (b) the unsteady moment of a Joukowski airfoil in a transverse gust. $M_\infty = .1$, thickness ratio = .12, camber = 0. $k_1 = 0.0, 0.01, 0.03, 0.06, 0.1, 0.2, 0.3, 0.45, 0.6, 0.8, 1.0, 1.3, 1.6, 2.0, 2.5, 3.0, 3.5, 4.0$.
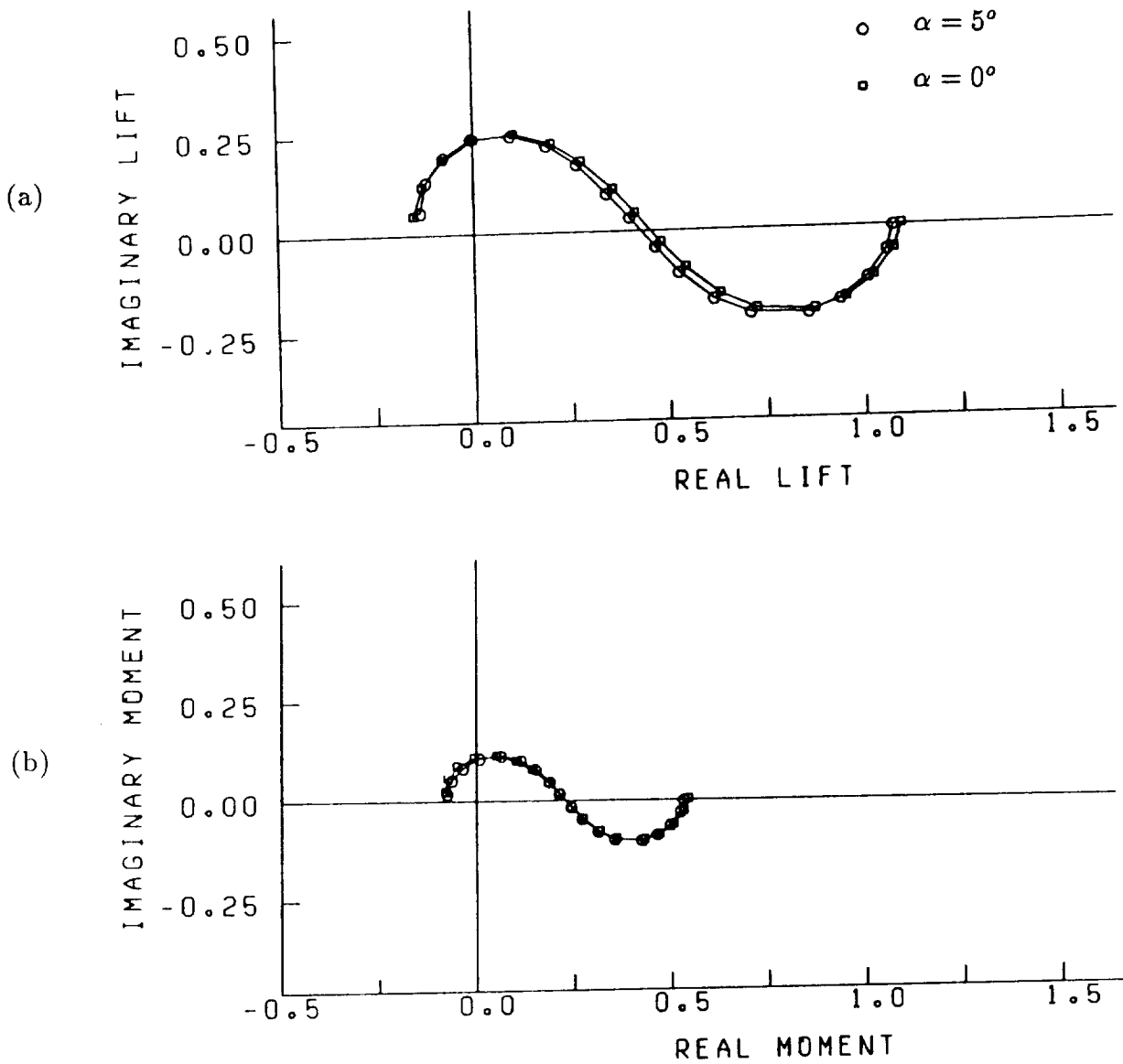
Figure 84. Effect of mean airfoil loading on (a) the unsteady lift and (b) the unsteady moment of a Joukowski airfoil in a transverse gust. $M_\infty = .1$, thickness ratio $= .12$, camber $= 0$. $k_1 = 0.0, 0.01, 0.03$, $0.06, 0.1, 0.2, 0.3, 0.45, 0.6, 0.8, 1.0, 1.3, 1.6, 2.0, 2.5, 3.0, 3.5, 4.0$.

(a)

(b)
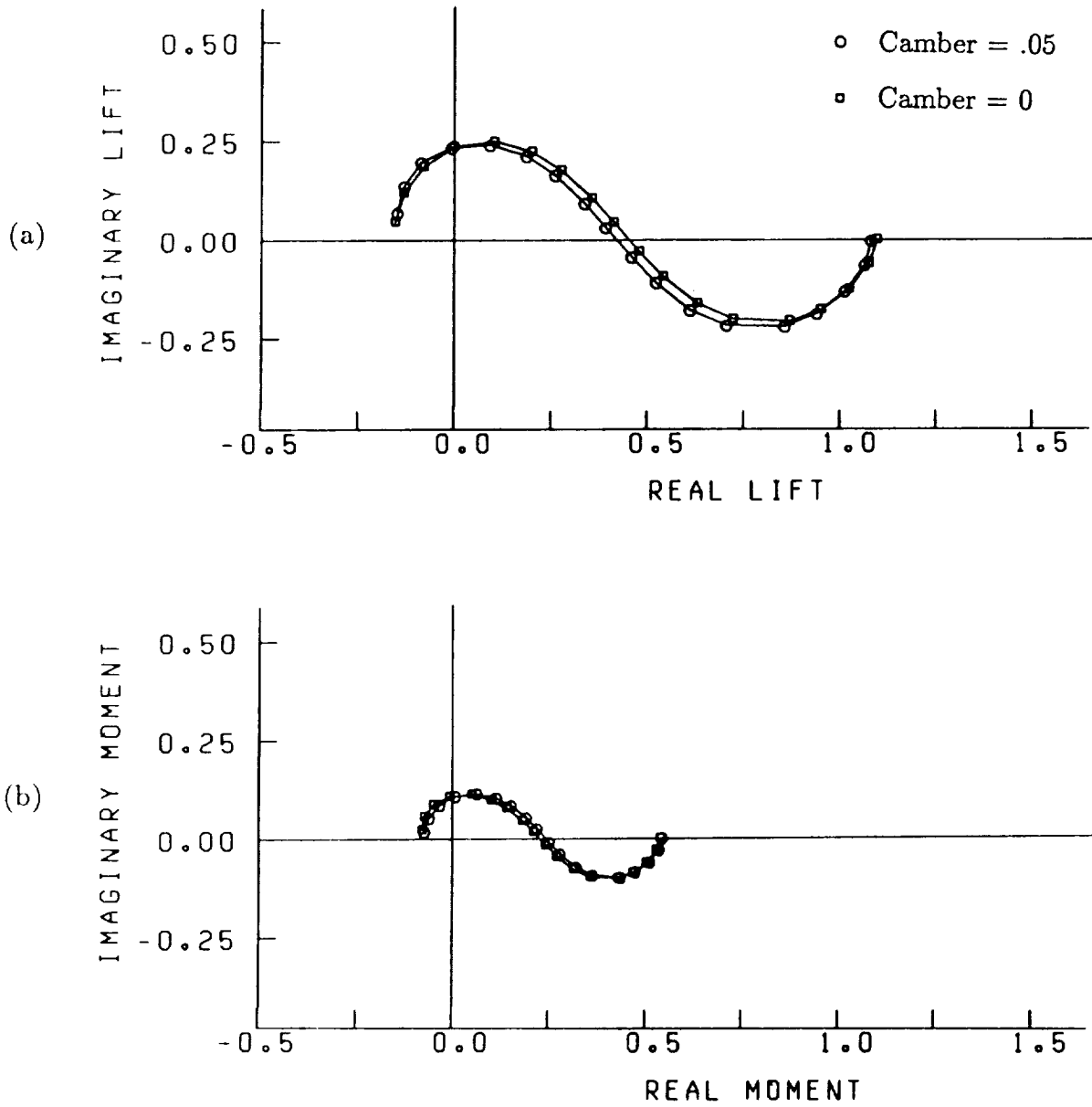
Figure 85. Effect of mean airfoil loading on (a) the unsteady lift and (b) the unsteady moment of a Joukowski airfoil in a transverse gust. $M_\infty = .1$, thickness ratio $= .12$, $\alpha = 0^\circ$. $k_1 = 0.0, 0.01, 0.03, 0.06,$ 0.1, 0.2, 0.3, 0.45, 0.6, 0.8, 1.0, 1.3, 1.6, 2.0, 2.5, 3.0, 3.5, 4.0.

154
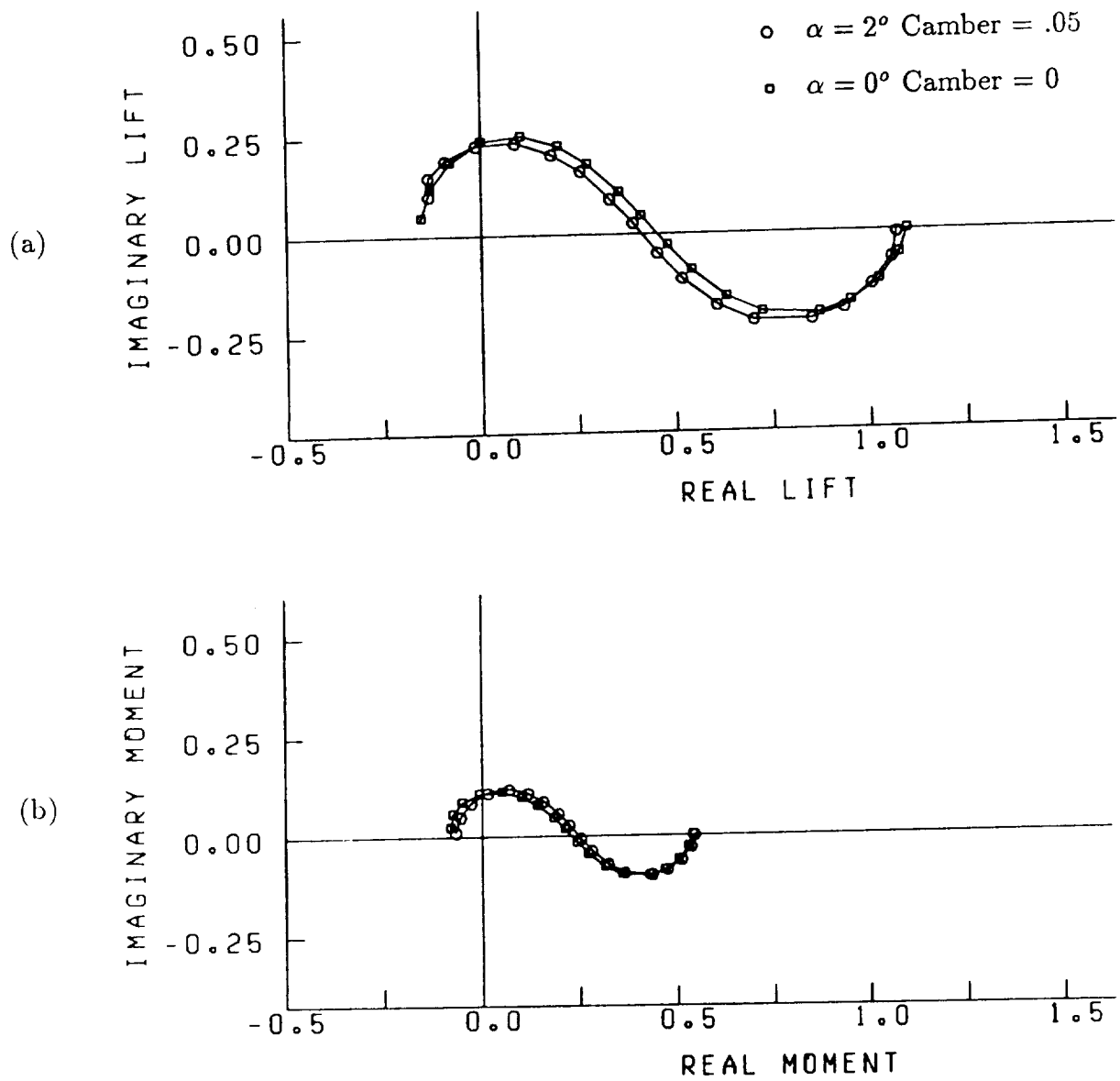
Figure 86.   Effect of mean airfoil loading on (a) the unsteady lift and (b) the
unsteady moment of a Joukowski airfoil in a transverse gust.
$M_\infty = .1$, thickness ratio = .12. $k_1 = 0.0, 0.01, 0.03, 0.06,$
0.1, 0.2, 0.3, 0.45, 0.6, 0.8, 1.0, 1.3, 1.6, 2.0, 2.5, 3.0, 3.5, 4.0.
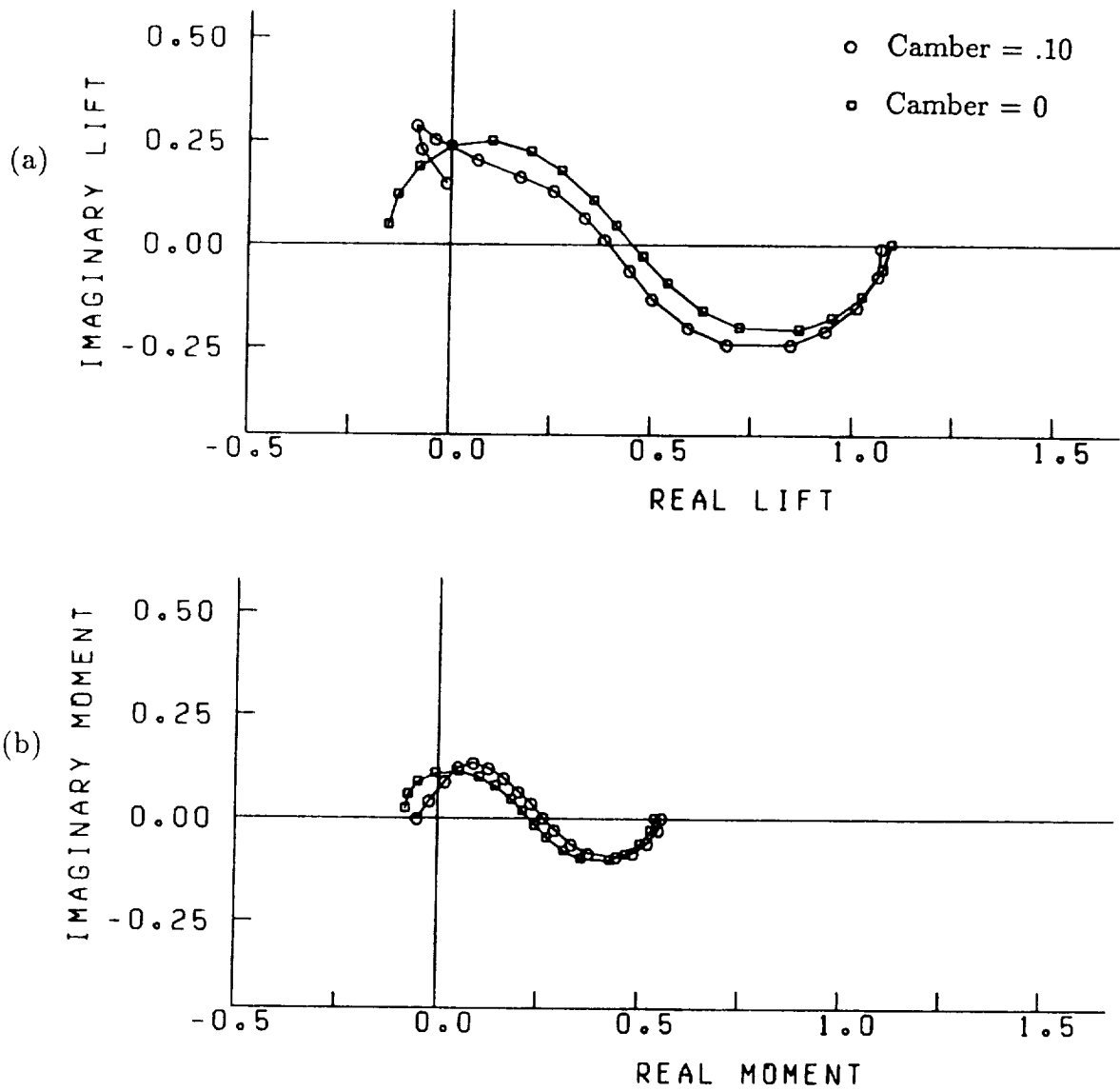
Figure 87. Effect of mean airfoil loading on (a) the unsteady lift and (b) the
unsteady moment of a Joukowski airfoil in a transverse gust.
$M_\infty = .1$, thickness ratio $= .12$, $\alpha = 0^o$. $k_1 = 0.0, 0.01, 0.03, 0.06$,
0.1, 0.2, 0.3, 0.45, 0.6, 0.8, 1.0, 1.3, 1.6, 2.0, 2.5, 3.0, 3.5, 4.0.
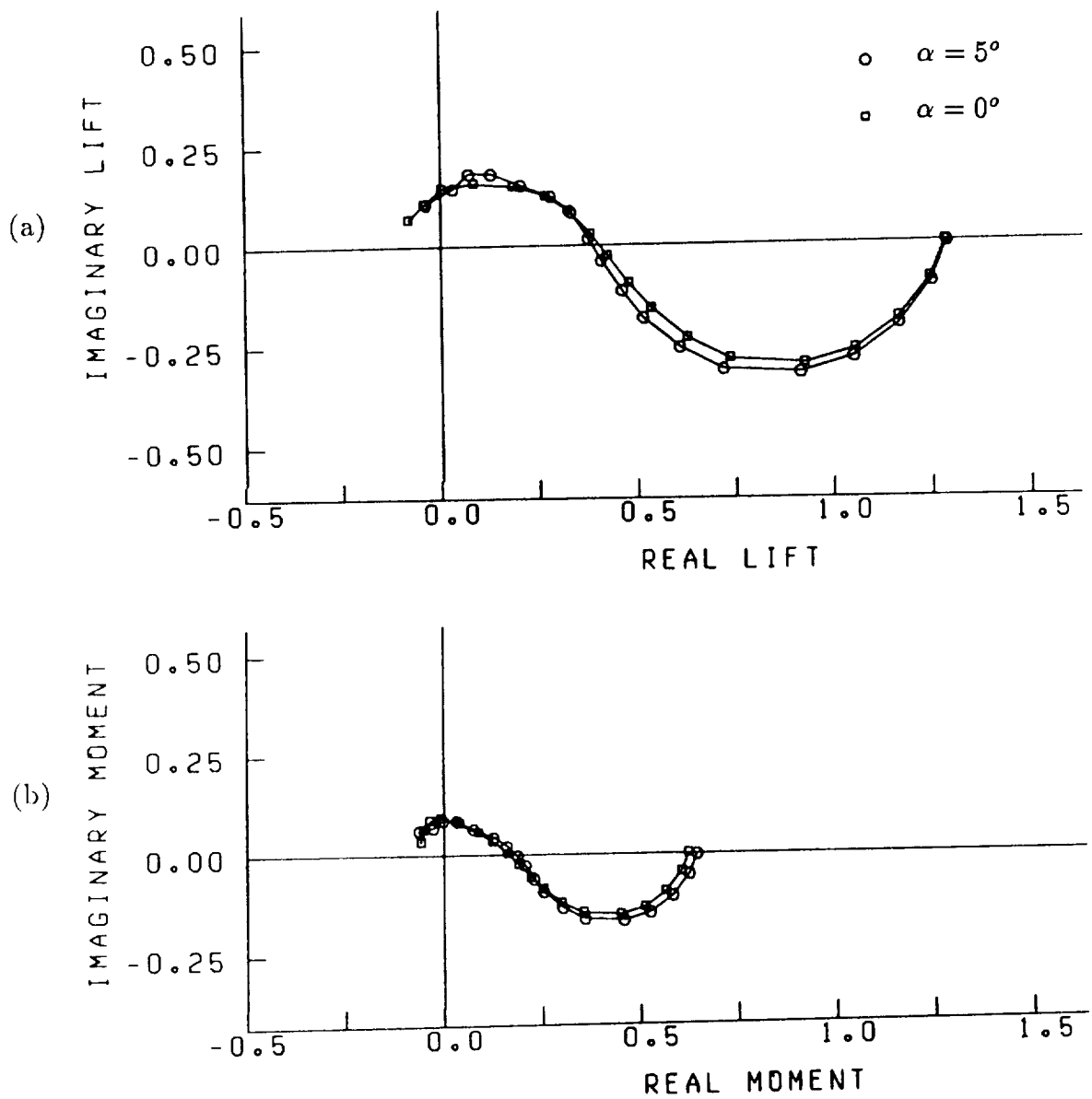
Figure 88. Effect of mean airfoil loading on (a) the unsteady lift and (b) the unsteady moment of a Joukowski airfoil in a transverse gust. $M_\infty = .5$, thickness ratio $= .12$, camber $= 0$. $k_1 = 0.0, 0.01, 0.03, 0.06, 0.1, 0.2, 0.3, 0.45, 0.6, 0.8, 1.0, 1.3, 1.6, 2.0, 2.5, 3.0, 3.5, 4.0$.
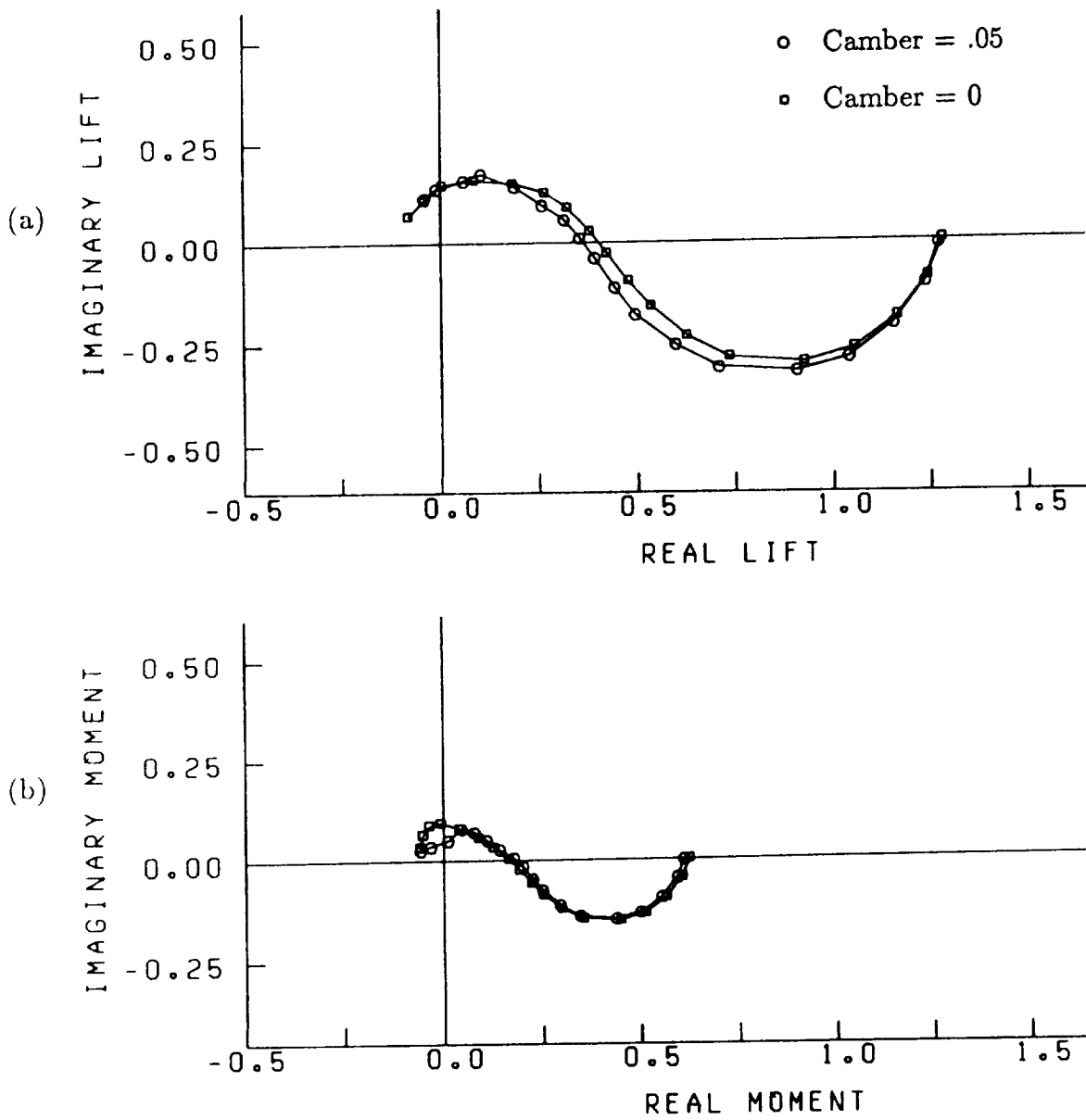
Figure 89. Effect of mean airfoil loading on (a) the unsteady lift and (b) the unsteady moment of a Joukowski airfoil in a transverse gust. $M_\infty = .5$, thickness ratio $= .12$, $\alpha = 0°$. $k_1 = 0.0, 0.01, 0.03, 0.06, 0.1, 0.2, 0.3, 0.45, 0.6, 0.8, 1.0, 1.3, 1.6, 2.0, 2.5, 3.0, 3.5, 4.0$.
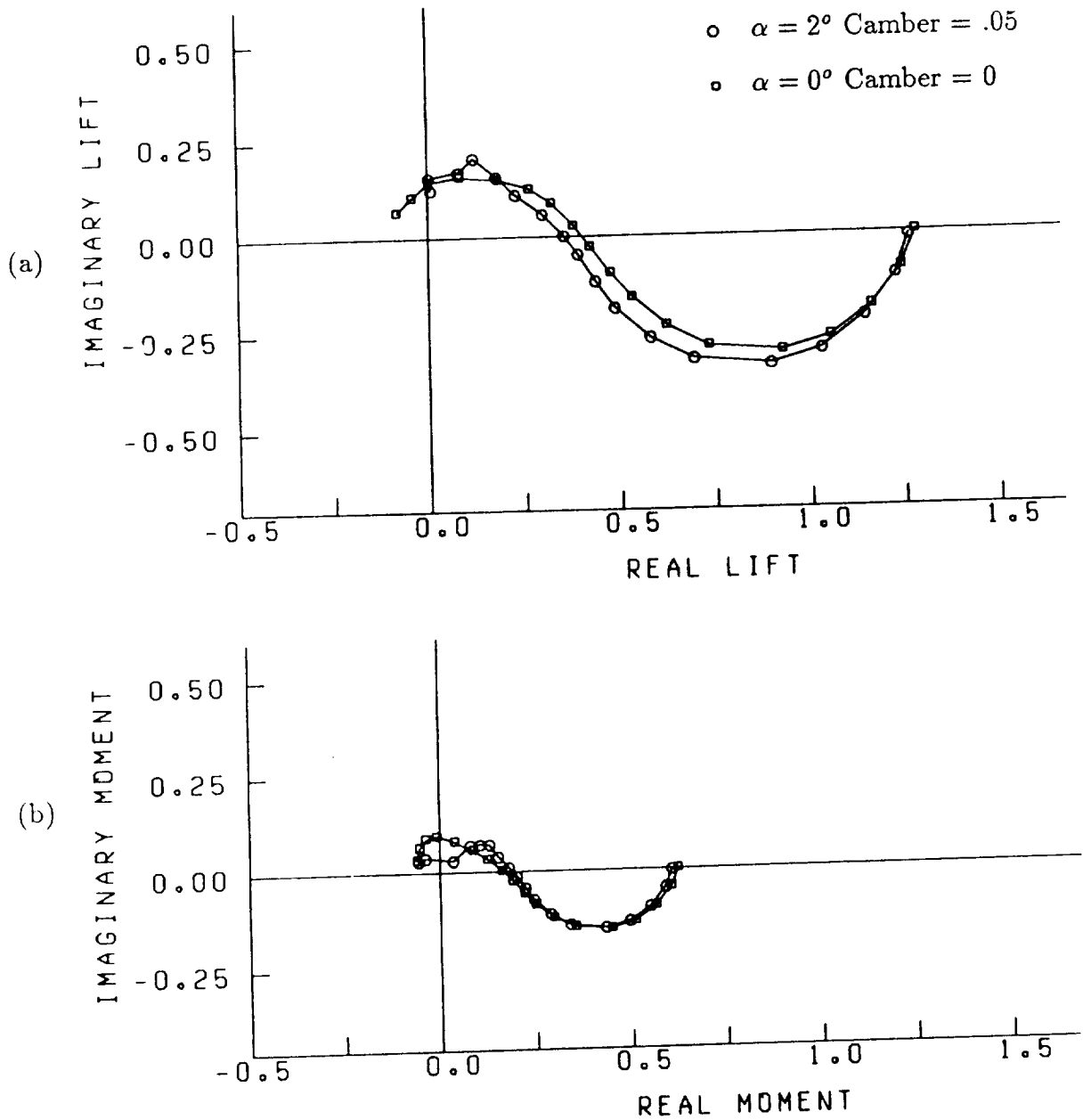
Figure 90. Effect of mean airfoil loading on (a) the unsteady lift and (b) the unsteady moment of a Joukowski airfoil in a transverse gust. $M_\infty = .5$, thickness ratio $= .12$. $k_1 = 0.0, 0.01, 0.03, 0.06, 0.1, 0.2, 0.3, 0.45, 0.6, 0.8, 1.0, 1.3, 1.6, 2.0, 2.5, 3.0, 3.5, 4.0.$
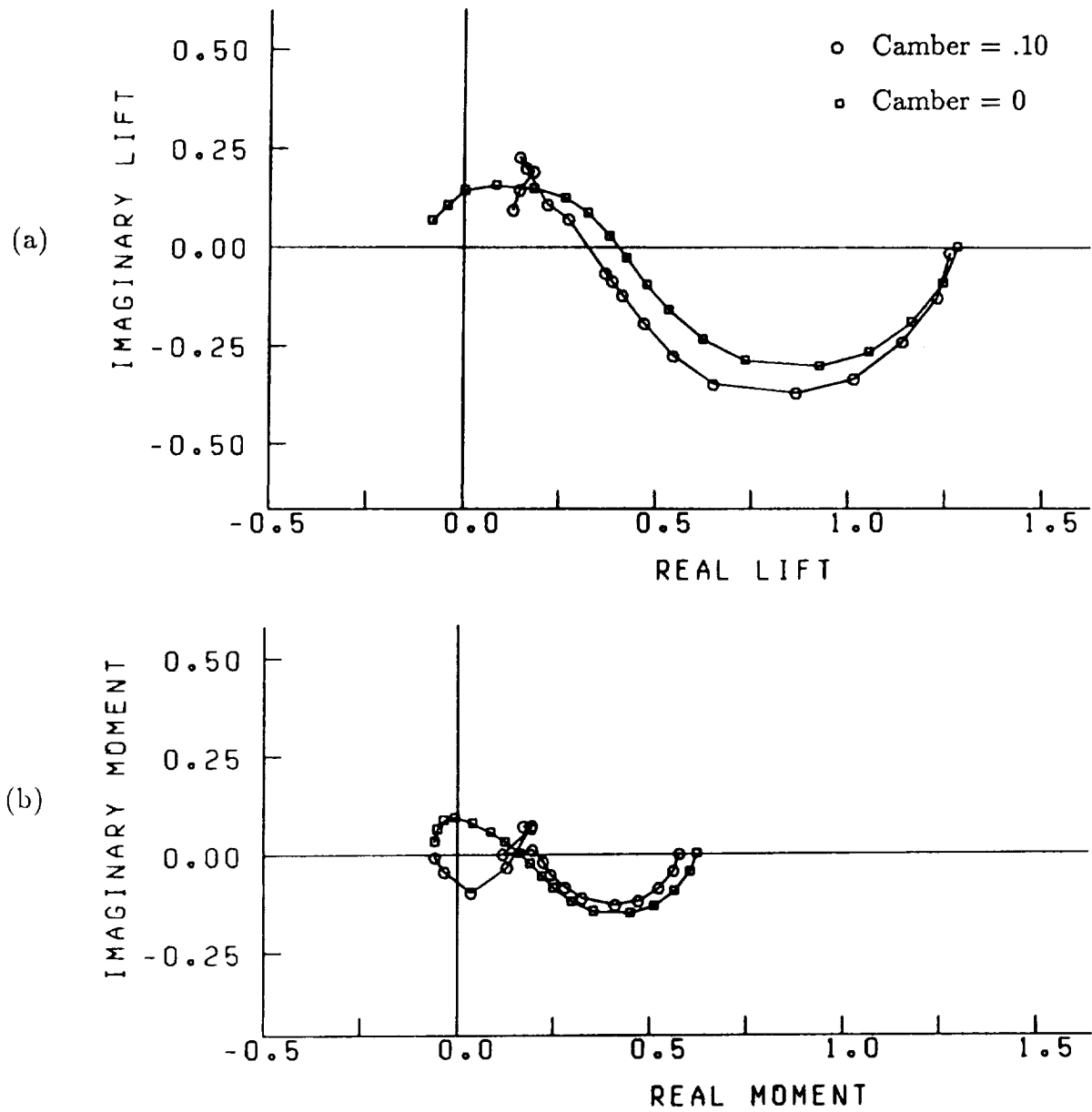
Figure 91. Effect of mean airfoil loading on (a) the unsteady lift and (b) the unsteady moment of a Joukowski airfoil in a transverse gust. $M_\infty = .5$, thickness ratio $= .12$, $\alpha = 0^\circ$. $k_1 = 0.0, 0.01, 0.03, 0.06, 0.1, 0.2, 0.3, 0.45, 0.6, 0.8, 1.0, 1.3, 1.6, 2.0, 2.5, 3.0, 3.5, 4.0$.
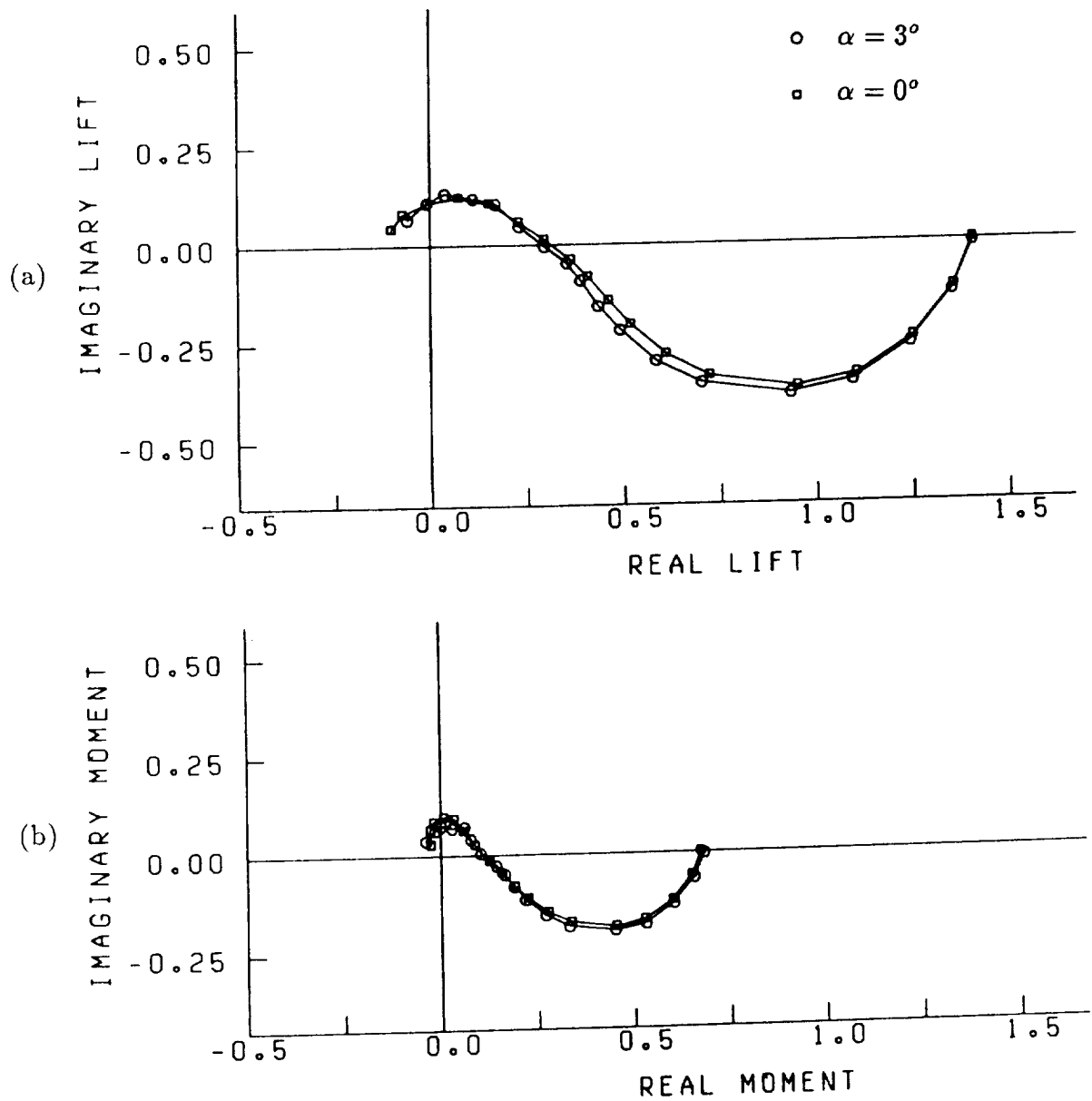
Figure 92.   Effect of mean airfoil loading on (a) the unsteady lift and (b) the
unsteady moment of a Joukowski airfoil in a transverse gust.
$M_\infty = .6$, thickness ratio $= .12$, camber $= 0$. $k_1 = 0.0, 0.01, 0.03,$
$0.06, 0.1, 0.2, 0.3, 0.45, 0.6, 0.8, 1.0, 1.3, 1.6, 2.0, 2.5, 3.0, 3.5, 4.0.$
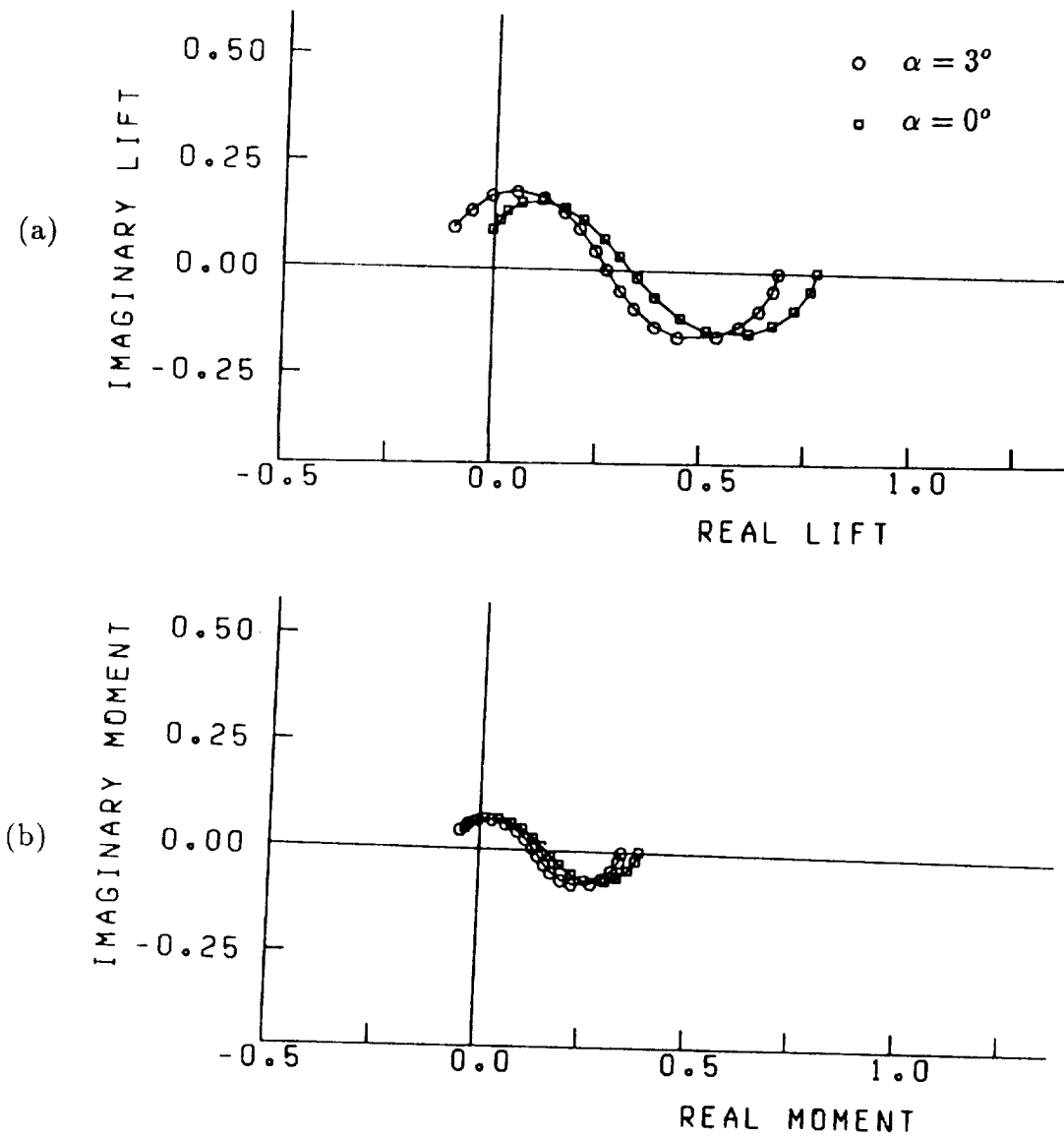
Figure 93. Effect of mean airfoil loading on (a) the unsteady lift and (b) the unsteady moment of a Joukowski airfoil in a transverse and longitudinal gust. $M_\infty = .1$, thickness ratio $= .12$, camber $= 0$. $k_1 = 0.0, 0.01, 0.03, 0.06, 0.1, 0.2, 0.3, 0.45, 0.6, 0.8, 1.0, 1.3, 1.6, 2.0, 2.5, 3.0, 3.5, 4.0.$ $-a_1 = a_2 = .7071$, $k_1 = k_2$, $a_3 = k_3 = 0$.
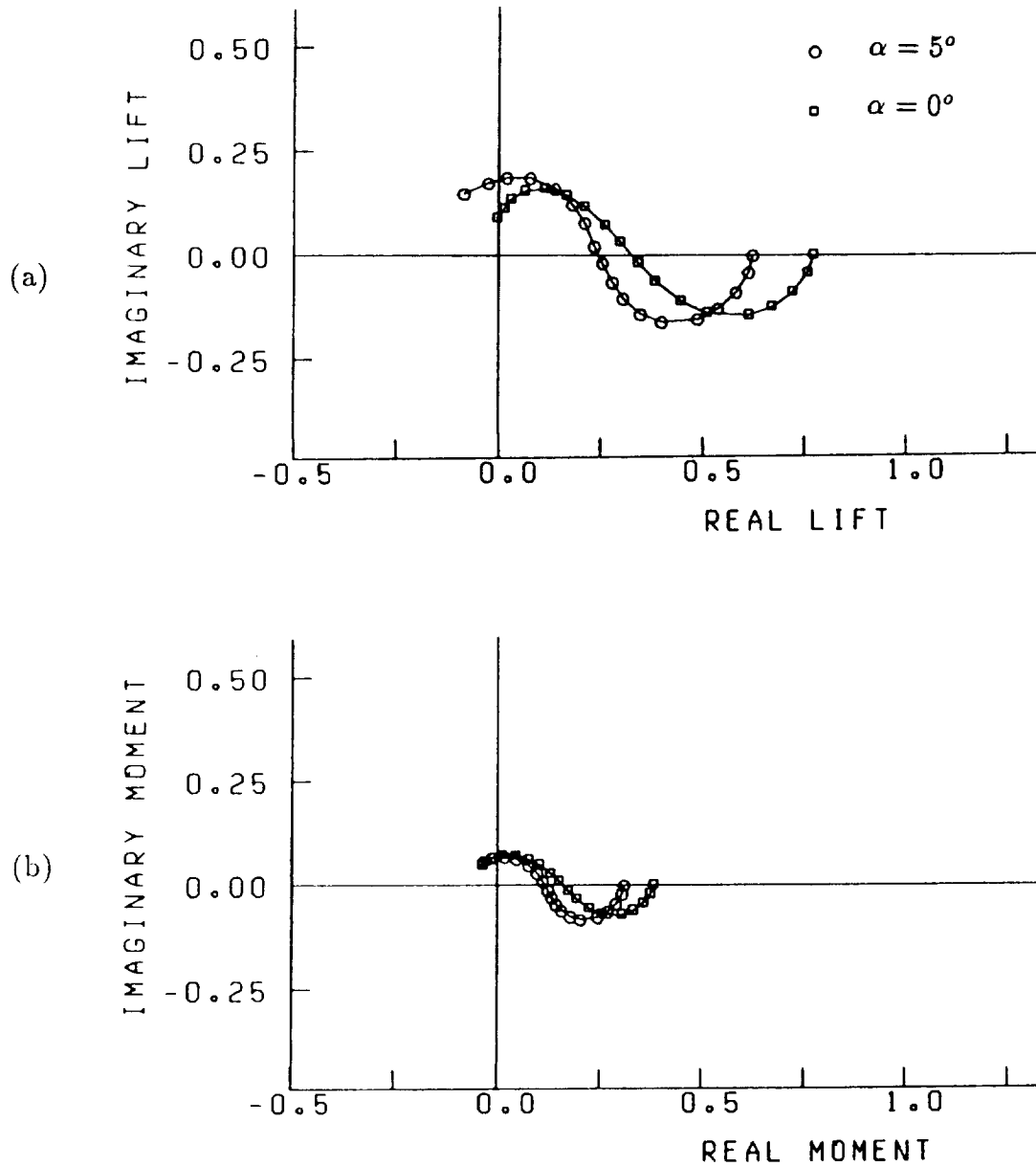
Figure 94. Effect of mean airfoil loading on (a) the unsteady lift and (b) the unsteady moment of a Joukowski airfoil in a transverse and longitudinal gust. $M_\infty = .1$, thickness ratio $= .12$, camber $= 0$. $k_1 = 0.0, 0.01, 0.03, 0.06, 0.1, 0.2, 0.3, 0.45, 0.6, 0.8, 1.0, 1.3, 1.6, 2.0, 2.5, 3.0, 3.5, 4.0.$ $-a_1 = a_2 = .7071,$ $k_1 = k_2,$ $a_3 = k_3 = 0.$

163
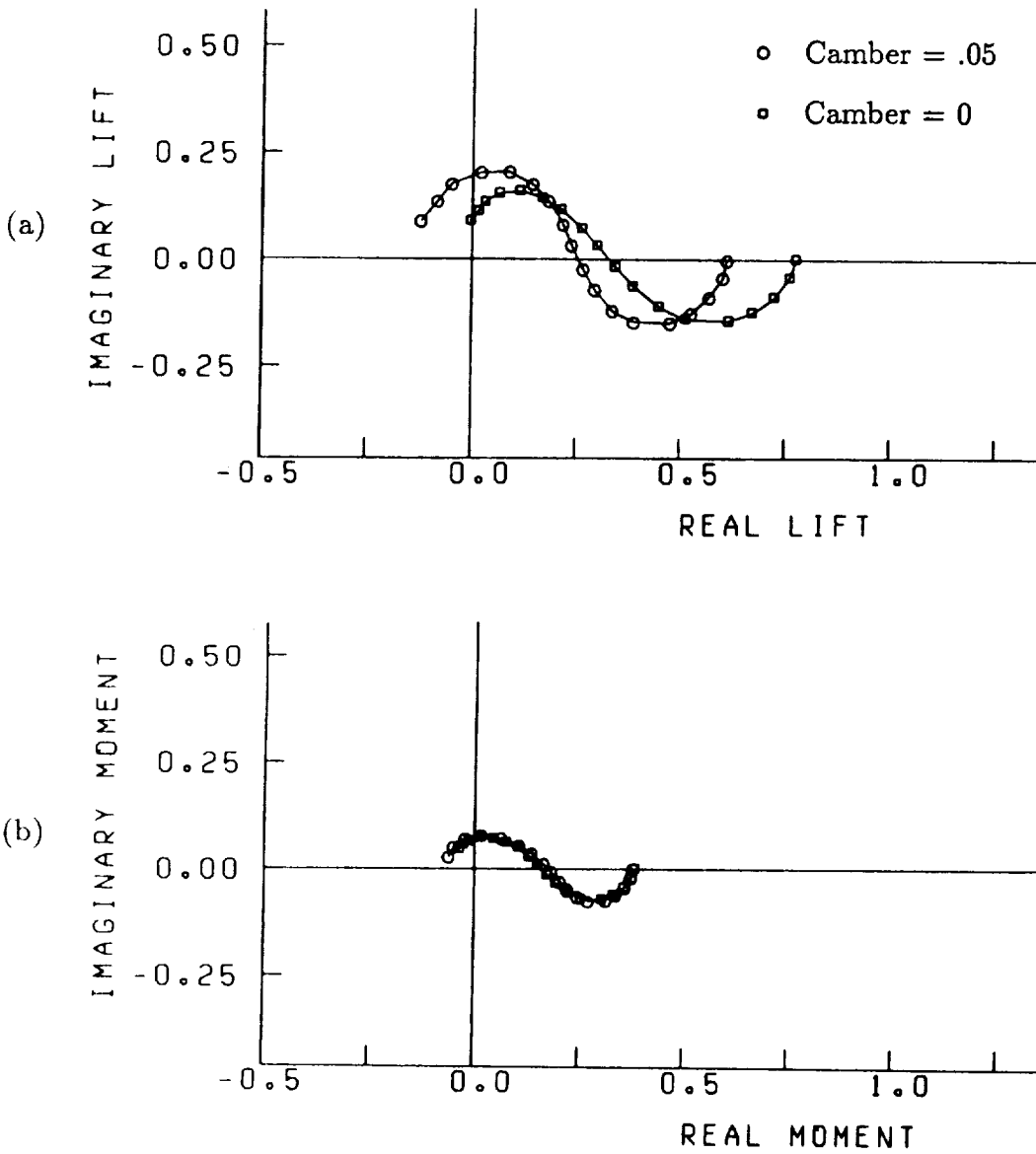
Figure 95.   Effect of mean airfoil loading on (a) the unsteady lift and (b) the unsteady moment of a Joukowski airfoil in a transverse and longitudinal gust. $M_\infty = .1$, thickness ratio $= .12$, $\alpha = 0°$.
$k_1 = 0.0, 0.01, 0.03, 0.06, 0.1, 0.2, 0.3, 0.45, 0.6, 0.8, 1.0, 1.3, 1.6, 2.0, 2.5, 3.0, 3.5, 4.0.$ $-a_1 = a_2 = .7071$, $k_1 = k_2$, $a_3 = k_3 = 0$.

(a)

(b)

$\quad\circ\quad \alpha = 2^{\circ}$ Camber $= .05$

$\quad\square\quad \alpha = 0^{\circ}$ Camber $= 0$
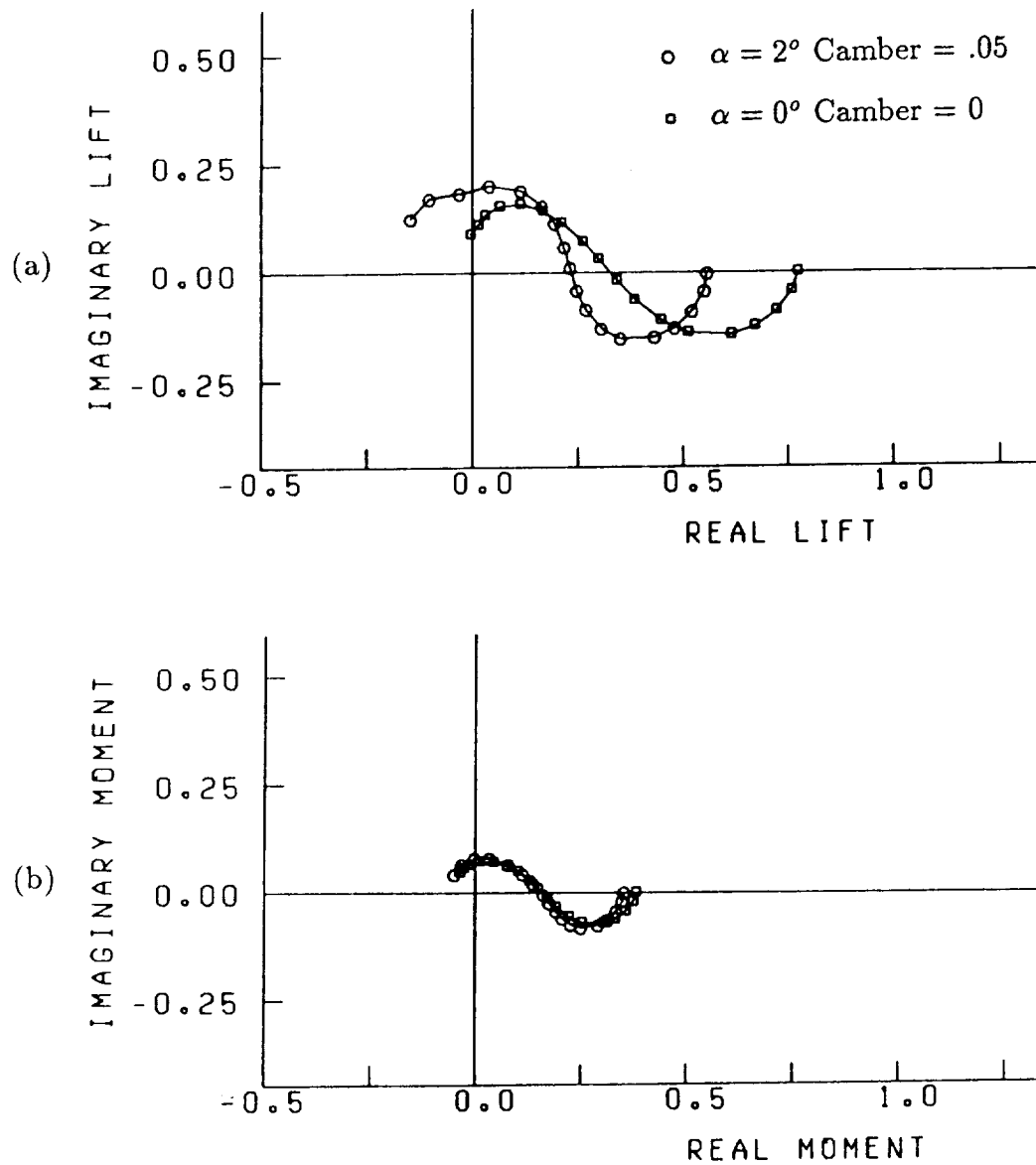
Figure 96. Effect of mean airfoil loading on (a) the unsteady lift and (b) the unsteady moment of a Joukowski airfoil in a transverse and longitudinal gust. $M_{\infty} = .1$, thickness ratio $= .12$. $k_1 = 0.0, 0.01, 0.03, 0.06, 0.1, 0.2, 0.3, 0.45, 0.6, 0.8, 1.0, 1.3, 1.6,$ $2.0, 2.5, 3.0, 3.5, 4.0.$ $-a_1 = a_2 = .7071$, $k_1 = k_2$, $a_3 = k_3 = 0$.

165
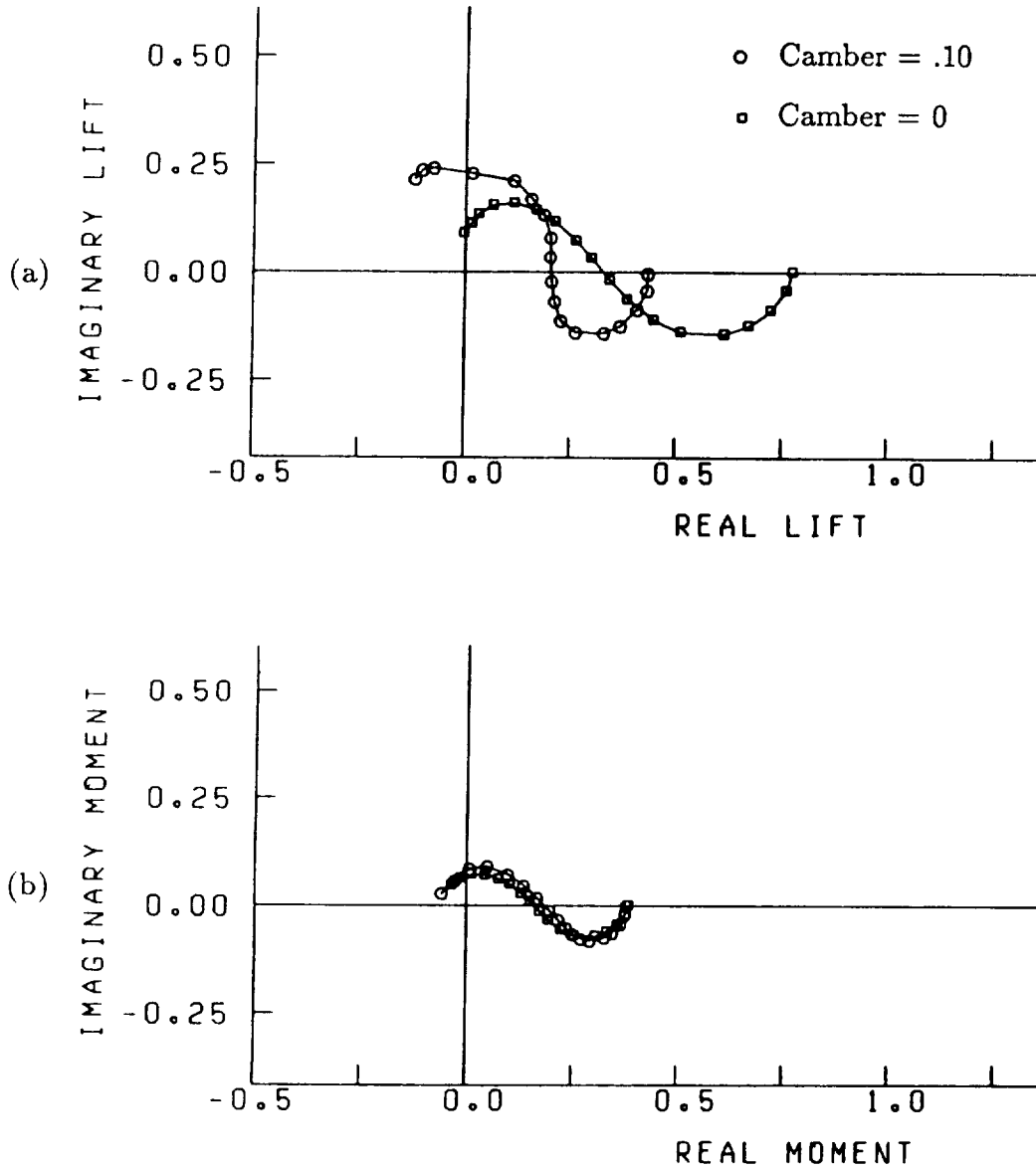
Figure 97. Effect of mean airfoil loading on (a) the unsteady lift and (b) the unsteady moment of a Joukowski airfoil in a transverse and longitudinal gust. $M_\infty = .1$, thickness ratio $= .12$, $\alpha = 0^\circ$. $k_1 = 0.0, 0.01, 0.03, 0.06, 0.1, 0.2, 0.3, 0.45, 0.6, 0.8, 1.0, 1.3, 1.6, 2.0, 2.5, 3.0, 3.5, 4.0$. $-a_1 = a_2 = .7071$, $k_1 = k_2$, $a_3 = k_3 = 0$.
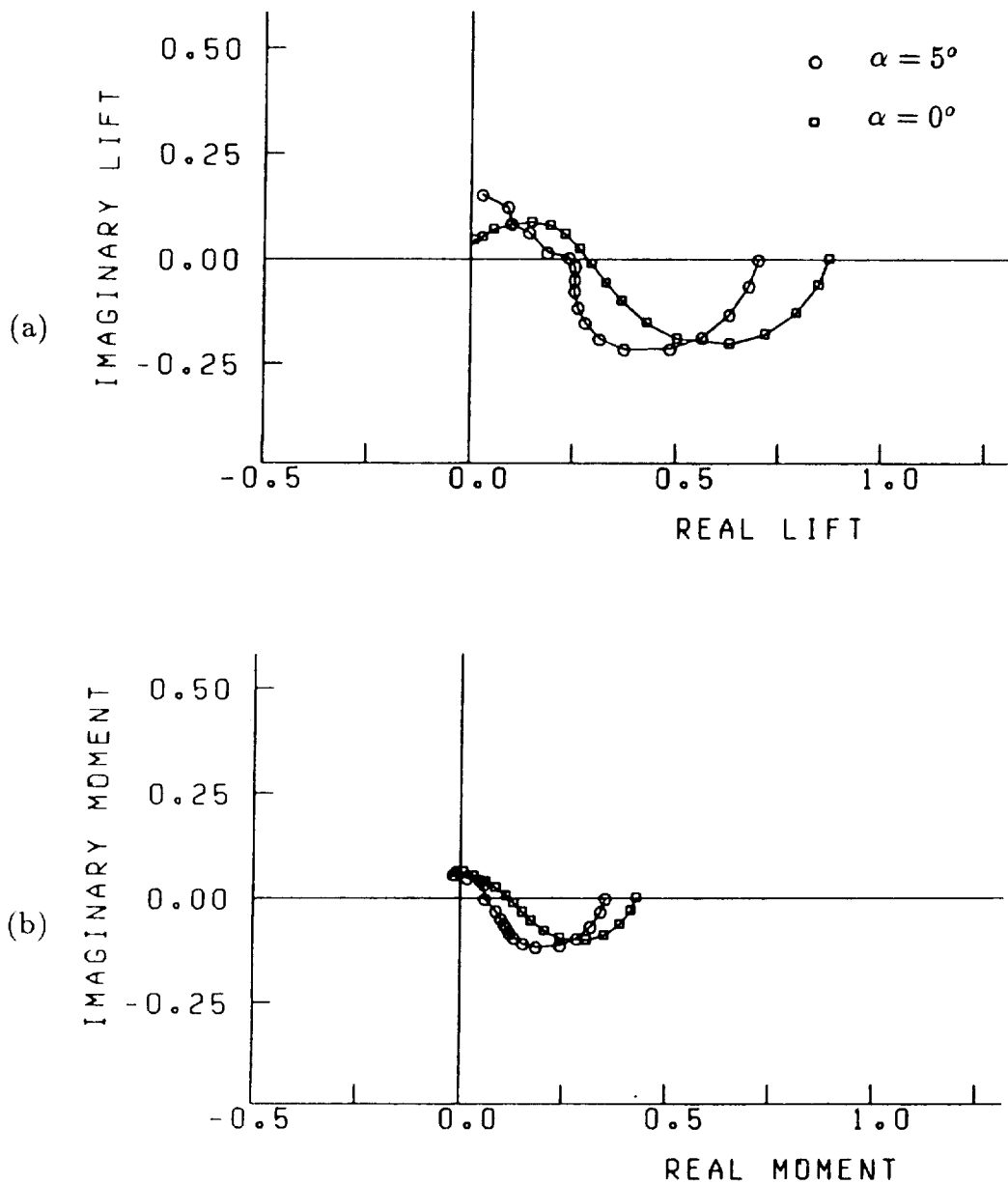
Figure 98. Effect of mean airfoil loading on (a) the unsteady lift and (b) the unsteady moment of a Joukowski airfoil in a transverse and longitudinal gust. $M_\infty = .5$, thickness ratio $= .12$, camber $= 0$. $k_1 = 0.0, 0.01, 0.03, 0.06, 0.1, 0.2, 0.3, 0.45, 0.6, 0.8, 1.0, 1.3, 1.6,$ 2.0, 2.5, 3.0, 3.5, 4.0. $-a_1 = a_2 = .7071$, $k_1 = k_2$, $a_3 = k_3 = 0$.
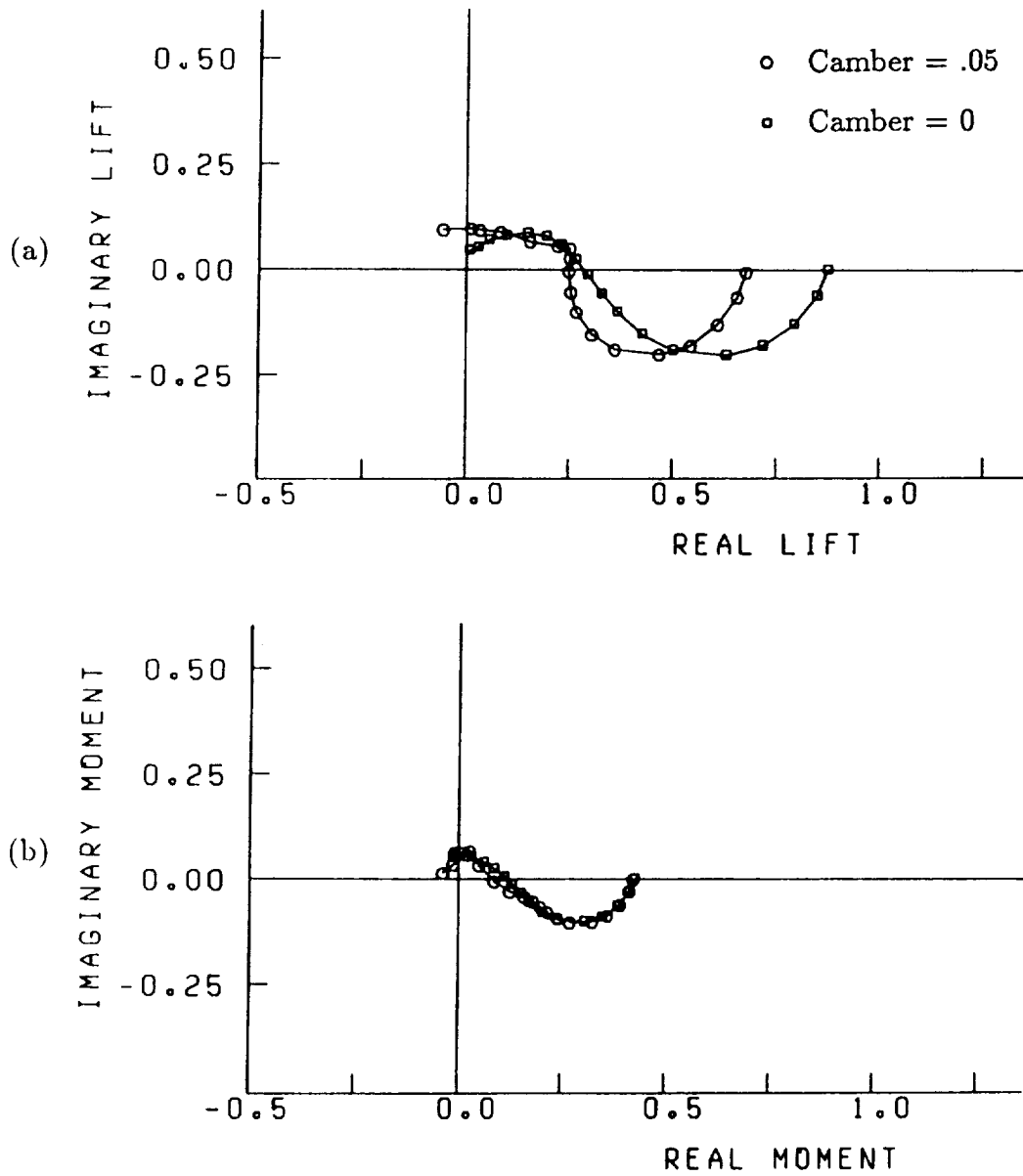
Figure 99. Effect of mean airfoil loading on (a) the unsteady lift and (b) the unsteady moment of a Joukowski airfoil in a transverse and longitudinal gust. $M_\infty = .5$, thickness ratio $= .12$, $\alpha = 0^\circ$.
$k_1 = 0.0, 0.01, 0.03, 0.06, 0.1, 0.2, 0.3, 0.45, 0.6, 0.8, 1.0, 1.3, 1.6, 2.0, 2.5, 3.0, 3.5, 4.0$. $-a_1 = a_2 = .7071$, $k_1 = k_2$, $a_3 = k_3 = 0$.
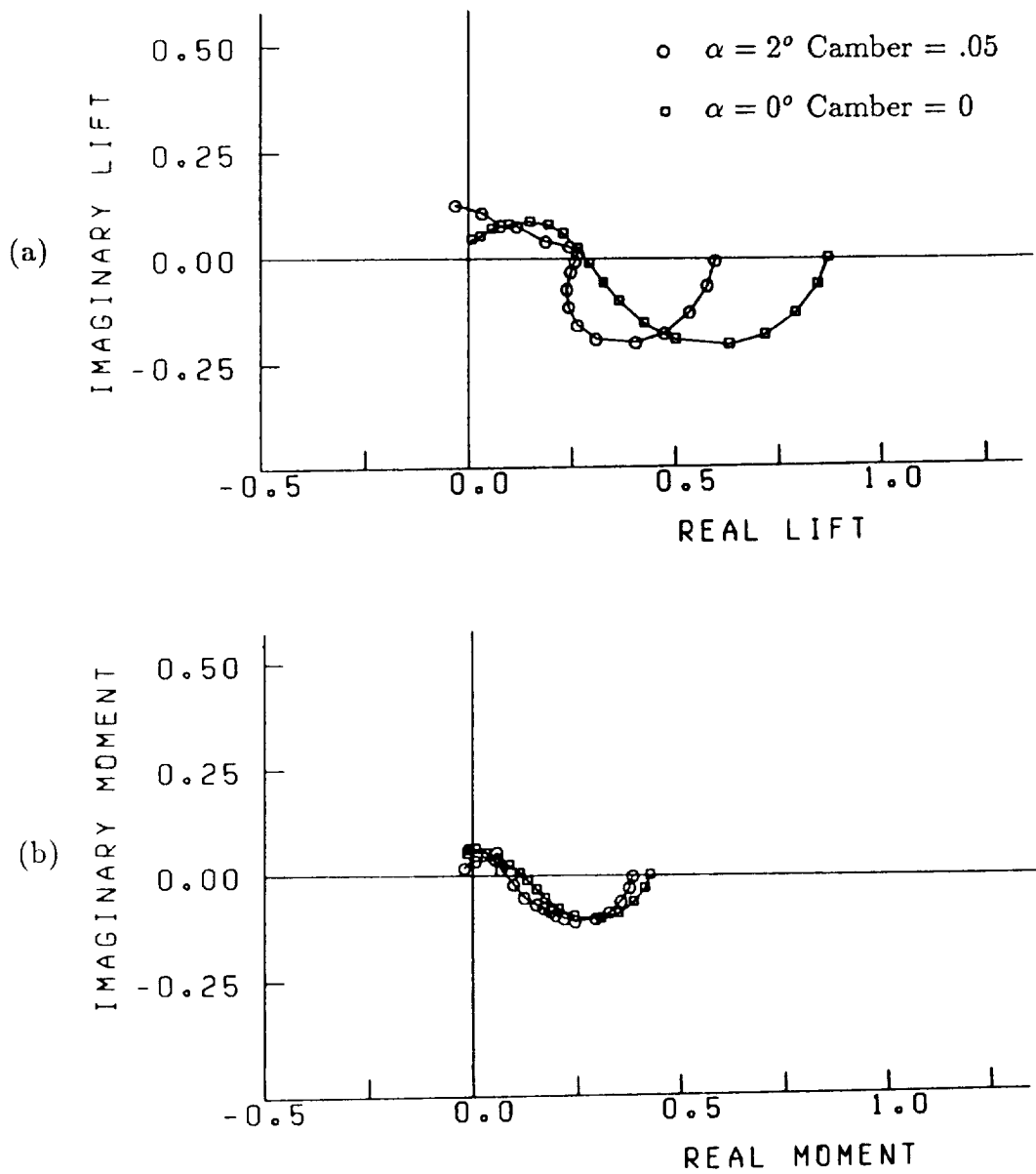
Figure 100. Effect of mean airfoil loading on (a) the unsteady lift and (b) the unsteady moment of a Joukowski airfoil in a transverse and longitudinal gust. $M_\infty = .5$, thickness ratio $= .12$. $k_1 = 0.0, 0.01, 0.03, 0.06, 0.1, 0.2, 0.3, 0.45, 0.6, 0.8, 1.0, 1.3, 1.6, 2.0, 2.5, 3.0, 3.5, 4.0.$ $-a_1 = a_2 = .7071,$ $k_1 = k_2,$ $a_3 = k_3 = 0.$
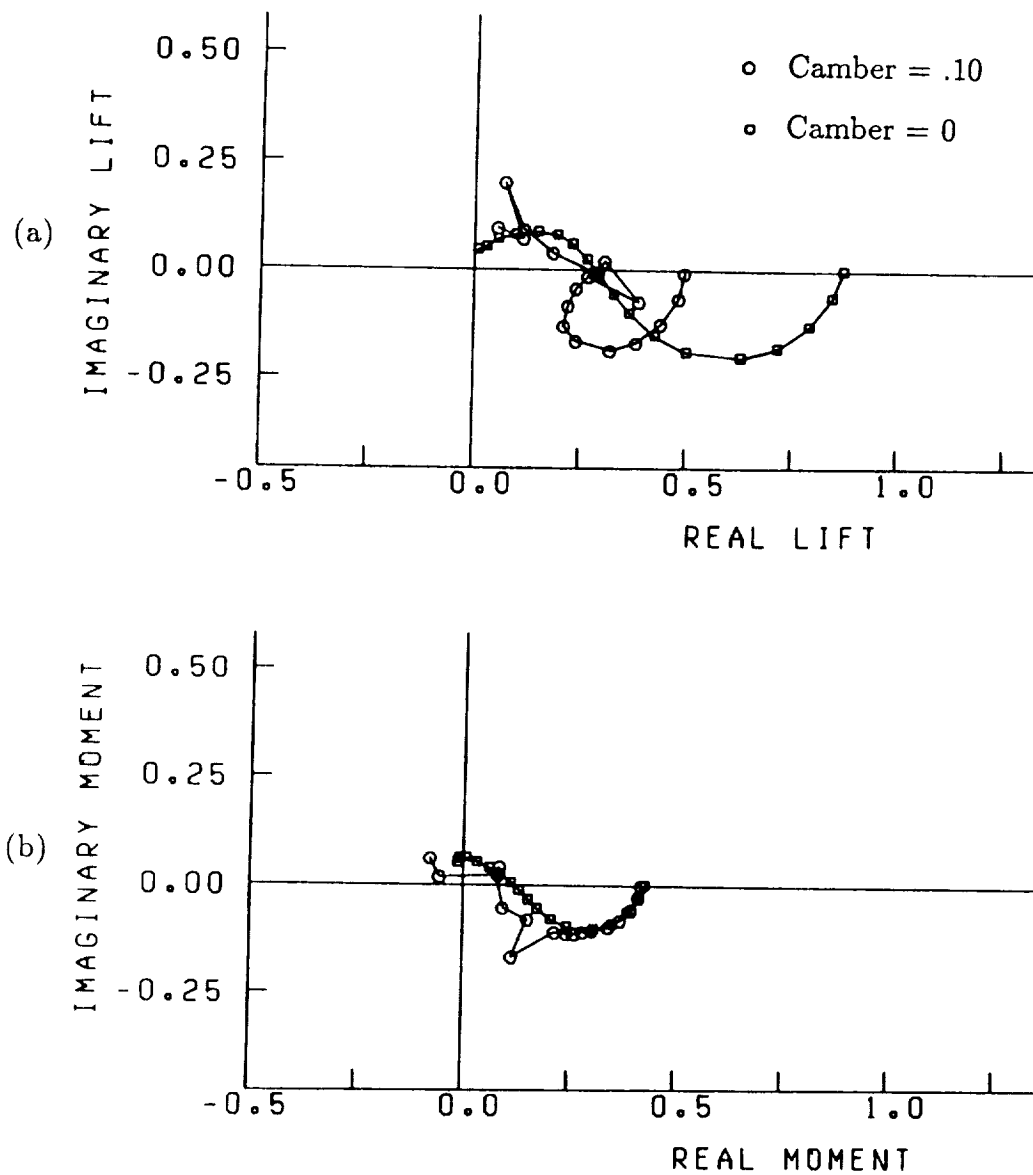
Figure 101. Effect of mean airfoil loading on (a) the unsteady lift and (b) the unsteady moment of a Joukowski airfoil in a transverse and longitudinal gust. $M_\infty = .5$, thickness ratio $= .12$, $\alpha = 0°$. $k_1 = 0.0, 0.01, 0.03, 0.06, 0.1, 0.2, 0.3, 0.45, 0.6, 0.8, 1.0, 1.3, 1.6, 2.0, 2.5, 3.0, 3.5, 4.0$. $-a_1 = a_2 = .7071$, $k_1 = k_2$, $a_3 = k_3 = 0$.
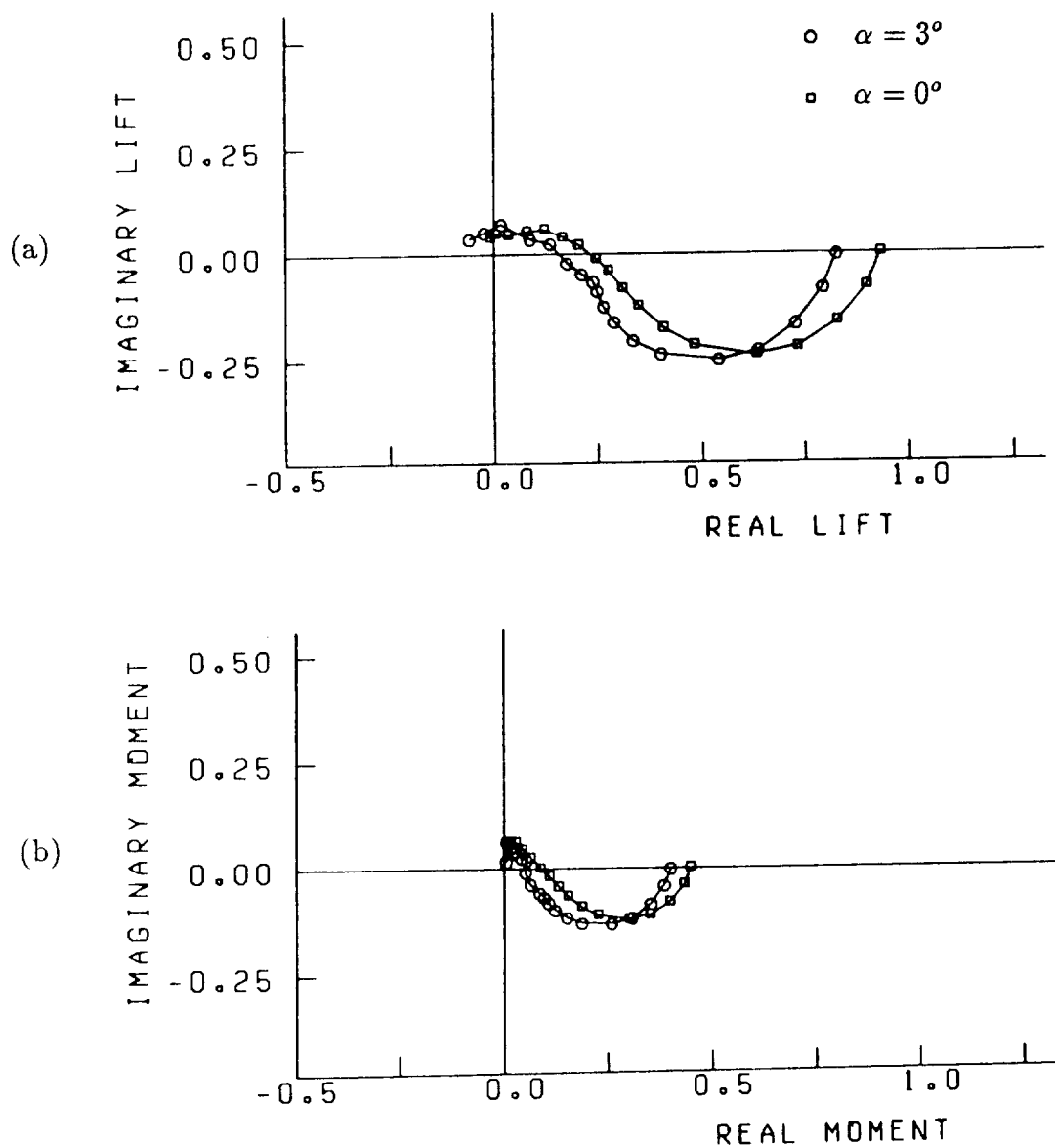
Figure 102. Effect of mean airfoil loading on (a) the unsteady lift and (b) the unsteady moment of a Joukowski airfoil in a transverse and longitudinal gust. $M_\infty = .6$, thickness ratio $= .12$, camber $= 0$. $k_1 = 0.0, 0.01, 0.03, 0.06, 0.1, 0.2, 0.3, 0.45, 0.6, 0.8, 1.0, 1.3, 1.6, 2.0, 2.5, 3.0, 3.5, 4.0.$ $-a_1 = a_2 = .7071,$ $k_1 = k_2,$ $a_3 = k_3 = 0.$
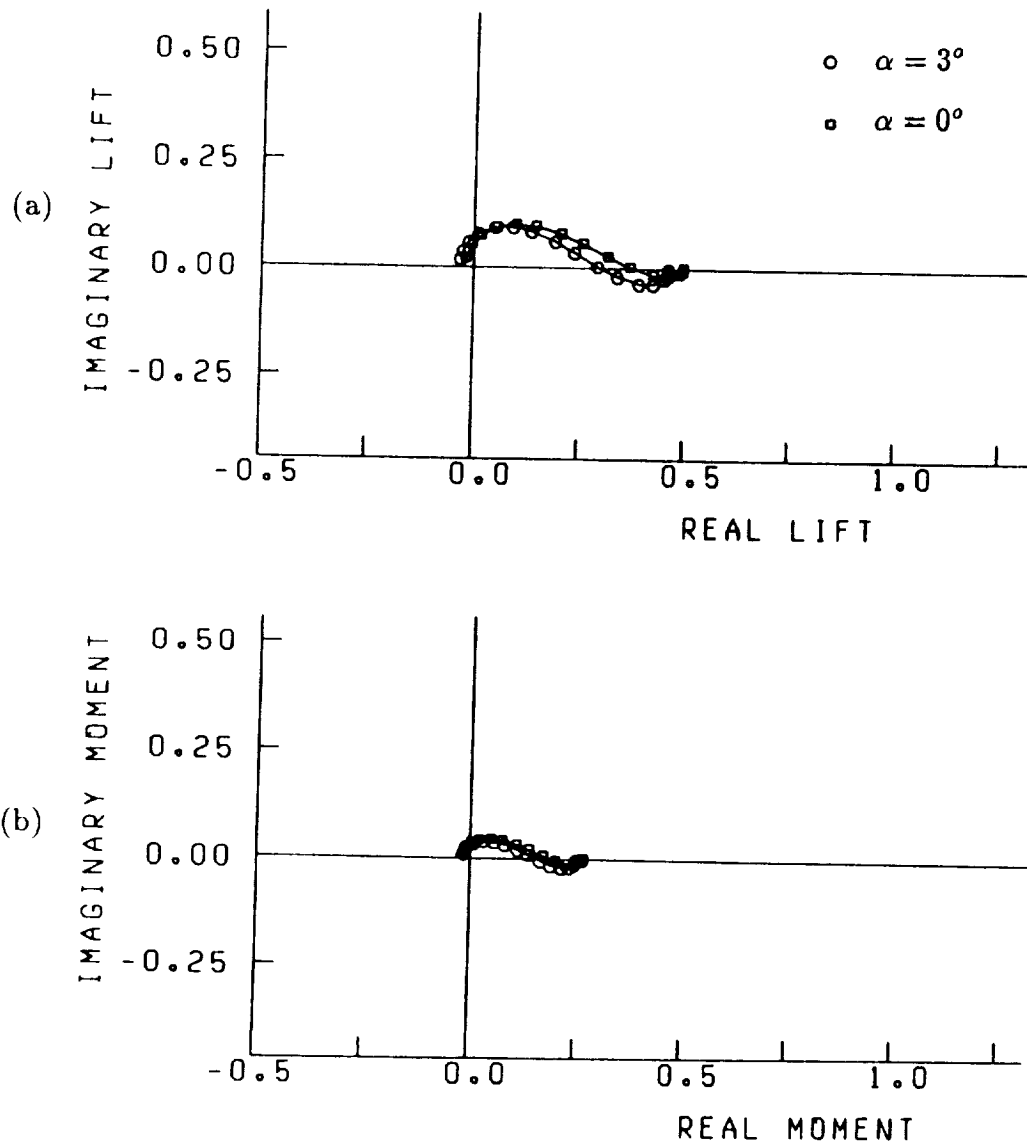
Figure 103. Effect of mean airfoil loading on (a) the unsteady lift and (b) the unsteady moment of a Joukowski airfoil in a three-dimensional gust. $M_\infty = .1$, thickness ratio $= .12$, camber $= 0$. $k_1 = 0.0$, 0.01, 0.03, 0.06, 0.1, 0.2, 0.3, 0.45, 0.6, 0.8, 1.0, 1.3, 1.6, 2.0, 2.5, 3.0, 3.5, 4.0. $k_3 = 0.4$, $|\vec{a}| = 1$, $\frac{a_2}{a_1} = -\frac{7}{4}$, $k_1 = k_2$, $\vec{a} \cdot \vec{k} = 0$, $a_2 > 0$.
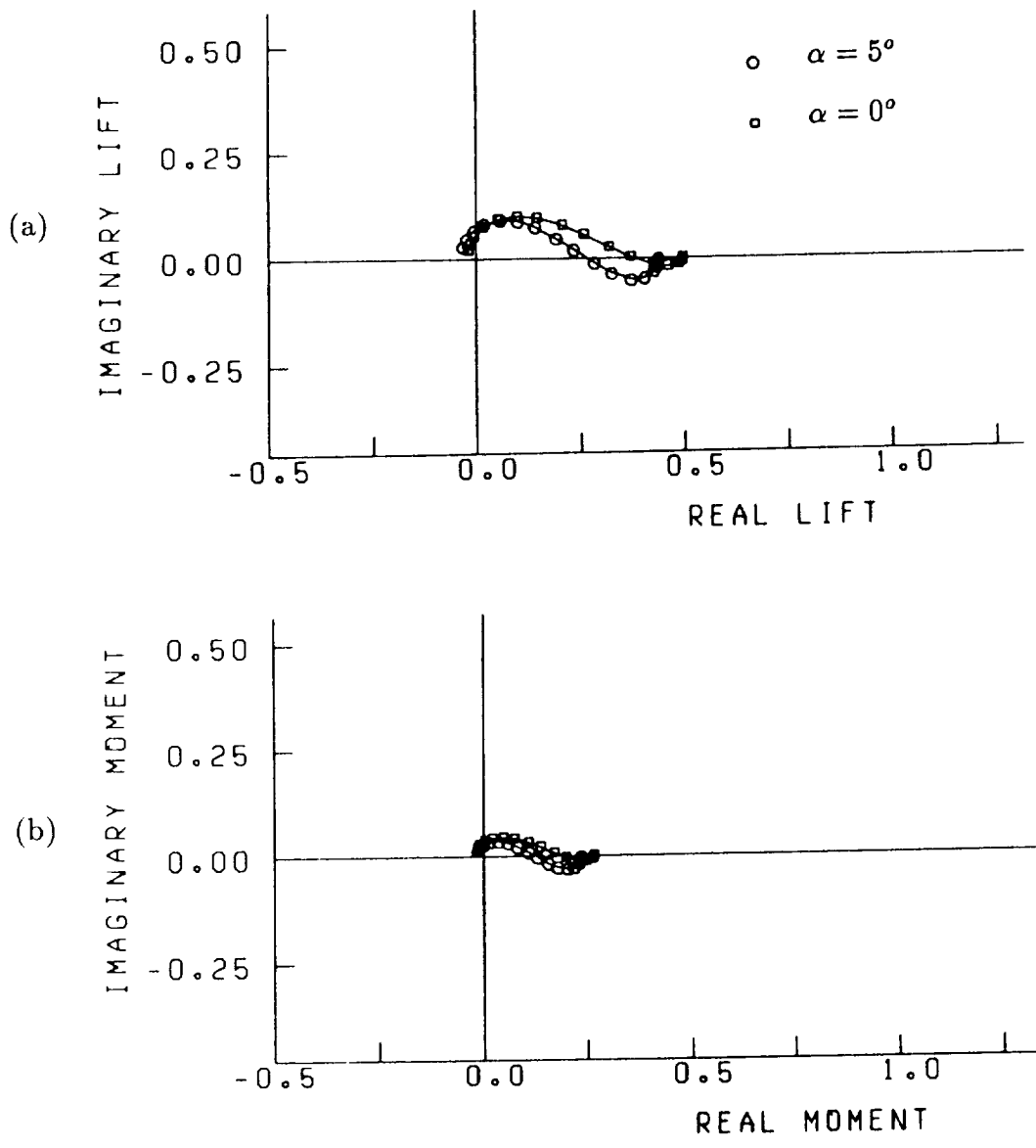
Figure 104.   Effect of mean airfoil loading on (a) the unsteady lift and (b) the unsteady moment of a Joukowski airfoil in a three-dimensional gust. $M_\infty = .1$, thickness ratio $= .12$, camber $= 0$. $k_1 = 0.0$, 0.01, 0.03, 0.06, 0.1, 0.2, 0.3, 0.45, 0.6, 0.8, 1.0, 1.3, 1.6, 2.0, 2.5, 3.0, 3.5, 4.0. $k_3 = 0.4$, $|\vec{a}| = 1$, $\frac{a_2}{a_1} = -\frac{7}{4}$, $k_1 = k_2$, $\vec{a} \cdot \vec{k} = 0$, $a_2 > 0$.

(a)

(b)
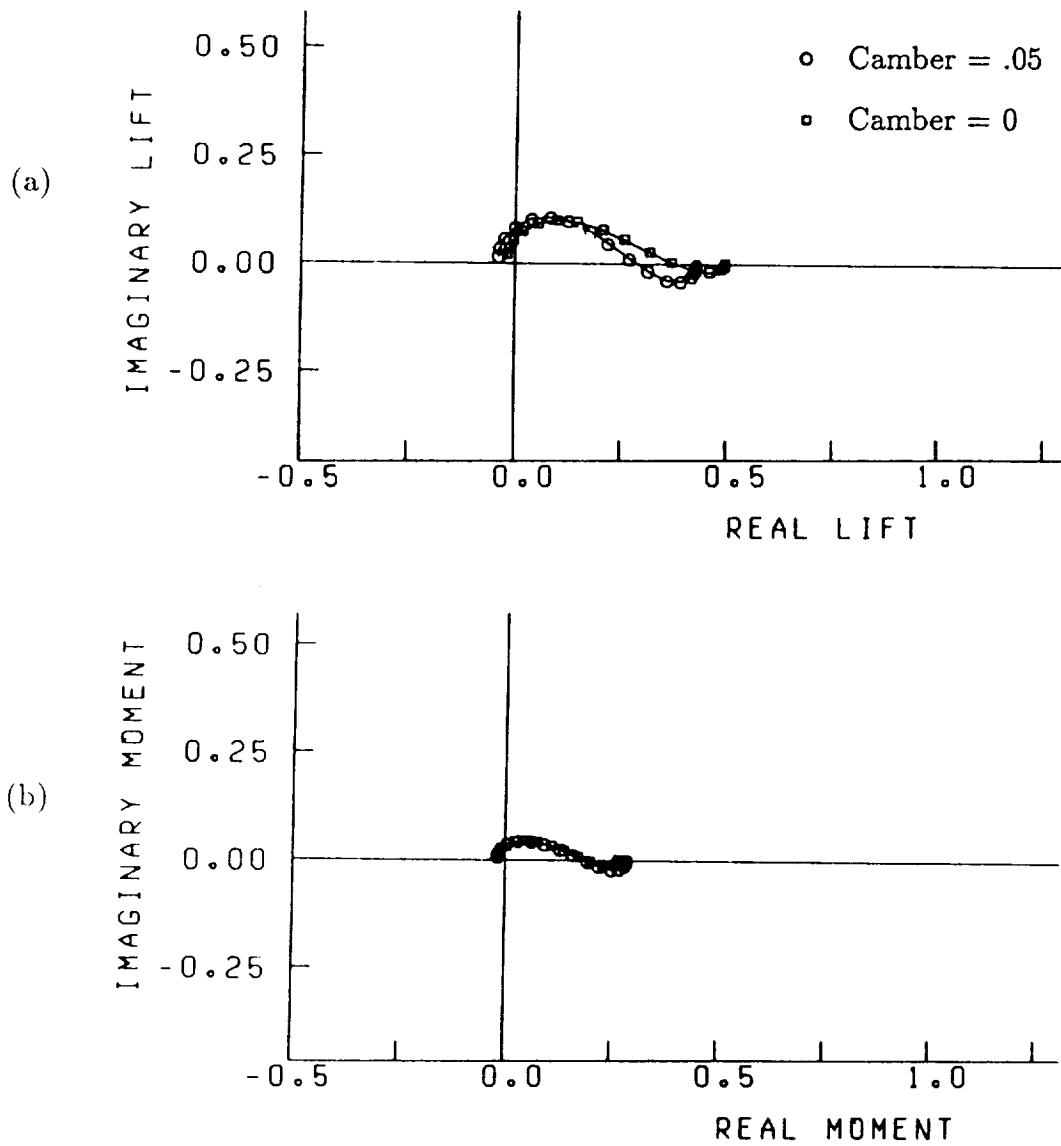
Figure 105.   Effect of mean airfoil loading on (a) the unsteady lift and (b) the
unsteady moment of a Joukowski airfoil in a three-dimensional
gust. $M_\infty = .1$, thickness ratio $= .12$, $\alpha = 0^\circ$. $k_1 = 0.0$,
0.01, 0.03, 0.06, 0.1, 0.2, 0.3, 0.45, 0.6, 0.8, 1.0, 1.3, 1.6, 2.0, 2.5,
3.0, 3.5, 4.0. $k_3 = 0.4$, $|\vec{a}| = 1$, $\frac{a_2}{a_1} = -\frac{7}{4}$, $k_1 = k_2$, $\vec{a} \cdot \vec{k} = 0$,
$a_2 > 0$.
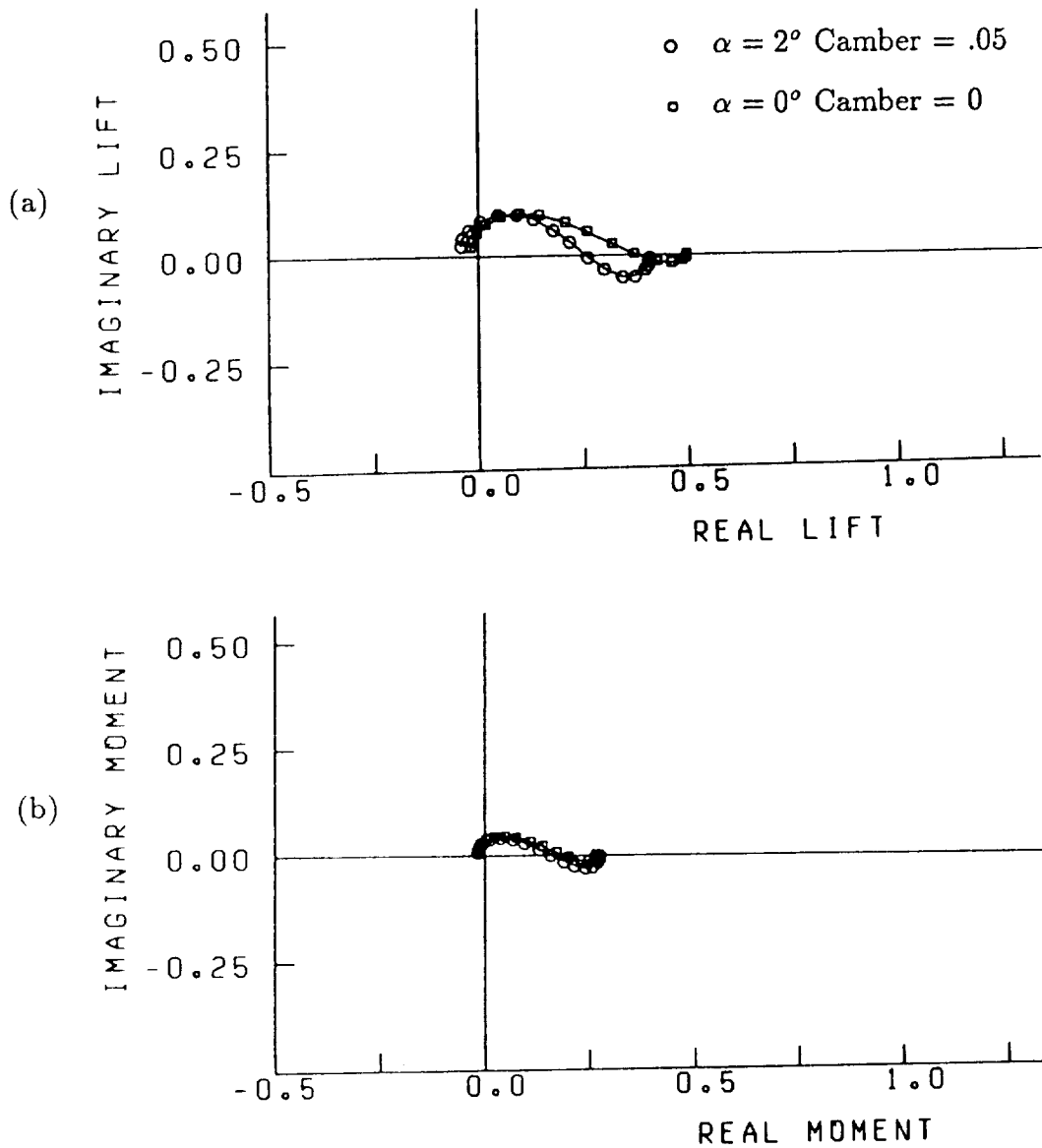
Figure 106. Effect of mean airfoil loading on (a) the unsteady lift and (b) the unsteady moment of a Joukowski airfoil in a three-dimensional gust. $M_\infty = .1$, thickness ratio $= .12$. $k_1 = 0.0$, $0.01, 0.03, 0.06, 0.1, 0.2, 0.3, 0.45, 0.6, 0.8, 1.0, 1.3, 1.6, 2.0, 2.5,$ $3.0, 3.5, 4.0$. $k_3 = 0.4$, $|\vec{a}| = 1$, $\frac{a_2}{a_1} = -\frac{7}{4}$, $k_1 = k_2$, $\vec{a} \cdot \vec{k} = 0$, $a_2 > 0$.

175
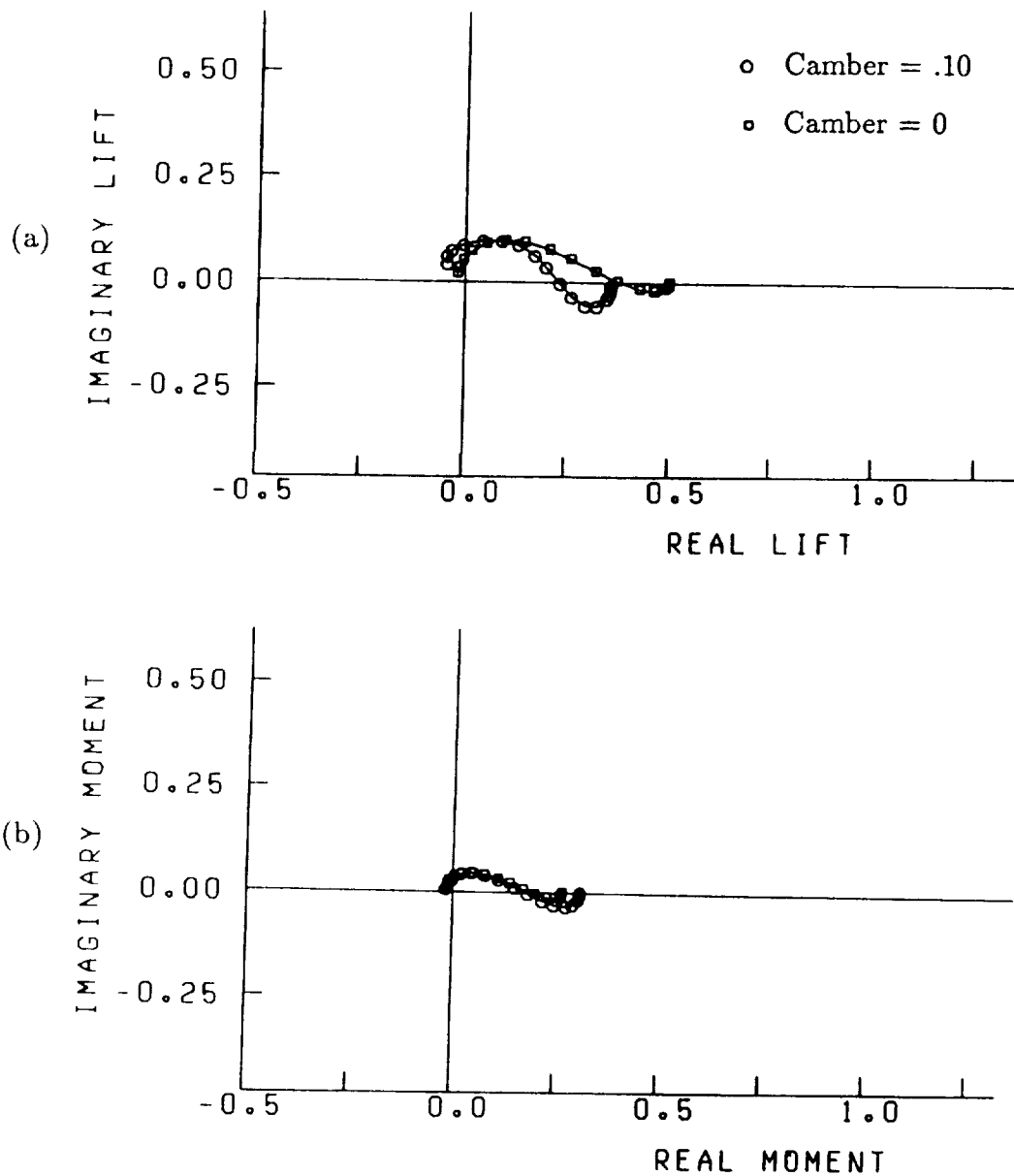
Figure 107. Effect of mean airfoil loading on (a) the unsteady lift and (b) the unsteady moment of a Joukowski airfoil in a three-dimensional gust. $M_\infty = .1$, thickness ratio $= .12$, $\alpha = 0°$. $k_1 = 0.0$, 0.01, 0.03, 0.06, 0.1, 0.2, 0.3, 0.45, 0.6, 0.8, 1.0, 1.3, 1.6, 2.0, 2.5, 3.0, 3.5, 4.0. $k_3 = 0.4$, $|\vec{a}| = 1$, $\frac{a_2}{a_1} = -\frac{7}{4}$, $k_1 = k_2$, $\vec{a} \cdot \vec{k} = 0$, $a_2 > 0$.

176

(a)

(b)
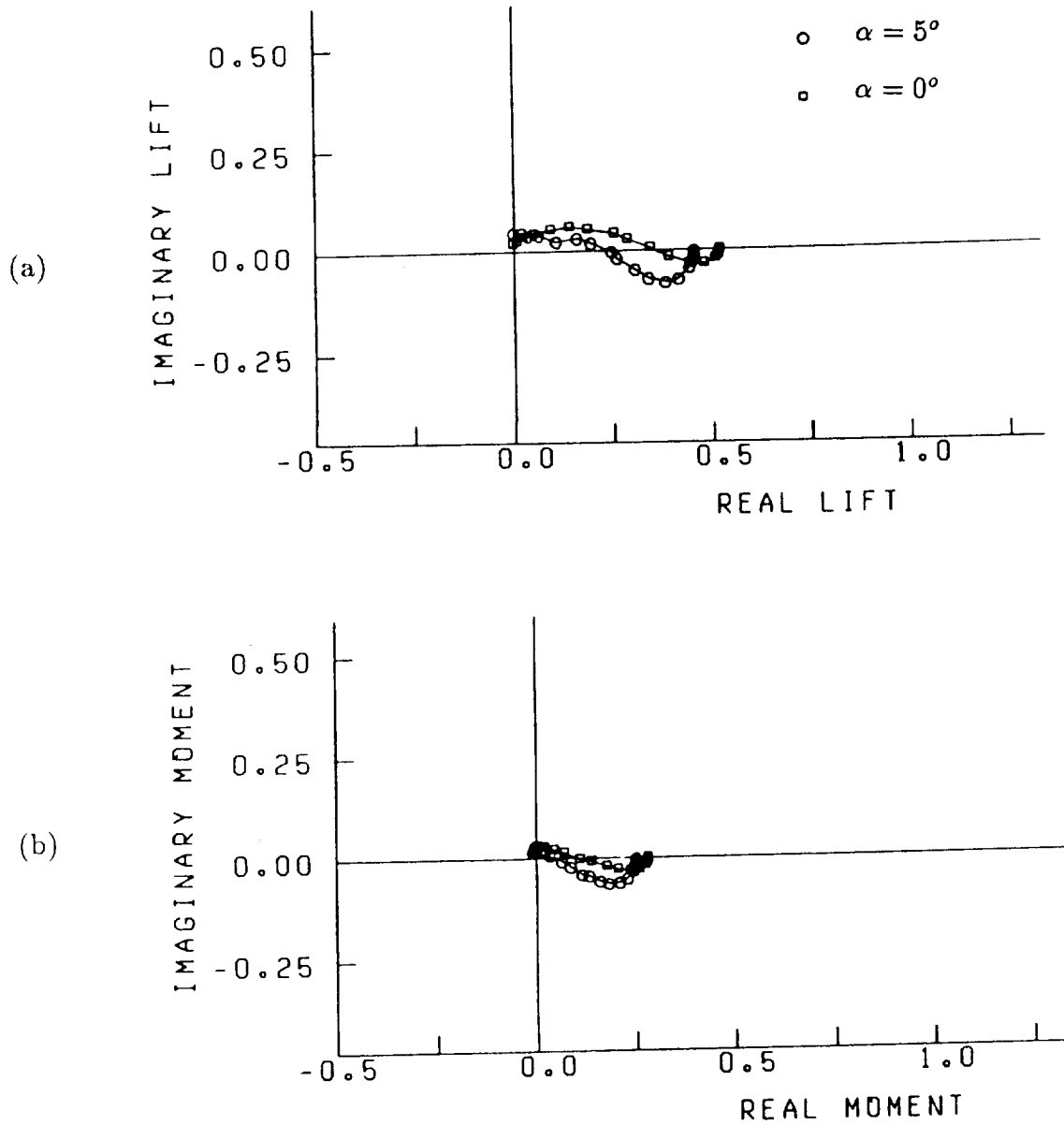
Figure 108. Effect of mean airfoil loading on (a) the unsteady lift and (b) the unsteady moment of a Joukowski airfoil in a three-dimensional gust. $M_\infty = .5$, thickness ratio $= .12$, camber $= 0$. $k_1 = 0.0$, 0.01, 0.03, 0.06, 0.1, 0.2, 0.3, 0.45, 0.6, 0.8, 1.0, 1.3, 1.6, 2.0, 2.5, 3.0, 3.5, 4.0. $k_3 = 0.4$, $|\vec{a}| = 1$, $\frac{a_2}{a_1} = -\frac{7}{4}$, $k_1 = k_2$, $\vec{a} \cdot \vec{k} = 0$, $a_2 > 0$.

177
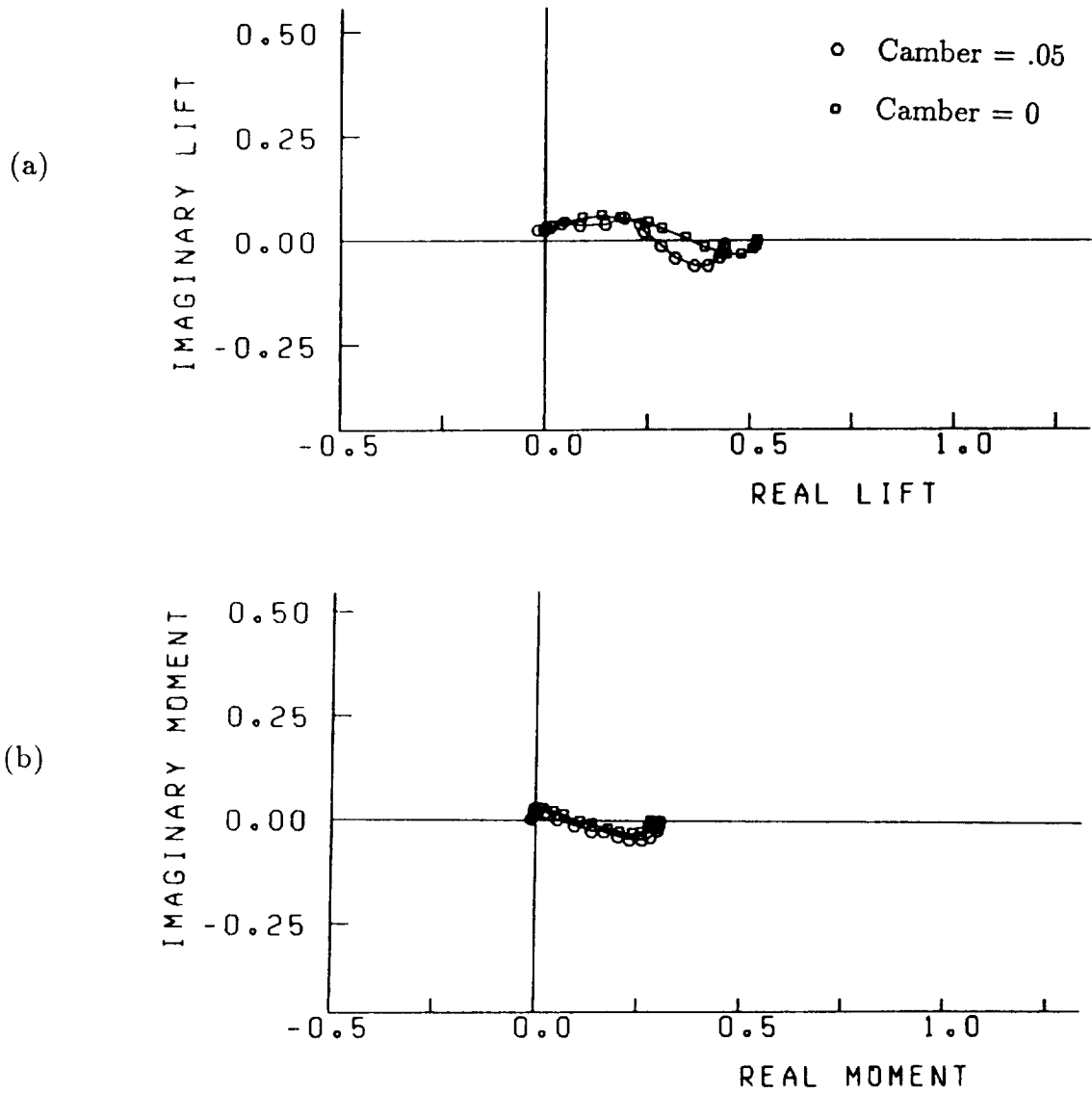
Figure 109. Effect of mean airfoil loading on (a) the unsteady lift and (b) the unsteady moment of a Joukowski airfoil in a three-dimensional gust. $M_\infty = .5$, thickness ratio $= .12$, $\alpha = 0°$. $k_1 = 0.0$, 0.01, 0.03, 0.06, 0.1, 0.2, 0.3, 0.45, 0.6, 0.8, 1.0, 1.3, 1.6, 2.0, 2.5, 3.0, 3.5, 4.0. $k_3 = 0.4$, $|\vec{a}| = 1$, $\frac{a_2}{a_1} = -\frac{7}{4}$, $k_1 = k_2$, $\vec{a} \cdot \vec{k} = 0$, $a_2 > 0$.
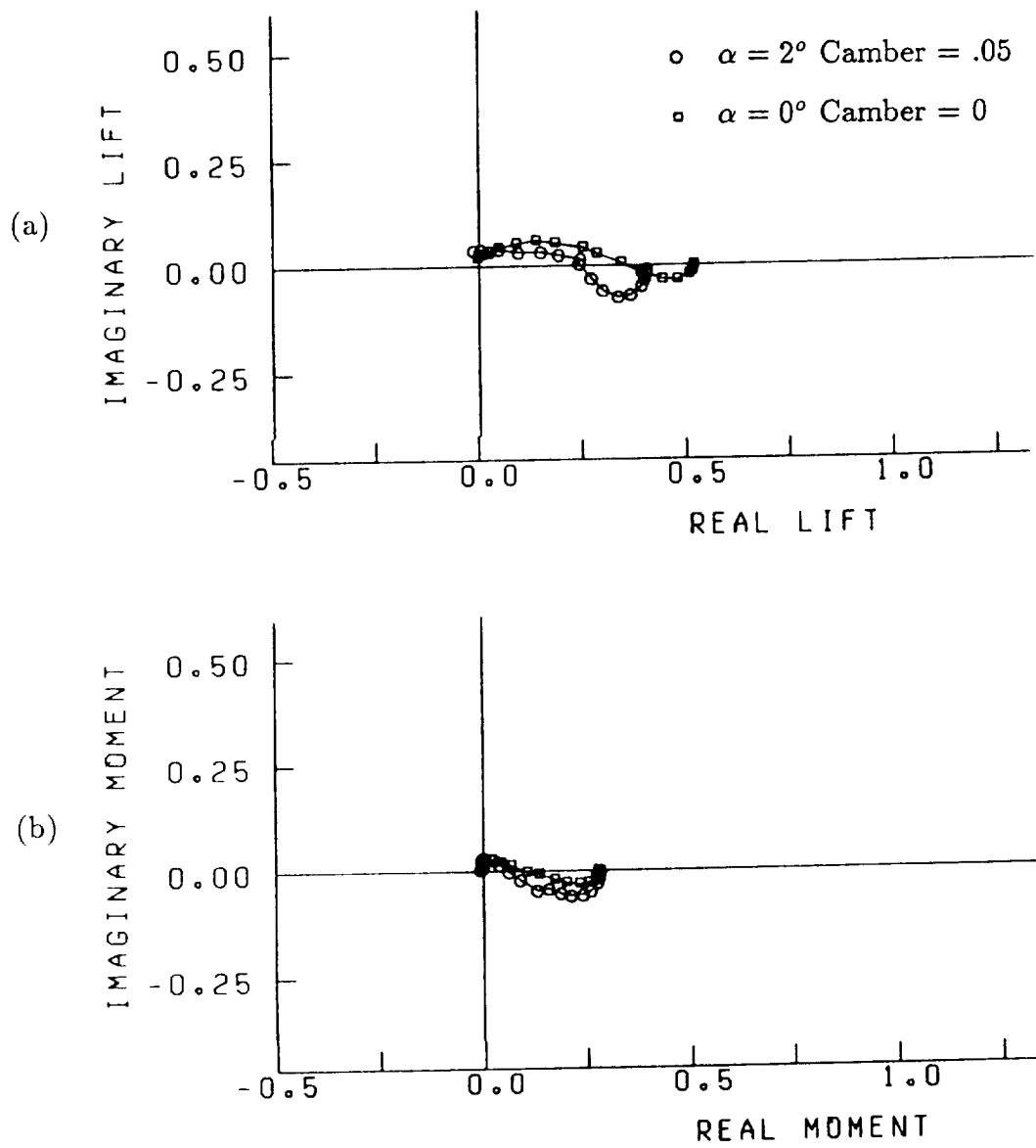
Figure 110. Effect of mean airfoil loading on (a) the unsteady lift and (b) the unsteady moment of a Joukowski airfoil in a three-dimensional gust. $M_\infty = .5$, thickness ratio $= .12$. $k_1 = 0.0$, 0.01, 0.03, 0.06, 0.1, 0.2, 0.3, 0.45, 0.6, 0.8, 1.0, 1.3, 1.6, 2.0, 2.5, 3.0, 3.5, 4.0. $k_3 = 0.4$, $|\vec{a}| = 1$, $\frac{a_2}{a_1} = -\frac{7}{4}$, $k_1 = k_2$, $\vec{a} \cdot \vec{k} = 0$, $a_2 > 0$.

179

(a)

(b)
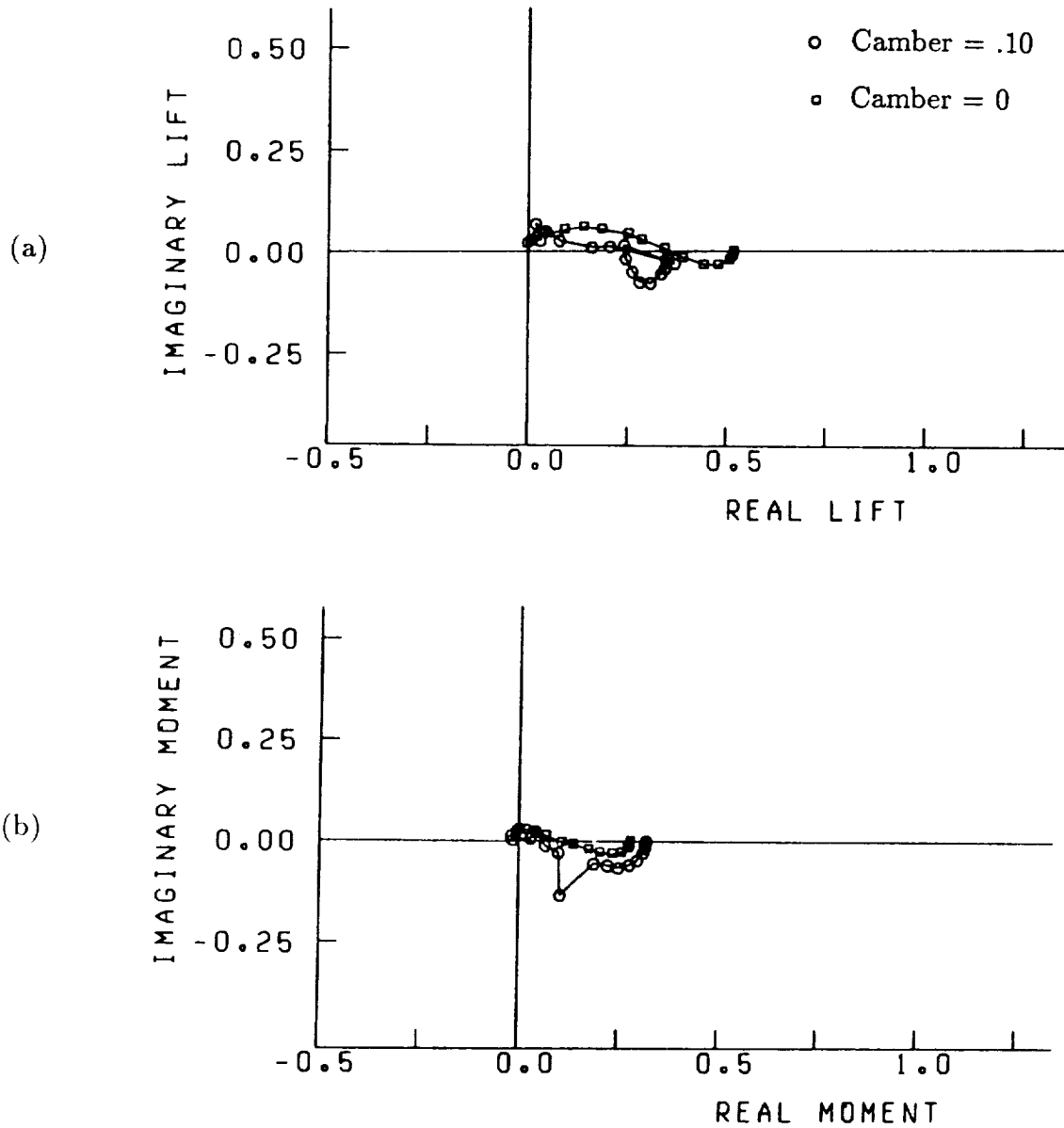
Figure 111. Effect of mean airfoil loading on (a) the unsteady lift and (b) the unsteady moment of a Joukowski airfoil in a three-dimensional gust. $M_\infty = .5$, thickness ratio $= .12$, $\alpha = 0^o$. $k_1 = 0.0$, 0.01, 0.03, 0.06, 0.1, 0.2, 0.3, 0.45, 0.6, 0.8, 1.0, 1.3, 1.6, 2.0, 2.5, 3.0, 3.5, 4.0. $k_3 = 0.4$, $|\vec{a}| = 1$, $\frac{a_2}{a_1} = -\frac{7}{4}$, $k_1 = k_2$, $\vec{a} \cdot \vec{k} = 0$, $a_2 > 0$.
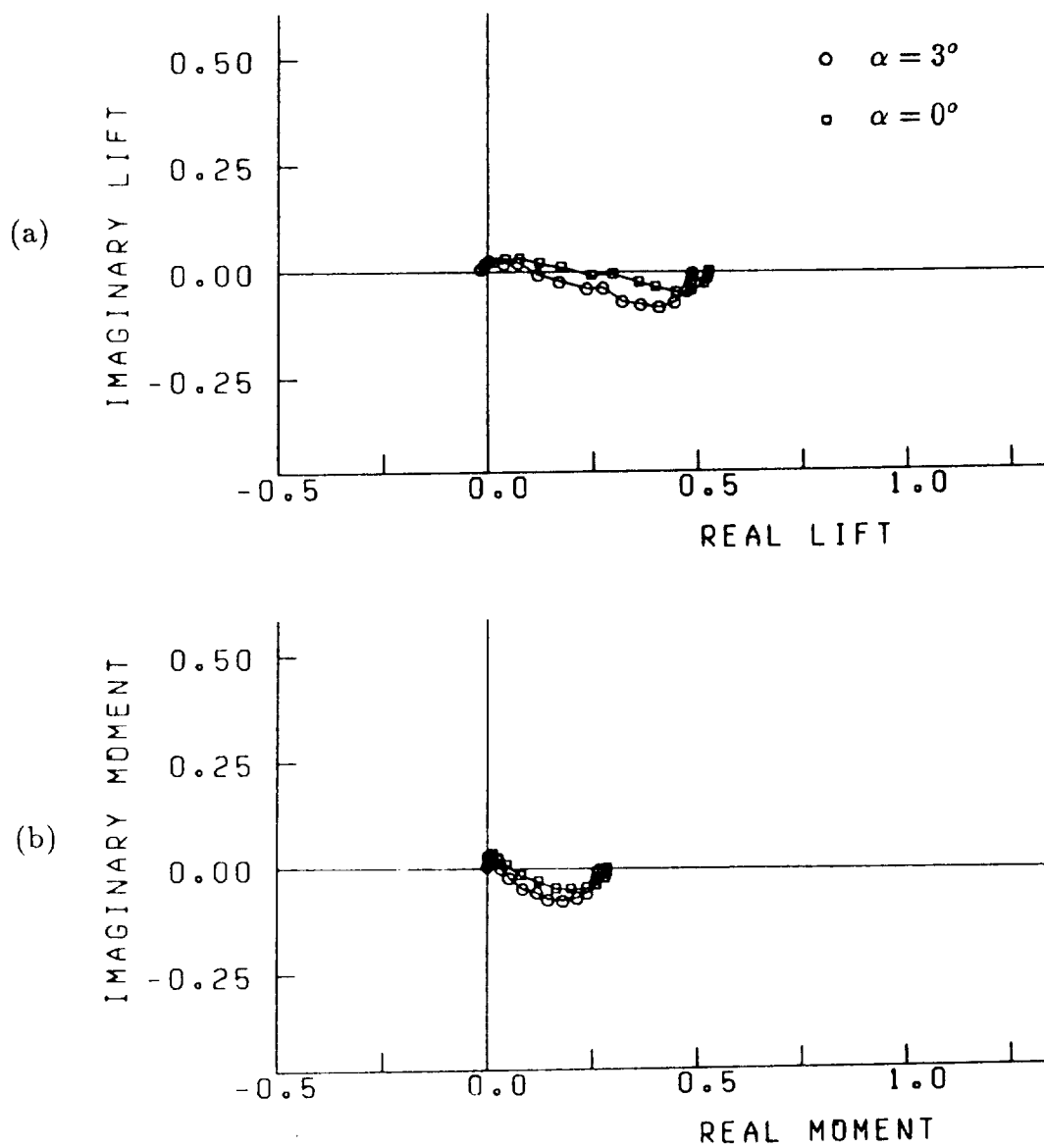
Figure 112.   Effect of mean airfoil loading on (a) the unsteady lift and (b) the unsteady moment of a Joukowski airfoil in a three-dimensional gust. $M_\infty = .6$, thickness ratio $= .12$, camber $= 0$. $k_1 = 0.0$, 0.01, 0.03, 0.06, 0.1, 0.2, 0.3, 0.45, 0.6, 0.8, 1.0, 1.3, 1.6, 2.0, 2.5, 3.0, 3.5, 4.0. $k_3 = 0.4$, $|\vec{a}| = 1$, $\frac{a_2}{a_1} = -\frac{7}{4}$, $k_1 = k_2$, $\vec{a} \cdot \vec{k} = 0$, $a_2 > 0$.

181
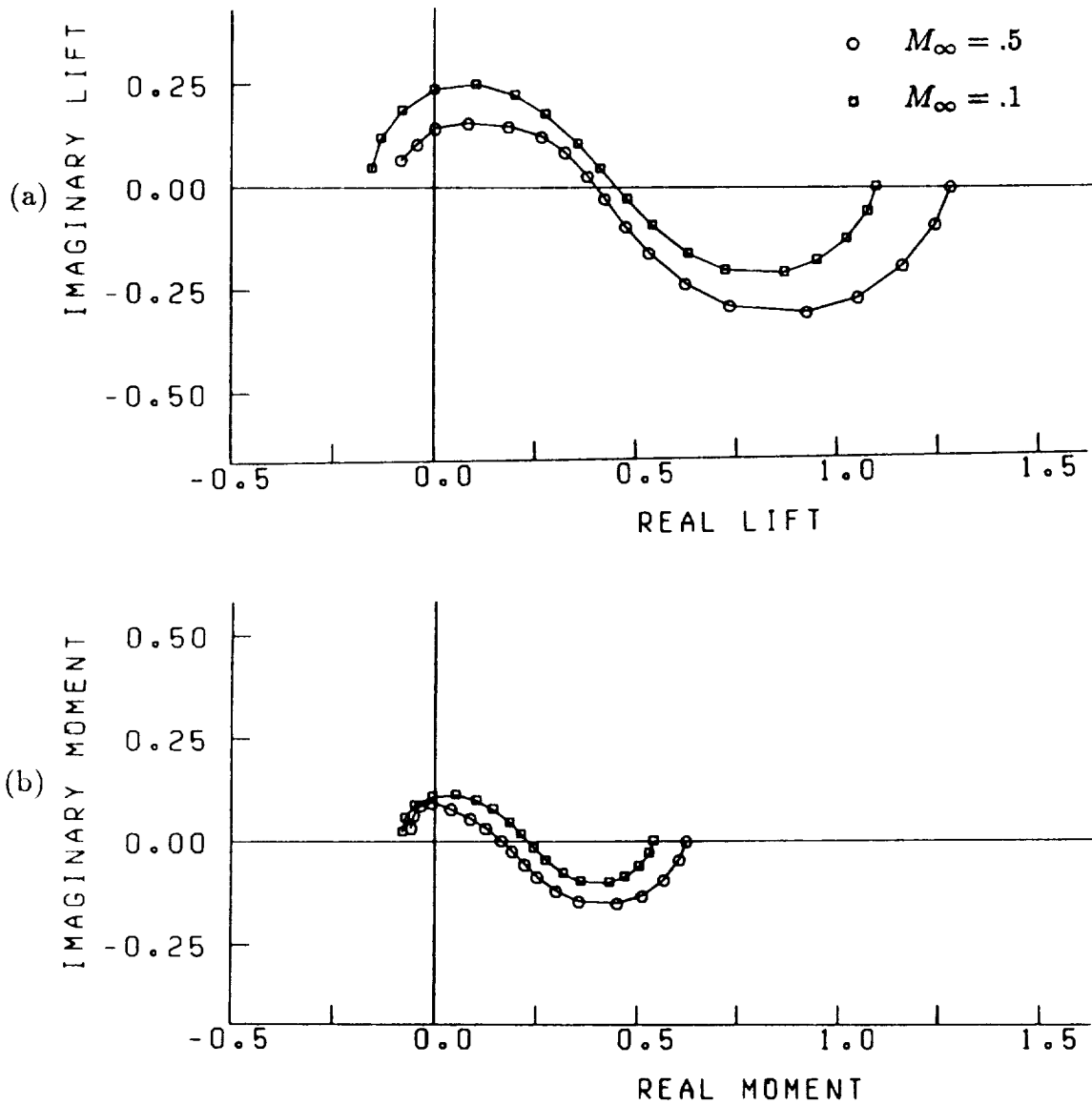
Figure 113. Effect of Mach number on (a) the unsteady lift and (b) the unsteady moment of a Joukowski airfoil in a transverse gust. $\alpha = 0^o$, thickness ratio $= .12$, camber $= 0$. $k_1 = 0.0, 0.01, 0.03, 0.06, 0.1, 0.2, 0.3, 0.45, 0.6, 0.8, 1.0, 1.3, 1.6, 2.0, 2.5, 3.0, 3.5, 4.0$.
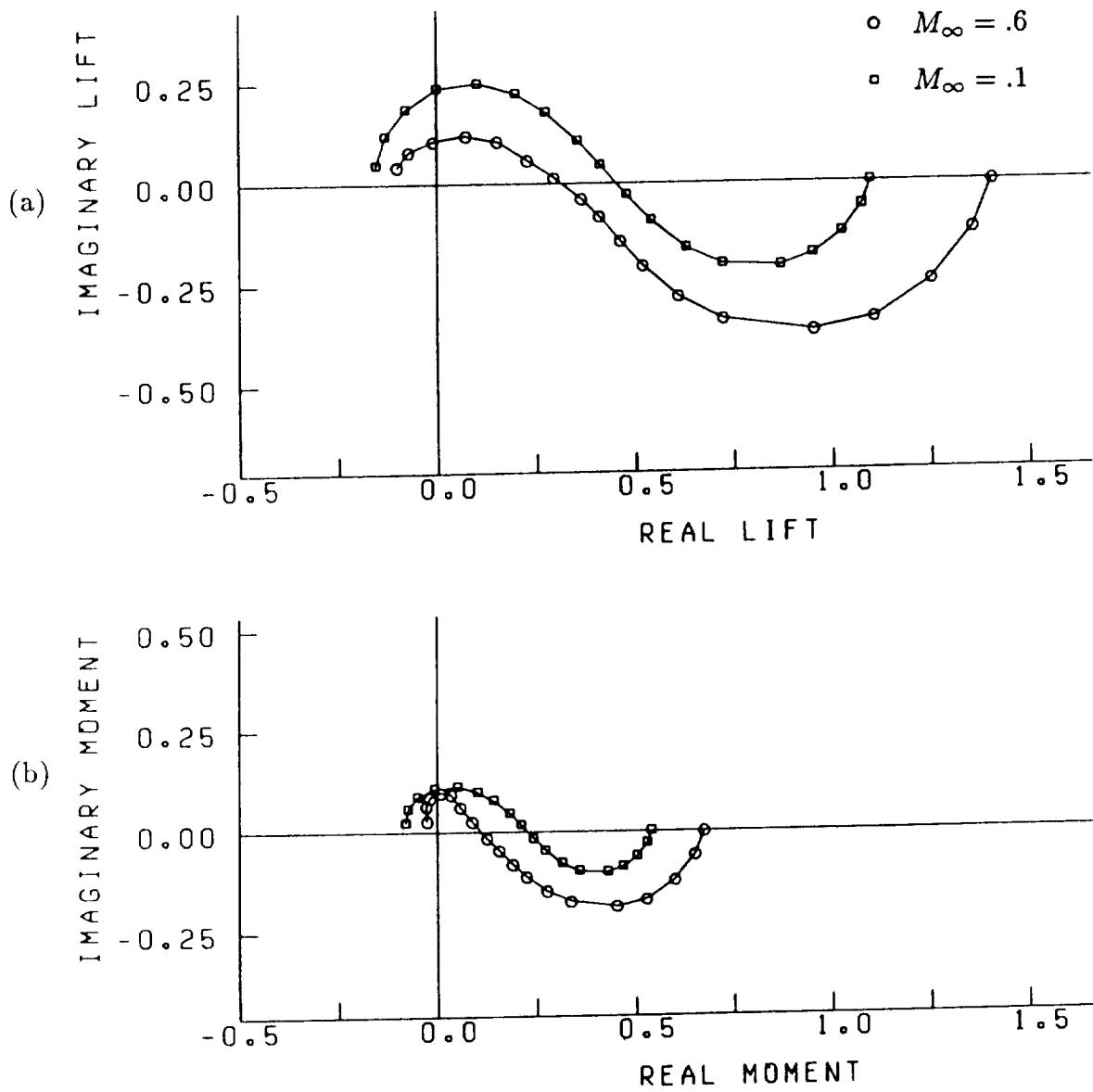
Figure 114. Effect of Mach number on (a) the unsteady lift and (b) the
unsteady moment of a Joukowski airfoil in a transverse gust.
$\alpha = 0^o$, thickness ratio = .12, camber = 0. $k_1 = 0.0, 0.01,$
0.03, 0.06, 0.1, 0.2, 0.3, 0.45, 0.6, 0.8, 1.0, 1.3, 1.6, 2.0, 2.5,
3.0, 3.5, 4.0.
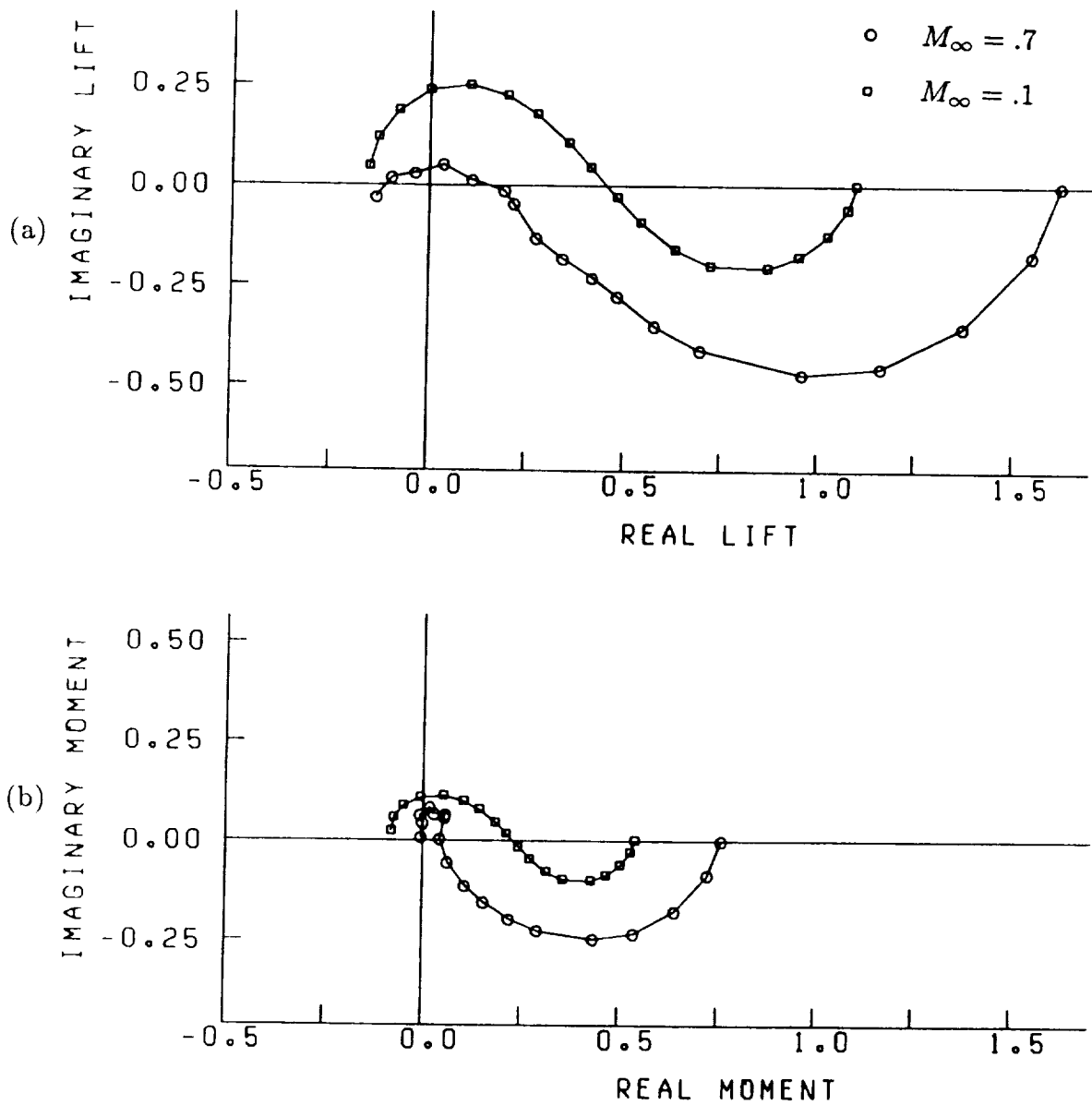
Figure 115.   Effect of Mach number on (a) the unsteady lift and (b) the
unsteady moment of a Joukowski airfoil in a transverse gust.
$\alpha = 0^o$, thickness ratio $= .12$, camber $= 0$. $k_1 = 0.0, 0.01,$
0.03, 0.06, 0.1, 0.2, 0.3, 0.45, 0.6, 0.8, 1.0, 1.3, 1.6, 2.0, 2.5,
3.0, 3.5, 4.0.
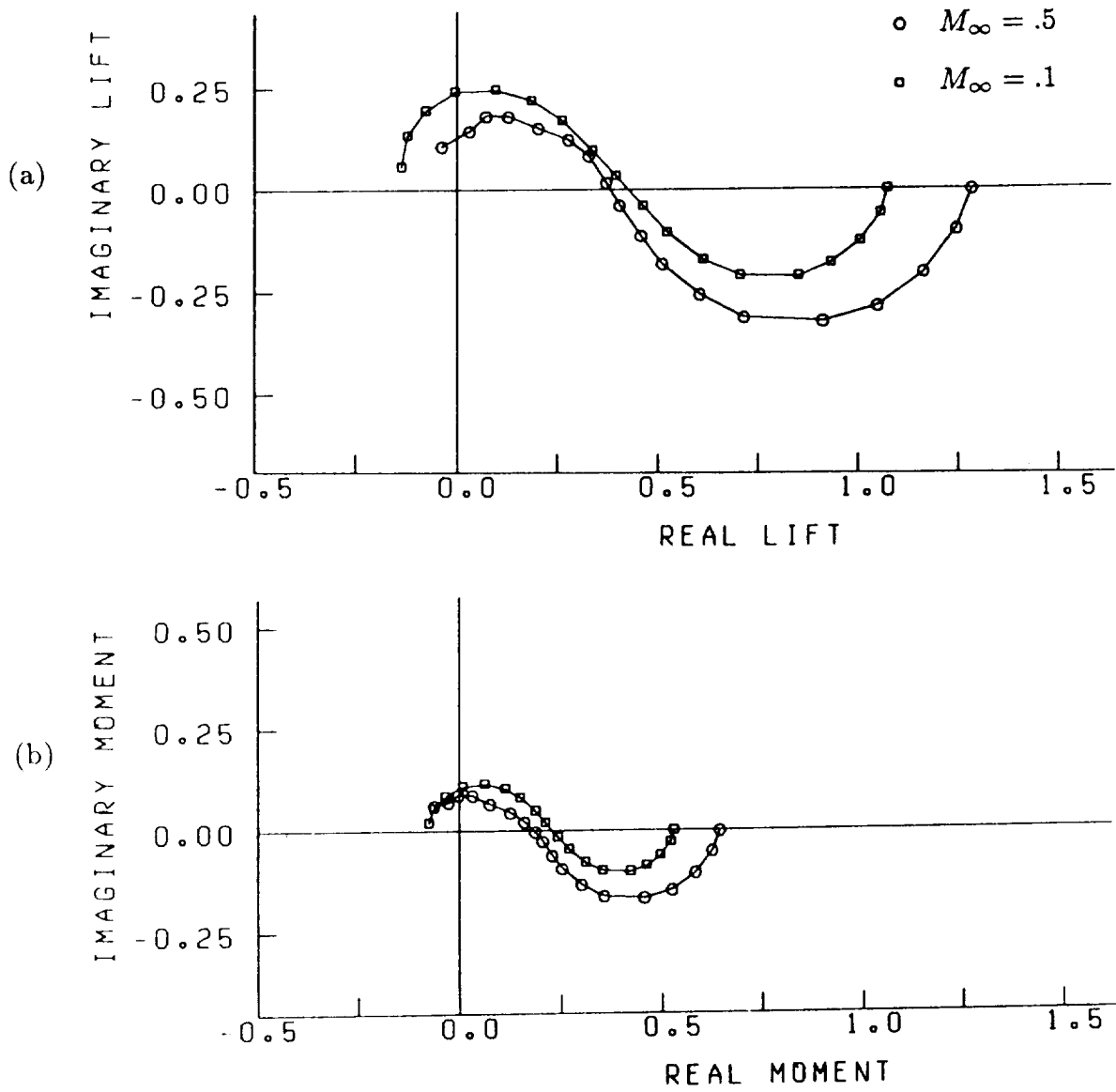
Figure 116. Effect of Mach number on (a) the unsteady lift and (b) the unsteady moment of a Joukowski airfoil in a transverse gust. $\alpha = 5^{\circ}$, thickness ratio $= .12$, camber $= 0$. $k_1 = 0.0, 0.01, 0.03, 0.06, 0.1, 0.2, 0.3, 0.45, 0.6, 0.8, 1.0, 1.3, 1.6, 2.0, 2.5, 3.0, 3.5, 4.0$.
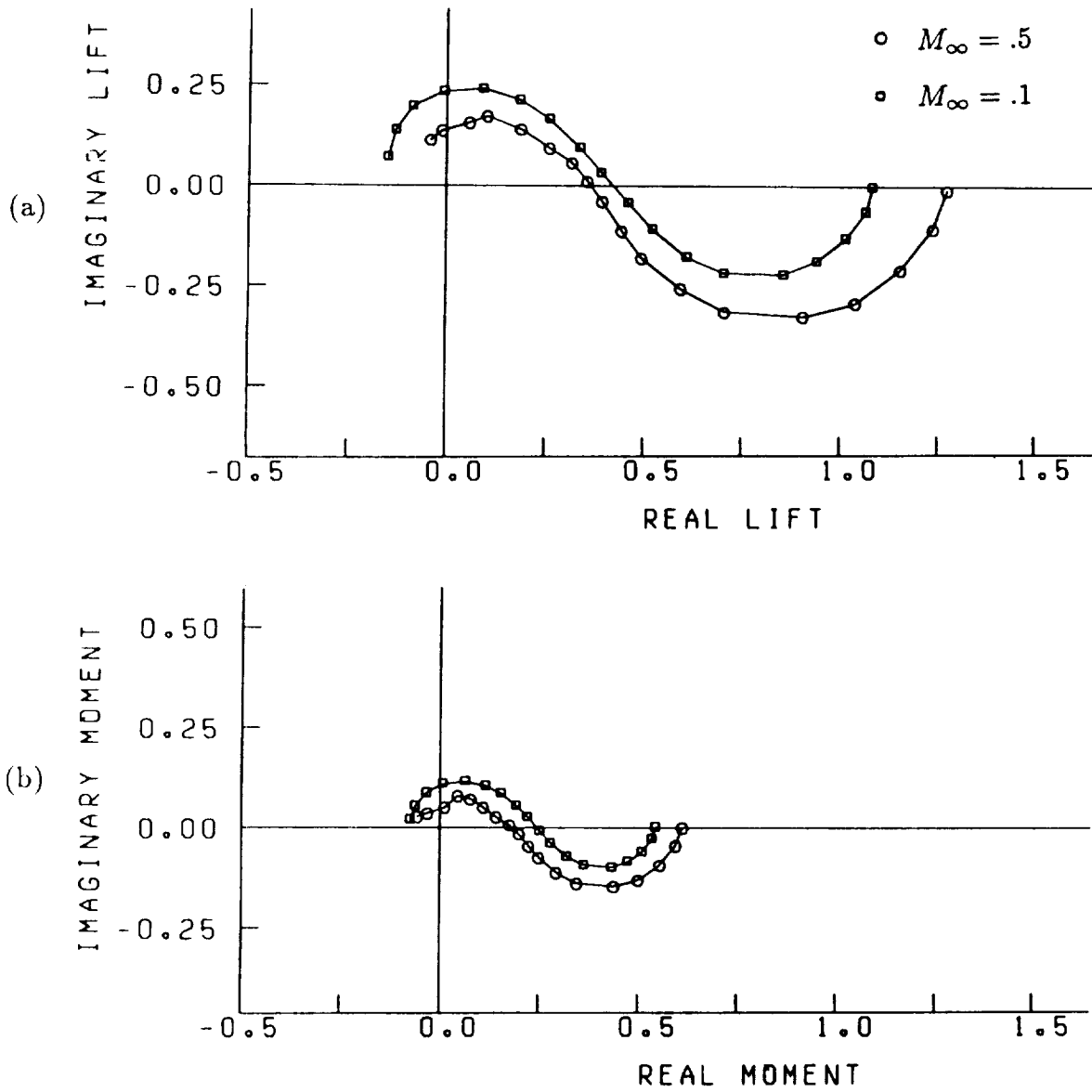
Figure 117.   Effect of Mach number on (a) the unsteady lift and (b) the
unsteady moment of a Joukowski airfoil in a transverse gust.
$\alpha = 0^o$, thickness ratio $= .12$, camber $= .05$. $k_1 = 0.0, 0.01$,
0.03, 0.06, 0.1, 0.2, 0.3, 0.45, 0.6, 0.8, 1.0, 1.3, 1.6, 2.0, 2.5,
3.0, 3.5, 4.0.

186
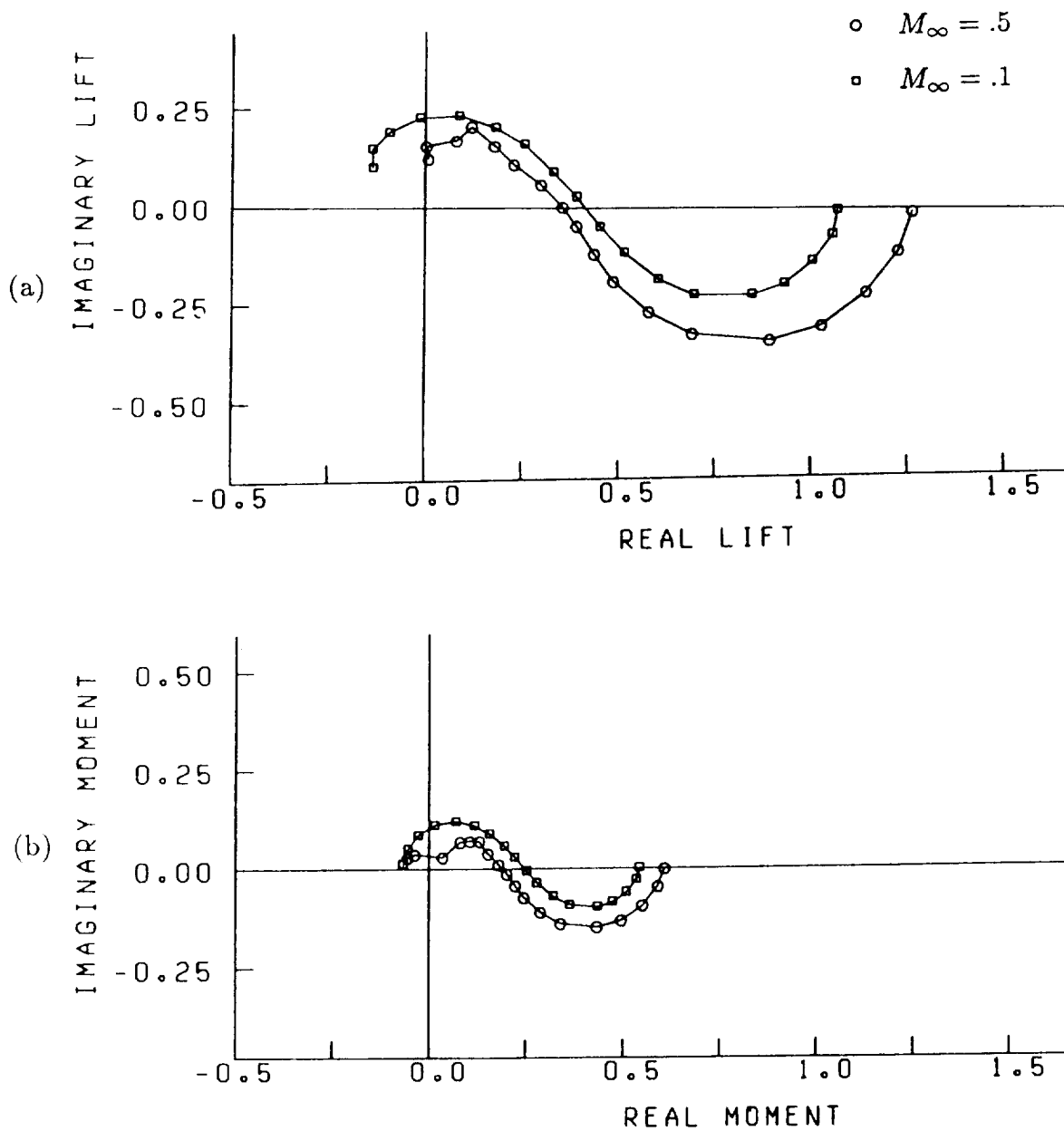
Figure 118. Effect of Mach number on (a) the unsteady lift and (b) the unsteady moment of a Joukowski airfoil in a transverse gust. $\alpha = 2^o$, thickness ratio = .12, camber = .05. k_1 = 0.0, 0.01, 0.03, 0.06, 0.1, 0.2, 0.3, 0.45, 0.6, 0.8, 1.0, 1.3, 1.6, 2.0, 2.5, 3.0, 3.5, 4.0.
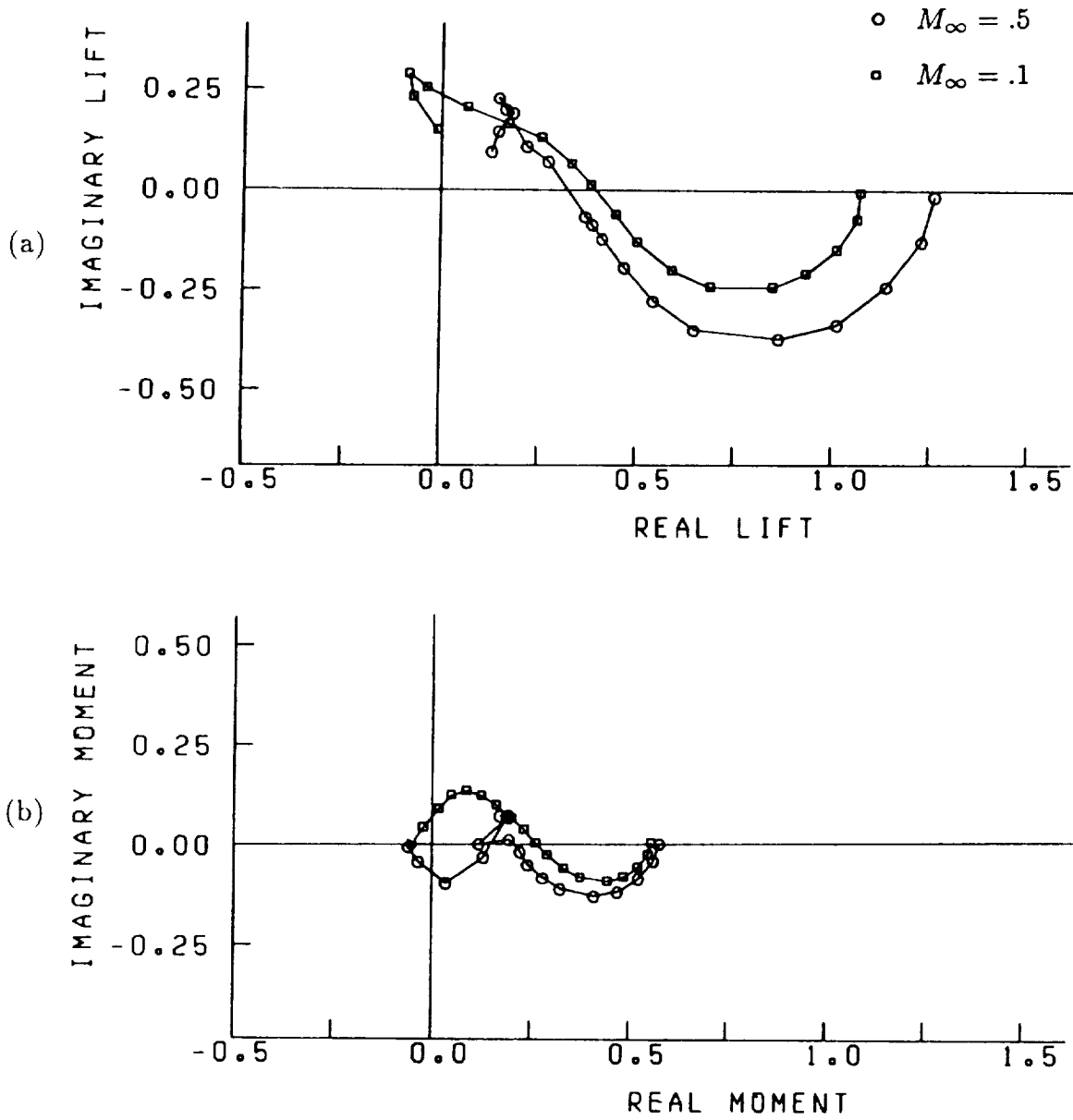
Figure 119. Effect of Mach number on (a) the unsteady lift and (b) the
unsteady moment of a Joukowski airfoil in a transverse gust.
$\alpha = 0^o$, thickness ratio $= .12$, camber $= .10$. $k_1 = 0.0, 0.01$,
0.03, 0.06, 0.1, 0.2, 0.3, 0.45, 0.6, 0.8, 1.0, 1.3, 1.6, 2.0, 2.5,
.3.0, 3.5, 4.0.
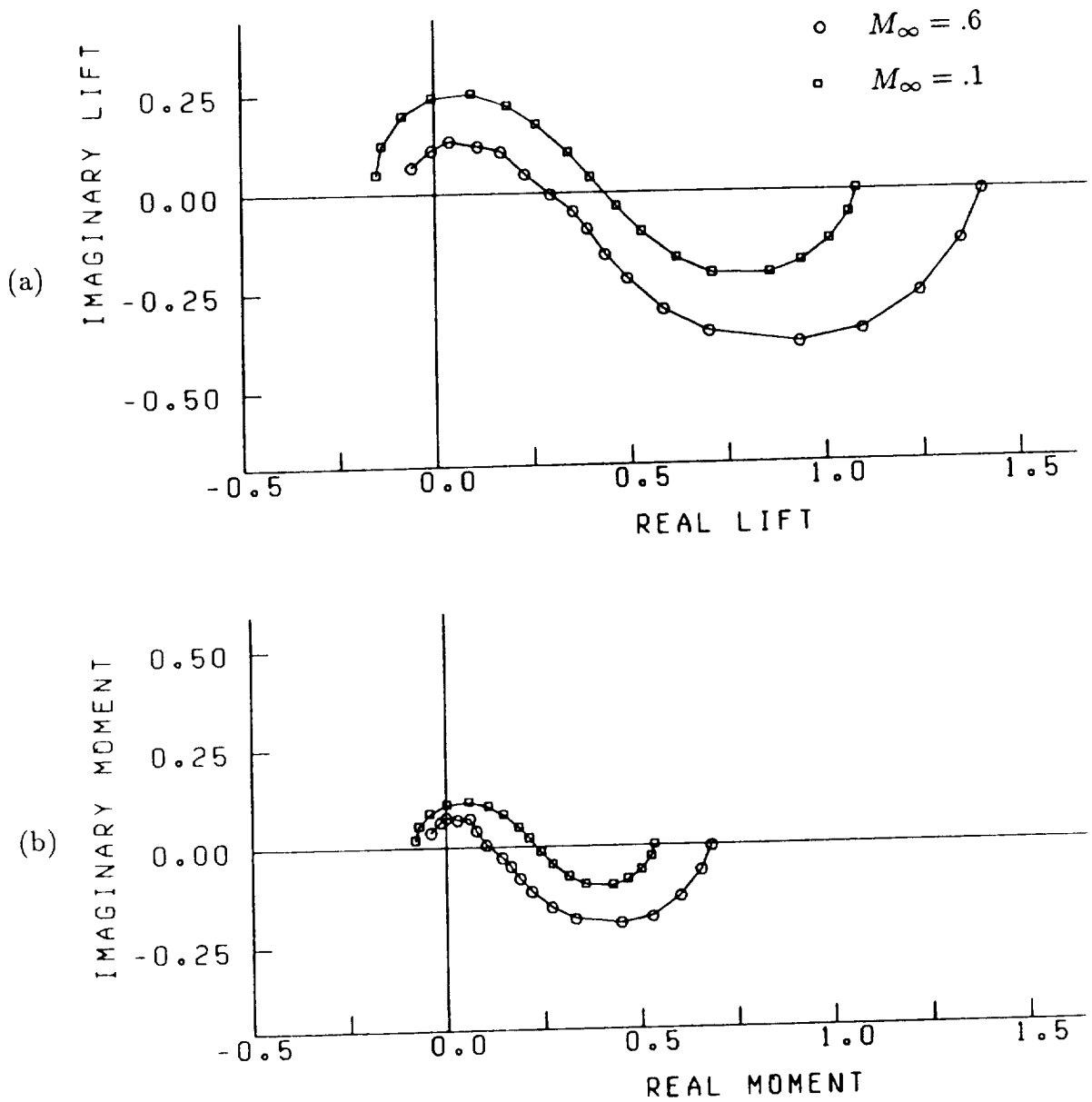
Figure 120. Effect of Mach number on (a) the unsteady lift and (b) the unsteady moment of a Joukowski airfoil in a transverse gust. $\alpha = 3°$, thickness ratio $= .12$, camber $= 0$. $k_1 = 0.0$, 0.01, 0.03, 0.06, 0.1, 0.2, 0.3, 0.45, 0.6, 0.8, 1.0, 1.3, 1.6, 2.0, 2.5, 3.0, 3.5, 4.0.
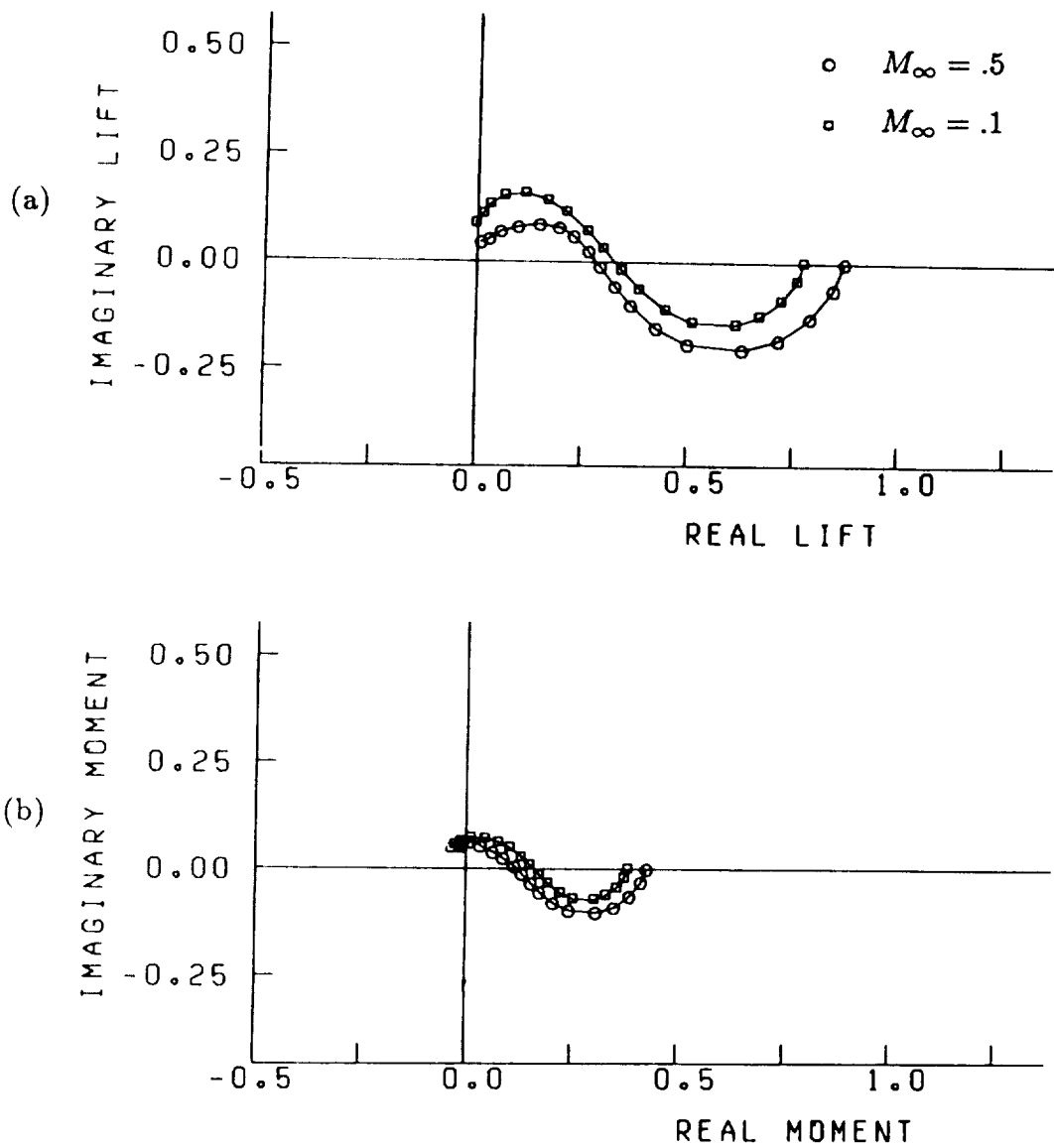
Figure 121.   Effect of Mach number on (a) the unsteady lift and (b) the
unsteady moment of a Joukowski airfoil in a transverse and
longitudinal gust.   thickness ratio = .12, $\alpha = 0^{o}$, camber = 0.
k_1 = 0.0, 0.01, 0.03, 0.06, 0.1, 0.2, 0.3, 0.45, 0.6, 0.8, 1.0,
1.3, 1.6, 2.0, 2.5, 3.0, 3.5, 4.0. $-a_1 = a_2 = .7071$, $k_1 = k_2$,
$a_3 = k_3 = 0$.

Figure 122. Effect of Mach number on (a) the unsteady lift and (b) the unsteady moment of a Joukowski airfoil in a transverse and longitudinal gust. thickness ratio = .12, $\alpha = 0^o$, camber = 0. k_1 = 0.0, 0.01, 0.03, 0.06, 0.1, 0.2, 0.3, 0.45, 0.6, 0.8, 1.0, 1.3, 1.6, 2.0, 2.5, 3.0, 3.5, 4.0. $-a_1 = a_2 = .7071$, $k_1 = k_2$, $a_3 = k_3 = 0$.

191

Figure 123. Effect of Mach number on (a) the unsteady lift and (b) the unsteady moment of a Joukowski airfoil in a transverse and longitudinal gust. thickness ratio $= .12$, $\alpha = 0^o$, camber $= 0$. $k_1 = 0.0, 0.01, 0.03, 0.06, 0.1, 0.2, 0.3, 0.45, 0.6, 0.8, 1.0,$ $1.3, 1.6, 2.0, 2.5, 3.0, 3.5, 4.0.$ $-a_1 = a_2 = .7071$, $k_1 = k_2$, $a_3 = k_3 = 0$.

192

Figure 124.   Effect of Mach number on (a) the unsteady lift and (b) the
unsteady moment of a Joukowski airfoil in a transverse and
longitudinal gust. thickness ratio $= .12$, $\alpha = 5^{o}$, camber $= 0$.
$k_1 = 0.0, 0.01, 0.03, 0.06, 0.1, 0.2, 0.3, 0.45, 0.6, 0.8, 1.0,$
$1.3, 1.6, 2.0, 2.5, 3.0, 3.5, 4.0.$ $-a_1 = a_2 = .7071,$ $k_1 = k_2,$
$a_3 = k_3 = 0.$

193
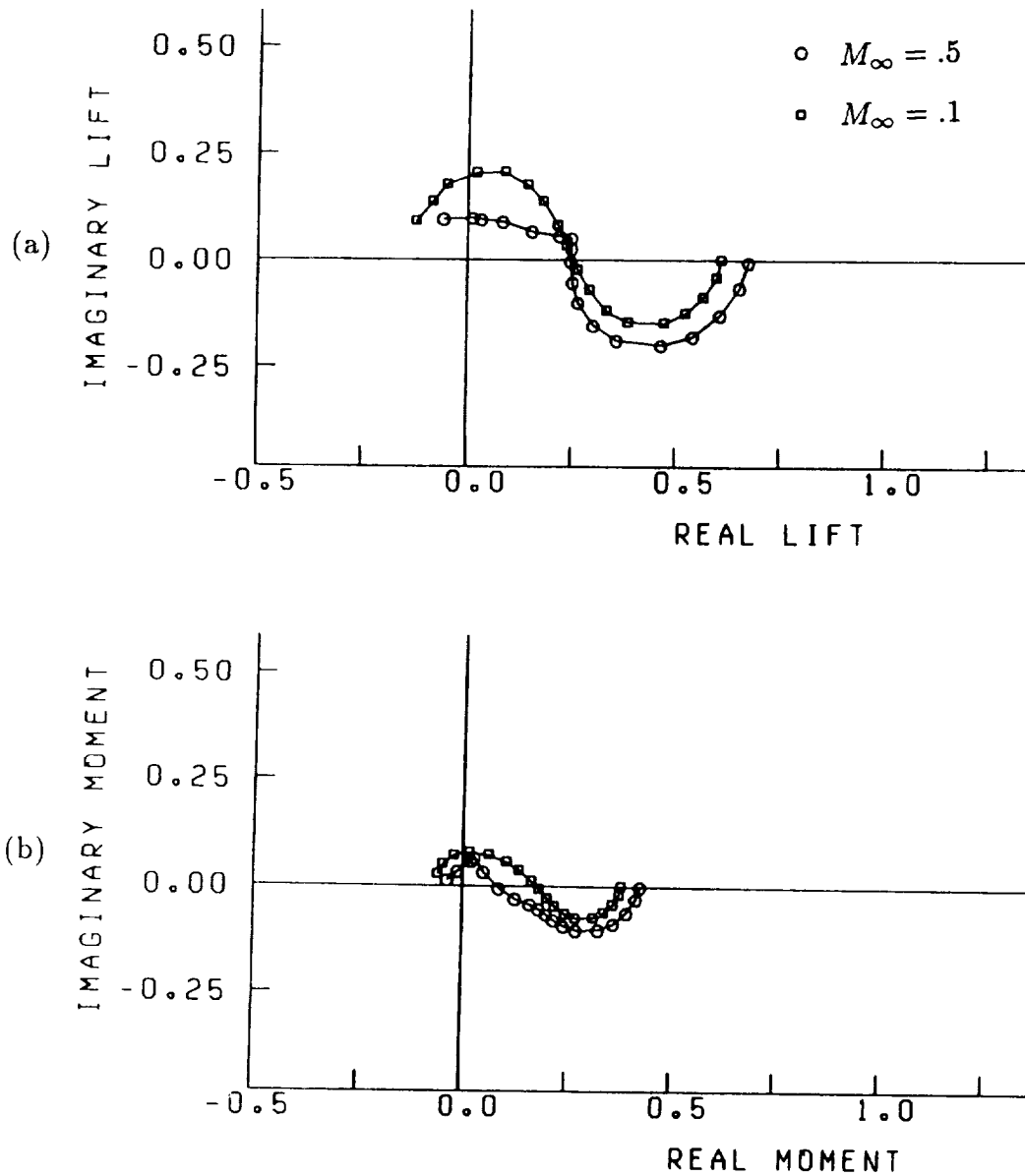
Figure 125.   Effect of Mach number on (a) the unsteady lift and (b) the unsteady moment of a Joukowski airfoil in a transverse and longitudinal gust.   thickness ratio = .12, $\alpha = 0°$,   camber = .05. k_1 = 0.0, 0.01, 0.03, 0.06, 0.1, 0.2, 0.3, 0.45, 0.6, 0.8, 1.0, 1.3, 1.6, 2.0, 2.5, 3.0, 3.5, 4.0. $-a_1 = a_2 = .7071$, $k_1 = k_2$, $a_3 = k_3 = 0$.

(a)

(b)
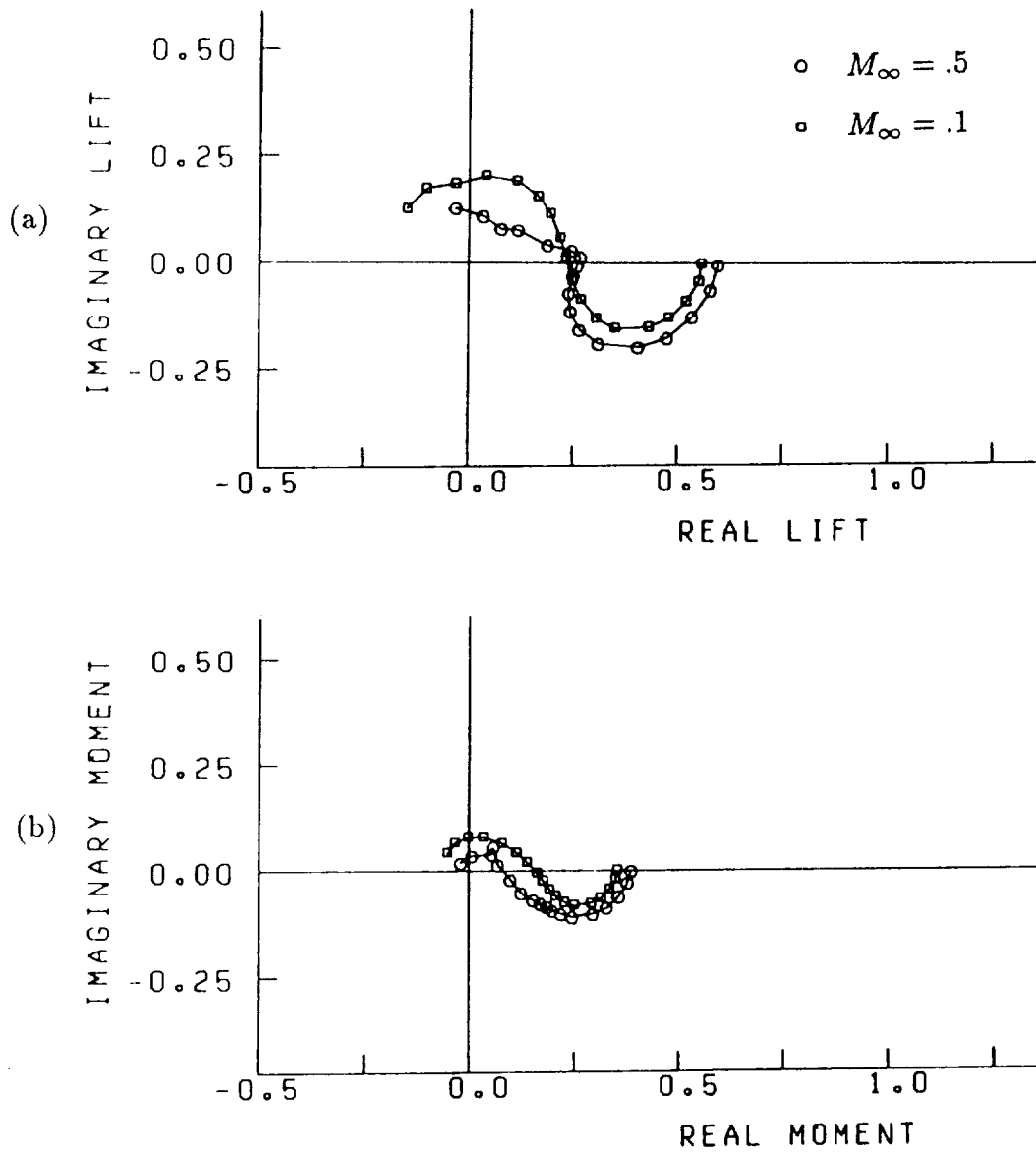
Figure 126. Effect of Mach number on (a) the unsteady lift and (b) the unsteady moment of a Joukowski airfoil in a transverse and longitudinal gust. thickness ratio = .12, $\alpha = 2^o$, camber = .05. $k_1 = 0.0, 0.01, 0.03, 0.06, 0.1, 0.2, 0.3, 0.45, 0.6, 0.8, 1.0,$ 1.3, 1.6, 2.0, 2.5, 3.0, 3.5, 4.0. $-a_1 = a_2 = .7071$, $k_1 = k_2$, $a_3 = k_3 = 0$.
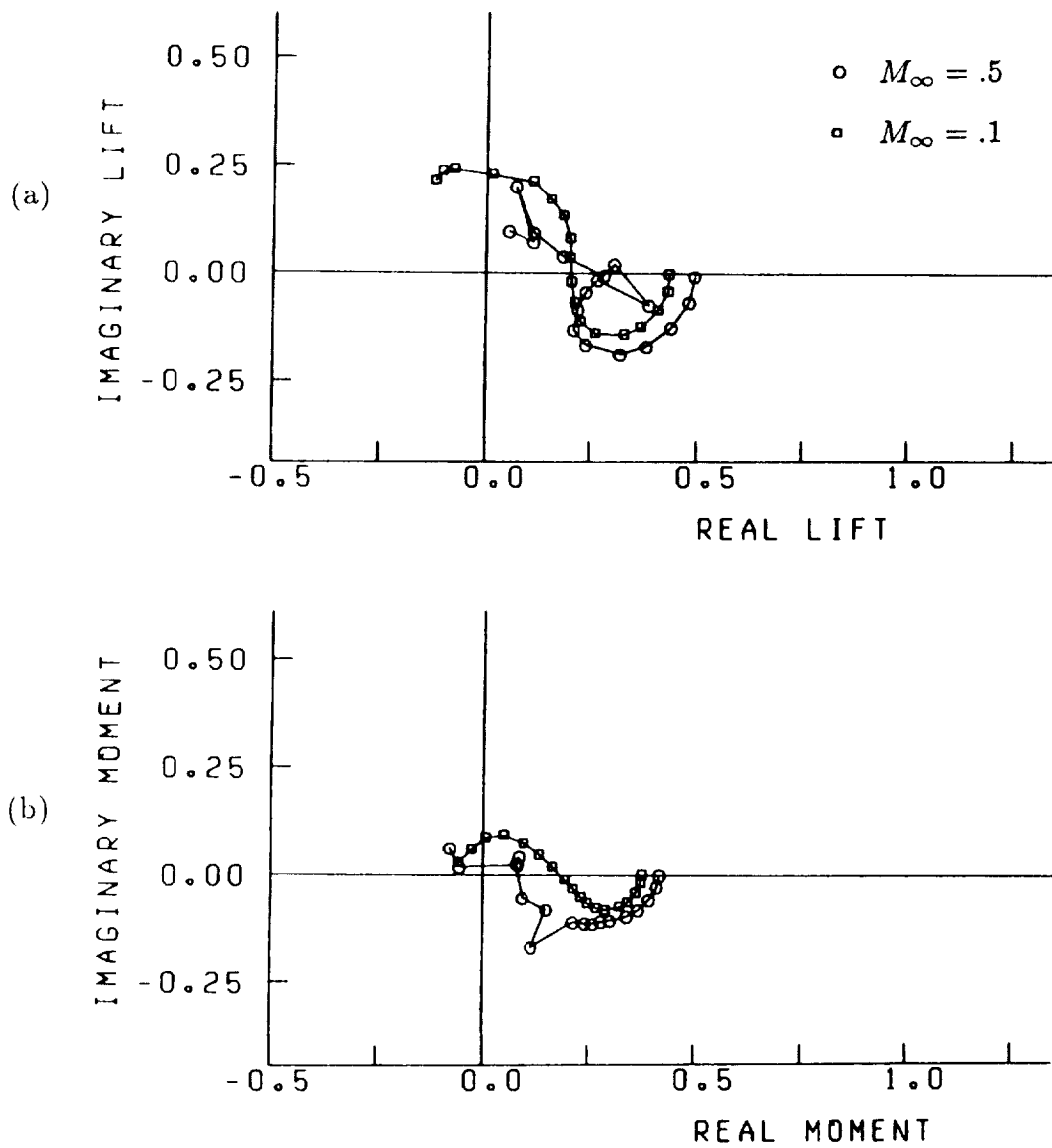
Figure 127. Effect of Mach number on (a) the unsteady lift and (b) the unsteady moment of a Joukowski airfoil in a transverse and longitudinal gust. thickness ratio = .12, $\alpha = 0^o$, camber = .10. $k_1 = 0.0, 0.01, 0.03, 0.06, 0.1, 0.2, 0.3, 0.45, 0.6, 0.8, 1.0,$ 1.3, 1.6, 2.0, 2.5, 3.0, 3.5, 4.0. $-a_1 = a_2 = .7071$, $k_1 = k_2$, $a_3 = k_3 = 0$.

Figure 128.   Effect of Mach number on (a) the unsteady lift and (b) the unsteady moment of a Joukowski airfoil in a transverse and longitudinal gust.   thickness ratio $= .12$, $\alpha = 3^{o}$,   camber $= 0$. $k_1 = 0.0$, 0.01, 0.03, 0.06, 0.1, 0.2, 0.3, 0.45, 0.6, 0.8, 1.0, 1.3, 1.6, 2.0, 2.5, 3.0, 3.5, 4.0. $-a_1 = a_2 = .7071$, $k_1 = k_2$, $a_3 = k_3 = 0$.

197
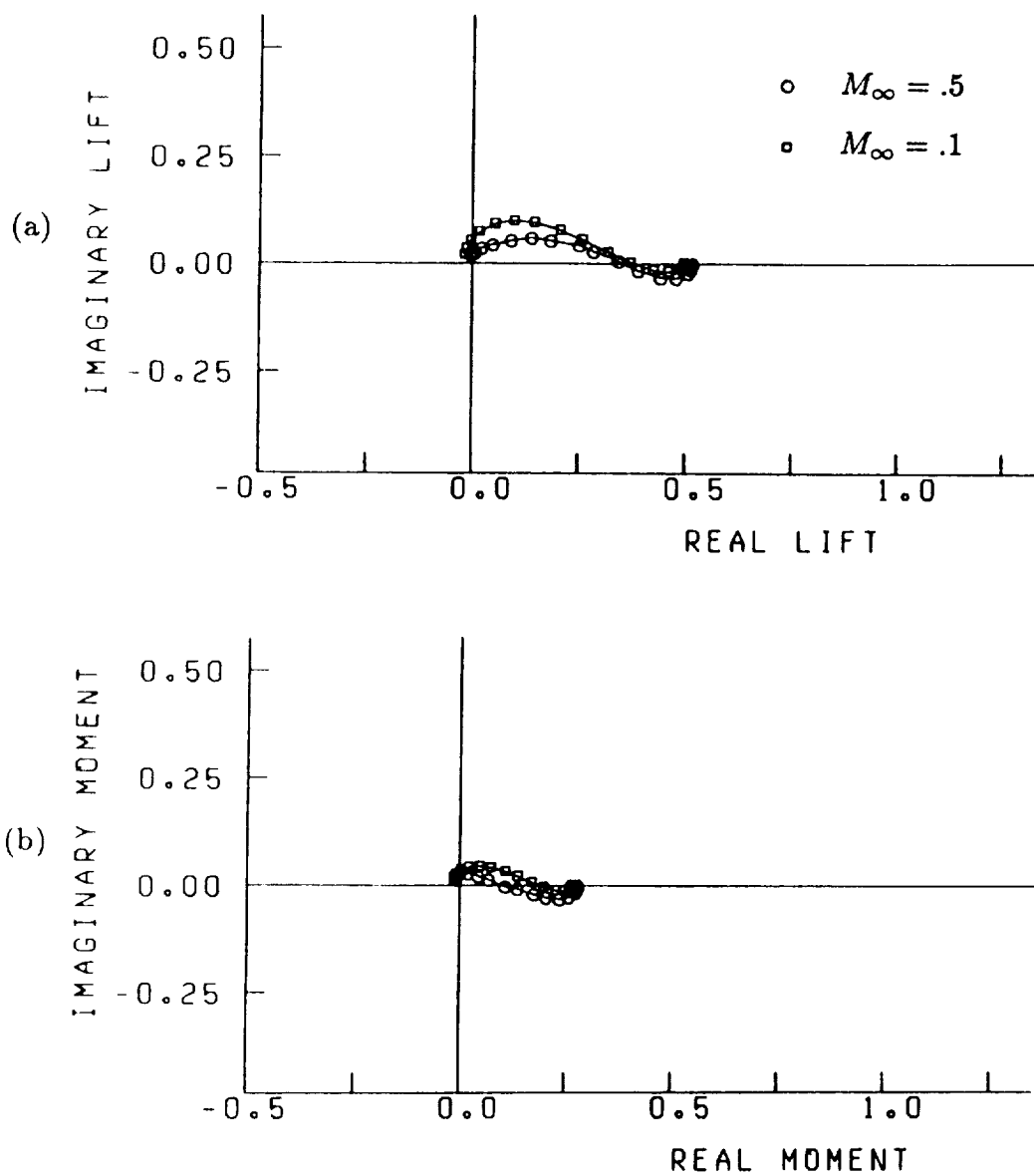
Figure 129. Effect of Mach number on (a) the unsteady lift and (b) the unsteady moment of a Joukowski airfoil in a three-dimensional gust. $\alpha = 0°$, thickness ratio $= .12$, camber $= 0$. $k_1 = 0.0$, $0.01, 0.03, 0.06, 0.1, 0.2, 0.3, 0.45, 0.6, 0.8, 1.0, 1.3, 1.6, 2.0, 2.5$, $3.0, 3.5, 4.0$. $k_3 = 0.4$, $|\vec{a}| = 1$, $\frac{a_2}{a_1} = -\frac{7}{4}$, $k_1 = k_2$, $\vec{a} \cdot \vec{k} = 0$, $a_2 > 0$.
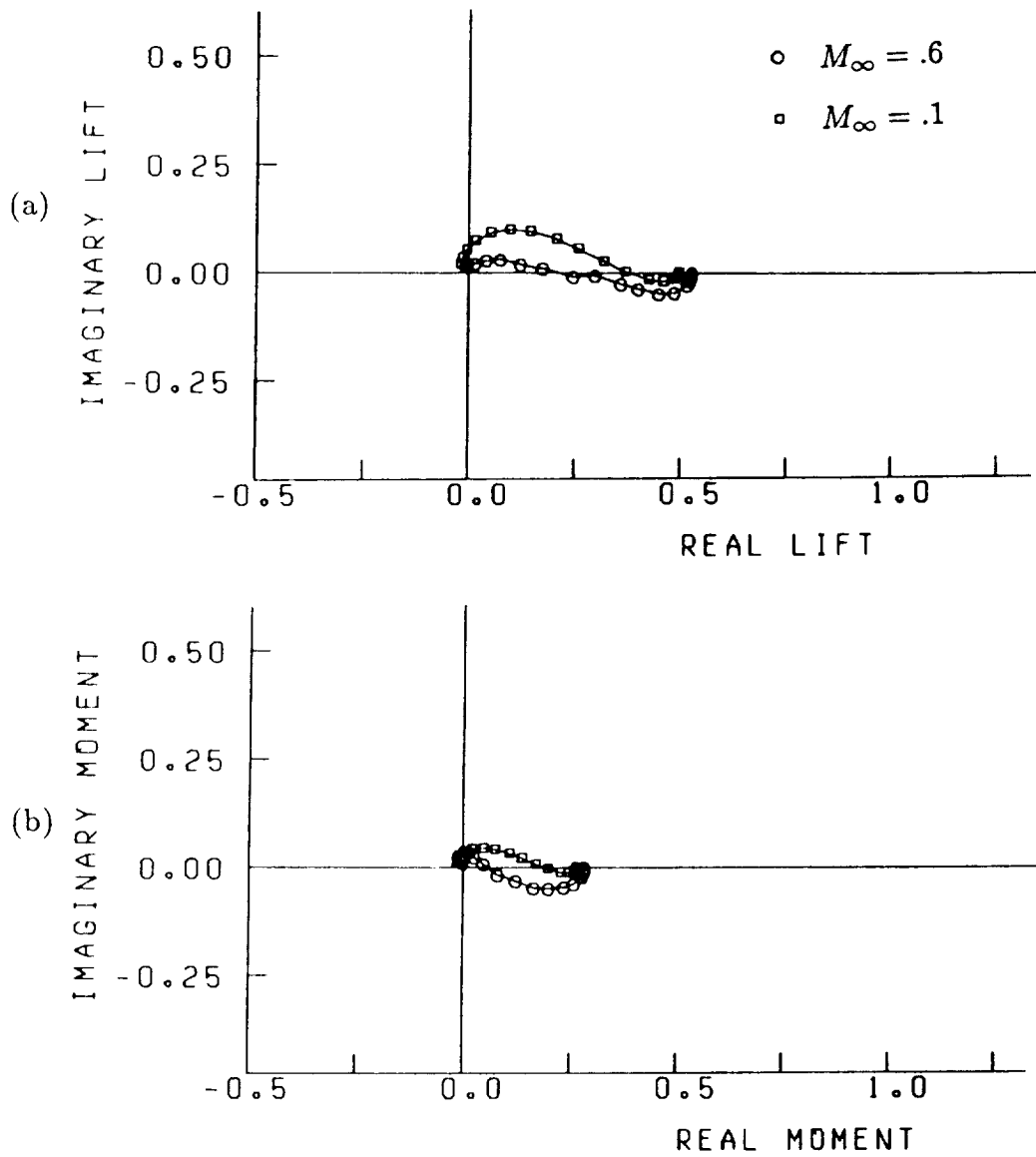
Figure 130. Effect of Mach number on (a) the unsteady lift and (b) the unsteady moment of a Joukowski airfoil in a three-dimensional gust. $\alpha = 0^o$, thickness ratio $= .12$, camber $= 0$. $k_1 = 0.0$, 0.01, 0.03, 0.06, 0.1, 0.2, 0.3, 0.45, 0.6, 0.8, 1.0, 1.3, 1.6, 2.0, 2.5, 3.0, 3.5, 4.0. $k_3 = 0.4$, $|\vec{a}| = 1$, $\frac{a_2}{a_1} = -\frac{7}{4}$, $k_1 = k_2$, $\vec{a} \cdot \vec{k} = 0$, $a_2 > 0$.

199
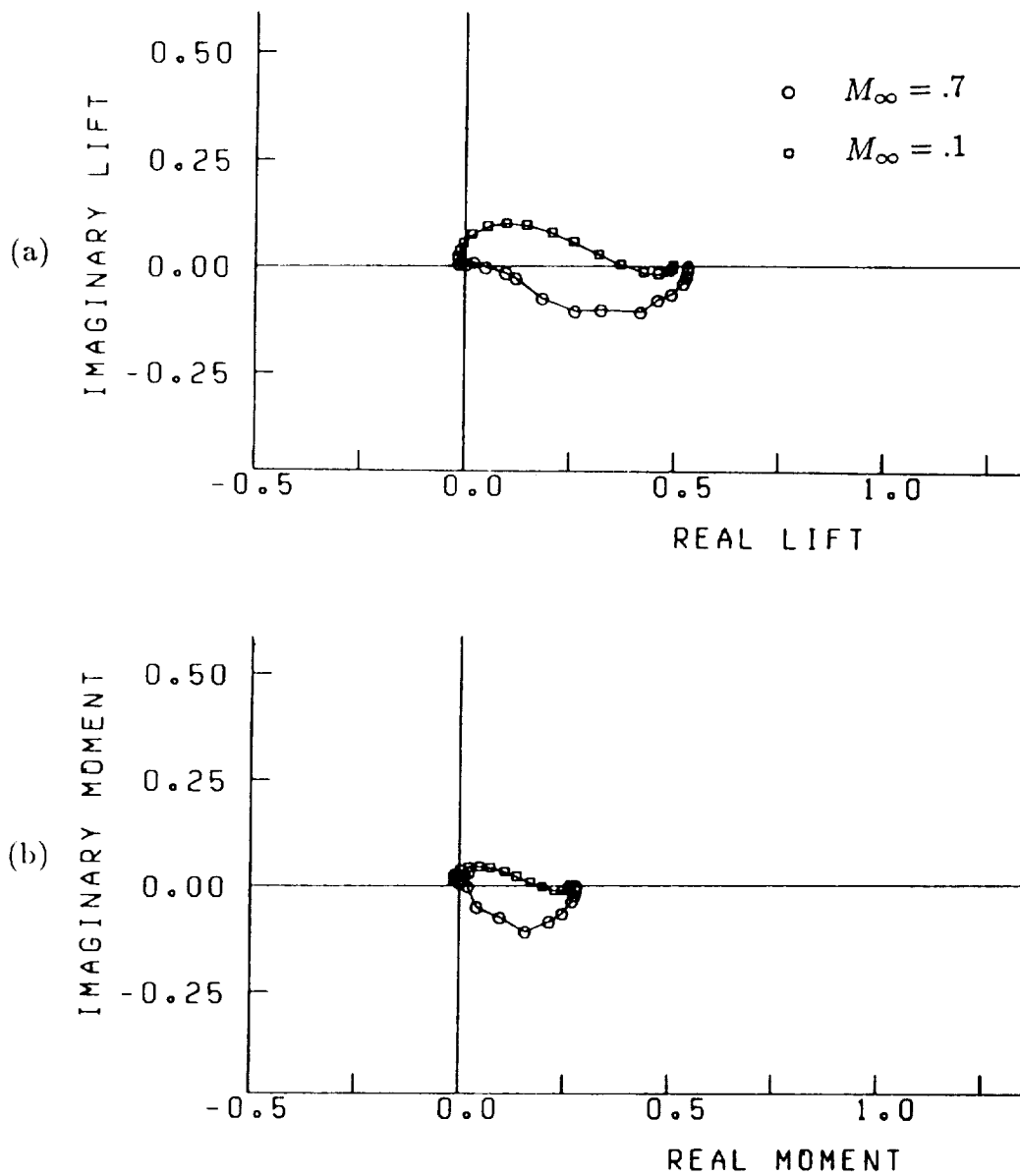
Figure 131. Effect of Mach number on (a) the unsteady lift and (b) the
unsteady moment of a Joukowski airfoil in a three-dimensional
gust. $\alpha = 0^o$, thickness ratio = .12, camber = 0. k_1 = 0.0,
0.01, 0.03, 0.06, 0.1, 0.2, 0.3, 0.45, 0.6, 0.8, 1.0, 1.3, 1.6, 2.0, 2.5,
3.0, 3.5, 4.0. $k_3 = 0.4$, $|\vec{a}| = 1$, $\frac{a_2}{a_1} = -\frac{7}{4}$, $k_1 = k_2$, $\vec{a} \cdot \vec{k} = 0$,
$a_2 > 0$.
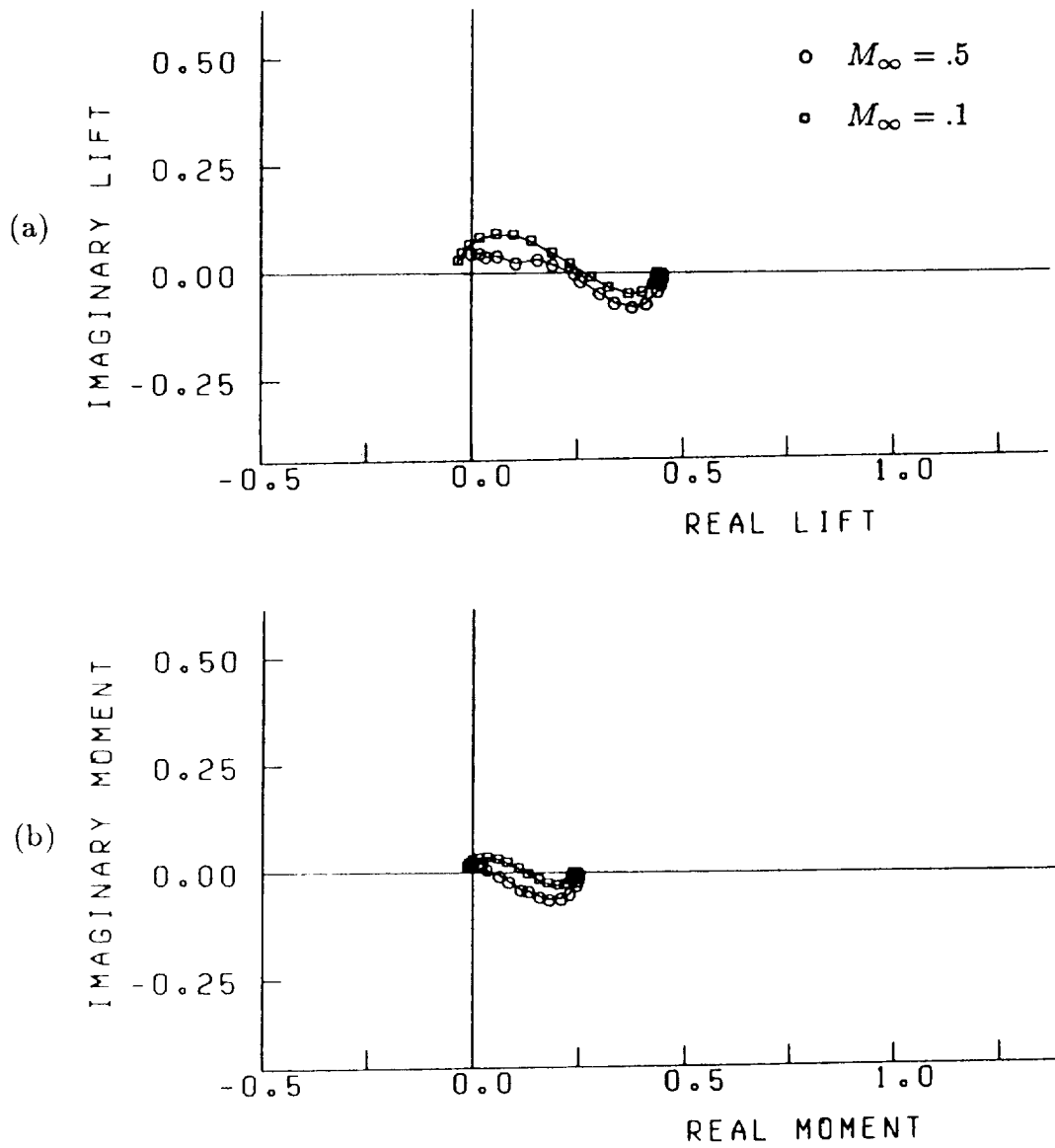
Figure 132. Effect of Mach number on (a) the unsteady lift and (b) the unsteady moment of a Joukowski airfoil in a three-dimensional gust. $\alpha = 5^\circ$, thickness ratio $= .12$, camber $= 0$. $k_1 = 0.0$, 0.01, 0.03, 0.06, 0.1, 0.2, 0.3, 0.45, 0.6, 0.8, 1.0, 1.3, 1.6, 2.0, 2.5, 3.0, 3.5, 4.0. $k_3 = 0.4$, $|\vec{a}| = 1$, $\frac{a_2}{a_1} = -\frac{7}{4}$, $k_1 = k_2$, $\vec{a} \cdot \vec{k} = 0$, $a_2 > 0$.
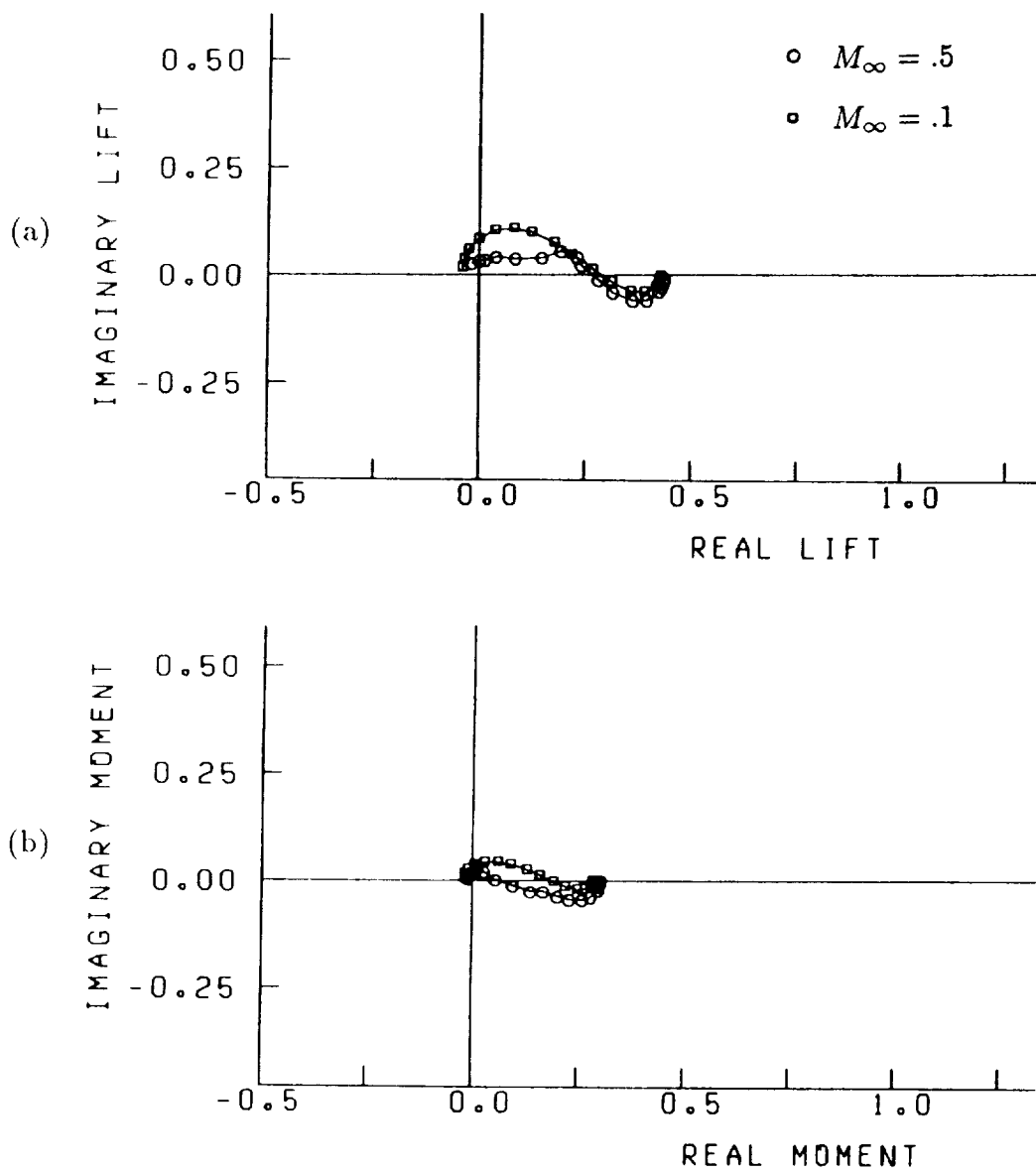
Figure 133. Effect of Mach number on (a) the unsteady lift and (b) the unsteady moment of a Joukowski airfoil in a three-dimensional gust. $\alpha = 0^o$, thickness ratio $= .12$, camber $= .05$. $k_1 = 0.0$, 0.01, 0.03, 0.06, 0.1, 0.2, 0.3, 0.45, 0.6, 0.8, 1.0, 1.3, 1.6, 2.0, 2.5, 3.0, 3.5, 4.0. $k_3 = 0.4$, $|\vec{a}| = 1$, $\frac{a_2}{a_1} = -\frac{7}{4}$, $k_1 = k_2$, $\vec{a} \cdot \vec{k} = 0$, $a_2 > 0$.
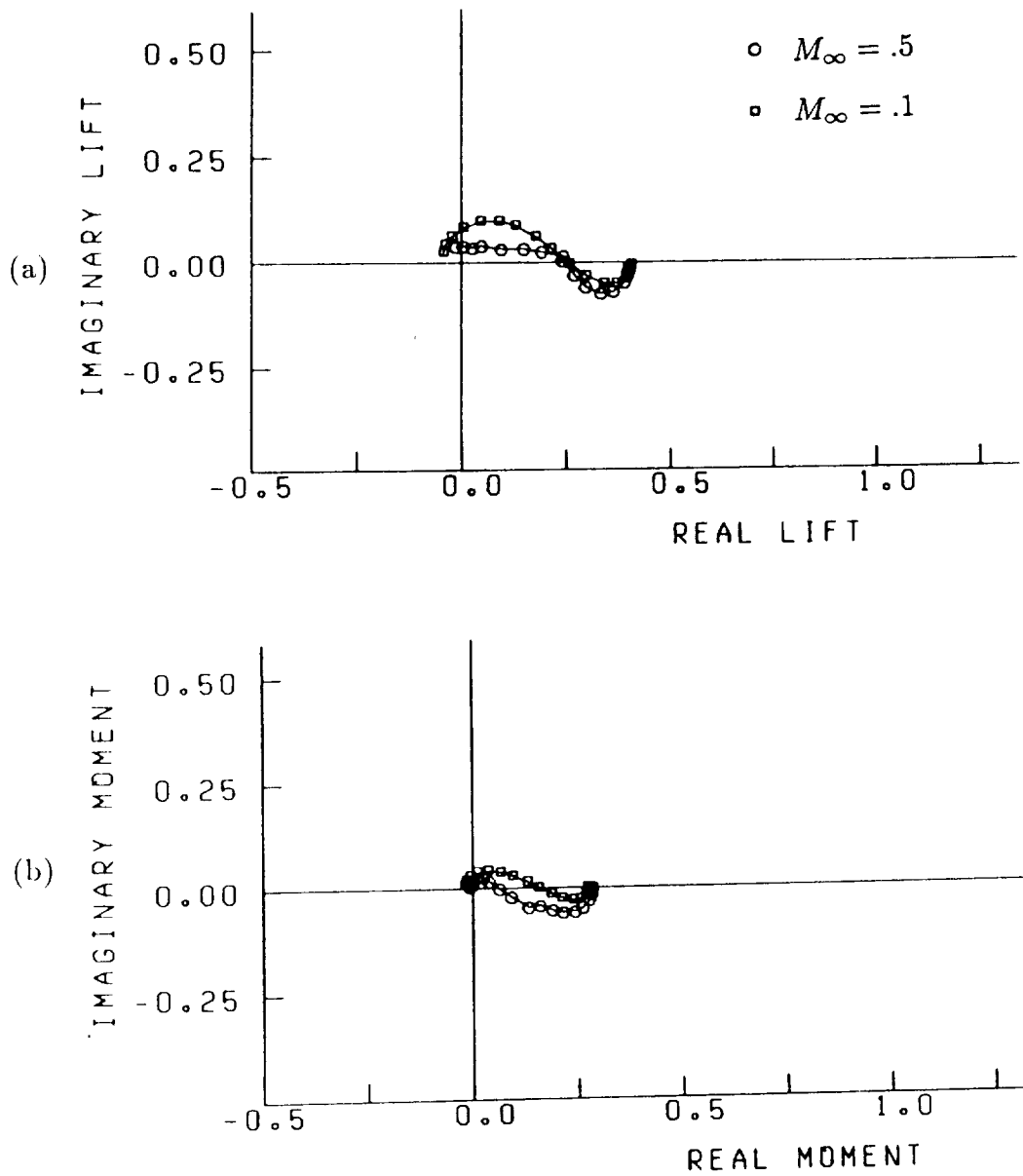
Figure 134.   Effect of Mach number on (a) the unsteady lift and (b) the unsteady moment of a Joukowski airfoil in a three-dimensional gust. $\alpha = 2^o$, thickness ratio $= .12$, camber $= .05$. $k_1 = 0.0$, 0.01, 0.03, 0.06, 0.1, 0.2, 0.3, 0.45, 0.6, 0.8, 1.0, 1.3, 1.6, 2.0, 2.5, 3.0, 3.5, 4.0. $k_3 = 0.4$, $|\vec{a}| = 1$, $\frac{a_2}{a_1} = -\frac{7}{4}$, $k_1 = k_2$, $\vec{a} \cdot \vec{k} = 0$, $a_2 > 0$.
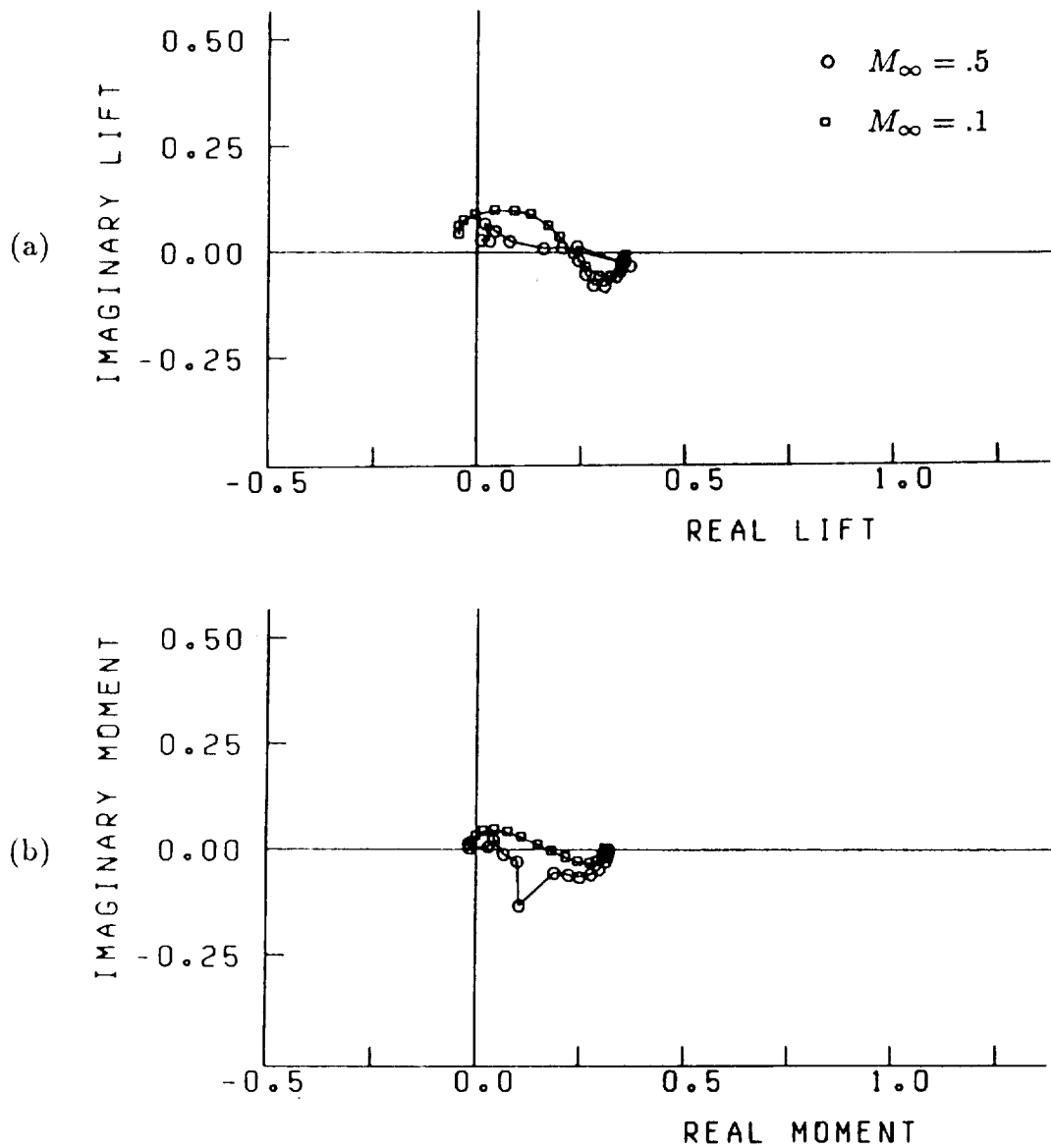
Figure 135. Effect of Mach number on (a) the unsteady lift and (b) the unsteady moment of a Joukowski airfoil in a three-dimensional gust. $\alpha = 0°$, thickness ratio = .12, camber = .10. $k_1 = 0.0$, 0.01, 0.03, 0.06, 0.1, 0.2, 0.3, 0.45, 0.6, 0.8, 1.0, 1.3, 1.6, 2.0, 2.5, 3.0, 3.5, 4.0. $k_3 = 0.4$, $|\vec{a}| = 1$, $\frac{a_2}{a_1} = -\frac{7}{4}$, $k_1 = k_2$, $\vec{a} \cdot \vec{k} = 0$, $a_2 > 0$.
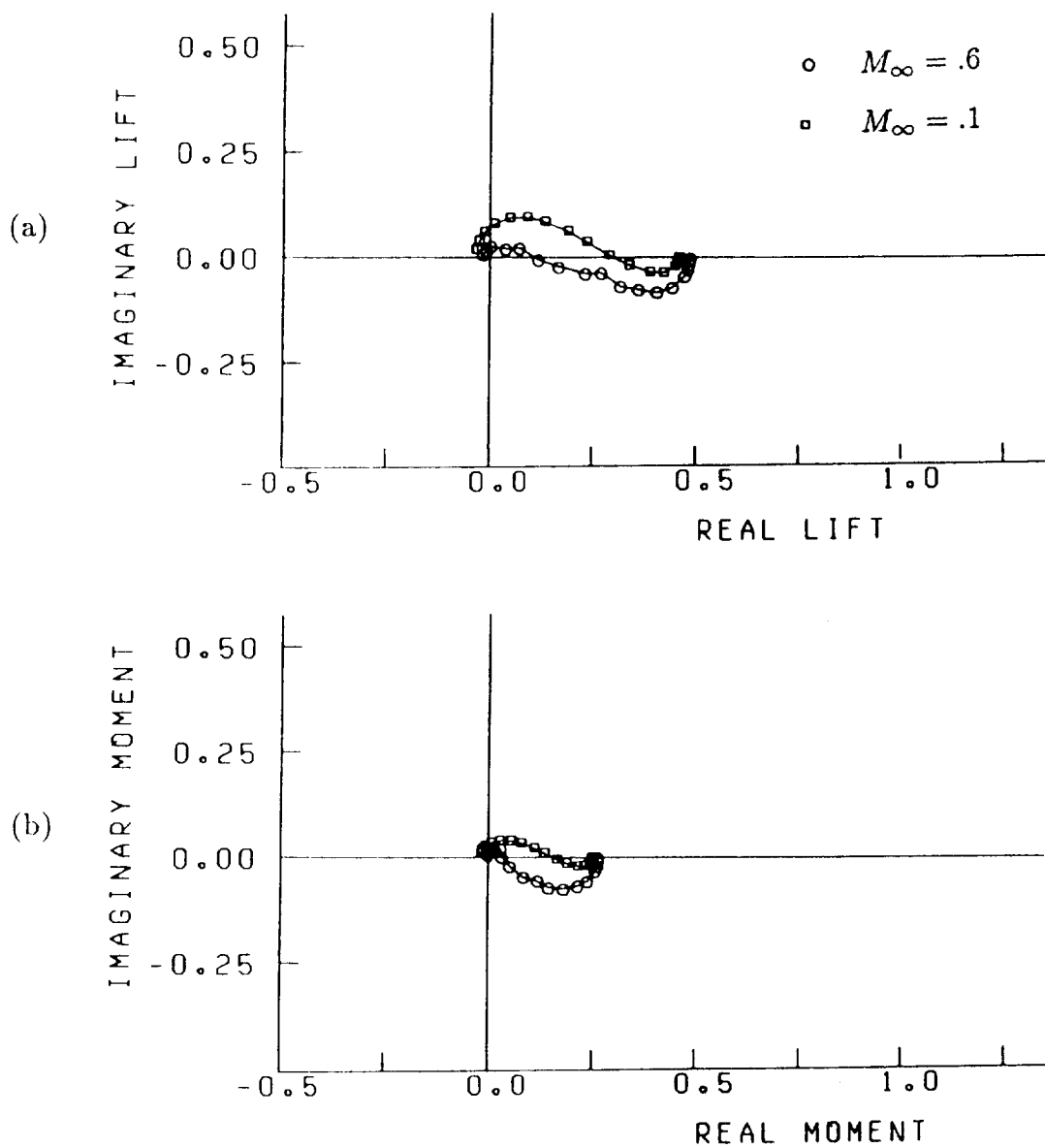
Figure 136. Effect of Mach number on (a) the unsteady lift and (b) the unsteady moment of a Joukowski airfoil in a three-dimensional gust. $\alpha = 3^o$, thickness ratio $= .12$, camber $= 0$. $k_1 = 0.0$, 0.01, 0.03, 0.06, 0.1, 0.2, 0.3, 0.45, 0.6, 0.8, 1.0, 1.3, 1.6, 2.0, 2.5, 3.0, 3.5, 4.0. $k_3 = 0.4$, $|\vec{a}| = 1$, $\frac{a_2}{a_1} = -\frac{7}{4}$, $k_1 = k_2$, $\vec{a} \cdot \vec{k} = 0$, $a_2 > 0$.

REFERENCES

1. Theodorsen, T., *NACA Tech. Rep. 496, 1935.*

2. Sears, W. R., "Some Aspects of Non-stationary Airfoil Theory and Its Practical Applications." *J. Aero. Sci.,* Vol. 8, No. 3, 1941, pp. 104-108.

3. Possio, C., "L'Azione Aerodinamica sul Profilo Oscillante in un Fluido Compressible a Velocita Ipsonora," *L'Aerotecnica XVIII,* 4, 1938.

4. Atassi, H. M., "Unsteady Vortical Disturbances Around Bodies," *Proceedings of the Tenth U. S. National Congress of Applied Mechanics,* J.P. Lamb, ed., ASME, 1986, pp. 475-484.

5. Horlock, J. H., *Trans. ASME D: Basic Engng* 90, 494, 1968.

6. Naumann, H., and Yeh., H., *ASME Paper* 72-GT-30, 1972.

7. Goldstein, M. E. and Atassi, H. M., "A Complete Second-Order Theory for the Unsteady Flow About an Airfoil Due to a Periodic Gust," *J. Fluid Mech.,* Vol. 74, 1976, pp. 741-765.

8. Atassi, H. M., "The Sears Problem for a Lifting Airfoil Revisited - New Results," *J. Fluid Mech.* Vol. 141, 1984, pp. 109-122.

9. Prandtl, L., "Attaining a Steady Air Stream in Wind Tunnels," NASA Tech. Memo., No. 726, 1933.

10. Taylor, G. I., "Turbulence in a Contracting Stream," *Z. Angew. Math. Mech.,* 15, 1935, pp. 91-96.

11. Ribner, H. S. and Tucker, M., "Spectrum of Turbulence in a Contracting Stream," *NACA Report No. 1113, 1953.*

12. Batchelor, G. K. and Proudman, I., "The Effect of Rapid Distortion of a Fluid in Turbulent Motion," *Quart. J. Mech. Appl. Math. 1,* 1954, pp. 83-103.

13. Graham, J. M. R., "Similarity Rules for Thin Aerofoils in Non-Stationary Subsonic Flows," *J. Fluid Mech.,* Vol. 43, 1970, pp. 753-766.

14. Ballhaus, W. F., and Goorjian, P. M., "Implicit Finite-Difference Computations of Unsteady Transonic Flows about Airfoils," *AIAA J.*, Vol. 15, Dec 1977, pp. 1728-1735.

15. Goorjian, P. M., "Implicit Computations of Unsteady Transonic Flow Governed by the Full Potential Equation in the Conservation Form," AIAA Paper 80-0150, 1980.

16. Sankar, N. L., Malone, J. B., and., Tassa, Y., "An Implicit Conservative Algorithm for Steady and Unsteady Three Dimensional Transonic Flows," AIAA Paper 81-1016, Palo Alto, CA, 1981, pp. 199-212.

17. Goorjian, P. M., and Guruswamy, G. P., "Unsteady Transonic Aerodynamic and Aeroelastic Calculations About Airfoils and Wings," NASA TM 85986, Aug., 1984.

18. Verdon, J. M., and Caspar, J. R., "A Linearized Unsteady Aerodynamic Analysis for Transonic Cascades," *J. Fluid Mech.*, Vol. 149, 1984, pp. 403-429.

19. McCroskey, W. J. and Goorjian, P. M., "Interactions of Airfoils with Gusts and Concentrated Vortices in Unsteady Transonic Flow," AIAA Paper 83-1691, July 1983.

20. McCroskey, W. J., "The Effects of Gusts on the Fluctuating Airloads of Airfoils in Transonic Flow," *Journal of Aircraft*, Vol. 22, No. 3, March 1985, pp. 236-243.

21. Giles, M., "Calculation of Unsteady Wake/Rotor Interactions," AIAA Paper 87-0006, Jan. 1985.

22. Rai, M. M., "Unsteady Three Dimensional Navier- Stokes Simulations of Turbine Rotor-Stator Interaction," AIAA Paper 87-2058, June 1987.

23. Jorgenson, P. C. E., and Chima, R. V., "An Explicit Runge-Kutta Method for Unsteady Rotor/Stator Interaction," AIAA Paper 88-0049, Jan. 1988.

24. Janus, J. M. and Whitfield, D. L., "A Simple Time-Accurate Turbomachinery Algorithm with Numerical Solutions of an Uneven Blade Count Configuration," AIAA Paper 89-0206, Jan. 1989.

25. Nallasamy, M., and Groeneweg, J., "Unsteady Euler Analysis of the Flow Field of a Propfan at an Angle of Attack," AIAA Paper 90-0339, Jan. 1990.

26. Goldstein, M. E., "Unsteady Vortical and Entropic Distortions of Potential Flows Round Arbitrary Obstacles," *J. Fluid Mech.*, Vol. 89, 1978, pp. 433-468.

27. Hunt, J. C. R., "A Theory of Turbulent Flow Round Two-Dimensional Bluff Bodies," *J. Fluid Mech.*, Vol. 61, 1973, pp. 625-706.

28. Atassi, H. M. and Grzedzinski, J., "Unsteady Disturbances of Streaming Motions Around Bodies," *J. Fluid Mech.*, Vol. 209, Dec. 1989, pp. 385-403.

29. Atassi, H. M. and Grzedzinski, J., "Three-Dimensional Periodic Distortions of Flows Around Lifting Airfoils," University of Notre Dame Report, Aerodynamics Group, No. 8, 1986.

30. Atassi, H. M. and Scott, J. R., "Analysis of Nonuniform Subsonic Flows About a Row of Moving Blades," *Proceedings of the Fourth International Symposium on Unsteady Aerodynamics and Aeroelasticity of Turbomachines and Propellers*, H. E. Gallus and S. Servaty, eds., Institute fur Strahlantriebe und Turbomachine, University of Aachen, Federal Republic of Germany, 1988, pp. 39-67.

31. Scott, J. R. and Atassi, H. M., "Numerical Solution of Periodic Vortical Flows About a Thin Airfoil," AIAA Paper 89-1691, June, 1989.

32. Dusey, M. P., "Acoustic Radiation from a Thin Airfoil in Nonuniform Subsonic Flow," M. S. Dissertation, University of Notre Dame, Notre Dame, IN, 1989.

33. Atassi, H. M. and Dusey, M. P., "Acoustic Radiation from a Thin Airfoil Due to Periodic Gusts in Subsonic Flows," Notre Dame Report in preparation, University of Notre Dame, Notre Dame, IN, 1990.

16. Abstract

A numerical method is developed for solving periodic, three-dimensional, vortical flows around lifting airfoils in subsonic flow. The first-order method that is presented fully accounts for the distortion effects of the nonuniform mean flow on the convected upstream vortical disturbances. The unsteady velocity is split into a vortical component which is a known function of the upstream flow conditions and the Lagrangian coordinates of the mean flow, and an irrotational field whose potential satisfies a nonconstant-coefficient, inhomogeneous, convective wave equation. Using an elliptic coordinate transformation, the unsteady boundary value problem is solved in the frequency domain on grids which are determined as a function of the Mach number and reduced frequency. The numerical scheme is validated through extensive comparisons with known solutions to unsteady vortical flow problems. In general, it is seen that the agreement between the numerical and analytical results is very good for reduced frequencies ranging from 0 to 4, and for Mach numbers ranging from .1 to .8. Numerical results are also presented for a wide variety of flow configurations for the purpose of determining the effects of airfoil thickness, angle of attack, camber, and Mach number on the unsteady lift and moment of airfoils subjected to periodic vortical gusts. It is seen that each of these parameters can have a significant effect on the unsteady airfoil response to the incident disturbances, and that the effect depends strongly upon the reduced frequency and the dimensionality of the gust. For a one-dimensional (transverse) or two-dimensional (transverse and longitudinal) gust, the results indicate that airfoil thickness increases the unsteady lift and moment at the low reduced frequencies but decreases it at the high reduced frequencies. It is seen that mean airfoil loading leads to a significant reduction in the unsteady lift for the low reduced frequencies for both the 2-D and 3-D gust cases, but has little effect for the 1-D case. Finally, the results show that an increase in airfoil Mach number leads to a significant increase in the unsteady lift and moment for the low reduced frequencies, but a significant decrease for the high reduced frequencies.

17. Key Words (Suggested by Author(s)) Vortical; Unsteady; Airfoils; Turbomachinery; Turboprop; Numerical; Propeller; Wings	18. Distribution Statement Unclassified – Unlimited Subject Category 02

19. Security Classif. (of this report) Unclassified	20. Security Classif. (of this page) Unclassified	21. No. of pages 213	22. Price* A05